NASA / TP-2000-209867

Investigation of Electromagnetic Field Threat to Fuel Tank Wiring of a Transport Aircraft

Jay J. Ely, Truong X. Nguyen, Kenneth L. Dudley, Stephen A. Scearce, and Fred B. Beck
Langley Research Center, Hampton, Virginia

Manohar D. Deshpande
NYMA, Inc., Hampton, Virginia

C. R. Cockrell
Langley Research Center, Hampton, Virginia

March 2000

The NASA STI Program Office ... in Profile

Since its founding, NASA has been dedicated to the advancement of aeronautics and space science. The NASA Scientific and Technical Information (STI) Program Office plays a key part in helping NASA maintain this important role.

The NASA STI Program Office is operated by Langley Research Center, the lead center for NASA's scientific and technical information. The NASA STI Program Office provides access to the NASA STI Database, the largest collection of aeronautical and space science STI in the world. The Program Office is also NASA's institutional mechanism for disseminating the results of its research and development activities. These results are published by NASA in the NASA STI Report Series, which includes the following report types:

- TECHNICAL PUBLICATION. Reports of completed research or a major significant phase of research that present the results of NASA programs and include extensive data or theoretical analysis. Includes compilations of significant scientific and technical data and information deemed to be of continuing reference value. NASA counterpart of peer-reviewed formal professional papers, but having less stringent limitations on manuscript length and extent of graphic presentations.

- TECHNICAL MEMORANDUM. Scientific and technical findings that are preliminary or of specialized interest, e.g., quick release reports, working papers, and bibliographies that contain minimal annotation. Does not contain extensive analysis.
- CONTRACTOR REPORT. Scientific and technical findings by NASA-sponsored contractors and grantees.
- CONFERENCE PUBLICATION. Collected papers from scientific and technical conferences, symposia, seminars, or other meetings sponsored or co-sponsored by NASA.

- SPECIAL PUBLICATION. Scientific, technical, or historical information from NASA programs, projects, and missions, often concerned with subjects having substantial public interest.

- TECHNICAL TRANSLATION. English-language translations of foreign scientific and technical material pertinent to NASA's mission.

Specialized services that complement the STI Program Office's diverse offerings include creating custom thesauri, building customized databases, organizing and publishing research results ... even providing videos.

For more information about the NASA STI Program Office, see the following:

- Access the NASA STI Program Home Page at *http://www.sti.nasa.gov*

- E-mail your question via the Internet to help@sti.nasa.gov

- Fax your question to the NASA STI Help Desk at (301) 621-0134

- Phone the NASA STI Help Desk at (301) 621-0390

- Write to:
  NASA STI Help Desk
  NASA Center for AeroSpace Information
  7121 Standard Drive
  Hanover, MD 21076-1320

NASA / TP-2000-209867

Investigation of Electromagnetic Field Threat to Fuel Tank Wiring of a Transport Aircraft

Jay J. Ely, Truong X. Nguyen, Kenneth L. Dudley, Stephen A. Scearce, and Fred B. Beck
Langley Research Center, Hampton, Virginia

Manohar D. Deshpande
NYMA, Inc., Hampton, Virginia

C. R. Cockrell
Langley Research Center, Hampton, Virginia

National Aeronautics and
Space Administration

Langley Research Center
Hampton, Virginia 23681-2199

March 2000

The use of trademarks or names of manufacturers in this report is for accurate reporting and does not constitute an official endorsement, either expressed or implied, of such products or manufacturers by the National Aeronautics and Space Administration.

Available from:

NASA Center for AeroSpace Information (CASI)
7121 Standard Drive
Hanover, MD 21076-1320
(301) 621-0390

National Technical Information Service (NTIS)
5285 Port Royal Road
Springfield, VA 22161-2171
(703) 605-6000

Acknowledgements

NSWC Contributors: Michael O. Hatfield, Robert E. Richardson, and Arturo Lopez. Mr. Hatfield provided consultation and technical expertise regarding the selection of a retired aircraft, and in performing the aircraft measurements. His knowledge of reverberation measurement methodology, instrumentation and theory were highly valued in developing a efficient and effective means of collecting aircraft data. Dr. Richardson provided consultation, and performed time-domain comparison measurements to supplement the aircraft CWT reverberation data reported in Section 4.4.2.1. He also performed the isolated fuel probe tests reported in Section 4.4.4. Mr. Lopez provided the UVTRON® ionization detection devices, along with associated circuitry, and advice.

LTI Contributors: Franklin A. Fisher, Edward J. Rupke, J. Anderson Plumer, Keith Crouch. Mr. Fisher was a valuable resource in the areas of electrical sparks and factors governing the ignition of aircraft fuel. As part of this investigation, Mr. Fisher provided a report outlining a traditional understanding of electrical breakdown, heating, and fuel combustion, and supplements the knowledge with available information regarding aircraft fuel-vapor ignition by RF sources. Mr. Rupke, Mr. Plumer, and Mr. Crouch provided valuable consultation regarding aircraft wiring inspections, detection of electrical discharge, and fuel combustion processes.

Douglas J. Hughes: IIT Research Institute, JSC Support Group. Mr. Hughes provided manufacturers data regarding PED emissions, that served as a basis for additional analysis reported herein. Also, Mr. Hughes provided supplemental data regarding RF sources below 30 MHz frequency, external to TWA-800 at the time of the accident.

Thomas G. Campbell: Head, Electromagnetics Research Branch (ERB), Airborne Systems Competency, for developing the relationship with the NTSB and initiating the reimbursable task agreements which enabled the LaRC investigations.

Reuben A. Williams: Responsible for managing the High Intensity Radiated Fields Laboratory (ERB) in support of numerous experiments as part of this activity. In addition, Mr. Williams provided significant contributions at critical stages of this project, which enabled the overall success of the LaRC effort. Examples of this support include developing an effective and timely contract with AAR for EM testing on a center wing fuel tank, procuring the necessary sensors for laboratory FQIS testing; and for the overall resource allocations for all LaRC tasks.

Max Williams, Lockheed-Martin Corporation: Fabrication and design of numerous laboratory setups and test fixtures. The experimental test goals of this effort could not have been achieved without the assistance of Mr. Williams.

Sandra Koppen, Lockheed – Martin, Corporation: Test control software was required for laboratory and remote operations with little preparation time, and a high degree of reliability. Ms. Koppen was responsible for all data acquisition and control software used in experimental testing, as well as assistance reviewing the final draft.

Bob Glover, Lockheed-Martin Corporation: Assisted with the seemingly impossible task setting up a contractual mechanism for enabling AAR Roswell to be funded in the short period of time required to support the test schedule. Remote test operations could not have occurred without his support.

Elden Ross, Self-employed: Assisted LaRC engineers with information sources and timely updates to relevant aircraft accident and incident reports and articles. Performed an in-depth ASRS and PED incident data analysis as a supplementary tool related to the effort.

Acknowledgements continued

AAR Roswell: Provided retired aircraft access and mechanical support. The value of the measurement data is directly related to the fact that aircraft fuel tank measurements were performed. This would not have been possible otherwise.

Elite Structural Services: Several 12-hour days were required for remote operations to collect the required fuel tank data. The efficiency and professionalism of the Elite Structural Services team was crucial to these aircraft measurement tasks.

Tony Clark: (NASA Marshall Space Flight Center): Mr. Clark provided unique references regarding dielectric breakdown in alternating fields. This information was related to previous programs (some decades old), supported by previous MSFC researchers. Much of this information could not be found in other references.

Stephen A. Borg: Mr. Borg, of the LaRC Aerodynamic Measurements Branch, was a resource for providing and operating the Thermal Imaging System in the laboratory testing. In addition to his other assigned duties, his expertise and willingness to support the test schedule was greatly appreciated.

Brian H. Bailie: Mr. Bailie was instrumental in assembling the original cover page, contents section, and converting the Appendix D to electronic form. He was also a valuable resource for assembling interim presentations during the effort.

Contents

i Abstract vii
ii Executive Summary vii
iii Symbols and Abbreviations ix

1 Introduction 1
1.1 Background Information. 1
1.2 Areas and Limits of the Investigation. 2
1.3 Approach. 2
1.3.1 Quantifying the Source [A(f)] 3
1.3.2 Estimating the Path Factor [B(f)], Phased Approach 4
1.3.3 Estimating the Event Power [C(f)] 4
1.3.4 Appendices 5
1.4 Participating Agencies. 5
1.5 References for Section 1 5

2 FQIS and Aircraft Description 5
2.1 The Capacitive Fuel Probe 8
2.2 Connectors and Cables 9
2.3 References for Section 2 12

3 Determination of Threat from RF Sources ***External*** to Aircraft 13
3.1 Introduction. 13
3.2 Symbols for Section 3 14
3.3 Initial Analysis 15
3.3.1 Estimation of Maximum Available Energy 15
3.3.2 TWA Electromagnetic Environment versus Standard HIRF Environments. 16
3.4 Analytical Modeling 18
3.4.1 Development of the Method of Moments. 20
3.4.2 Input Impedance of FQIS Wire. 23
3.4.3 Energy Delivered to CWT by FQIS Wire. 23
3.5 Numerical and Experimental Validation of the Modal/MoM Code. 25
3.6 Numerical Estimation of EM Threat to the CWT of a B-747-100 Due to FQIS Wiring. . 32
3.6.1 Choice of Frequency Sampling 32
3.6.2 Choice of Number of Cavity Modes 33
3.6.3 Choice of Number of Aperture Modes 33
3.6.4 FQIS Wire Length Selection 33
3.6.5 CPU Time Requirement 38
3.7 Conclusions for External Analysis 39
3.8 References for Section 3 39

4 Determination of Threat from Portable RF Sources ***Internal*** to Aircraft. 41
4.1 Introduction. 41
4.1.1 Baseline Measurement on Actual Aircraft 41
4.1.2 Acquisition of FQIS Components, Installation in Laboratory 43
4.1.3 Duplication of Field Measurements in Laboratory, Comparisons 44
4.1.4 Detailed Measurements in Laboratory 44
4.1.5 Detailed Outline of Section 4 45

4.2 Symbols for Section 4 47
4.3 Estimation of Threat From Typical PEDs 48
4.3.1 Portable Transmitters' Manufacturer Specifications 48
4.3.2 Typical Transmitter Characteristics Based on ANSI C63.18-1997 48
4.3.3 Determination of FCC Limits 49
4.3.4 Summary of PED Threat Levels 49
4.4 Characterization of Aircraft and Laboratory FQIS Installations 51
4.4.1 FQIS Impedance Measurements. 51
4.4.2 Cavity Reverberation Measurements 71
4.4.3 Aircraft Measurements of Passenger Cabin Coupling to CWT and CWT FQIS Wiring 84
4.4.4 Isolated Fuel Probe Tests. 97
4.4.5 Detailed Measurement of FQIS Installed in Laboratory 101
4.5 RF Induced Ionization, Discharge, Heating of FQIS Installed in Laboratory Chamber . 119
4.5.1 Estimation of CWT Voltage and Current Magnitudes Induced by RF 119
4.5.2 "Weakening" of Worst-Case Test Points 125
4.5.3 Detection Methods 126
4.5.4 Validation of Discharge Detection Devices with Electrostatic Discharge Gun . . . 128
4.5.5 "Full" PED Threat Level Test 130
4.5.6 Minimum Power for Discharge Test 133
4.5.7 Supplementary Analysis Regarding Threats Below 30 MHz 136
4.6 Conclusions for Internal Analysis 139
4.7 References for Section 4 140

5 Final Discussion and Overall Conclusions 141
5.1 Results of External Analysis 141
5.2 Results of Internal Analysis 142
5.3 Notes and Applicability 143

Appendix A: Definition of Terms A-1
Appendix B: Comparison of CWT Cavity Q with and Without the Antennas B-1
Appendix C: Mismatch Correction for Out-of-Band Antenna and 50 Ohms Cable Adapter . . . C-1
Appendix D: FQIS Impedance Measurement Theory D-1
Appendix E: Statistical Analysis of Transmission Line Impedance Using the Smith Chart E-1
Appendix F: RF Induced Voltage and Current Measurements in the Laboratory F-1
Appendix G: Manufacturers' Data of Representative Portable Intentional Transmitters G-1
Appendix H: Partial List of FCC Limits on PEDs H-1

Abstract

National Transportation Safety Board investigators have questioned whether an electrical discharge in the Fuel Quantity Indication System (FQIS) may have initiated the TWA-800 center wing tank explosion. Because the FQIS was designed to be incapable of producing such a discharge on its own, attention has been directed to mechanisms of outside electromagnetic influence. To support the investigation, the NASA Langley Research Center was tasked to study the potential for radiated electromagnetic fields from external radio frequency (RF) transmitters and passenger carried portable electronic devices (PEDs) to excite the FQIS enough to cause arcing, sparking or excessive heating within the fuel tank.

ii Executive Summary

The National Transportation Safety Board (NTSB) funded NASA Langley Research Center (LaRC) to perform two separate analysis tasks, with respect to the explosion of the center wing fuel tank (CWT) in the Trans World Airlines Flight 800 (TWA-800) accident. The first task was to use the "TWA Flight 800 Electromagnetic Environment" report, prepared by the Department of Defense Joint Spectrum Center (JSC), to determine worst-case energy levels that were available to couple onto fuel quantity indication system (FQIS) components from external radio frequency (RF) transmitters (military/civilian airborne, ship-based or ground-based). The second task was to investigate the threat from passenger carried portable electronic devices (PEDs).

For the first task, NASA LaRC researchers developed a new Modal Analysis/Method of Moments (MoM) code and demonstrated that it provides accurate results. The computational efficiency of the new code allows it to be applied to a volume comparable to that of a Boeing 747 Series 100 (B-747-100) passenger cabin. The frequency of a dominant external emitter was selected from the JSC report, and used to predict passenger cabin shielding effectiveness, and to model situations of wire coupling within the passenger cabin.

Two separately funded phases were proposed for the PED task. The purpose of Phase 1 was to study whether a typical PED could create an ionization event or excessive heating, if *all available* power was applied directly to the CWT FQIS wiring. The purpose of Phase 2 was to perform extensive computational aircraft modeling and aircraft coupling measurements to advance the understanding of how much power PEDs may induce onto aircraft wiring, and factors that may influence this coupling. Phase 1 of the PED task was funded, and is reported herein.

The Phase 1 test plan consisted of the following analysis and experimental testing:

1. Determination of a worst-case electromagnetic (EM) threat that may have been created by commercially available PEDs (in terms of power and frequency).
2. Characterization of the CWT and FQIS of a B-747-100 aircraft in terms of input impedance and cavity reverberation characteristics.
3. Removal of fuel probes and wiring from a retired B-747-100 aircraft and the subsequent installation of these components into a laboratory test chamber. Determination of RF power

required to achieve an ionization event or excessive heating in the laboratory installation.

4. Determination of scaling factors required to compare the aircraft and laboratory FQIS installations.
5. Assessment of existing guidelines and references for understanding how continuous RF signals may impart sufficient energy to ignite fuel vapors.

The NASA LaRC engineering team, partnering with Lightning Technologies, Inc. (LTI) and the Naval Surface Warfare Center (NSWC), successfully completed all required tasks. Item 5 from the above list was addressed in a separate report (NASA/TM-2000-210077). In addition, an engineering judgement was made to perform some limited coupling measurements originally designated as part of Phase 2. These measurements proved to be important for conclusion #2 below.

Conclusions:

1. Analysis was performed on the external RF transmitters identified by the JSC as *dominant emitters*. These dominant emitters were all pulsed sources, allowing the threat to be quantified in terms of energy, instead of power. The maximum available energy inside the TWA-800 passenger cabin from any dominant emitter was determined to be less than 0.1 mJ, which was below generally accepted estimates of the minimum energy level required to achieve ignition. A new NASA LaRC developed numerical analysis code estimated that the CWT FQIS coupled energy levels were several orders of magnitude less than the maximum available energy.

2. It was determined that the threat from most commercially available PEDs existed between 27 MHz and 1 GHz frequency, and was limited to less than 10 W of radiated power. A minimum power level of 10 W was applied to the FQIS terminals in the laboratory installation over a frequency band of 25 MHz to 1 GHz, with no electrical discharge or significant heating detected. However, by inducing an intermittent short circuit at a worst-case location for voltage enhancements, discharge events were induced when applying as little as 1.5 W of RF power. Considering the passenger cabin to CWT FQIS coupling loss, 1.5 W was at least 10 times greater than the maximum PED threat, even if the PED transmitted from an optimal coupling location in the passenger cabin.

3. Laboratory testing to determine the absolute minimum power required for a discharge was extended from 25 MHz down to 1 MHz frequency. This testing revealed that an intermittent short circuit could cause FQIS discharge events with as little as 0.17 W of power at frequencies below 10 MHz, when the short was placed at a worst-case location for voltage enhancements. While this finding was unexpected, analysis revealed that the whole TWA-800 aircraft could not have coupled more than 0.015 W of power in this frequency range from the surrounding EM environment at the time of the accident. Commercially available PEDs were determined to be insignificant in terms of radiated power below 25 MHz.

This effort focused exclusively on coupling and the potential for ionization/heating caused by FQIS components within the CWT, as the system is excited by non-aircraft generated EM signals. Aviation safety reporting databases indicate that such signals are far more likely to interfere with, and even damage, sensitive aircraft navigation sensors, displays, processors, and communication equipment.

iii Symbols and Abbreviations

$[C]$	Mutual coupling matrix between apertures and wire
U_{pr}	Amplitude of pth mode on r^{th} aperture
$[I_{rp}]$	Column matrix representing coupling between incident field and apertures
$[U]$	Column matrix representing modal amplitudes on apertures
$E_L(f)$	Complex energy density
x_{cr}, y_{cr}	Coordinates of center of rth aperture
d_0	Diameter of the FQIS wire
$\vec{J}_p$	Electric current along the FQIS wire
EFS	Electric Field Shielding
$\vec{M}_{rx}$	Equivalent magnetic current in the x-direction over r^{th} aperture
$\vec{M}_{ry}$	Equivalent magnetic current in the y-direction over r^{th} aperture
Δf	Frequency increment
$\vec{E}_{in}$	Incident electric field
$\vec{H}_{in}$	Incident magnetic field
$Z_{in}(f)$	Input impedance of the FQIS wire
L_r, W_r	Length and width of rth aperture
L_w	Length of the FQIS wire
$V_0(f)$	Open circuit voltage
Z_{ww}	Self impedance of the FQIS wire
$[Y]$	Square matrix representing mutual coupling between apertures
$\vec{E}_{apt}$	Total aperture field
I_0	Total current of FQIS wire
$\hat{n}$	Unit normal vector
$\hat{l}$	Unit vector along the FQIS wire
$\hat{x}, \hat{y}$	Unit vectors in the x – and y- directions, respectively
$\vec{E}_{ext}(\vec{M}_{rx})$	Scattered electric field (external)
$\vec{E}_{\text{int}}(\vec{M}_{rx})$	Scattered electric field (internal)

$\vec{H}_{ext}(\vec{M}_{rx})$	Scattered magnetic field (external)
$\vec{H}_{\text{int}}(\vec{M}_{rx})$	Scattered magnetic field (internal)
η_0	Free space impedance
τ	Pulse width in sec
Γ	Reflection Coefficient Magnitude= $\lvert\bar{\Gamma}\rvert$
$\bar{\Gamma}$	Complex Reflection Coefficient
λ	Wavelength
π	Pi. The circumference divided by the diameter of a circle.
(a,b,c)	x-, y-, and z-dimensions of rectangular cavity
A	Amplitude in volts/meter
A(f)	Source Power
AAR	AAR Aircraft Services, Inc., Roswell Division
AC	Alternating Current
AC/AMJ	Advisory Circular / Advisory Material Joint
ANSI	American National Standards Institute
Ant	Antenna
ASRS	Aviation Safety Reporting System
B(f)	Path Factor
B-747-100	Boeing-747 Series-100
C	Capacitance
C(f)	Event! Power, Minimum RF power required at FQIS connector for ionization event
CB	Citizens Band
CE(f)	Current Enhancement as a function of frequency
CISPR	Comite International Special des Perturbations Radioelectriques, International Special Committee on Radio Interference
CPU	Central Processing Unit
CTF	Current Transfer Function
CVSF	Current-Voltage Sampling Fixture
CWT	Center Wing Tank
dB	Decibel
dBi	Decibel referenced to an isotropic radiator
dBm	Decibel referenced to 1 mW
dBm/ m^2	Decibels referenced to 1 mW/m^2 (Power Density)
DoD	Department of Defense
DUT	Device Under Test
E	Electric Field

EEHWG	Electromagnetic Effects Harmonization Working Group
EFS	Electric Field Shielding
EIRP	Effective Isotropic Radiated Power
EM	Electromagnetic
EMI	Electromagnetic Interference
f	Frequency
f_c	Carrier Frequency
FCC	Federal Communications Commission
FDTD	Finite Difference Time Domain
FEM	Finite Element Method
FQIS	Fuel Quantity Indication System
GHz	GigaHertz (one billion cycles per second)
GMRS	General Mobile Radio Service
GPIB	General Purpose Interface Bus
G_{rcv_max}	Maximum Gain of a receiving antenna
G_{trans_max}	Maximum Gain of a transmitting antenna
H	Magnetic Field
HI Z	High Impedance
HIRF	High Intensity Radiated Fields
HP VEE	Hewlett Packard Visual Engineering Environment
H-pol	Horizontal Polarization
I(f)	Current as a function of frequency
IEC	International Electrotechnical Commission
IF_{probe}	current probe transfer function
J	Joules (Energy)
JSC	Joint Spectrum Center
kHz	kiloHertz (one thousand cycles per second)
LAN	Local Area Network
LaRC	Langley Research Center
LO Z COMP	Low Impedance Compensator
LO Z	Low Impedance
LTI	Lightning Technologies, Inc.
m	meter
MHz	MegaHertz (one million cycles per second)
MIL-STD	Military Standard
mJ	milliJoules (Energy)
mJ/m^2	milliJoules per meter squared (Energy Density)

MoM	Method of Moments
NASA	National Aeronautics and Space Administration
NAWCAD	Naval Air Warfare Center Aircraft Division
NIST	National Institute of Standards and Technology
NMi	Nautical Mile
NSWC	Naval Surface Warfare Center
NSWCDD	Naval Surface Warfare Center Dahlgren Division
NTSB	National Transportation Safety Board
P	Power
PCS	Personal Communication Services
PED	Portable Electronic Device or Personal Electronic Device
PRF	Pulse Repetition Frequency
Q	Quality Factor
R	Slant Range between two antennas
R_{ch}	Resistance of a charging resistor
R_d	Resistance of a discharging resistor
RF	Radio Frequency
RTCA	RTCA, formerly Radio Technical Committee on Aeronautics
R_x	Receive or Receiver
SA	Surface area (total)
sec	seconds
SHLD	Shield
SUT	System Under Test
TP	Test Point
TWA	Trans World Airlines
TWA-800	Trans World Airlines Flight 800
T_x	Transmit or Transmitter
U	Total energy
U_D	Energy density
V	Volts or Voltage
V(f)	Voltage as a function of frequency
V/cm	Volts per centimeter
V/m	Volts per meter (Field Intensity)
VE(f)	Voltage Enhancement as a function of frequency
VF_{probe}	voltage probe transfer function
V_{out}	Output Voltage
V-pol	Vertical Polarization

VSO	Volumetric Shutoff Control Unit
VSWR	Voltage Standing Wave Ratio
VTF	Voltage Transfer Function
W	Watts
Z	Impedance
Z_{in}	Input Impedance
Z_L	Load Impedance
Z_o	Characteristic Impedance
Z_T	Transfer Impedance

1 Introduction

1.1 Background Information

On July 17, 1996, the Trans World Airlines Flight 800 (TWA-800) Boeing 747 Series 100 (B-747-100) aircraft exploded and crashed into the Atlantic Ocean. The flight had departed 14 minutes earlier, traveling from New York's John F. Kennedy airport to Paris. Since then, the National Transportation Safety Board (NTSB) has led the largest transportation accident investigation in the nation's history. To date, it is believed that a fuel vapor ignition occurred in the center wing fuel tank (CWT). The cause of this ignition is still unresolved. Recent laboratory efforts have focused upon the potential for an electrical discharge in the CWT, resulting from applied electromagnetic (EM) signals.

During the first year of the investigation, some consideration had been applied to the possibility of EM interference as a factor in the crash. Later, in April, 1998, a special supplement entitled "The Fall of TWA 800: The Possibility of Electromagnetic Interference" was published in The New York Review of Books, by Harvard professor Elaine Scarry [Ref. 1-1]. This report, along with continued dialog between Ms. Scarry and NTSB Chairman Jim Hall, prefaced an increased concern for quantifying the actual threat from external high intensity radiated field (HIRF) sources. It became evident to NTSB investigators that the EM environment surrounding TWA-800 was rather complex, and included numerous ground-based, shipboard, and airborne radio frequency (RF) transmitters, some being classified by the military. As a result, the Department of Defense (DoD) Joint Spectrum Center (JSC) was contracted to perform a detailed analysis of the TWA-800 EM environment. Their report was published in January 1999, and incorporated into the NTSB TWA Flight 800 Public Hearing Exhibit Items as Exhibit 9A, Addendum 2 [Ref. 1-2]. The JSC reported that all dominant RF emitters in the TWA-800 area were pulsed sources, applying peak field intensities of up to 32.6 V/m.

Alternatively, it can be demonstrated that a portable radio transmitting about 5 W may generate field levels in excess of 100 V/m very close to its antenna. Portable electronic devices (PEDs) are typically operated over a wide range of frequencies and power levels, and can often be set to radiate continuously. When used inside an aircraft, PEDs can be placed within inches of aircraft wiring, and their emissions are not subject to airframe attenuation as are outside HIRF sources. NASA's Aviation Safety Reporting System (ASRS) documents numerous occurrences of suspected PED interference with aircraft systems. (See Figure 1.1-1.) The possibility of PED interference cannot be overlooked when investigating anomalous behavior of any electronic aircraft system.

While the likelihood for RF transmitters to interfere with aircraft systems is becoming better understood, their potential to create hazardous conditions with flammable vapors remains elusive. Very little quantitative information is available regarding specific frequency-power-distance-temperature combinations required for hazardous conditions with aviation fuels. The DoD has documented the threat to fuel and ordinance from hand-held transmitters with output power capabilities of as little as 1 W [Ref. 1-3].

In a letter to NTSB Chairman Jim Hall on July 30, 1998, NASA Langley Research Center (NASA LaRC) Director Dr. Jeremiah F. Creedon offered support in the TWA-800 investigation regarding EM field effects. Beginning with this offer, a continuing dialog has evolved. The NTSB requested NASA LaRC's Electromagnetic Research Branch to perform two separate analysis tasks contributing to the TWA-800 investigation. In the first task, the NTSB directed NASA LaRC to use the JSC EM environment report to determine worst-case energy levels that were available to couple onto fuel quantity indication system (FQIS) components from external RF transmitters (military/civilian airborne, ship-

based or ground-based), into the CWT. The second task was to investigate the threat from PEDs.

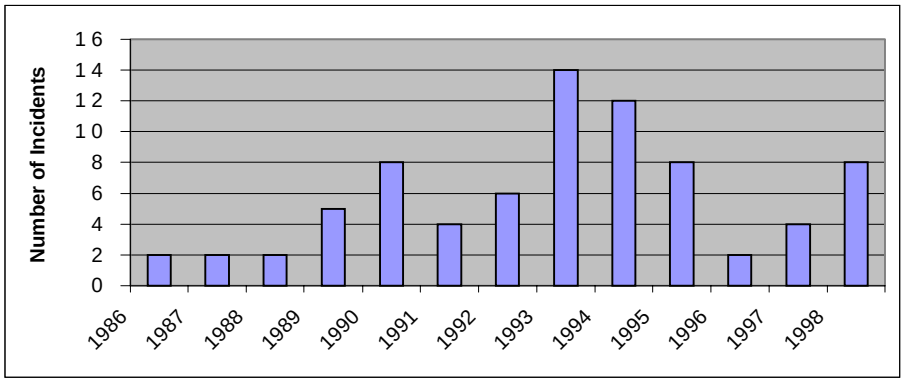

Figure 1.1-1: Total number of PED incidents reported to the NASA Aviation Safety Reporting System each year. This data includes all aircraft categories. (ASRS Search Request No. 5532, January 27, 1999.)

1.2 Areas and Limits of the Investigation

For the purposes of the TWA-800 investigation, four potential mechanisms (sources) of outside EM influence to the FQIS were identified:

1. Coupling from other aircraft systems.
2. Excitation from natural environmental effects (lightning, static electricity).
3. Excitation from man-made sources external to the aircraft (HIRF).
4. Excitation from passenger devices internal to the aircraft (PEDs).

Item 1 is the topic of a separately funded investigation contract with the Naval Air Warfare Center Aircraft Division (NAWCAD), in Patuxent River, M.D. Because of clear weather conditions at the time of the accident, item 2 was highly improbable. Analysis of items 3 and 4 are the subject of this report.

1.3 Approach

Using Figure 1.3-1 as a guide, three independent variables can be identified as follows:

A(f)= Worst-case EM emission threat (HIRF or PED Source Power)
B(f)= Worst-case coupling factor from source power to FQIS coupled power (Path Factor)
C(f)= Minimum RF Power required at FQIS connector for ionization/heating event (Event Power)

Each of these variables is dependent upon the frequency (f) of interest, but they are independent from one another at all frequencies. Essentially, B(f) is a transfer function that operates upon A(f), and the three terms are related by:

$$A(f) \bullet B(f) \geq C(f) \qquad (1.3\text{-}1)$$

If Equation (1.3-1) is true, there is the potential for RF-induced fuel vapor ignition.

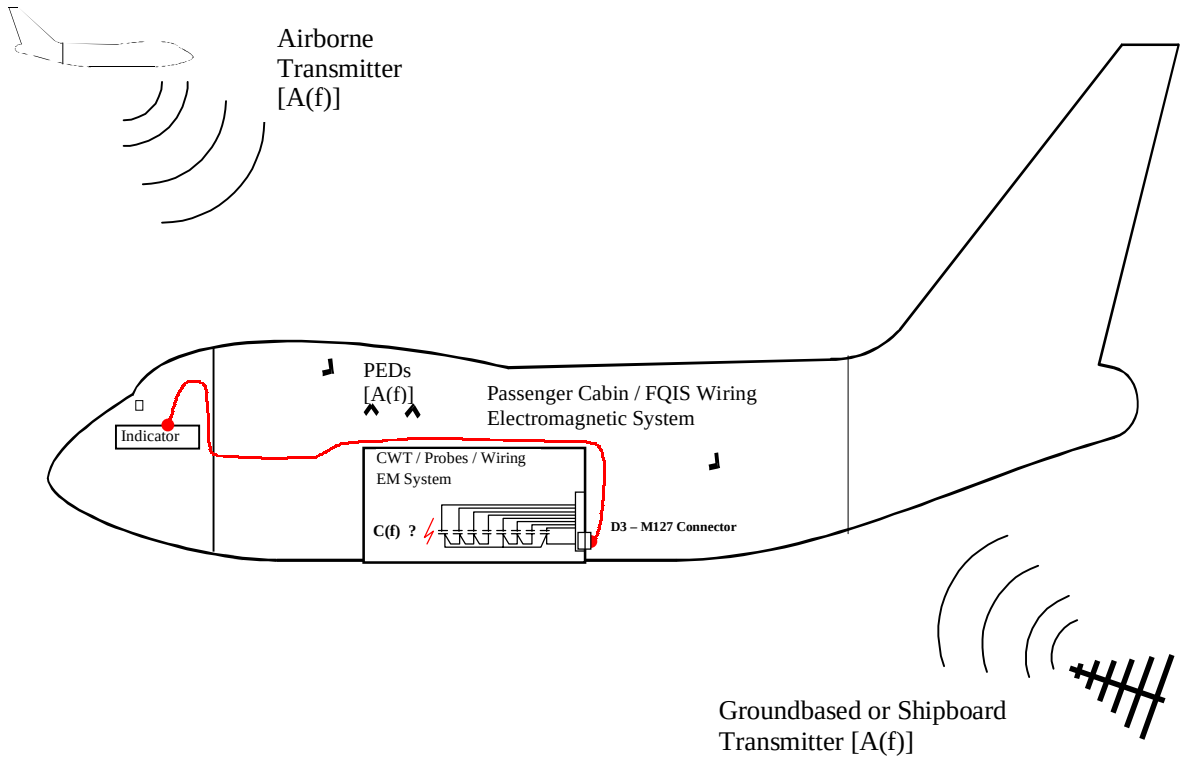

Figure 1.3-1: Characterization of EM coupling problem from external HIRF sources or PEDs to the CWT-probes-wiring EM system.

The approach of this report was to separately address this question for both external (HIRF, see Section 3), and internal (PED, see Section 4) cases.

1.3.1 Quantifying the Source [A(f)]

To evaluate the threat from HIRF sources located outside the aircraft, LaRC researchers used the dominant external emitters identified by JSC to calculate the total aircraft coupled power. Details of this work are given in Section 3.

The possibilities are seemingly endless when considering what type of PEDs people may wish to carry aboard a commercial transport aircraft. Aside from *unintentional* transmitters such as laptop computers, video games, AM/FM radios, tape players and compact disk players, passengers are also likely to possess a number of *intentional* transmitters. In 1996, items such as cellular phones, garage door openers, remote control toys, FM wireless microphones, handheld radios (citizen's band, police, fire, business, maritime, etc.), cordless phones and keyless entry transmitters could easily be found among the traveling public. The FAA recommends prohibiting operation of intentionally transmitting PEDs during flight [Ref. 1-4], however, adherence to the rules cannot be guaranteed. LaRC researchers found that intentional radiators occupy numerous frequency bands from 27 MHz to 6 GHz. To date, there is no definitive reference bounding the potential threat from these devices to affect aircraft systems. Substantial progress was made in this area, and details are provided in Section 4.3.

1.3.2 Estimating the Path Factor [B(f)], Phased Approach

Power radiated from outside the airplane, or from PEDs inside, is not 100% coupled onto the FQIS wiring. Factors such as frequency, orientation of source, orientation of aircraft, polarization, distance, and movement of items within the aircraft (aerosurfaces, doors, passengers, etc.) vastly affect coupling. An attenuation factor exists to account for this, and is often referred to as a *path factor*.

For a HIRF source external to the aircraft, two separate transfer functions are multiplied to determine the path factor. The first is the aircraft *shielding effectiveness* between the EM environment outside, as compared to inside the passenger cabin. The second is the path factor from a field source at some random location within the passenger cabin to the FQIS wiring. Section 3 describes the computational determination of coupling from HIRF sources in the JSC-defined TWA-800 EM environment, to CWT FQIS wiring.

For a PED source internal to the aircraft, two separate transfer functions are superimposed (added) to determine the path factor. The first is *indirect* coupling, and is primarily influenced by reverberation characteristics of the passenger cabin. The second is *direct* coupling, and is primarily influenced by the proximity of the threat to the FQIS wiring. Section 4 will describe the experimental determination of coupling from PEDs within a B-747-100 passenger cabin to the CWT FQIS wiring.

Originally, an extensive effort was envisioned to model the B-747-100 passenger cabin, and compute the worst-case coupling factor between an internal source and the CWT FQIS connector. The computational model would then be validated with aircraft coupling measurements, and could be applied to different aircraft and other aircraft systems as well. Such an effort would advance the state-of-the-art in aircraft EM coupling analysis tools, but would also be very costly.

The NTSB and NASA LaRC decided to take a more economical approach, and assume the maximum available power was applied directly to the CWT FQIS wiring, and perform the more extensive analysis as a second phase.

1.3.3 Estimating the Event Power [C(f)]

If a source transmitter operates in a pulsed mode, it may be possible to estimate its threat in terms of energy. Present fuel protection specifications and test procedures specify the minimum ignition energy for most light hydrocarbon fuels to be about 0.2 mJ [Ref. 1-5]. This specification proved to be very useful in the analysis that follows in Section 3.

Signals from PEDs however, are usually continuous and may therefore generate resonant and potentially cumulative effects upon aircraft systems. When continuous RF signals are applied to the CWT FQIS connector, peak voltages and currents at some locations in the CWT may exceed those present at the input. The question is at what level these voltages and currents may introduce an ionization event or localized heating phenomena into the fuel vapor mixture, of sufficient energy to cause ignition. Most of the LaRC effort (Section 4) was to establish a minimum guideline as to how much RF power is required to cause any ionization event or significant localized heating. Once this is established, it becomes an issue of how much more is required to threaten volatile fuel vapors.

Very few references or standards exist for evaluating the threat to fuel vapors from applied RF power. Present information suggests that hazards may exist with applied power of as little as 1 W. Reference 1-6 is a separate report, completed in support of the NASA LaRC effort. It contains a review of what is

currently known about spark phenomena and combustion, and summarizes what is currently known about ignition by RF sources.

1.3.4 Appendices

While it is the intention that this approach, test processes, data and conclusions will be relatively straightforward and understandable to the non-specialist, it is also important to document the more specialized details for completeness. A group of appendices are included to explain technical terms (Appendix A), measurement processes (Appendices C and F), theory and analysis (Appendices B, D, E, G and H).

1.4 Participating Agencies

1. NASA Langley Research Center, Hampton, Virginia.

2. Lightning Technologies, Inc. (LTI) , Pittsfield Massachusetts.

3. Naval Surface Warfare Center (NSWC), Dahlgren, Virginia. (The Joint Program Office for Special Technology Countermeasures "JPO-STC" funded Dr. R. E. Richardson, who performed some measurements and provided consultation.)

4. Joint Spectrum Center (JSC), Annapolis, Maryland.

1.5 References for Section 1

[1-1] E. Scarry, "The Fall of TWA-800: The Possibility of Electromagnetic Interference", The New York Review of Books, April 9, 1998, pp. 59-76

[1-2] M. Macrae and D. Hughes, "TWA Flight 800 Electromagnetic Environment", United States Department of Defense Joint Spectrum Center Report JSC-CR-99-006, January 1999

[1-3] Department of Defense Interface Standard, "Electromagnetic Environmental Effects Requirements for Systems", MIL-STD-464, March 18, 1997, Sec A5.8.2

[1-4] T. C. Accardi, "Use of Portable Electronic Devices Aboard Aircraft", FAA Advisory Circular AC No: 91.21-1, 8/20/1993

[1-5] F. A. Fisher, J. A. Plumer and R. A. Perala, *Lightning Protection of Aircraft*, Lightning Technologies Inc., 1990, p. 174.

[1-6] F. A. Fisher, "Some Notes on Sparks and Ignition of Fuels", NASA/TM-2000-210077, 3/2000.

2 FQIS and Aircraft Description

The TWA-800 aircraft was a B-747-100 model, and entered service in the early 1970's. The overall physical characteristics of the aircraft are well documented. For this series, fuselage length is 225 ft, with a maximum passenger cabin length of 187 ft. There are 98 windows on each side of the passenger cabin (each about 35 cm × 25 cm) for radiated fields to couple into (or out-of). Seating may be configured for approximately 450 passengers. [Ref. 2-1]

A transport aircraft is a highly complex EM system. The dynamic conditions of flight, passenger activity, and numerous modes of operation of other aircraft electronic systems result in an essentially infinite number of possible EM field distributions from a given source (internal or external). Fortunately, it is often not necessary to fully characterize an EM system when evaluating EM interference issues. Instead, calculations or measurements of EM coupling, impedance, shielding and attenuation may often be used to compare similarities and assess comparability between components and systems. These comparisons must, however, be done with sound engineering judgement and valid methods. For both the computational and experimental analyses herein, the approach was to make simplifying assumptions that always represent worst-case (maximum) coupling conditions.

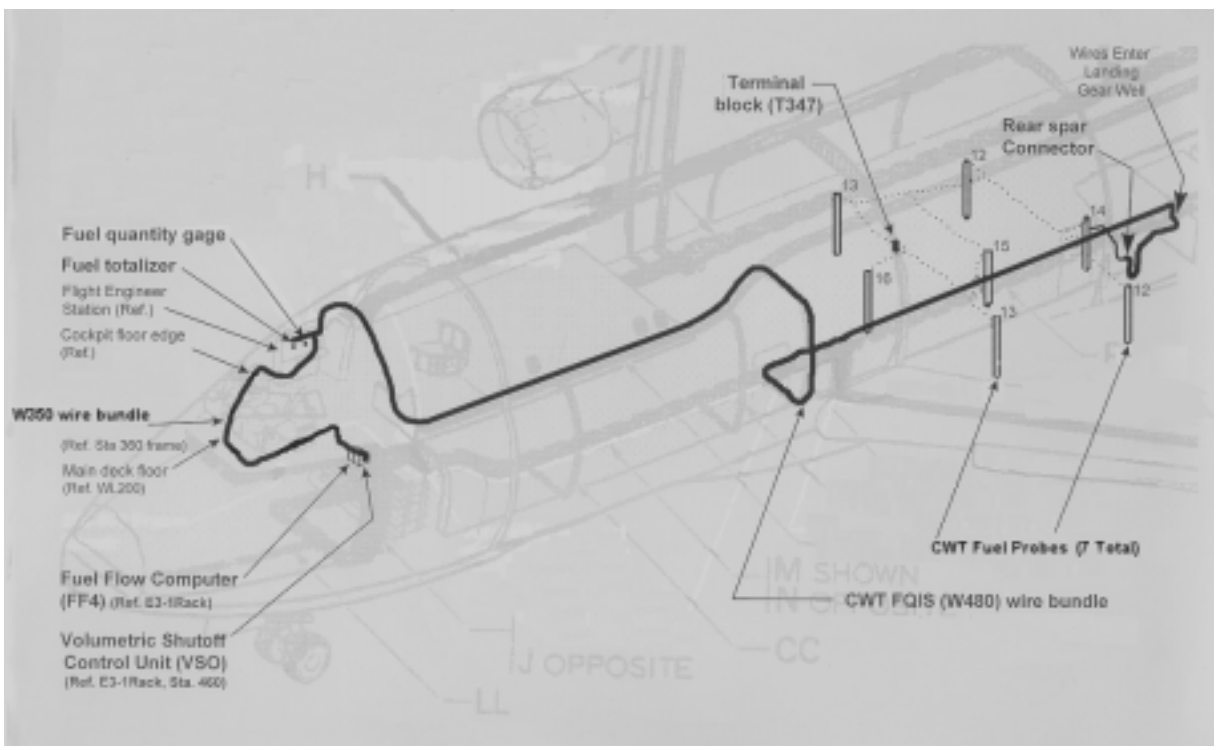

Figure 2-1: Overview diagram of B-747-100 FQIS installation (copied from NAWCAD draft test plan).

As stated previously, this report is primarily concerned with the potential for RF sources to couple enough power into the CWT via the FQIS, to cause arcing, sparking or excessive heating. In order to assess the potential for FQIS wiring to couple EM energy from the surrounding environment, and to approximate those conditions in the laboratory, a rough working knowledge of the system is required. Figure 2-1 shows a rendering of how the CWT FQIS components and wiring fit into the overall aircraft system.

A cut-out view of a B-747-100 CWT is shown in Figure 2-2, and a top view showing fuel quantity probe locations is shown in Figure 2-3. From this figure, it can be seen that there are six bays containing fuel. The CWT is situated directly beneath the passenger cabin floor, and is essentially the structural focus of wing to body attachment. Service access is obtained via two removable doors that may be reached from under the aircraft.

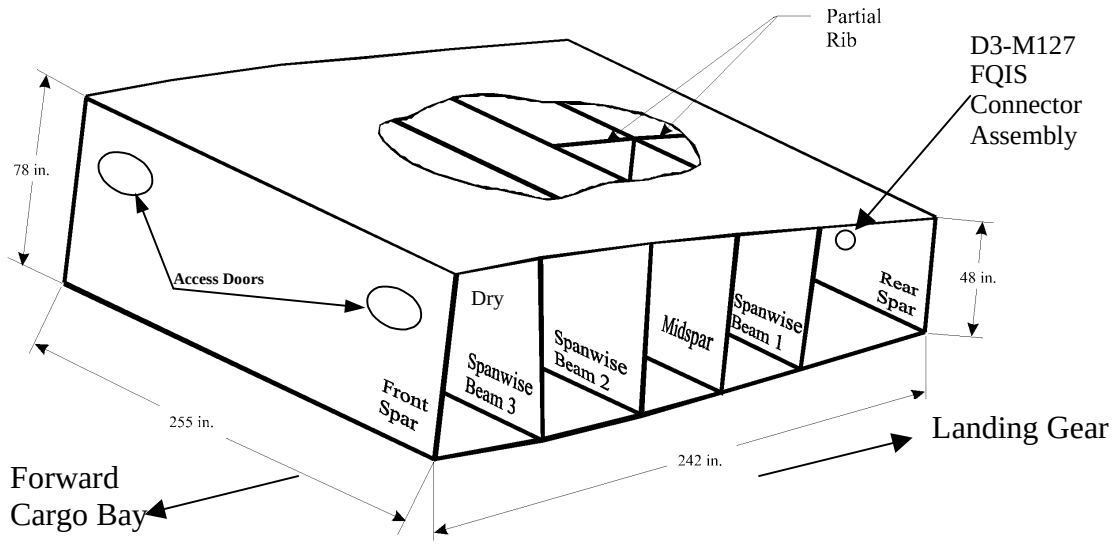

Figure 2-2: Perspective view of CWT
(copied from NTSB Public Hearing Item 20E, appendix A).

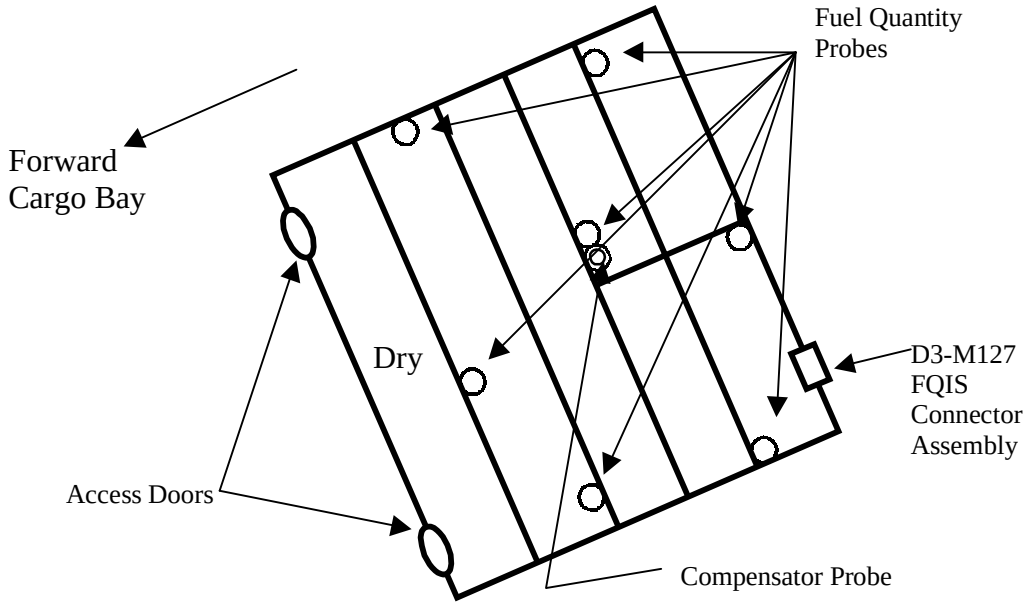

Figure 2-3: Top view of CWT showing fuel probe locations.

2.1 The Capacitive Fuel Probe

The B-747-100 FQIS measures fuel volume and density, allowing computation of fuel weight to be displayed on cockpit gages for each fuel tank. A group of capacitive fuel quantity probes are distributed throughout the volume of a given fuel tank. (See Figure 2-3.) Each fuel quantity probe consists of an electrically conductive tube surrounded by an outer tube. (See Figure 2.1-1.) When alternating electrical voltage is applied across the tubes, a displacement current will flow between them. The relationship between the voltage and current depends upon the capacitance between the two conductive tubes. As these probes are immersed in fuel, the capacitance value changes in proportion to the fuel level. Changes in capacitance of the fuel probe sensors are evaluated by a bridge circuit, which provides a signal to the electronic fuel indicators, which display aircraft fuel quantity to the flight or maintenance crew. [Ref. 2-2] A smaller *compensator* probe is placed near the bottom, center of a fuel tank, and is usually completely submerged in fuel. The compensator probe provides indication of fuel density. Wires are routed within the fuel tank to a terminal block located near the top of each probe, which has three terminal connections: HI Z (High impedance, inside tube), LO Z (Low Impedance, outside tube), and Ground (floating ground for HI Z shield). The silver-plated copper wiring and probe terminals are exposed to fuel and vapor.

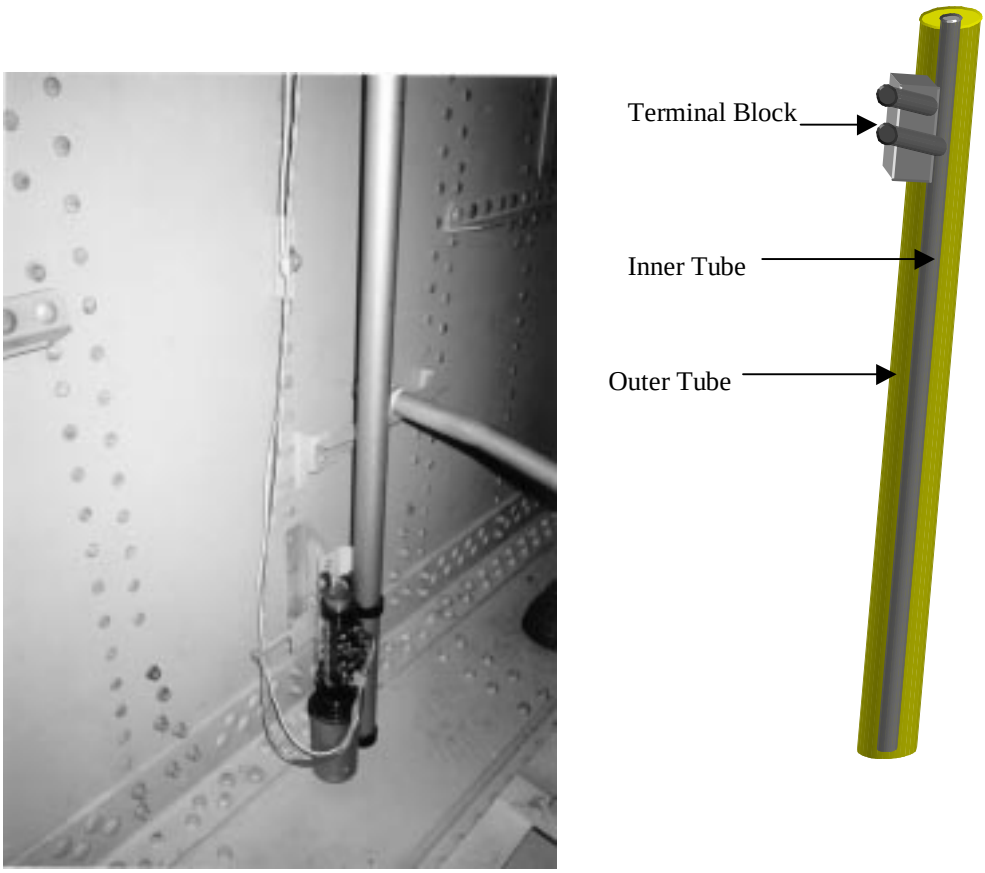

Figure 2.1-1: Diagram of fuel probe and picture of fuel probe and compensator probe in CWT.

2.2 Connectors and Cables

As shown in Figures 2-2 and 2-3, the fuel quantity probe wiring exits the CWT from the rear spar bulkhead, on the port side. This wiring utilizes a highly specialized connector assembly, which penetrates into the wheel well of the aircraft. This assembly, designated as an "Amphenol M127", allows individual access to each of the eight fuel probe LO Z conductors, as well as to the HI Z line. Half of the M127 connector assembly is internal to the CWT while the other half is external to the CWT; the halves are designed to mate from each side (CWT entry is required for installation/removal of the inside half). A diagram of the Amphenol M127 connector assembly, as viewed from the landing gear wheel well (dry) side, is shown in Figure 2.2-1.

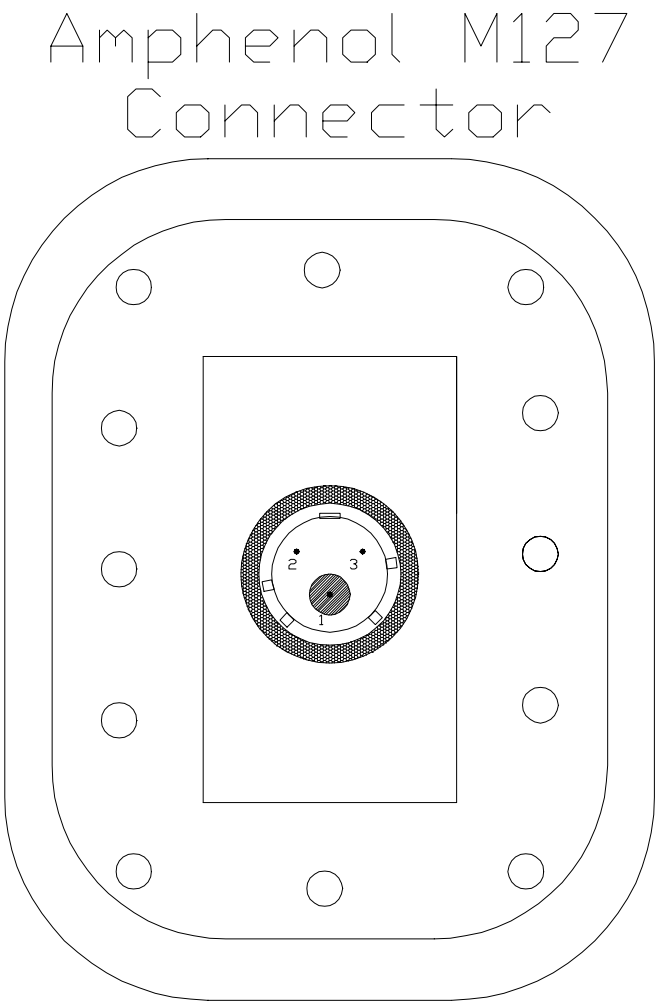

Figure 2.2-1: Amphenol M127 connector assembly, viewed from outside the CWT.

The most easily accessible portion of the M127 connector assembly consists of a round “Cannon” type connector, which provides access to only four conductors. (All seven LO Z fuel quantity probe wires are spliced together within the M127 assembly.) These four conductors provide all the signals required to be routed to the cockpit instruments for normal operation.

The “Amphenol D3” is a keyed connector designed to mate with the sealed Amphenol M127 connector assembly. The D3 connector is located at the end of a long cable that is routed from the engineer station on the flight deck of the aircraft to the CWT. The cable run consists of one white coaxial cable and two wires, one red and one blue. (This cable bundle provides a total of four conductors since both the center conductor and the shield of the coax can also be considered a signal path.) A diagram of the Amphenol D3 connector is shown in Figure 2.2-2. The conductors terminate in the D3 connector as pin 1, socket 2, socket 3, and shield. Pin 1, connected to the white cable, corresponds to the HI Z of the fuel probes. Socket 2, connected to the red wire, corresponds to the LO Z of the fuel probes. Socket 3, connected to the blue wire, corresponds to the LO Z of the compensator probe. The coaxial shield ties to all of the fuel probes and the compensator probe, but is electrically isolated from the aircraft structure.

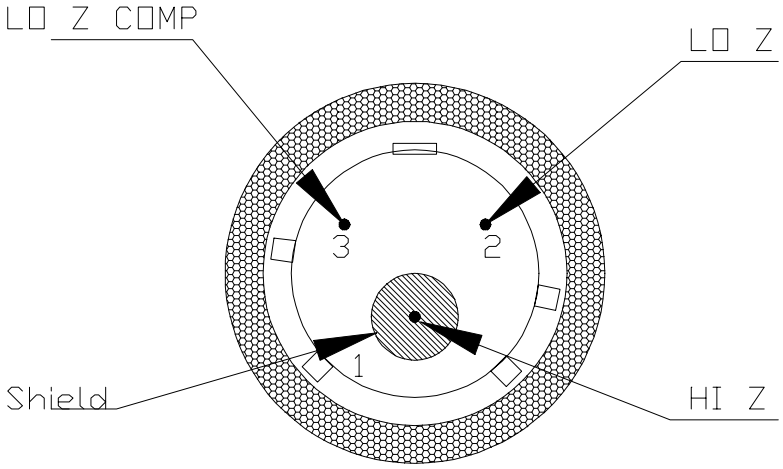

Figure 2.2-2: FQIS CWT Amphenol D3 connector schematic.

Although the LO Z fuel quantity probe lines are all spliced together at one point within the M127 assembly, the HI Z lines are spliced together in a distributed "daisy chain" fashion. The coaxial HI Z cable runs to the compensator probe first, where the center conductor connects to the probe terminal, and is spliced off to each subsequent fuel quantity probe. The shield of the coaxial cable is connected to floating ground terminals on the fuel probes and compensator probe that are labeled "SHLD". A schematic of this configuration is shown in Figure 2.2-3.

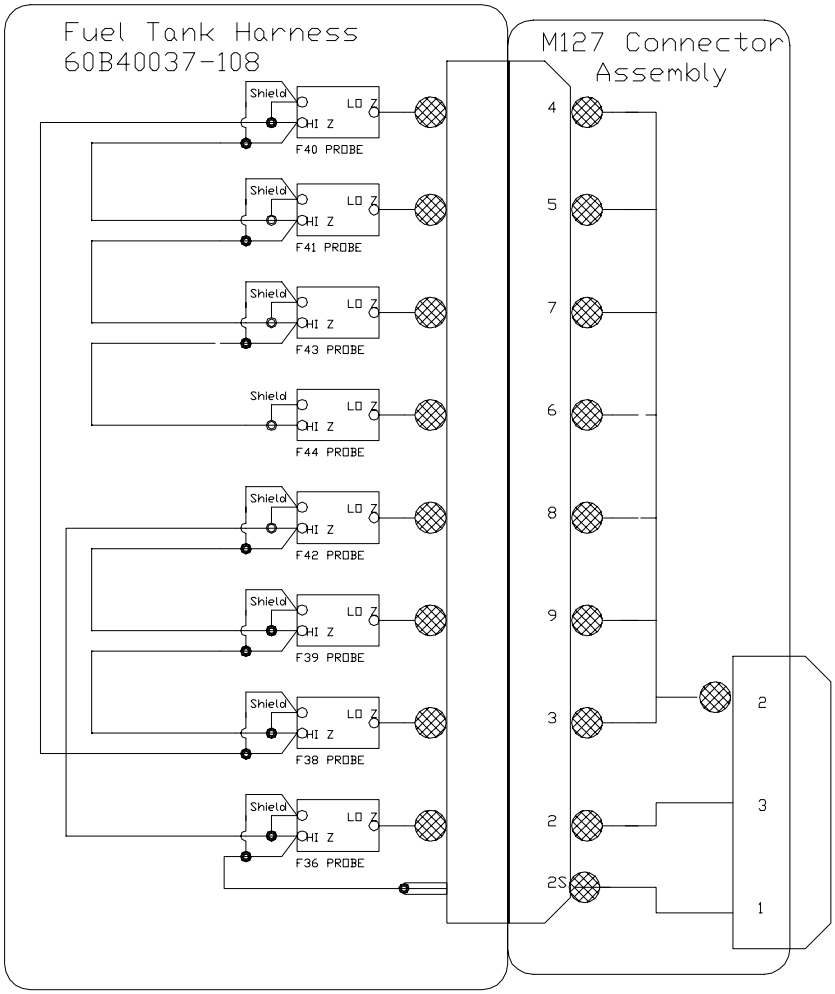

Figure 2.2-3: Schematic of the M127 connector assembly and FQIS components internal to the CWT.

The CWT contains approximately 900 ft of cables and wire routed through six compartmented bays. The seven fuel probes and one compensator probe are distributed through the various bays of the CWT as shown in Figure 2-3. The bays have relatively large access doors or openings and other penetrations to allow for fuel to equalize in level between the bays and to allow wiring to pass between the bays. All wiring is secured and electrically isolated from the aluminum structure using nylon cable clamps. Wiring penetrations from one bay to another are protected from chafing with nylon grommets. (See Figure 2.2-4.) During NASA LaRC aircraft test operations on a retired B-747-100 aircraft, Elite Structural Services personnel discovered damaged insulation on an exposed LO Z wire within the CWT. This damage occurred at the nylon grommet of a bay-to-bay penetration. The damaged wire, the surrounding structure, and associated fuel probe, were subsequently removed and sent to the NTSB for further analysis.

Figure 2.2-4: Example of wire routing inside the CWT showing the bulkhead standoffs and the pass through to the next bay.

2.3 References for Section 2

[2-1] CKC Laboratories, Inc., "Characterization of Air Transport Fleet", document prepared for Lawrence Livermore National Labs, July 1, 1991.

[2-2] T. K. Eismin, *Aircraft Electricity and Electronics*, 5th Edition, Glencoe Division, MacMillian/McGraw-Hill, 1994.

3 Determination of Threat from RF Sources External to Aircraft

3.1 Introduction

In this section, a numerical method to estimate energy delivered to the CWT due to EM waves through the FQIS wiring is presented. The EM waves can come from RF sources inside the cabin or external to the cabin. This section is focused on external radiators. The EM coupling to the region inside a cabin from radiators external to the aircraft depends upon the frequency, angle of incidence and polarization of the radiators. From studies conducted by the JSC, frequencies of dominant emitters present at the time of the TWA-800 disaster are reported in "TWA 800 Electromagnetic Environment" [Ref. 3-9]. As far as the angle of incidence and polarization are concerned, a worst-case scenario was considered. For maximum coupling, the EM waves were assumed at normal incidence to the fuselage. In the present study, the orientation of FQIS wiring and positioning was selected for maximum coupling.

The EM coupling threat to the CWT through the FQIS wiring can be estimated using two approaches. The first approach calculates the EM energy density at the location of TWA-800 incident from the data supplied by the JSC. From the energy density and the maximum aperture area available on the TWA-800, the maximum energy available to FQIS wire inside the aircraft cabin was calculated. To support the above approximation of the maximum available energy, a more accurate and computer intensive Modal/Method of Moments (MoM) numerical approach is also presented in this section.

For numerical estimations of the EM threat due to external sources, the following procedure was used. Since a microwave radar operating in the range mode uses pulse transmission, it was presumed that TWA-800 was illuminated by the EM pulse of width τ sec. An EM pulse of width τ was therefore assumed to be incident on the fuselage of a transport aircraft. Using the Fourier transform, the incident pulse in the time domain was transformed into the frequency domain. For each frequency, the voltage induced on a FQIS wire at a point where the FQIS wire is connected to the CWT was calculated using the MoM in conjunction with the cavity modal functions. Assuming the CWT presented a load impedance Z_L to the FQIS wires at the bulkhead connector, energy density delivered to the CWT load was calculated using simple equivalent circuit concepts. The energy density over the band of incident wave frequencies was calculated by repeated application of the MoM. The total energy delivered to the CWT load was then calculated by integrating the area under the energy density curve.

For applications of the MoM to the fuselage of a transport aircraft, the fuselage was assumed to be a large, rectangular cavity with rectangular windows on each side of its side-walls. The cavity was assumed to be homogeneous with no seats or other structures present. The normal incident plane wave induces electric fields on the apertures of the windows, which, in turn, will produce EM fields inside the cabin. The EM fields inside the cabin induce current on the FQIS wires. The amplitudes of electric fields in the apertures of windows and the current induced on the FQIS wiring were determined by using the Integral Equation Method in conjunction with the MoM. Other numerical methods such as the Finite Difference Time Domain (FDTD) method [Ref. 3-1] and the hybrid Finite Element/ MoM [Ref. 3-2] could also be used for estimation of EM threat, but these methods require excessive computing time and memory for electrically large enclosures and apertures. In the formation of the integral equation, the scattered EM fields inside the cabin due to windows and FQIS wires were determined using the cavity modal function, whereas the scattered EM fields outside the cabin due to windows were determined using the plane wave spectrum approach. From the knowledge of induced currents on the wire, power or energy delivered by the FQIS wiring to the CWT load was determined, as described for a single incident pulse in the previous paragraph. The computer code developed was numerically validated by comparison with other numerical techniques and also compared with experimental data available in the literature.

Since other numerical methods require large computer memory and central processing unit (CPU) time, validation was done with these methods for electrically small cavities over a lower frequency band. Since the mathematical formulation is valid at any frequency, the computer code developed here would yield correct results at higher frequencies provided a sufficiently large number of cavities and aperture modes were selected in the simulation.

3.2 Symbols for Section 3

A	Amplitude in volts/meter
(a,b,c)	x-, y-, and z-dimensions of rectangular cavity
$[C]$	Mutual coupling matrix between apertures and wire
d_0	Diameter of the FQIS wire
$\vec{E}_{in}$	Incident electric field
$\vec{E}_{ext}(\vec{M}_{rx})$	Scattered electric field (external)
$\vec{E}_{\text{int}}(\vec{M}_{rx})$	Scattered electric field (internal)
$\vec{E}_{apt}$	Total aperture field
$E_L(f)$	Complex energy density
f_c	Carrier frequency
$\vec{H}_{in}$	Incident magnetic field
$\vec{H}_{ext}(\vec{M}_{rx})$	Scattered magnetic field (external)
$\vec{H}_{\text{int}}(\vec{M}_{rx})$	Scattered magnetic field (internal)
I_0	Total current of FQIS wire
$[I_{rp}]$	Column matrix representing coupling between incident field and apertures
$\vec{J}_p$	Electric current along the FQIS wire
L_r, W_r	Length and width of rth aperture
L_w	Length of the FQIS wire
$\hat{l}$	Unit vector along the FQIS wire
$\vec{M}_{rx}$	Equivalent magnetic current in the x-direction over r^{th} aperture
$\vec{M}_{ry}$	Equivalent magnetic current in the y-direction over r^{th} aperture
$\hat{n}$	Unit normal vector
SA	Surface area (total)

U_D	Energy density
U	Total energy
U_{pr}	Amplitude of pth mode on r^{th} aperture
$[U]$	Column matrix representing modal amplitudes on apertures
$V_0(f)$	Open circuit voltage
$\hat{x}, \hat{y}$	Unit vectors in the x and y directions, respectively
x_{cr}, y_{cr}	Coordinates of center of rth aperture
$[Y]$	Square matrix representing mutual coupling between apertures
Z_{ww}	Self impedance of the FQIS wire
$Z_{in}(f)$	Input impedance of the FQIS wire
τ	Pulse width in seconds
η_0	Free space impedance
Δf	Frequency increment

(See Section **iii** for a more complete listing of symbols and abbreviations.)

3.3 Initial Analysis

3.3.1 Estimation of Maximum Available Energy

The total surface area available for EM energy to penetrate through the windows of an aircraft is given by: $(SA)_{Total}$ = Number of Windows × Area of Each Window. Since the total number of windows is 98 on each side of a B-747-100 and each window is of area equal to 0.35 m × 0.25 m, the maximum area available for EM penetration is $(SA)_{Total} = 8.575\ m^2$. The electric field intensity at the location of the TWA-800 incident from the JSC report for various dominant emitters (as reproduced in Table 3.1.1-1 [Ref. 3-9]) was obtained. Considering a dominant emitter specified in the JSC report, the maximum available energy density, at the location of TWA-800 accident was determined by $U_D = (|E_{max}|^2/\eta_o)\tau$, where E_{max} is the maximum field intensity in V/m, η_o is the free space impedance (equal to 120π), and τ is the pulse width in seconds. Considering the dominant emitter of highest strength from the Table 3.3.1-1, (i.e. dominant emitter at f = 2.875 GHz) the maximum energy density available to the TWA-800 aircraft was obtained as $U_D = (|32.713|^2/120\pi)(4\times10^{-6})\ J/m^2$. The maximum energy available to the TWA-800 aircraft was then obtained by multiplying U_D with the total surface area $(SA)_{Total}$. Hence $U = U_D \times (SA)_{Total} = 0.097 mJ$. These calculations for maximum available energy were repeated for all of the dominant emitters specified in the JSC report, and are given in the last row of the Table 3.3.1-1. It may be concluded that the maximum available energy for the dominant emitters identified by the JSC was less than 0.1 mJ. Considering the various coupling factors, the actual energy delivered to the CWT was several orders of magnitude less than 0.1 mJ.

DOMINANT EMITTERS						
FREQUENCY; GHz	**2.875**	**3.1-3.5**	**8.5-9.6**	**3.1-3.5**	**1.294**	**9.1**
EIRP; dBm	134.8	139.8	117.4	136.0	128.0	128.0
GAIN; dBi	46	42	34	38	35	44
DISTANCE; NMi	15.7	112.0	2.93	156.3	13.1	17.0
PULSE WIDTH; µSec	1.0;4.0	6.0;51.0	2.5	6.0;51.0	2.0	2.0
PRF; Pulses/Sec	1300;320	1840;152	400	1840;152	341	300
DUTY CYCLE	0.0013	0.011	0.001	0.011	0.00068	0.0006
POLARIZATION	H *or* V	V		V		V
POWER DENSITY; dBm/m²	34.531	22.465	31.712	15.770	29.304	26.989
FIELD INTENSITY; V/m	32.713	8.155	23.646	3.773	17.921	13.727
ENERGY DENSITY; mJ/m²	0.011355	0.009031	0.003708	0.001933	0.001704	0.00100
ENERGY; mJ (8.575m²)*	0.097	0.077	0.032	0.017	0.015	0.009

Table 3.3.1-1 Dominant emitter characteristics.

3.3.2 TWA Electromagnetic Environment versus Standard HIRF Environments

At the time of this writing, a new Advisory Circular/Advisory Material Joint (AC/AMJ 20.1317), providing certification guidance and methods regarding operation of electrical/electronic systems on an aircraft when it is exposed to external HIRF environments, was in the approval process. To develop the HIRF environments defined in this new document, an international working group, composed of European and American engineers, (Electromagnetic Effects Harmonization Working Group- EEHWG), was tasked to harmonize international data sources regarding the worldwide HIRF/Lightning EM environment. The new AC/AMJ will be very useful for defining a baseline EM environment that airborne equipment must typically operate in, as well as predicting the most severe environment that may be anticipated over its operational life. For the analysis, it was decided that the "Normal" and "Fixed Wing Severe" EM environments defined in AC/AMJ 20.1317 (Final Draft 8, March 1998) should be compared with the JSC-derived TWA-800 environment. This was done, and the results are shown in Figure 3.3.2-1. AC/AMJ 20.1317 contains the following definitions**:**

- "The Normal HIRF environment is an estimate of the electromagnetic field strength level in the airspace on and about airports/heliports in which routine departure and arrival operations take place. This estimate considers the operational characteristics of the high peak power microwave transmitters, which typically do not operate continuously at the maximum output levels."

- "The Fixed Wing Severe HIRF environment is a worst case estimate of the electromagnetic field strength levels in the airspace in which fixed wing flight operations are permitted."

From Figure 3.3.2-1, it can be concluded that the JSC-derived TWA-800 environment was far less severe than that encountered in routine departure and arrival operations.

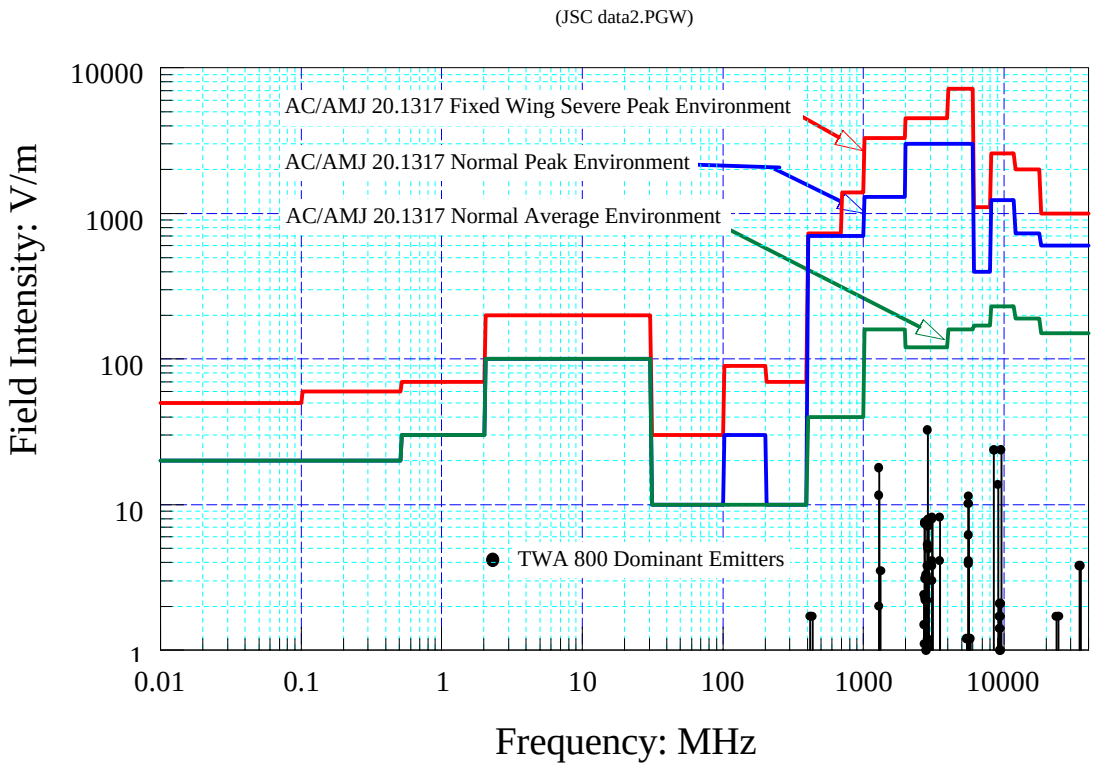

Figure 3.3.2-1: JSC TWA-800 EM environment versus proposed AC/AMJ 20.1317 HIRF environments.

3.4 Analytical Modeling

Figure 3.4-1 shows the geometry of a rectangular cavity with rectangular apertures with dimensions representing the fuselage of a B-747-100. The incident EM pulse can be represented by

$$\vec{E}_{in}(t) = \hat{y}ACos(2\pi f_c t) \text{ for } -\tau/2 \le t \le \tau/2$$
$$= 0\text{, Otherwise.} \qquad (3.4\text{-}1)$$

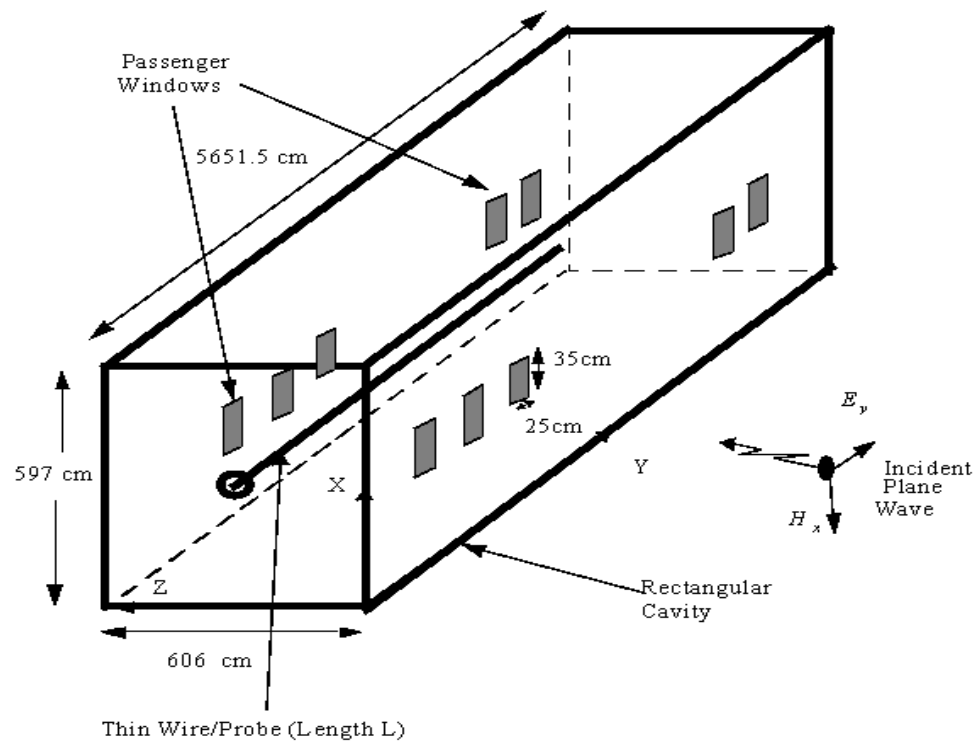

Figure 3.4-1: Closed rectangular cavity approximating B-747-100 fuselage with rectangular apertures on side walls representing passenger windows.

where A (V/cm) is the amplitude of the incident pulse, f_c is the radio frequency of the incident wave and τ is the pulse width in sec. The incident wave in the frequency domain can be written as

$$\vec{E}_{in}(f) = \hat{y}\frac{A\tau}{2}\left[\frac{Sin(\pi(f-f_c)\tau)}{\pi(f-f_c)\tau} + \frac{Sin(\pi(f+f_c)\tau)}{\pi(f+f_c)\tau}\right] \quad . \qquad (3.4\text{-}2)$$

Even though the spectrum contains energy density at all frequencies, most is concentrated in the main lobes, For a worst-case study, it will be approximated by

$$\vec{E}_{in}(f) = \hat{y}\frac{A\tau}{2}, \text{ for } f_c - \frac{1}{\tau} \le f \le f_c + \frac{1}{\tau} \text{ and } -f_c - \frac{1}{\tau} \le f \le -f_c + \frac{1}{\tau}. \tag{3.4-3}$$

The incident magnetic field is obtained from $\vec{E}_{in}(f)$ as

$$\vec{H}_{in}(f) = \hat{x}\frac{A\tau}{2\eta_0}, \text{ for } f_c - \frac{1}{\tau} \le f \le f_c + \frac{1}{\tau} \text{ and } -f_c - \frac{1}{\tau} \le f \le -f_c + \frac{1}{\tau}. \tag{3.4-4}$$

The incident field on the cavity induces electric fields on the windows and electric current on the representative FQIS wiring inside the rectangular cavity. The induced tangential electric fields on the window apertures can be replaced by the equivalent magnetic currents $\vec{M}_{1x}, \vec{M}_{1y}, \vec{M}_{2x}, \vec{M}_{2y}, ...\vec{M}_{Nx}, \vec{M}_{Ny}$. The problem, therefore, can be split into two parts: interior and exterior, as shown in Figure 3.4-2. The exterior and interior parts consist of the regions outside and inside the rectangular cavity, respectively. For the normal incidence and the y-directed polarization only $\vec{M}_{1x}, \vec{M}_{2x}, ...$ type of equivalent magnetic currents will be excited in the apertures.

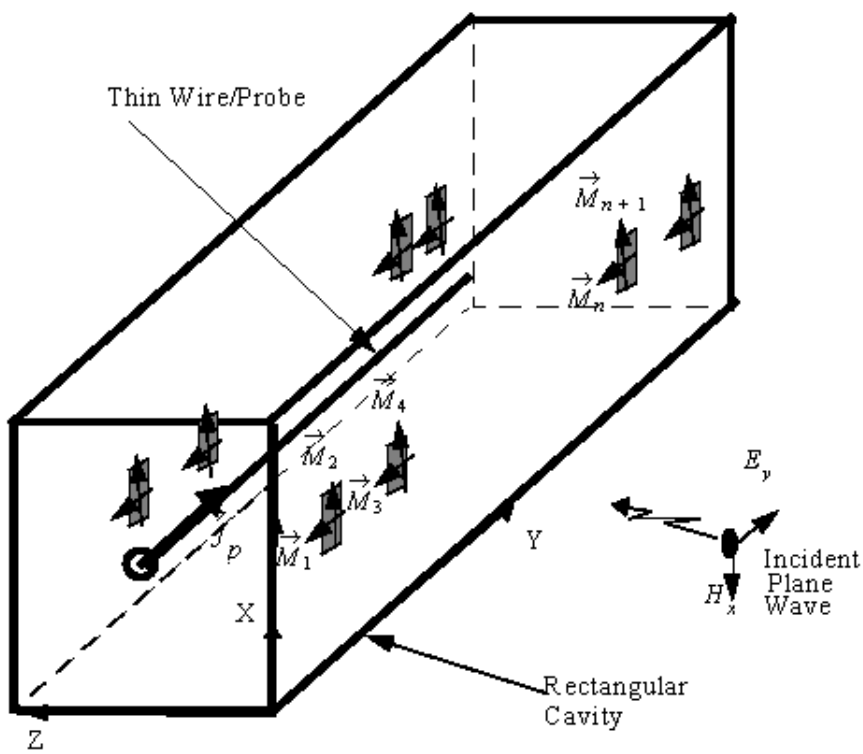

Figure 3.4-2: Analytical model for EM coupling calculation.

3.4.1 Development of the Method of Moments

Using the Plane Wave Spectrum approach [Ref. 3-3], the scattered electric field $\sum_{r=1}^{R} \vec{E}_{ext}(\vec{M}_{rx})$ and magnetic field $\sum_{r=1}^{R} \vec{H}_{ext}(\vec{M}_{rx})$ due to the equivalent magnetic currents exterior to the cavity are obtained. Likewise, using the cavity Green's function or cavity modal functions, the scattered electric field $\sum_{r=1}^{R} \vec{E}_{\text{int}}(\vec{M}_{rx})$ and magnetic field $\sum_{r=1}^{R} \vec{H}_{\text{int}\,t}(\vec{M}_{rx})$ due to the equivalent magnetic currents interior to the cavity are obtained. Also using the cavity modal functions, the scattered electric field $\vec{E}_{\text{int}}(\vec{J}_p)$ and the magnetic field $\vec{H}_{\text{int}}(\vec{J}_p)$ due to the current induced on the FQIS wiring are obtained. Continuity of the tangential magnetic fields across the window apertures yields

$$\left[\vec{H}_{in}(f) + \sum_{r=1}^{R} \vec{H}_{ext}(\vec{M}_{rx})\right] \times \hat{n} = \left[\sum_{r=1}^{R} \vec{H}_{\text{int}}(\vec{M}_{rx}) + \vec{H}_{\text{int}}(\vec{J}_p)\right] \times \hat{n} \ , \tag{3.4.1-1}$$

where $\hat{n}$ is the unit normal vector to the aperture drawn outward. Likewise, forcing the tangential electric field over the wire to zero yields

$$\left[\left[\sum_{r=1}^{R} \vec{E}_{\text{int}}(\vec{M}_{rx})\right] + E_{\text{int}}(\vec{J}_p)\right] \bullet \hat{l} = 0 \ , \tag{3.4.1-2}$$

where $\hat{l}$ is the unit vector along the FQIS wiring. Equations 3.4.1-1 and 3.4.1-2 are the required integral equations to be solved for the aperture voltages and the FQIS wire current. The tangential aperture electric fields over the windows can be expressed as

$$\vec{E}_{apt} = \hat{y} \sum_{r=1}^{R} \sum_{p=1,3..}^{P} \frac{U_{pr}}{W_r} Sin\left(\frac{p\pi}{L_r}\left(\frac{L_r}{2} + x - x_{cr}\right)\right)$$
$$\text{for } x_{cr} - \frac{L_r}{2} \le x \le x_{cr} + \frac{L_r}{2} \text{ and } y_{cr} - \frac{W_r}{2} \le y \le y_{cr} + \frac{W_r}{2} \quad , \tag{3.4.1-3}$$

where U_{pr} is the amplitude of pth mode on the rth aperture, (L_r, W_r) are the length and width of rth aperture, (x_{cr}, y_{cr}) are the coordinates of the center of the rth aperture. The equivalent magnetic currents over the apertures can be written as

$$\vec{M}_{rx} = -\hat{n} \times \hat{y} \sum_{p=1,3..}^{P} \frac{U_{pr}}{W_r} Sin\left(\frac{p\pi}{L_r}\left(\frac{L_r}{2} + x - x_{cr}\right)\right) \ . \tag{3.4.1-4}$$

The current induced on the FQIS wiring can be written as

$$\vec{J}_p = \hat{y}\frac{I_0}{\pi d_0}\frac{Sin(k_0(L_w - y))}{Sin(k_0 L_w)} \ , \tag{3.4.1-5}$$

where I_0 is the total current on the wire at the point where it is connected to the CWT, d_0 is the wire diameter, and L_w is the wire length. Selecting the expansion and testing functions for the magnetic currents on the apertures and electric current on the wire as given in Equations 3.4.1-4 and 3.4.1-5, respectively, the integral equations in (3.4.1-1) and (3.4.1-2) are transformed into a matrix equation given by

$$\begin{bmatrix} [Y] & [C] \\ [C]^T & Z_{ww} \end{bmatrix}\begin{bmatrix} [U] \\ I_0 \end{bmatrix} = \begin{bmatrix} [I_{rp}] \\ 0 \end{bmatrix} . \tag{3.4.1-6}$$

The admittance matrix $[Y]$ in Equation 3.4.1-6 represents mutual coupling between the modes on the apertures, the sub matrix $[C]$ represents the mutual coupling between the aperture modes and the FQIS wire current, and Z_{ww} represents the self-impedance of the FQIS wire. The elements of the admittance matrix are given by

$$\begin{aligned} Y_{rpr'p'} = & -\frac{j\omega}{k_0^{\ 2}}\sum_{m,n}^{\infty} -\frac{\varepsilon_0}{k_I}\frac{\varepsilon_{0m}\varepsilon_{0n}}{abSin(k_I c)}(k_0^{\ 2} - \left(\frac{m\pi}{a}\right)^2)Cos(k_I c)I_{rpmnx}I_{r'p'mnx} \\ & -\frac{\omega\varepsilon_0}{4\pi^2 k_0^{\ 2}}\int_{-\infty}^{\infty}\int_{-\infty}^{\infty}\Psi_{rpx}\left(\Psi_{r'p'x}\right)^*\frac{(k_0^{\ 2} - (k_x)^2)}{k_z}dk_x dk_y \ , \end{aligned} \tag{3.4.1-7}$$

if r and r' apertures are on the same side wall, and

$$Y_{rpr'p'} = -\frac{j\omega}{k_0^{\ 2}}\sum_{m,n}^{\infty} -\frac{\varepsilon_0}{k_I}\frac{\varepsilon_{0m}\varepsilon_{0n}}{abSin(k_I c)}(k_0^{\ 2} - \left(\frac{m\pi}{a}\right)^2)Cos(k_I c)I_{rpmnx}I_{r'p'mnx} \ , \tag{3.4.1-8}$$

if r and r' are on different walls of the cavity. The expression for I_{rpmnx} is given by

$$\begin{aligned} I_{rpmnx} = & \frac{-p\pi L_r}{((p\pi)^2 - \left(\frac{m\pi L_r}{a}\right)^2)}\left[\cos(p\pi)Sin(\frac{m\pi}{a}(L_r + x_{cr})) + Sin(\frac{m\pi}{a}(L_r - x_{cr}))\right] \\ & \frac{Sin(\frac{n\pi W_r}{2b})}{\frac{n\pi W_r}{2b}}Cos(\frac{n\pi y_{cr}}{b}) \ , \end{aligned} \tag{3.4.1-9}$$

and $I_{r'p'mnx}$ is the same as Equation 3.4.1-9, with r, p replaced with r', p', respectively. The expression

for Ψ_{rpx} is given by

$$\Psi_{rpx} = \frac{L_r W_r}{2j} e^{-jk_x x_{cr} - jk_y y_{cr}} \left[e^{j\frac{p\pi}{2}} \frac{Sin(\frac{p\pi}{2} - \frac{k_x L_r}{2})}{\frac{p\pi}{2} - \frac{k_x L_r}{2}} - e^{-j\frac{p\pi}{2}} \frac{Sin(\frac{p\pi}{2} + \frac{k_x L_r}{2})}{\frac{p\pi}{2} + \frac{k_x L_r}{2}} \right] \frac{Sin(\frac{k_y W_r}{2})}{\frac{k_y W_r}{2}} . \tag{3.4.1-10}$$

$(\Psi_{r'p'x})^*$ is the complex conjugate of $\Psi_{r'p'x}$, where r, p in Equation 3.4.1-10 is replaced by r', p', respectively. The elements of the coupling matrix $[C]$ are given by

$$C_{pq} = -\sum_{m,n}^{\infty} \frac{\varepsilon_{0m}\varepsilon_{0n}}{ab} \frac{Sin(k_I(c - z_p))}{Sin(k_I c)} Sin(\frac{m\pi x_p}{a}) F_{1n} I_{rpmnx} , \tag{3.4.1-11}$$

where $$F_{1n} = \frac{k_0}{Sin(k_o L_w)} (Cos(k_o L_w) - Cos(\frac{n\pi L_w}{b})) \tag{3.4.1-12}$$

and (x_p, y_p, z_p) are the coordinates of the point where the FQIS wire connects to the CWT. The self-impedance of the FQIS wire is given by

$$Z_{ww} = -j \frac{\omega\mu_0}{4(k_0)^2} \sum_{m,n}^{\infty} \frac{\varepsilon_{0m}\varepsilon_{0n}}{abk_I} ((k_0)^2 - (\frac{n\pi}{b})^2) Sin^2(\frac{m\pi x_p}{a}) F_{1n} F_{1n} \left[\frac{Sin(\frac{m\pi d_0}{2a})}{\frac{m\pi d_0}{2a}} \right] \left\{ \frac{Sin(k_I(c - z_p)) Sin(k_I(c - \frac{d_0}{2}))}{Sin(k_I c)} + \frac{Sin(k_I z_p)) Sin(k_I(c - z_p - \frac{d_0}{2}))}{Sin(k_I c)} \right\}$$

$$- j \frac{\omega\mu_0}{4(k_0)^2} \sum_{m,n}^{\infty} \frac{\varepsilon_{0m}\varepsilon_{0n}}{abk_I} ((k_0)^2 - (\frac{n\pi}{b})^2) Sin^2(\frac{m\pi x_p}{a}) F_{1n} F_{1n} \left\{ \frac{Sin(k_I(c - z_p)) F_{0z} + Sin(k_I z_p)) F_{cz}}{k_I d_0 Sin(k_I c)} \right\} \left[2\cos(\frac{m\pi}{a} \frac{d_0}{2}) \right] , \tag{3.4.1-13}$$

where $$F_{0z} = Cos(k_I(z_p - \frac{d_0}{2})) - Cos(k_I z_p)$$

$$F_{cz} = Cos(k_I(c - z_p - \frac{d_0}{2})) - Cos(k_I(c - z_p))$$

$$k_I = \sqrt{(k_0)^2 - \left(\frac{m\pi}{a}\right)^2 - \left(\frac{n\pi}{b}\right)^2} \qquad \text{If } (k_0)^2 \geq \left(\frac{m\pi}{a}\right)^2 + \left(\frac{n\pi}{b}\right)^2$$

$$k_I = -j\sqrt{\left(\frac{m\pi}{a}\right)^2 + \left(\frac{n\pi}{b}\right)^2 - (k_0)^2} \qquad \text{If } \left(\frac{m\pi}{a}\right)^2 + \left(\frac{n\pi}{b}\right)^2 \geq (k_0)^2 .$$

The elements of the column matrix on the right hand side of Equation 3.4.1-6 are calculated from

$$I_{rp} = \int\int_{overr} \vec{H}_{in}(f) \bullet \hat{y} \times \hat{n} \frac{1}{W_r} Sin(\frac{p\pi}{L_r}(\frac{L_r}{2} + x - x_{cr}))dxdy \ . \tag{3.4.1-14}$$

3.4.2 Input Impedance of the FQIS Wire

The input impedance of the FQIS wiring inside the cavity was determined by assuming that the FQIS wire is fed at the point (x_p, y_p, z_p) by a delta gap generator [Ref. 3-4]. In this transmission mode, the matrix equation (3.4.1-6) takes the form

$$\begin{bmatrix} [Y] & [C] \\ [C]^T & Z_{pp} \end{bmatrix} \begin{bmatrix} [U] \\ I_0' \end{bmatrix} = \begin{bmatrix} [0] \\ 1 \end{bmatrix}, \tag{3.4.2-1}$$

where I_0' is the unknown current on the FQIS wire when assumed to be excited by a delta gap source at the CWT connection. From the solution of Equation 3.4.2-1, the input impedance of the FQIS wire inside the cavity is determined from

$$Z_{in}(f) = 1./I_0'(f) \ . \tag{3.4.2-2}$$

This impedance is needed in determining the open-circuit voltage at the CWT connection for external excitations.

3.4.3 Energy Delivered to CWT by FQIS Wire

The open-circuit voltage induced on the FQIS wire due to the external EM source is given by

$$V_0(f) = Z_{in}(f) I_0(f) \ . \tag{3.4.3-1}$$

If $Z_L(f)$ is the load impedance presented by the CWT at point (x_p, y_p, z_p), looking into the CWT, the complex energy density in J/Hz, is obtained from simple circuit calculations as

$$E_L(f) = \frac{(A\tau)^2}{2} Z_L(f) \frac{|V_0(f)|^2}{|(Z_L(f) + Z_{in}(f)|^2} \ . \tag{3.4.3-2}$$

If the frequency band of the incident wave is divided into Q frequencies, then

$$\Delta f = \frac{2}{\tau Q} \ . \tag{3.4.3-3}$$

Selecting the frequency $f_q = f_c - \frac{1}{\tau} + (q-1)\Delta f$, energy density, using Equation 3.4.3-2 is calculated at f_q where $q = 1,2,3....Q$. The total energy delivered to the CWT by the FQIS wire is then calculated from

$$E_{Total} = \sum_{q=1}^{Q} \Delta f \ \mathrm{Re}(E_L(f_q)) \ . \tag{3.4.3-4}$$

3.5 Numerical and Experimental Validation of the Modal/MoM Code

Case I: A Thin Rectangular Aperture on a Small Rectangular Box

For numerical and experimental validation of the Modal/MoM code, a rectangular box of size $(30\times12\times30)\,\text{cm}^3$, with a thin rectangular aperture of size $(10\times0.5)\ \text{cm}^2$, located at the center of one of its walls (i.e. $x_{c1}=15\,\text{cm},\ y_{c1}=6\,\text{cm},\ z_c=0\,\text{cm}$) and illuminated by the y-directed linearly-polarized plane wave of unit amplitude, was considered. The Electric Field Shielding (EFS) is defined [Ref. 3-5] as

$$EFS = 20Log\left(\frac{|E_{yf}|}{|E_{yc}|}\right)\ , \tag{3.5-1}$$

where E_{yc} and E_{yf} are the y-component of electric fields at the center of the rectangular box when the box is present and absent, respectively. The EFS was calculated using the Modal/MoM code and is presented in Figure 3.5-1 along with the numerical results obtained using the FDTD method [Ref. 3-6] and the transmission line method [Ref. 3-5]. The numerical results are also compared with measurements [Ref. 3-5]. Since the introduction of a wire in the measurement method for probing the field strength disturbs the electric field inside the box, the measured data are scattered. A good agreement between the present method and the measured data, within the uncertainty involved in the measurements, validated the present code for a thin single aperture located at the center of one of the walls.

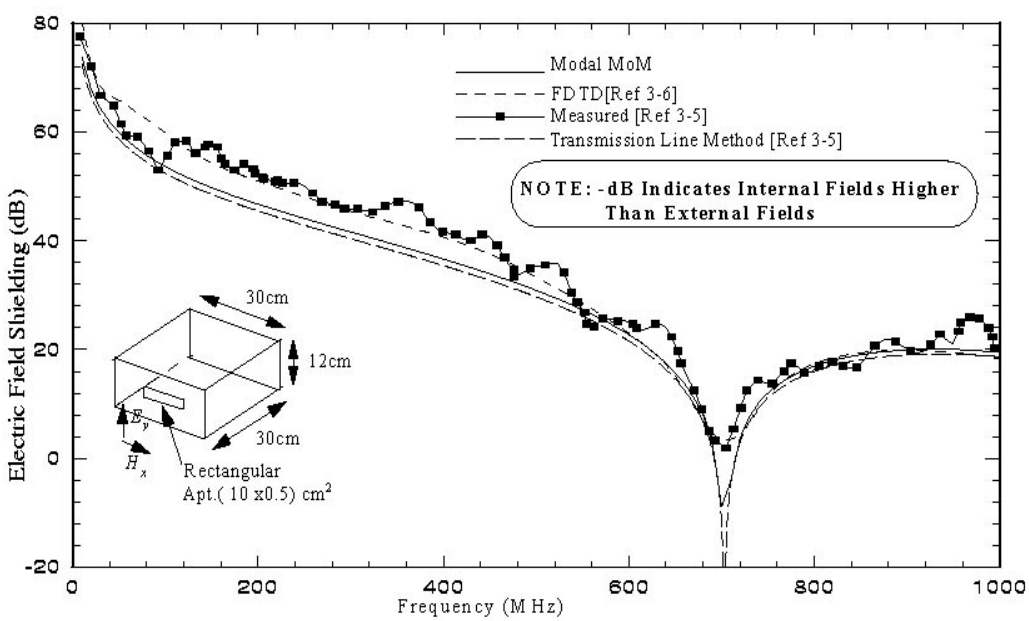

Figure 3.5-1: EFS at the center of a 30 x 12 x 30 cm^3 enclosure with a 10 x 0.5 cm^2 aperture, with the aperture center located at x=15, y=6 cm, in the z = 0 plane.

Case II: A Thick Rectangular Aperture on a Small Rectangular Box

For numerical and experimental validation of the Modal/MoM code for a thick rectangular aperture, a rectangular box of size $(30\times12\times30)\,\text{cm}^3$, with a thick rectangular aperture of size $(20\times3)\,\text{cm}^2$, located at the center of one of its walls (i.e. $x_{c1}=15\,\text{cm},\ y_{c1}=6\,\text{cm},\ z_c=0\,\text{cm}$), and illuminated by the y-directed linearly-polarized plane wave of unit amplitude, was considered. The EFS, as defined in Equation 3.5-1, was computed at the center of the box and is plotted in Figure 3.5-2. Figure 3.5-2 also includes numerical results obtained using the Finite Element Method (FEM) [Ref. 3-2], the FDTD method [Ref. 3-6], and the transmission line method [Ref. 3-5]. There is good agreement between all four numerical methods, therefore supporting the validity of the Modal/MoM code. The experimental data shown in the Figure 3.5-2 are scattered around the true value due to perturbation of field due to the measuring probe.

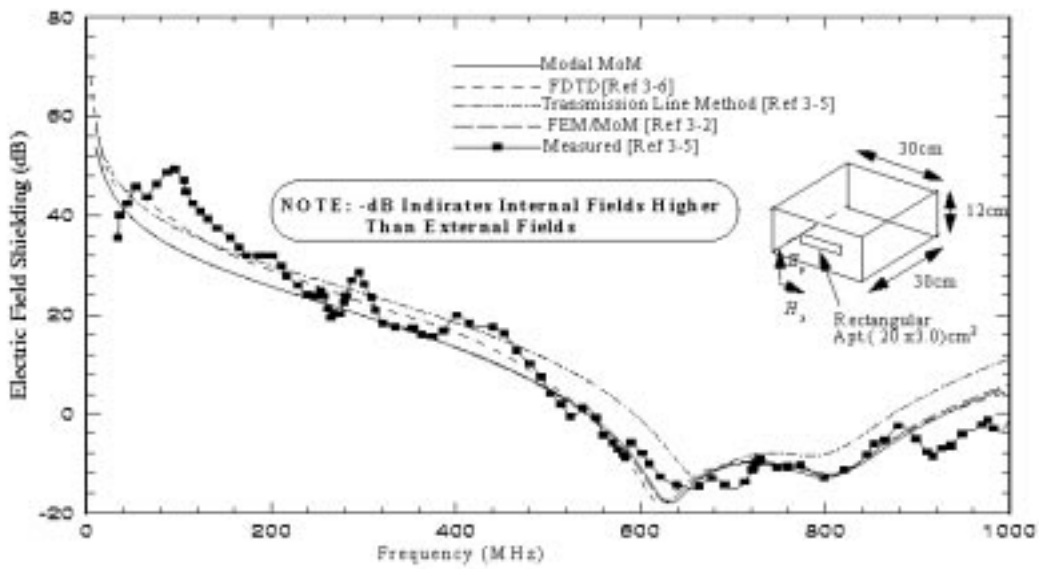

Figure 3.5-2: EFS at the center of a 30 x 12 x 30 cm^3 enclosure with a 20 x 3.0 cm^2 aperture, with the aperture center located at x=15, y=6 cm, in the z = 0 plane.

Case III: Two Wide Apertures on Opposite Walls of Rectangular Box

For further validation of the Modal/MoM code, a rectangular box with two apertures; one located on each wall as shown in Figure 3.5-3, was considered. The dimensions of the rectangular box are $(30\times12\times30)\,\text{cm}^3$ with rectangular apertures; one on each wall, and having sizes $(20\times3)\,\text{cm}^2$, $(20\times8)\,\text{cm}^2$, and $(30\times12)\,\text{cm}^2$, and located at the center of each wall. (i.e. $x_{c1} = 15$ cm, $y_{c1} = 6$ cm, $z_c = 0$ cm.) It is assumed that the $z = 0$ face of the box is illuminated by the y-directed linearly polarized plane wave of unit amplitude. The EFS, as defined in Equation 3.5-1 at the center of the box was computed and is plotted in Figure 3.5-3 along with the numerical results obtained using the FEM method. The excellent agreement between the two numerical methods validates the Modal/MoM code for a rectangular box with apertures on each side. Small discrepancies at the upper end of the frequency band in Figure 3.5-3 may be attributed to numerical inaccuracy due to the discretization levels used in the numerical methods.

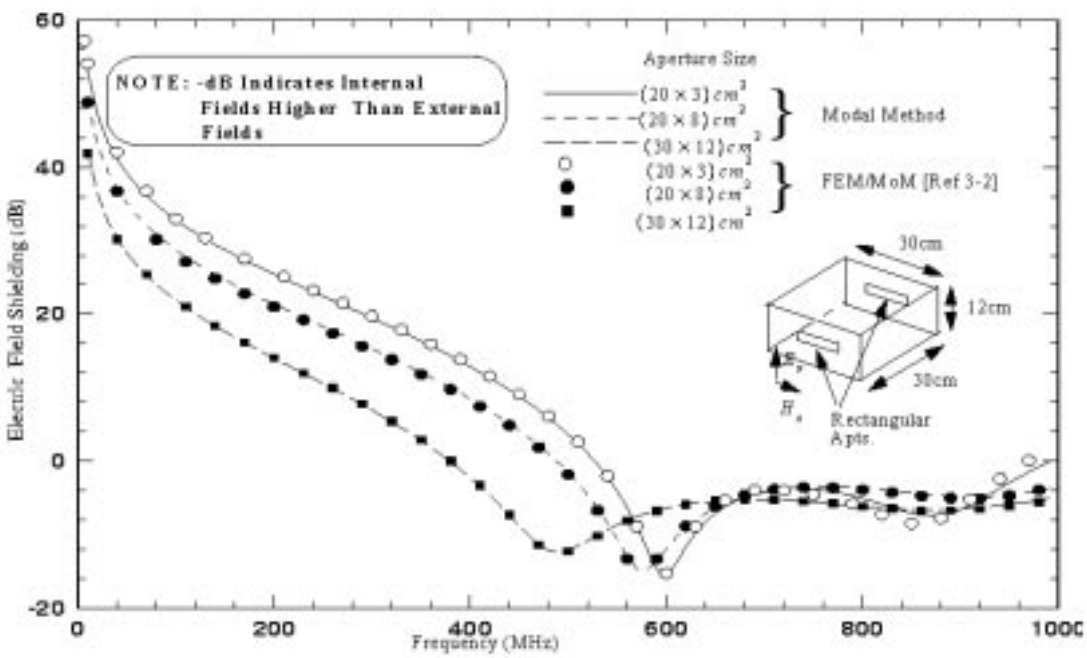

Figure 3.5-3: EFS of rectangular enclosure of size (30 x 12 x 30) cm ^{3} with two identical rectangular apertures (one on each side) of various sizes when illuminated by incident plane wave at normal incidence.

Case IV: Off-Center Multi-Apertures on Opposite Walls of a Rectangular Box

For validation of the case when apertures are displaced from the center of the walls of a rectangular box, a rectangular box with four apertures as shown in Figure 3.5-4 was considered. The rectangular box of size $(60\times12\times30)\,\text{cm}^3$ has four rectangular apertures, two on each wall having sizes $(20\times8)\,\text{cm}^2$, and located as shown in Figure 3.5-4. It is assumed that the $z=0$ face of the box is illuminated by the y-directed linearly-polarized plane wave of unit amplitude. The EFS, as defined in Equation 3.5-1 and calculated at the center of the box, was computed and is plotted in Figure 3.5-4 for multi-modes on each aperture. Also in Figure 3.5-4, the numerical results obtained using the FEM method are presented. Excellent agreement between the two different approaches over the lower frequencies validates the Modal/MoM code for off-centered apertures. The discrepancies in the results at higher frequencies may be attributed to the discretization level used in the FEM method.

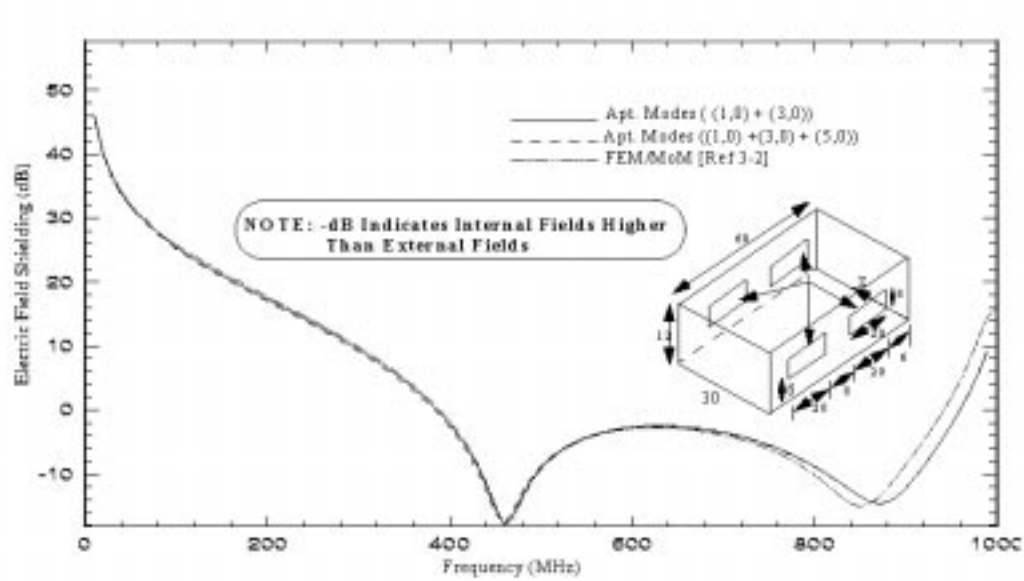

Figure 3.5-4: EFS of rectangular cavity with four rectangular apertures. Observation point (x=30, y=6, z=15) cm. All dimensions are in cm.

Case V: A Thin Cylindrical Wire in a Closed Cavity

To validate the wire formulation used in the Modal/MoM code, the case of a thin cylindrical wire of finite diameter, located inside a closed rectangular cavity, was considered. The code can analyze a finite-diameter cylinder aligned along the x, y, or z-axis of the cavity. For numerical validation, a rectangular, closed cavity of size $(2.29 \times 1.02 \times 4.19)\,\text{cm}^3$, with a wire of size (length = 0.87cm, diameter = 0.13cm) along the y-direction, and fed at (1.145, 0.0, 1.0) cm by a delta gap source was analyzed. The input impedance calculated using the Modal/MoM code is presented in Figure 3.5-5 along with the earlier numerical and experimental published results [Ref. 3-7]. The input reactance calculated using the present Modal/MoM code agrees well with the measured data.

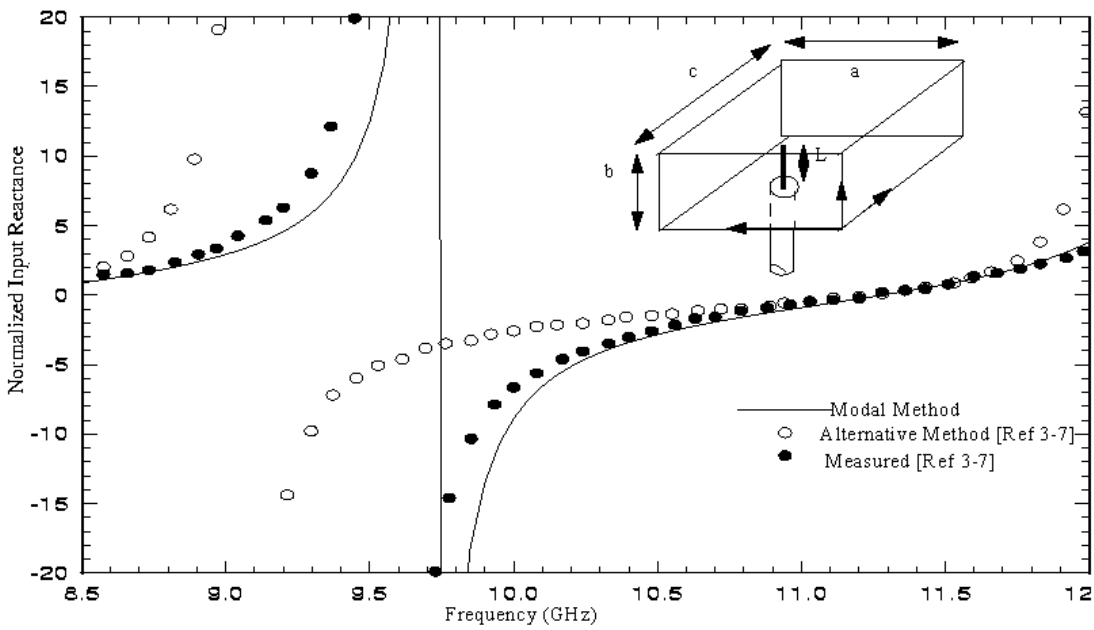

Figure 3.5-5: Normalized input reactance of coaxial probe feeding closed rectangular cavity at point (x_p,y_p,z_p). Dimensions of cavity a =2.29 cm, b = 1.02 cm, c = 4.19 cm, x_p = a/2, y_p = 0.0, z_p = 1.0 cm, L = 0.87 cm, diameter of probe = 0.14 cm.

Case VI: A Thin Cylindrical Wire Radiating inside Semi-Infinite Rectangular Waveguide

To validate the wire aperture coupling component of the Modal/MoM code, a thin wire exciting a semi-infinite rectangular waveguide, as shown in Figure 3.5-6, was considered. The waveguide and wire dimensions are as given in the Figure 3.5-6. Using the Modal/MoM code, $(k_0 d_0 - \beta_{10} L)$ values for constant X_{in} = 0 and R_{in} = 50, 75, and 100 Ohms were calculated and are presented in Figure 3.5-6 along with the earlier published results [Ref. 3-8]. The excellent agreement between the numerical results obtained from the present code and earlier published results validate the wire-aperture coupling component of the present formulation.

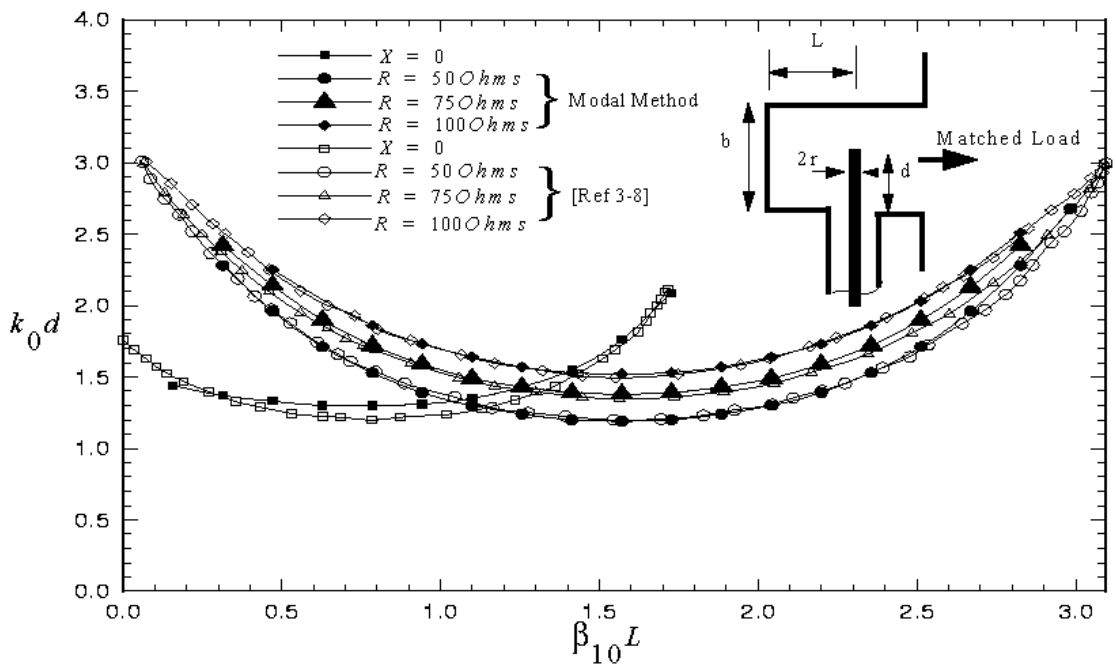

Figure 3.5-6: X = 0 and R = constant contours in $(k_0 d - \beta_{10} L)$ plane for a semi-infinite rectangular waveguide terminated into a matched load. Dimensions of waveguide: a = 2.29 cm (into page), b = 1.02 cm, r = 0.05a, λ = 3.14 cm.

Case VII: A Thin Cylindrical Wire In an Open-Ended Rectangular Waveguide

In Case VI, a thin wire in a semi-infinite rectangular waveguide was considered to check the wire aperture coupling formulation of the present code. However, when the apertures are radiating into free space, a different formulation was used. In order to check the validity of the interaction of a wire and radiating apertures, a thin wire exciting a rectangular cavity with one end open in an infinite ground plane was considered. The dimensions of the wire and cavity used for numerical simulation are shown in Figure 3.5-7. The input impedance calculated using the Modal/MoM code is shown in Figure 3.5-7 along with the numerical results obtained using the FEM method. A small disagreement between the numerical results is due to the finite discretization level used in the FEM method. The small perturbation around 10 GHz in the imaginary part of the input impedance is due to a cavity mode going from below cut-off frequency to above cut-off frequency.

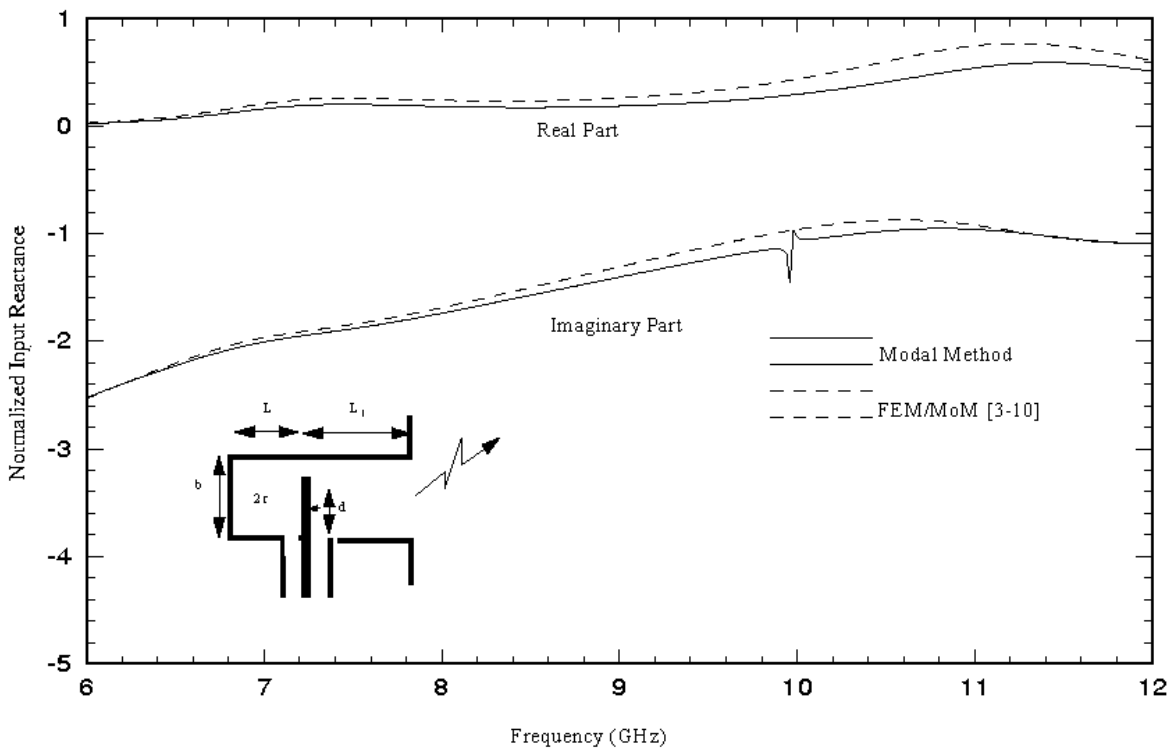

Figure 3.5-7: Normalized input impedance of coaxial line feeding rectangular waveguide. Waveguide dimensions: a = 2.29 cm (into page), b = 1.02 cm, L = 0.81 cm, L_1 = 1.19 cm, d = 0.4 cm, r = 0.065 cm.

3.6 Numerical Estimation of EM Threat to the CWT of a B-747-100 Due to FQIS Wiring

Quantitatively, the EM coupling threat to the CWT, through the FQIS wire, was defined in terms of total energy (J) delivered to the CWT, by the FQIS wire. In this section, the EM threat to the CWT of the B-747-100 due to the dominant emitter at frequency $f_c = 1.294\,\text{GHz}$ (as specified in the Table 3.3.1-1) was estimated using the Modal/MoM code developed and validated in the previous section. Though the present code was validated for smaller size cavities at lower frequencies, the mathematical formulation is valid at any higher frequency. Hence the code will give valid results at higher frequencies, provided the input parameters discussed below are properly selected. The rectangular cavity representing the B-747-100 with passenger windows is shown in Figure 3.4-1. The FQIS wire which runs along the fuselage was assumed to be along the y-direction; i.e., along the length of the fuselage. Various lengths of the FQIS wire were simulated.

The critical parameters that must be selected properly in the use of the Modal/MoM code are

1. Frequency Sampling, (Δf)
2. Number of Cavity Modes, (m,n)
3. Number of Aperture Modes, (p,q)

To achieve accurate results, a sufficient number of cavity modes, aperture modes, and frequency samples must be selected in using the Modal/MoM code. However, the computation time increases with an increase in those parameters. To achieve accuracy in the EM threat estimation at reasonable CPU time, therefore, the following choices of the above parameters were made.

3.6.1 Choice of Frequency Sampling

The frequency spectrum of the incident EM wave is spread around the carrier frequency (i.e., dominant emitter frequency) and depends upon the pulse width. The frequency spread is given by $\left(f_c - \frac{1}{\tau}\right) - \left(f_c + \frac{1}{\tau}\right)$. The spacing between two successive frequency points is given by $\Delta f = \frac{2}{\tau Q}$, where Q is the number of sampling points, should be sufficiently small to observe all peaks and nulls in the energy density spectrum. The peaks and valleys in the energy density depend upon the number of propagating modes inside the cavity. The number of propagating modes inside the cavity increases with f_c. Therefore, Δf must be small for higher f_c or a large number of sampling points for higher f_c must be selected. CPU time increases very rapidly with an increase in f_c. In order to make a dominant emitter energy calculation in a reasonable CPU time, the lowest frequency dominant emitter at $f_c = 1.294\,\text{GHz}$ was selected. From the Table 3.3.1-1, the pulse width for this dominant emitter was $2\mu s$, which gives the bandwidth of 0.5 MHz between the first nulls. However, to include the contribution from the second lobe, the bandwidth of 1.00 MHz was considered. Therefore, the spectrum of incident plane waves occurs over the band $1.2935 - 1.2945\ \text{GHz}$. Over this band, it was determined that approximately 1000 propagating modes could exist. The spacing between two successive frequency points was selected to be $\Delta f = 0.000001\ \text{GHz}$.

3.6.2 Choice of Number of Cavity Modes

At the frequency $f_c = 1.294$ GHz and for normal incidence, the cavity modes exist for $m = 1,3,.....$, and $n = 0,1,2.....$ However, for the frequency band of 1 MHz around the center frequency $f_c = 1.294$ GHz, propagating modes occur for $m = 1,3,.....53.$ and $n = 0,1,2.....490$ and were used in the numerical simulation.

3.6.3 Choice of Number of Aperture Modes

At the frequency $f_c = 1.294$ GHz and a window size of 35×25 cm^2, the aperture modes, which are above cut off, are for $p = 1, 3$. Therefore, the aperture windows can support $(1,0)$ and $(3,0)$ modes. The numerical simulation at $f_c = 1.294$ GHz for these two aperture modes was performed.

3.6.4 FQIS Wire Length Selection

The length of FQIS wire selected for the numerical simulation must be the same as the actual length of the FQIS wiring inside the B-747-100 aircraft. However, for a worst-case study, a length that will couple maximum EM energy must be selected. In order for the wire to couple maximum energy, it is postulated that wire lengths of $n\frac{\lambda}{4}$, where n is an odd integer, are required. For the numerical simulation, a wire of length $1420\,\text{cm}$, which is close to 61.25λ at $f_c = 1.294$ GHz, was selected. Table 3.6.4-1 gives the numerical values of various parameters selected for the EM threat estimation at $f_c = 1.294$ GHz. Since the CPU time to calculate the energy delivered to the CWT load at $f_c = 1.294$ GHz was large, and more confidence was needed for calculations at higher frequencies, it was felt the number of frequency sample points and FQIS wire lengths selected should be validated at a lower frequency. To validate these choices, a sensitivity study at half the lowest dominant emitter frequency ($f_c = 0.647$ GHz) over the bandwidth $0.6465 \sim 0.6475$ GHz and at the frequency sampling rate of 0.000004 GHz was conducted. The number of propagating modes over the bandwidth was found to be around 250. Selecting the frequency sampling rate at $0.000004\,\text{GHz}$ gives the sampling points equal to the number of propagating modes inside the cavity.

At this carrier frequency with 1 μs pulse width, the EM threats were calculated at very coarse (ie., Δf= 0.000004 GHz) frequency spacing for the FQIS wire lengths in the range $4213.678\,\text{cm} \le L_w \le 4244.107\,\text{cm}$. The calculated EM threats, in terms of total energy delivered to measured CWT load $Z_L = 79.449 - j60.242\,\text{Ohms}$, is shown in Figure 3.6.4-1. The method used to measure the CWT load impedance, Z_L, is described in Section 4.4.1 of this report.

Center Frequency, GHz	**1.294**
Input Spectrum	1.2935-1.2945 GHz
Frequency Sampling Rate	0.000001 GHz
Incident Electric Field Intensity	1V/cm
Rect. Cavity Size	(594.0 x 5651.5 x 606.0) cm3
Window Size	(35.0 x 25.0)cm2
Number of Windows	176, (88 on each side)
Window Locations on z=0 Plane	xc = 297.0 cm, Equally Spaced Along y-direction (Spacing = 63.5 cm)
Window Locations on z = 606.0 Plane	xc = 297.0 cm, Equally Spaced along y-direction(Spacing (63.5 cm)
Number Aperture Modes	2 Modes ((1,0) + (3,0))
Number of Cavity Modes	m=1,3,.....53, n = 0,1,2.....500
Wire Size	Length = 1420.0 cm, Dia. = 0.343 cm
Wire Feed Point	(297.0, 0.0, 303.0) cm
Load Impedance (measured)	79.449-j60.242 Ohms
Total Energy Delivered	4.47 x 10^{-9}Joules

Table 3.6.4-1: Parameter selection for FQIS wiring simulation.

Using the parameters as described above and with a finer frequency sample ($\Delta f = 0.00001\,\text{GHz}$) and a wire length 4231.066 cm, energy delivered to Z_L was re-calculated and is shown as the solid square in Figure 3.6.4-1. Figure 3.6.4-1 shows that when sampling points are equal or greater than the number of propagating modes, the EM threats calculated in Joules are constant. For the same length of the FQIS wire, EM threats were calculated at a very coarse frequency sampling ($\Delta f = 0.000001$ GHz) and it was found that the EM threats were approximately 20 percent below the EM threat number with a finer frequency spacing. The spectral energy density plot, when sampled at a rate equal to or greater than the number of propagating modes, estimates the entire energy in the signal coupled to the FQIS wire. The minimum sampling rate also ensures that no peak or null in the spectral density is missed. It is believed that $\Delta f = 0.000001\,\text{GHz}$ was, therefore, sufficient to pick up all peaks and nulls in the energy density spectrum around the dominant emitter at $f_c = 1.294\,\text{GHz}$. From Figure 3.6.4-1, the energy delivered to the FQIS wire is at the maximum when the wire length is around 91.25λ , and at the minimum when the wire length is around 91.00λ . It may, therefore, be concluded that the FQIS wire of length $n\lambda/4$, where n is an odd integer, will pick up maximum energy.

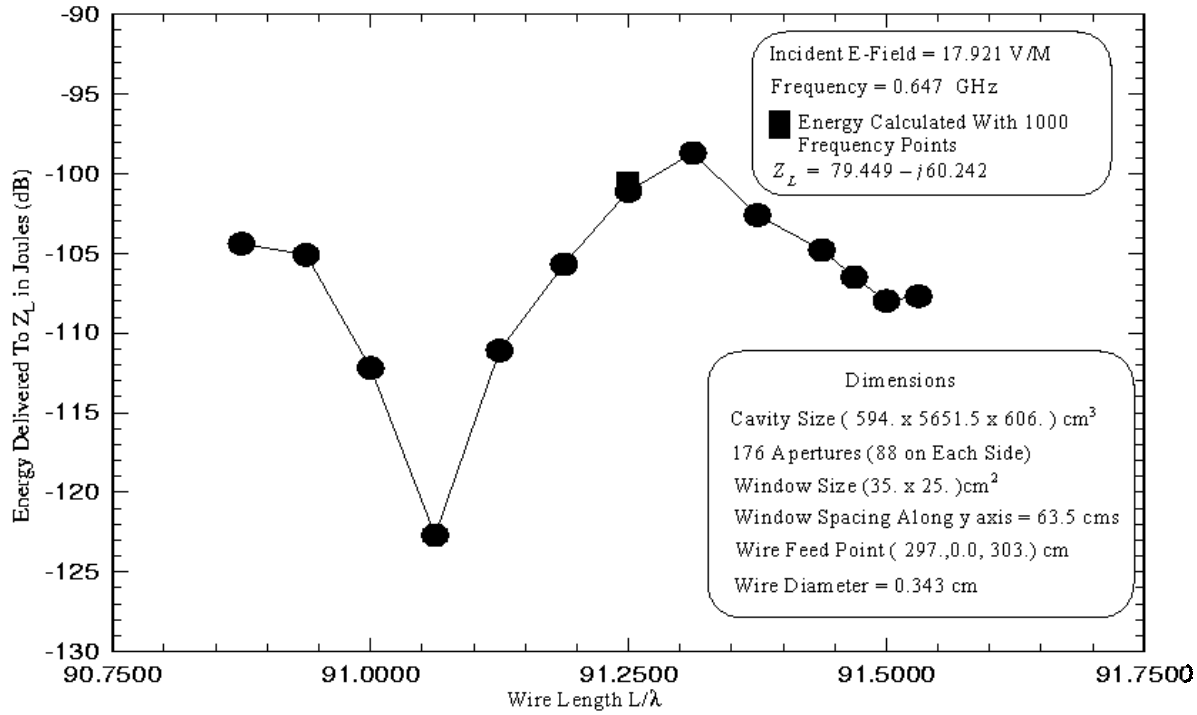

Figure 3.6.4-1: Energy delivered to load Z_L connected to wire of length L/λ inside a simulated B-747-100 passenger cabin due to external EM source.

After validating the choices of frequency sampling points and the FQIS wire lengths, the EM threats at $f_c = 1.294\,\text{GHz}$ were calculated for the parameters given in Table 3.6.4-1. For the parameters given in Table 3.6.4-1, and a FQIS wire length $L_w = 1420.00\,\text{cm}$, the input impedance of the FQIS wire residing inside the cavity was calculated over the given frequency band and plotted in Figure 3.6.4-2. The wild variation in the input impedance was due to the presence of a large number of propagating modes inside the cavity and the assumption of no loss inside the cavity.

The open-circuit voltage developed at the connection point, due to an external EM source over the given band, was also calculated using the Modal/MoM code and plotted in Figure 3.6.4-3. Using the Equation 3.4.3-4, the real energy density was calculated over the band and plotted in Figure 3.6.4-4. The measured CWT load impedance of $Z_L = 79.449 - j60.242$ Ohms was used in calculating the energy density. The area under the energy density curve gives the total energy delivered to the CWT by the FQIS wire due to an external EM source. For an external source of 1 V/cm, the energy delivered to the CWT load was found to be $E_{Total} = 1.4839\text{x}10^{-9}\,\text{J}$. From Table 3.3.1-1, the total energy delivered to the CWT due to field strength of $17.921\,\text{V/m}$ was calculated as $E_{Total} = (0.17921)^2 \times 1.4839 \times 10^{-9}\,\text{J}$. The numerical calculations shown in Figures 3.6.4-2 to 3.6.4-4 are repeated for the FQIS wire lengths shown in Table 3.6.4-2. The total energy in dB delivered to the CWT load for various FQIS wire lengths is plotted in Figure 3.6.4-5 along with the total energy that a monopole of the same length (but without the aircraft environment) will receive. These numbers may be considered as an upper bound on the energy delivered to the FQIS wire. Maximum energy will be delivered to the CWT if the CWT load impedance

is the complex conjugate of the input impedance of the FQIS wire. Assuming the CWT load to be the complex conjugate of the input impedance of the FQIS wire (i.e., $Z_L = (Z_{in})^*$), the maximum real energy delivered to the CWT was calculated and plotted in Figure 3.6.4-5.

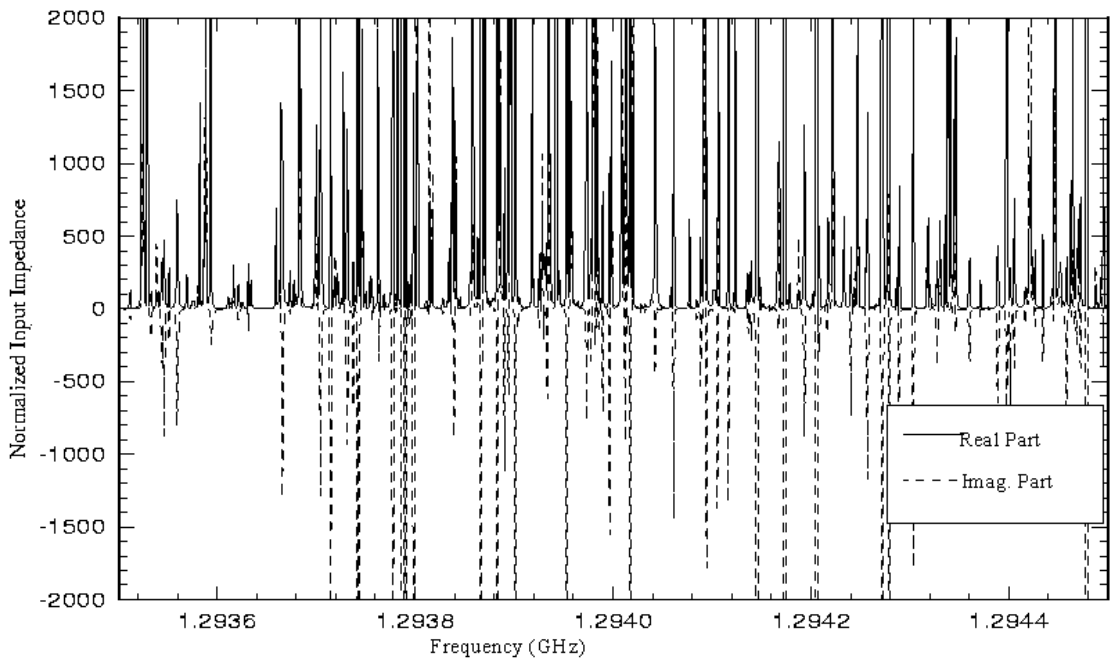

Figure 3.6.4-2: Normalized calculated input impedance of simulated FQIS wire in a rectangular cavity. Dimensions of cavity and FQIS wire are given in Table 3.6.4-1.

FQIS Wire Length (cm)	Length in Wave Lengths	Energy Delivered in Joules for 1V/cm Z_L=79.449-j60.242	Energy Delivered in Joules for 0.17921V/cm	Energy in dB	Energy Delivered in Joules for 1V/cm $Z_L=(Z_{in})^*$	Energy Delivered in Joules for 0.17921V/cm	Energy in dB	For Free Space Mono-pole(Energy in dB)
1420.00	61.25	4.47×10^{-9}	1.44×10^{-10}	-98.4	1.42×10^{-7}	4.56×10^{-9}	-83.4	-75.3
2834.235	122.25	3.87×10^{-9}	1.24×10^{-10}	-99.1	1.53×10^{-7}	4.91×10^{-9}	-83.1	-79.1
4225.270	182.25	4.771×10^{-9}	1.53×10^{-9}	-88.1	5.05×10^{-7}	1.62×10^{-8}	-77.9	
5639.25	243.25	1.76×10^{-9}	5.65×10^{-10}	-92.5	3.42×10^{-7}	1.10×10^{-8}	-79.6	

Table 3.6.4-2 Energy delivered to CWT by various FQIS wire lengths

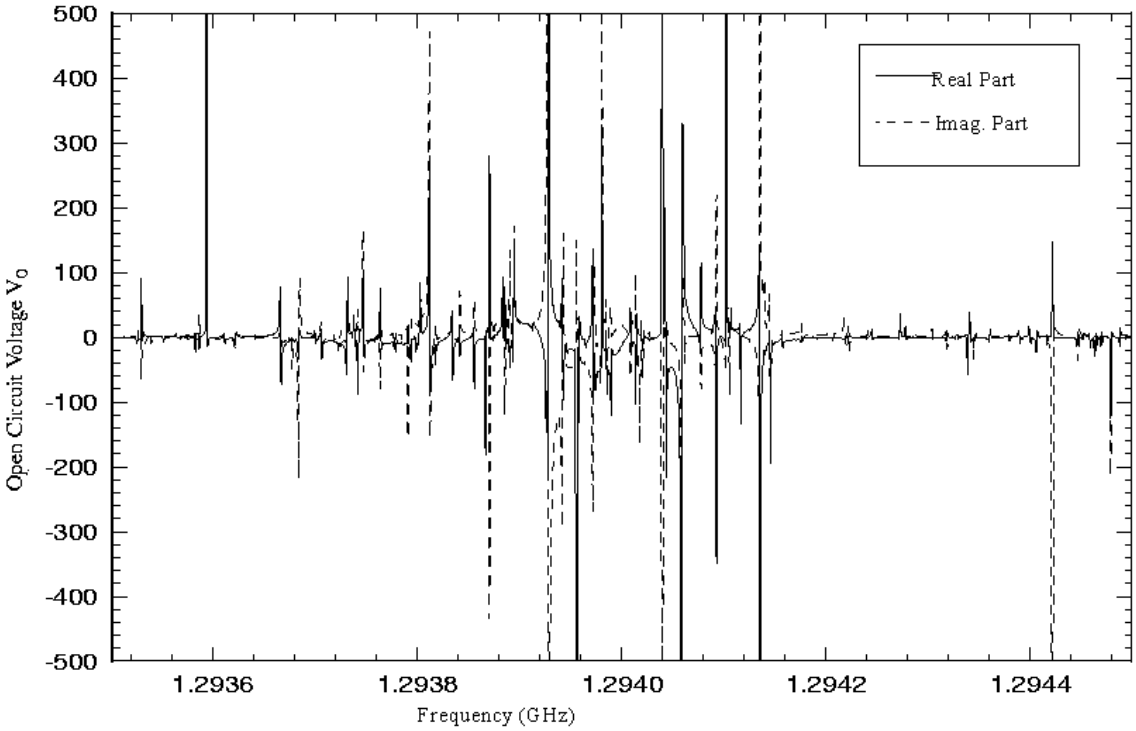

Figure 3.6.4-3: Open-circuit voltage at the connection point of FQIS wire and CWT. Dimensions of cavity and FQIS wire are given in Table 3.6.4-1.

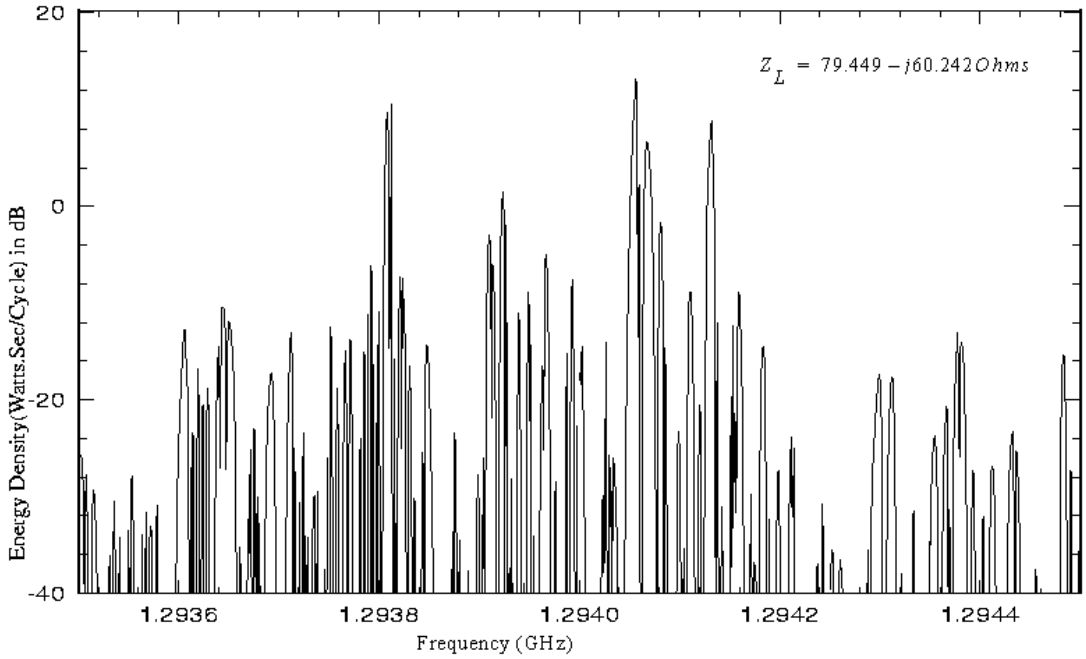

Figure 3.6.4-4: Energy density in (Watts × Sec)/Cycle in dB delivered to CWT load real (Z_L). Dimensions of cavity and FQIS wire are given in Table 3.6.4-1.

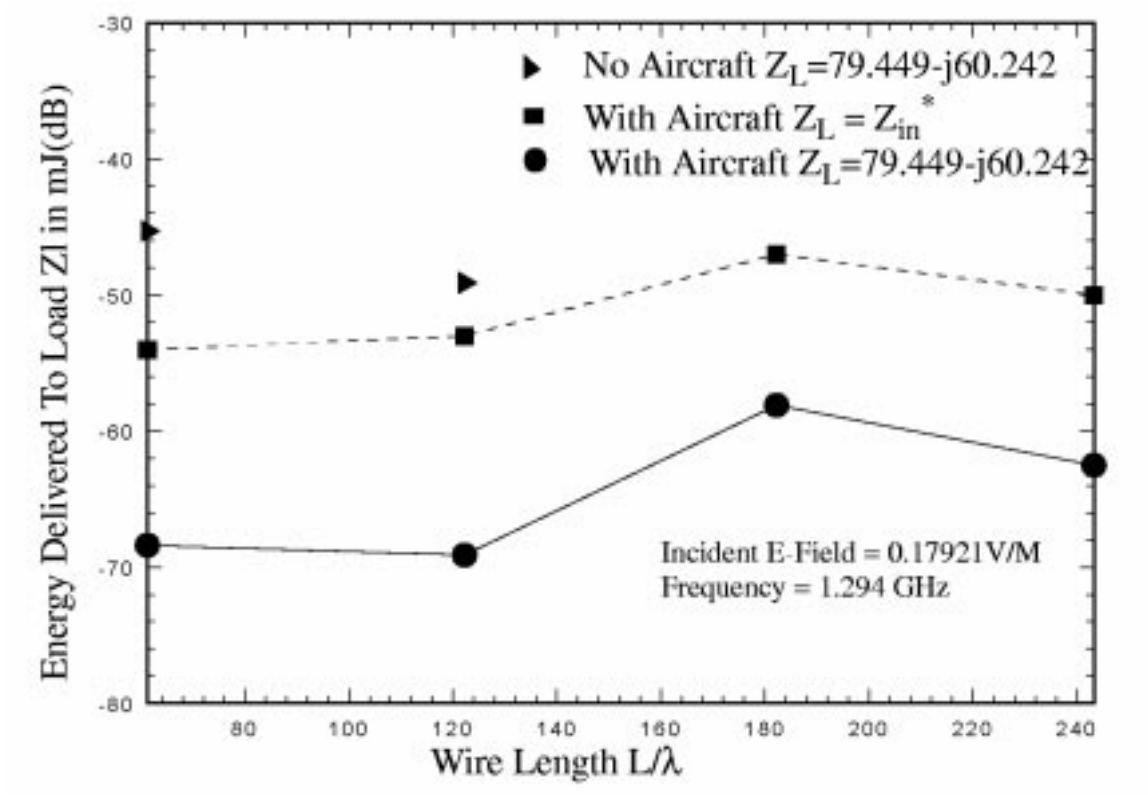

Figure 3.6.4-5: Energy delivered to load Z_L due to external EM source. Z_L is connected to a wire of length L/l, inside a simulated B-747-100 passenger cabin. Dimensions of cavity and FQIS wire are given in Table 3.6.4-1.

3.6.5 CPU Time Requirement

The CPU time (on a Silicon Graphics Incorporated, Origin 2000 machine) required for estimation of the EM threats in Joules at $, f_c = 0.647\,\text{GHz}$ was found to be 7 hours. Also, from the numerical simulation at $f_c = 1.294\,\text{GHz}$, the CPU time required for the EM threat estimation was found to be 182 hours. Using information of the CPU time required for calculations at $f_c = 0.647\,\text{GHz}$ and $f_c = 1.294\,\text{GHz}$, projected CPU times for higher frequencies were calculated. For the EM threat estimations for higher frequencies, the projected CPU times are given as 14000 CPU hours at $f_c = 2.875\,\text{GHz}$, 4.5×10^4 CPU hours at $f_c = 3.5\,\text{GHz}$, and 8.4×10^7 CPU hours at $f_c = 9.6\,\text{GHz}$.

3.7 Conclusions for External Analysis

An analytical approach to estimate EM threats from external RF sources to the CWT FQIS wiring of a B-747-100 was presented.

Using the maximum field strengths from signal sources identified by the JSC as dominant emitters, the maximum energy available inside the aircraft passenger cabin for each source was estimated using simple formulas. These dominant emitters were all pulsed sources, allowing the threat to be quantified in terms of energy, instead of power. The total available energy inside the aircraft cabin from the maximum dominant emitter (f= 2.875 GHz) was found to be less than 0.1 mJ. Even if this total energy could have been focused into a single discharge event, it was still below the generally accepted estimate of the minimum energy level (0.2 mJ) required to achieve ignition.

To provide a more accurate estimate of how much energy could actually be coupled to the FQIS wiring within the passenger cabin from external sources, numerical modeling was used. The B-747-100 fuselage was assumed to be a large rectangular cavity with rectangular windows on each side. The cavity was assumed to be homogeneous and lossless, with no seats or other structures present. A new, NASA LaRC developed numerical simulation technique, using a rectangular cavity Green's function and the integral equation method, estimated EM threats to the CWT due to external EM sources. The Modal/MoM code was validated through agreement with other analytical techniques and measurements. The Modal/MoM approach resulted in a lower number of unknowns compared to other numerical methods, such as the FEM and FDTD methods. Therefore, this new method was able to solve the large-size problems up to frequencies of 1-2 GHz. When applied to the available energy from the 1.294 GHz emitter source, the Modal/MoM approach estimated that CWT FQIS coupled energy levels were several orders of magnitude ($(1 \text{ to } 30) \times 10^{-4}$) less than the maximum available energy.

3.8 References for Section 3

[3-1] K. S. Kunz and R. J. Luebbers, *The Finite Difference Time Domain Methods for Electromagnetics*, Orlando, FL., CRC, 1993

[3-2] C. J. Reddy and M. D. Deshpande, " User's manual for CBS3DS Version 1.0, " NASA Contractor's Report 198236, Oct. 1995.

[3-3] R. F. Harrington, *Time-Harmonic Electromagnetic Fields*, McGraw-Hill Book Company, New York, 1961.

[3-4] C. A. Balanis, *Advanced Engineering Electromagnetics*, John Wiley & Sons, New York, 1989.

[3-5] M. P. Robinson, et al., "Analytical formulation for the shielding effectiveness of enclosures with apertures, " IEEE Trans, on Electromagnetic Compatibility, Vol. EMC –40, No. 3, pp.240-247, August 1998.

[3-6] FDTD data provided by Arizona State University

[3-7] M. S. Leong, et al., "Input impedance of a coaxial probe located inside a rectangular cavity, " IEEE Trans. On Microwave Theory and Techniques, Vol. MTT-44, No. 7, pp.1161-1164, July 1996.

[3-8] R. E. Collin, *Field Theory of Guided Waves*, McGraw-Hill Book Company, New York, 1960.

[3-9] M. Macrae and D. Hughes, "TWA Flight 800 Electromagnetic Environment", United States Department of Defense Joint Spectrum Center Report JSC-CR-99-006, January 1999

[3-10] C. J. Reddy, "User's manual for FEMOM3DR Version 1.0," NASA CR-1998-208709, September 1998.

4 Determination of Threat from Portable RF Sources Internal to Aircraft

4.1 Introduction

In the previous section, numerical techniques were applied to determine worst-case energy levels that could be made available to CWT wiring from pulsed HIRF sources external to the aircraft. The threat from PEDs carried aboard the aircraft does not lend itself to the same computational analysis for two primary reasons. First, virtually all PED sources transmit in a continuous or continuously modulated fashion. Thus, the threat may not be evaluated in terms of energy. Most widely known data regarding fuel-vapor ignition hazards are given in terms of energy, whereas very little information is available in terms of RF power. Experimental testing was necessary to establish the minimum RF power required for hazard conditions with the specific system. Second, there is the potential for near-field *direct* illumination of FQIS wiring with sources internal to the aircraft. For the external source problem, *in*direct illumination was the only option. Direct illumination quickly becomes dominant for close proximity coupling, especially in an electromagnetically lossy environment. Direct coupling is highly dependent upon very specific boundary conditions and varies drastically with frequency, which makes it exceedingly difficult to computationally model in an aircraft system.

This section (4) details the experimental techniques used to estimate the potential for arcing, sparking or excessive heating to occur upon FQIS wiring within the CWT, caused by PEDs internal to the aircraft. The EM threat from RF power radiated by other aircraft systems (communications, navigation) is not addressed.

4.1.1 Baseline Measurements on Actual Aircraft

A number of measurement alternatives were considered for this investigation. The original objective could have been met by either building a scale model of a CWT, or by transporting an actual B-747-100 CWT to NASA LaRC. Such a tank was found to be located in Mojave, California, and is pictured in Figure 4.1.1-1. The cost of transporting this CWT to NASA LaRC was found to be prohibitive, however.

Because of previous support of NTSB activities, NASA LaRC engineers had experience with an aircraft salvage operation in Roswell, New Mexico. The facility, AAR Aircraft Services, Inc., Roswell Division, possessed several retired B-747-100 aircraft, with FQIS installations that the NTSB determined were similar to that of TWA-800. It was found that the funding level and schedule could support baseline measurements on a whole aircraft, allowing a unique and unprecedented opportunity to obtain the most accurate baseline possible. A contract was established with AAR Roswell to allow measurements on two different aircraft (on two different occasions). A picture of one of these aircraft is shown in Figure 4.1.1-2.

The approach was to focus upon input impedance measurements of the CWT FQIS connector, and to measure the CWT reverberation characteristics. As part of the AAR Roswell contract, certified fuel tank mechanic support from Elite Structural Services (El Paso, Texas) was included. This support allowed detailed measurements of CWT EM reverberation and coupling characteristics to be performed, and actual wiring and components to be removed for laboratory study.

Figure 4.1.1-1: B-747-100 aircraft CWT that was previously removed as part of the TWA-800 investigation by the NTSB, and resting in Mojave, California.

Figure 4.1.1-2: Retired B-747-100 aircraft at AAR facility in Roswell, New Mexico.

4.1.2 Acquisition of FQIS Components, Installation in Laboratory

NASA LaRC's contract with AAR Aircraft Services, Inc. provided for the removal of all FQIS wiring, all eight fuel quantity probes, the M127 connector, and terminal strip. All components were received at NASA LaRC in excellent condition, allowing re-installation into a laboratory reverberation chamber. (See Figure 4.1.2-1.)

There were some significant differences between NASA LaRC's reverberation chamber "B" and an actual aircraft CWT. First, the laboratory chamber was made of steel, not aluminum. While its overall volume was similar to the CWT, the overall dimensions were different, and the interior was not divided into sub-cavities. An actual CWT also has penetrations for fuel and vent lines that are not necessarily secure from EM leakage. These were all factors of concern. Also required was the ability to measure voltage and current on the installation, and to be able to detect ionization events and localized heating. For practical purposes, a compromise installation was agreed upon to meet the following guidelines:

- The system was backed with an aluminum sheet. Fuel probes and wiring were installed with separation distances from structure identical to that of the aircraft installation (to approximate the common mode impedances in the aircraft). Nylon cable clamps recovered from the actual aircraft CWT were used in the laboratory installation.
- The installation dimensions were confined to fit within the field-of-view of infrared camera and ionization detection instruments (as best as possible).
- The aluminum sheet was painted black to minimize infrared reflection.
- A shielded box was installed to isolate the FQIS M127 connection from both the reverberation chamber (to prevent interference with the approximated CWT RF environment) and the RF generating equipment (for personnel safety).
- The installation was documented with photographs, and noteworthy characteristics were recorded.

Fuel Probes Installed in B-747-100 Fuel Tank

Fuel Probes Installed in NASA LaRC Reverberation Chamber

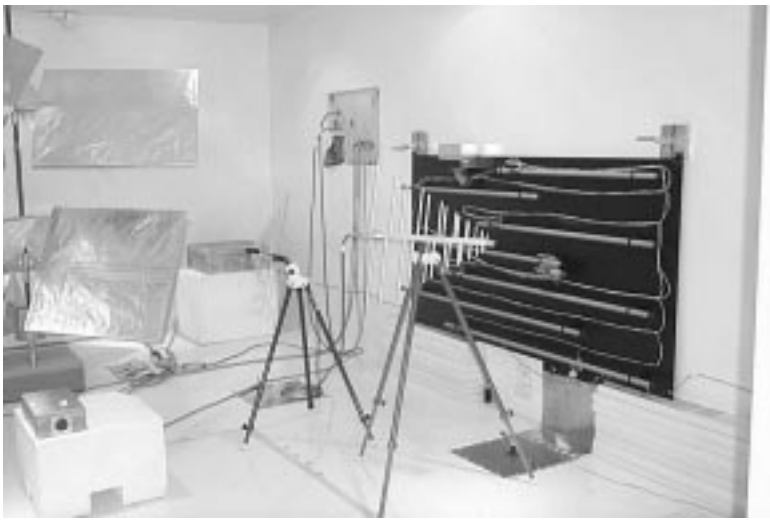

Figure 4.1.2-1: Fuel quantity probes and all internal wiring were removed from the CWT of a retired B-747-100 aircraft, and installed into NASA LaRC reverberation chamber "B".

As shown in Figure 4.1.2-1, all fuel probes, wiring and connectors were transferred to a 4 ft × 8 ft sheet of aluminum, and installed in a NASA LaRC reverberation chamber. The aluminum sheet was bonded to the chamber floor with a 20 in. section of copper sheet. The installation is frequently described as a "FQIS Simulator" in this report.

The approach was to perform the best practical laboratory installation, and perform measurements to establish EM similarity to an actual aircraft. The comparison data provided limits of comparability and scaling factors.

4.1.3 Duplication of Field Measurements in Laboratory, Comparisons

Sections 4.4.1 to 4.4.4 focus upon the experimental effort to establish EM comparability between the aircraft CWT FQIS and the laboratory installation. Based upon engineering judgement and experience, it was determined that the following factors needed to be addressed in establishing this comparability:

1. Section 4.3 shows that typical PEDs operate from 27 MHz to about 6000 MHz frequency. Therefore, it was deemed necessary to characterize the CWT and FQIS as an integrated EM system within this frequency range.
2. Show comparability between the aircraft CWT FQIS input impedance versus that of the laboratory installation. (See Section 4.4.1.)
3. Generate scale factors to describe the reverberation differences between an actual CWT versus reverberation chamber. (See Section 4.4.2)
4. Determine whether the FQIS wiring was actually the dominant path for RF signals to penetrate the CWT. (See Section 4.4.3, and also 4.4.5.5.)
5. Measure coupling characteristics between actual CWT cavities, and determine how to account for or approximate this coupling in the laboratory. (See Section 4.4.2.)
6. Determine the degree to which fuel will affect coupling and electrical resonant characteristics. (See Section 4.4.4.)

4.1.4 Detailed Measurements in Laboratory

With comparability limitations and scaling factors relating laboratory data to aircraft data, it was possible to apply the advantages of the laboratory's improved accessibility, safety and sophisticated instrumentation. The first goal was to obtain a more detailed understanding of how voltages and currents can be distributed throughout the system, when RF power is applied. Section 4.4.5 will outline the extensive effort to evaluate the EM response of the entire CWT FQIS in terms of currents and voltage with the following variables:

- Measurements at numerous locations
- Measurements at numerous frequencies
- Excitation of different wires (and combinations of wires) into the CWT
- Excitation by radiated fields only

The second goal was to determine frequencies and minimum power levels at which an ionization event or excessive heating phenomenon could occur. Using the previously obtained data, specific test conditions (and locations) for maximum induced currents and voltages were identified. The test setup was then modified to maximize the likelihood for an ionization/heating event at these locations. Details and results of this effort are provided in Section 4.5.

4.1.5 Detailed Outline of Section 4

Section 4 of this report contains over 100 pages of descriptions, diagrams, photographs and analyses and, therefore, represents the majority of report content. Up to five levels of subsections were required to cover the necessary detail. To avoid unnecessary confusion, only three levels of subsections were included in the Contents section at the front of this document. The following outline is provided to assist the reader in locating figures, tables and equations, as they are referenced outside their own subsections.

4 Determination of Threat from Portable RF Sources Internal to Aircraft. 41
4.1 Introduction. 41
4.1.1 Baseline Measurement on Actual Aircraft 41
4.1.2 Acquisition of FQIS Components, Installation in Laboratory 43
4.1.3 Duplication of Field Measurements in Laboratory, Comparisons 44
4.1.4 Detailed Measurements in Laboratory 44
4.1.5 Detailed Outline of Section 4. 45
4.2 Symbols for Section 4 47
4.3 Estimation of Threat From Typical PEDs 48
4.3.1 Portable Transmitters' Manufacturer Specifications 48
4.3.2 Typical Transmitter Characteristics Based on ANSI C63.18-1997 48
4.3.3 Determination of FCC Limits 49
4.3.4 Summary of PED Threat Levels 49
4.4 Characterization of Aircraft and Laboratory FQIS Installations 51
4.4.1 FQIS Impedance Measurements. 51
4.4.1.1 Retired B-747-100 CWT (Roswell, New Mexico) 51
4.4.1.1.1 Network Analyzer Measurement Methodology and Technique 52
4.4.1.1.2 Instrument Setup 52
4.4.1.1.3 Adapters 53
4.4.1.1.4 Systematic Errors 54
4.4.1.1.5 Calibration. 54
4.4.1.1.6 Connector Compensation 54
4.4.1.1.7 Retired B-747-100 Measurement Results 55
4.4.1.1.8 Resistance and Capacitance Measurement Technique and Results 57
4.4.1.2 LaRC Reverberation Chamber "B", with FQIS Components Installed 57
4.4.1.2.1 Network Analyzer Measurement Methodology and Technique 59
4.4.1.2.2 Laboratory FQIS Simulator Impedance Measurement Results 60
4.4.1.2.3 Resistance and Capacitance Measurement Results for the simulated FQIS 61
4.4.1.3 Comparisons of EM Similarity
4.4.2 Cavity Reverberation Measurements 71
4.4.2.1 Retired B-747-100 CWT (Roswell, New Mexico) 71
4.4.2.1.1 Description of the CWT 71
4.4.2.1.2 Peak Cavity Coupling Factor- Measurement Setup 72
4.4.2.1.3 Peak Cavity Coupling Factor- Results 77
4.4.2.1.4 Bay 1 to Bay 3 Radiated Field Coupling 79
4.4.2.2 LaRC Reverberation Chamber "B", with FQIS Components Installed 81
4.4.2.3 Comparisons of EM Similarity 82
4.4.3 Aircraft Measurements of Passenger Cabin Coupling to CWT and CWT FQIS Wiring 84
4.4.3.1 Measurement Method, Applicability and Results 84

4.4.3.1.1 Power on the FQIS Wiring at CWT Entry 84
4.4.3.1.2 Coupling from Passenger Cabin to Antenna Inside CWT 89
4.4.3.2 Application to PED Threat Levels 94
4.4.4 Isolated Fuel Probe Tests 97
4.4.4.1 Measurement Setup 97
4.4.4.2 Results and Conclusions 98
4.4.5 Detailed Measurement of FQIS Installed in Laboratory 101
4.4.5.1 Laboratory Setup 101
4.4.5.2 Instrument Setup 103
4.4.5.3 Current Enhancement Measurements 104
4.4.5.4 Voltage Enhancement Measurements 105
4.4.5.5 Conducted versus Radiated Excitation Comparison 106
4.4.5.5.1 Experiment Setup 107
4.4.5.5.2 Experiment Data 107
4.4.5.5.3 Analysis of Experiment Data 109
4.4.5.6 Selection of Maximum Voltage and Current Enhancement Positions 111
4.5 RF Induced Ionization, Discharge, Heating of FQIS Installed in Laboratory Chamber . . 119
4.5.1 Estimation of CWT Voltage and Current Magnitudes Induced by RF 119
4.5.2 “Weakening” of Worst-Case Test Points 125
4.5.2.1 Reduced Current Carrying Capacity at Current Enhancement Location 126
4.5.2.2 Intermittent Short Condition at Voltage Enhancement Location 126
4.5.3 Detection Methods 126
4.5.3.1 Visible Camera 126
4.5.3.2 Infrared Imaging System 126
4.5.3.3 UVTron® 128
4.5.3.4 AM Radio 128
4.5.3.5 Night Vision System 128
4.5.4 Validation of Discharge Detection Devices with Electrostatic Discharge Gun 128
4.5.5 “Full” PED Threat Level Test 130
4.5.5.1 Test Setup 130
4.5.5.2 Test Results 132
4.5.6 Minimum Power for Discharge Test 133
4.5.6.1 Test Setup 133
4.5.6.2 Test Results 134
4.5.7 Supplementary Analysis Regarding Threats Below 30 MHz 136
4.6 Conclusions for Internal Analysis 139
4.7 References for Section 4 140

4.2 Symbols for Section 4

π	pi. The circumference divided by the diameter of a circle.
λ	Wavelength
$\overline{\Gamma}$	Complex Reflection Coefficient
Γ	Reflection Coefficient Magnitude
C	Capacitance
CE(f)	Current Enhancement as a function of frequency
CTF	Current transfer function
f	frequency
G_{trans_max}	Maximum Gain of a transmitting antenna
G_{rcv_max}	Maximum Gain of a receiving antenna
I(f)	Current as a function of frequency
IF_{probe}	current probe transfer function
P	Power
Q	Quality Factor
R	Slant Range between two antennas
R_{ch}	Resistance of a charging resistor
R_d	Resistance of a discharging resistor
V(f)	Voltage as a function of frequency
VE(f)	Voltage Enhancement as a function of frequency
VF_{probe}	voltage probe transfer function
VTF	Voltage transfer function
Z	Impedance
Z_{in}	Input Impedance
Z_L	Load Impedance
Z_o	Characteristic Impedance
Z_T	Transfer Impedance

(See Section **iii** for a more complete listing of symbols and abbreviations.)

4.3 Estimation of Threat from Typical PEDs

Communication, data transfer, and signaling devices are designed specifically to emit RF power. These are referred to as *Intentional Radiators*. Virtually all electronic devices will also radiate some degree of EM power *unintentionally* when they are operating. In the United States, the Federal Communications Commission (FCC) regulates how much power commercial PEDs may radiate intentionally and unintentionally.

Under the support of the NTSB, the JSC provided NASA LaRC with a summary listing of emissions from PEDs [Ref. 4-1]. These sources included unintentional radiators such as compact disk players and portable computers, and intentional radiators such as wireless phones. From the report, power output from unintentional radiators was in the range of mV/meter, whereas the power output from intentional radiators was as high as 5-10 W. As a result, this effort was concentrated on intentional radiating sources only. The scope of this effort was limited to typical, commercially available devices. Damaged devices, devices developed for military use, and those modified to exceed the regulation limits were not considered.

For this effort, information on the threats was gathered from three information sources: typical device manufacturer's specifications, ANSI C63.18-1997 for typical transmitters for radiated electromagnetic immunity testing of medical devices, and the Federal Communication Commissions (FCC) regulations. More details about these information sources are described below.

4.3.1 Portable Transmitters' Manufacturer Specifications

The JSC report [Ref. 4-1] provided specifications of several typical PED transmitters. These included analog cellular phones, digital personal communication system (PCS) phones, wireless local area networks (LANs), two-way pagers, and, most importantly, the commercial and military two-way radios, which have the highest radiated power ratings of all devices considered.

Built on the JSC's efforts, data on a larger number of similar devices were compiled and added to the list. The combined list of almost 50 devices along with their operating frequencies and maximum rated powers, are shown in Appendix G. In addition, the data are plotted in Figure 4.3.4-1, to be shown later.

4.3.2 Typical Transmitter Characteristics based on ANSI C63.18-1997

A good start for typical PEDs was given in ANSI C63.18-1997 "Recommended Practice for an On-Site, Ad Hoc Test Method for Estimating Radiated Electromagnetic Immunity of Medical Devices to Specific Radio-Frequency Transmitters." Some data from the standard are shown in Table 4.3.2-1.

There were additional transmitters in the ANSI C63.18-1997 that were omitted from Table 4.3.2-1, because of their low probability of being on the airplane. These included 250 W paging transmitters, 25 W mobile radios (typically mounted to a vehicle or boat), 10-100 W police/ambulance radios (presumably mounted to vehicles). CISPR 11 and CISPR 22 devices were also eliminated due to extremely low power levels that are in fractions of a μW.

Data in this table are also summarized and plotted in Figure 4.3.4-1.

Product	Frequency (MHz)	Power (W)
Hand-held transceivers	27, 49, 138-470	5
Wireless LANs	912, 2400	0.1
Personal digital assistants	896-940	4
Radio modems	896-901	10
Cellular Telephones	800-900	0.6
Personal communications satellite telephones	1610-1626.5	1
Licensed PCS equipment	1850-1910	1

Table 4.3.2-1: Typical PEDs and their output power levels. Data from ANSI C63.18-1997.

4.3.3 Determination of FCC Limits

Also of interest were the FCC power limits on PEDs. With the exception of *federal government spectrum*, the maximum radiated power from any legally used PED in the United States must be below the FCC limits, by regulation. Federal government spectrum is controlled by the National Telecommunications & Information Administration (NTIA). Most information on federal government spectrum, especially on military frequencies, was classified, and will not be considered here.

A manual search was made through about nine parts of the FCC's regulations that pertain to PEDs. Many of the specifications appeared ambiguous, possibly because some limits are not yet defined. In addition, some power level limits were different for different applications, even though the allocated frequencies were the same. In fact, many currently available products had power outputs higher than the gathered FCC limits. This fact was taken to mean that these products were either covered under different FCC limits, or had applications other than what the data indicated. The gathered FCC limits are shown in Appendix H, and are plotted in Figure 4.3.4-1.

4.3.4 Summary of PED Threat Levels

Figure 4.3.4-1 summarizes the threats data collected thus far using the above information sources. As seen from the chart, most devices radiate 6 W or less, except at 27 MHz and at 900 MHz. At 27 MHz, the FCC limit is 25 W for a few devices. At 900 MHz, the ANSI standard shows 10 W maximum for radio modems. For the purpose of determining a worst-case threat at any given frequency, only the highest radiated power level at that frequency was considered.

The data presented in Figure 4.3.4-1 show that intentionally transmitting PED frequencies are limited to between 25 MHz and 2.6 GHz. The FCC allocates spectrum to about 6 GHz, however. Based on the data, the frequency range for characterizing the EM coupling performance of a B-747-100 CWT was chosen to be from 25 MHz to 6.5 GHz. The threat levels presented in Figure 4.3.4-1 were applied to the results of Sections 4.4.2 and 4.4.3 for determining the maximum power coupled into the fuel tank and its wiring. The results are presented in Section 4.4.3.2.

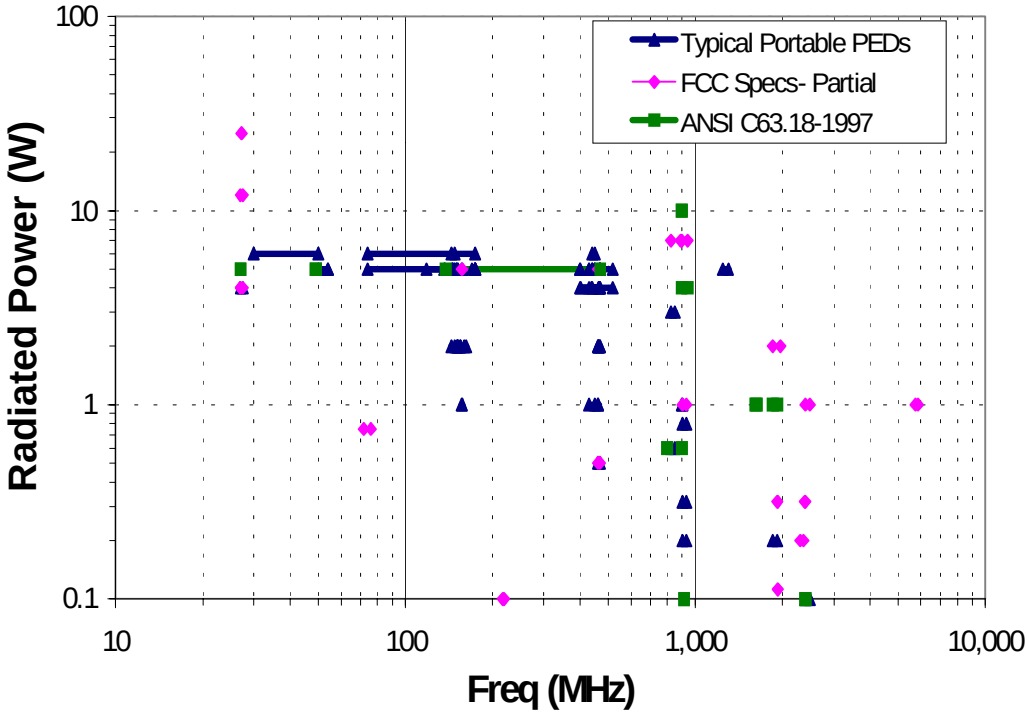

Figure 4.3.4-1: PED threat levels.

4.4 Characterization of Aircraft and Laboratory FQIS Installations

The objective of this section (4.4) is to show limits of comparability between the aircraft and the laboratory FQIS installations. A series of FQIS input impedance measurements were performed on the aircraft and in the laboratory reverberation chamber. Impedance values were compared between the two installations, and results are summarized in Section 4.4.1. Section 4.4.2 establishes comparability of the reverberation characteristics of a B-747-100 CWT, as compared to a NASA LaRC reverberation chamber. Section 4.4.3 describes the frequency dependent coupling between the passenger cabin and the CWT of a B-747-100.

In addition to direct comparison measurements between aircraft and laboratory FQIS installations, some additional measurements were required to prepare for the high-power RF testing described in Section 4.5. To determine how the resonant characteristics of a fuel probe may change during normal operation, the fuel probe's RF reflection was examined as a function of frequency and fuel level. Details are provided in Section 4.4.4. In Section 4.4.5, extensive measurements of RF induced currents and voltages are described. Data from these measurements were used to select particular test locations exhibiting maximum voltage and current enhancements, caused by a particular mode of RF excitation.

4.4.1 FQIS Impedance Measurements

The objective of the FQIS impedance measurements was to electrically characterize the FQIS system contained within the CWT of a B-747-100, and to compare the electrical characteristics to those of the FQIS installation at NASA LaRC. The electrical characteristics were a function of the wiring, the fuel probes, associated connectors that form the fuel measuring system, and the spatial position of each of the components in the installation. The input impedance of the FQIS system was measured at the frequencies of possible PED frequencies as determined from the study described in Section 4.3. This series of measurements was performed with a network analyzer. A DC resistance check and a capacitance check were also performed. This section provides measurement descriptions of the tests on the actual aircraft and in the laboratory installation.

4.4.1.1 Retired B-747-100 CWT (Roswell, New Mexico)

Figure 4.4.1.1-1 shows the D3 input connector to the FQIS CWT installation. A total of three signal pins, one signal shield, and the aircraft chassis are shown in the figure. The input impedance measurements were performed in the left wheel well at the FQIS interface connector on the aft of the fuel tank. The signal descriptions and corresponding pin numbers for the D3 connector are explained in Section 2. The baseline DC values for the resistance and capacitance were taken for all combinations of the pins. The frequency dependant impedance was measured for each non-trivial combination of these pins.

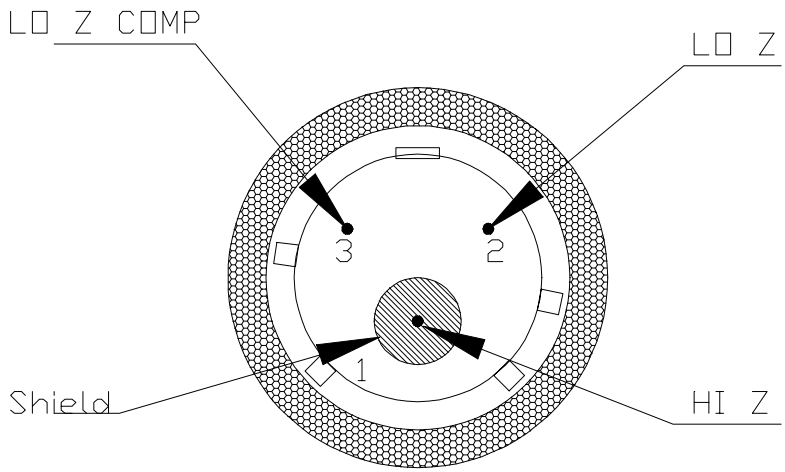

Figure 4.4.1.1-1: FQIS CWT Amphenol D3 connector schematic.

4.4.1.1.1 Network Analyzer Measurement Methodology and Technique

There are several measurement techniques available for conducting impedance measurements. These include the Auto Balancing Bridge method, a current-voltage probe technique, Frequency Domain Network Analysis, and Time Domain Network Analysis. These methods vary in complexity, frequency response, and accuracy depending on the system to which they are applied. To measure the aircraft system described in this report, the Fixed Bridge Method of impedance measurements was selected. This method, as described in Appendix D, utilizes a network analyzer with an S-parameter test set, calibration standards, and connector compensation. The advantages include minimization of cable mismatch, rapid measurements, wide frequency range, better directivity provided by the test set, excellent repeatability, calibration enhanced accuracy, and automation. The network analyzer allows the operator to focus on measurement results rather than measurement technique.

4.4.1.1.2 Instrument Setup

For the impedance measurements of the aircraft FQIS, a vector network analyzer was used and configured as depicted in Figure 4.4.1.1.2-1. A data acquisition computer was connected to the network analyzer via the general-purpose interface bus (GPIB) to facilitate the storage of data for later display and plotting. A test port cable was connected to the reflection port of the S-parameter test set of the network analyzer. An adapter device allowed for connection between the test port cable and the FQIS test lead, which connected directly to the M127 connector assembly. This adapter made it possible to directly inject signals through this interface, onto the FQIS wiring, and to the fuel probes within the CWT.

The network analyzer was configured to operate on channel one with 201 points per sweep at a sweep rate of 100 msec. The frequency span was established at a start frequency of 300 kHz and a stop frequency at 1 GHz. This configuration of the network analyzer equates to a measurement resolution of 5 MHz. This resolution allowed complete measurements of the full test matrix in a reasonable amount of time. For a general impedance comparison between the actual aircraft CWT impedance and the laboratory FQIS simulator, the resolution was sufficient to show the similarity of the average values of the impedance.

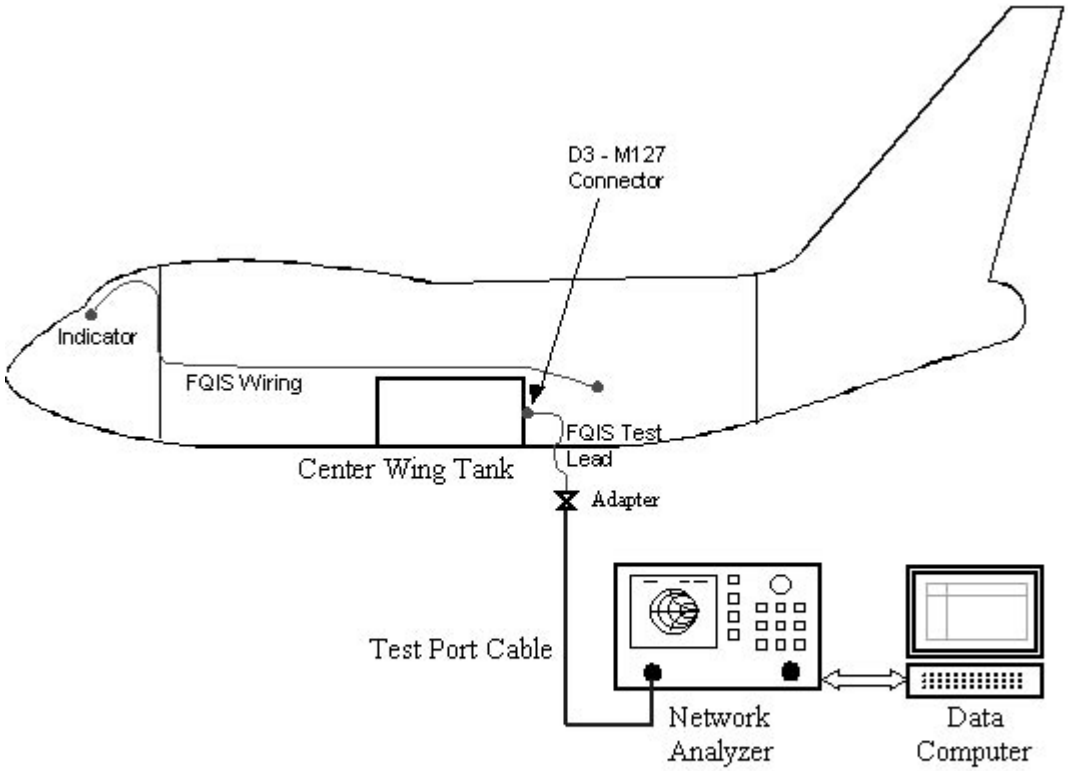

Figure 4.4.1.1.2-1: Aircraft FQIS impedance measurement setup.

4.4.1.1.3 Adapters

The two special adapters, which allowed for calibration and connection to the D-3 FQIS test lead that connected to the M127 connector of the CWT, were designed and constructed in the lab. The adapters were designed for the system being tested and for the set of calibration standards using similar connectors. The test adapter connected the N-type test port cable to the single conductors of the D-3 test lead. A calibration adapter connected the calibration standards directly to the test adapter. This configuration allowed the calibration reference plane to be defined at the end of the adapter. With the test adapter and the test port cable included during the calibration process, any associated errors were characterized within the calibration and removed from the measurement data. A compensation technique was used for the calibration adapter, and will be described in Section 4.4.1.1.6. The D-3 FQIS test lead was not included in the calibration because it was connected after the adapter. However, test lead lengths do not become a factor until the length is a significant portion of the wavelengths of the frequencies being measured. The D-3 test lead was insignificant in length compared to the length of the wires that comprise the FQIS. A section of the external FQIS wiring was used as the test lead.

4.4.1.1.4 Systematic Errors

There are various systematic errors associated with any measurement system. These errors are due to the imperfections associated with any real measuring device. A perfect system has infinite dynamic range, no impedance mismatches, and infinite directivity for every frequency. The systematic errors inherent to the network analyzer used for the B-747-100 FQIS impedance measurements were removed by calibration with a known set of standards traceable to the National Institute of Standards and Technology (NIST). Calibrating out the system errors added a high degree of accuracy and repeatability to the FQIS impedance measurements. [Ref. 4-2]

4.4.1.1.5 Calibration

Calibration of the network analyzer was performed before every unique FQIS impedance measurement sequence conducted on the B-747-100. The network analyzer was calibrated using the reflection 1-port calibration method to remove the system effects of tracking (frequency response), source match, and directivity. The specified calibration standards (Open, Short, and Load) were attached to the measurement system to force a known boundary condition at a specific location at the end of the adapter on the test port cable. The "Open" established the open-circuit boundary condition (infinite ohms). The "Short" established the short-circuit boundary condition (zero ohms). The "Load" established the matched-circuit boundary condition to the characteristic impedance of the measuring instrument (50 ohms). This calibration improved the measurement by defining the reference plane or point where the measurement accuracy was known. All of the B-747-100 FQIS impedance measurements were referenced to this point. [Ref. 4-3]

4.4.1.1.6 Connector Compensation

It is often the case that the cable impedance is determined by the low-frequency response, up to around 500 MHz, where mismatch effects are still small. However, at frequencies around 1 GHz and higher, uncompensated lengths of fixtures, adapters, or connectors can affect the value obtained from the measurement of a cable's impedance. In general, as the connector return loss becomes worse, it will have a greater effect on impedance measurements.

A connector compensation technique was performed to compensate for the calibration adapter. The calibration adapter, though used during calibration, did not remain a component during actual measurements. The added residual effect to the calibration by the adapter was removed using the compensation technique called Open/Short + Delay compensation. An electrical delay, representative of the adapter length, was used to negate the effects of the adapter. The residual impedance due to the electrical length or phase shift of the calibration adapter was measured and then the measurement system was compensated with electrical delay to yield the true value of impedance for the aircraft FQIS. [Ref. 4-3]

4.4.1.1.7 Retired B-747-100 CWT Measurement Results.

As described in Section 4.4.1.1.2, the network analyzer was configured to measure a set of 201 frequency points from 300 kHz – 1 GHz. The input impedance values of the FQIS system were recorded at each of these frequencies. Impedance is a specification that is defined only at a discrete frequency. However, when commonly referred to, the impedance of a cable is an average of the impedance values over a frequency range. For this investigation, cable impedance was the average impedance presented at the input of the D3 – M127 connector interface of the CWT over the frequency span from 300 kHz to 1000 MHz. This frequency range is representative of the frequencies where PED threats are most likely to occur. The average impedance magnitude can be approximated by:

$$\left|Z_{avg}\right| = \frac{\sum_{F_{min}}^{F_{max}} \left|Z_{in}(f_i)\right|}{\left(F_{max} - F_{min}\right)}. \qquad (4.4.1.1.7\text{-}1)$$

Z_{in} is the input impedance as a discrete function of frequency
F_{max} and F_{min} are the frequency bounds of the desired average
f_i is the discrete measurement frequency

The data gathered in the input impedance measurement were saved as a set of text data files on the data acquisition computer. Table 4.4.1.1.7-1 shows the average impedance values calculated using Equation 4.4.1.1.7-1. The average values of the impedance provided a simple representation of the impedance of the FQIS installation.

AIRCRAFT						
SIGNAL		**REFERENCE**	**PIN**		**PIN**	**Average Impedance (Ohms)**
HI Z	to	LO Z COMP	1 center	to	3	193.9
HI Z	to	SHIELD	1 center	to	1 shell	60.9
LO Z COMP	to	SHEILD	3	to	1 shell	54.7
LO Z COMP	to	AIRFRAME CHASSIS	3	to	Airframe	395.1
HI Z	to	AIRFRAME CHASSIS	1 center	to	Airframe	273.0
HI Z	to	LO Z	1 center	to	2	188.8
LO Z	to	SHIELD	2	to	1 shell	183.3
LO Z	to	AIRFRAME CHASSIS	2	to	Airframe	323.5
SHIELD	to	AIRFRAME CHASSIS	1 shell	to	Airframe	265.3

Table 4.4.1.7-1: Aircraft CWT FQIS average impedance measurement data.

4.4.1.1.8 Resistance and Capacitance Measurement Technique and Results

The measurements described in Section 4.4.1 represent the complex value of the impedance that was measured at an individual frequency. This value is a complex combination of the DC resistance and the reactance at the discrete frequency. The values for the DC resistance and the capacitance were measured with a calibrated commercial off-the-shelf hand-held digital voltmeter (DVM). Therefore, there was no on-sight calibration required to acquire these data. Because of the simplicity of the measurement device, a complete description of the operation of the DVM will not be discussed here. In general, the contact areas were kept clean and a non-intrusive method of attaching the DVM was followed.

SIGNAL		Reference	PIN		PIN	Aircraft DC Resistance (Ohms)	Aircraft DC Capacitance (nF)
HI Z	to	LO Z COMP	1 center	to	3	>20 M	1.36
HI Z	to	SHIELD	1 center	to	1 shell	>20 M	8.57
HI Z	to	LO Z	1 center	to	2	>20 M	2.32
SHIELD	to	LO Z	1 shell	to	2	>20 M	2.27
SHIELD	to	LO Z COMP	1 shell	to	3	>20 M	1.50
LO Z COMP	to	LO Z	3	to	2	>20 M	1.39
LO Z	to	AIRFRAME CHASSIS	2	to	Airframe Chassis	>20 M	1.41
LO Z COMP	to	AIRFRAME CHASSIS	3	to	Airframe Chassis	>20 M	1.86
AIRFRAME CHASSIS	to	LO Z	Airframe Chassis	to	2	>20 M	1.45
HI Z	to	AIRFRAME CHASSIS	1 center	to	Airframe Chassis	>20 M	1.32
SHIELD	to	AIRFRAME CHASSIS	1 shell	to	Airframe Chassis	>20 M	1.45
AIRFRAME CHASSIS	to	AIRFRAME CHASSIS	Airframe Chassis	to	Airframe Chassis	0.1	NA

Table 4.4.1.1.8-1: DC resistance and capacitance measurements conducted on the B-747-100 Aircraft FQIS internal to the CWT.

Table 4.4.1.1.8-1 contains the measurement results for DVM measurements performed in Roswell, NM. Because of the small data acquisition time required to perform these measurements, all possible combinations of the connectors were measured. These data provided a baseline to ensure the FQIS laboratory installation was correct.

4.4.1.2 LaRC Reverberation Chamber "B", with FQIS Components Installed

An FQIS simulator was designed and fabricated at NASA LaRC, and was installed in reverberation chamber "B" of the HIRF laboratory. The FQIS simulator was described in Section 4.1.3 and is shown in detail in Figure 4.4.1.2-1.

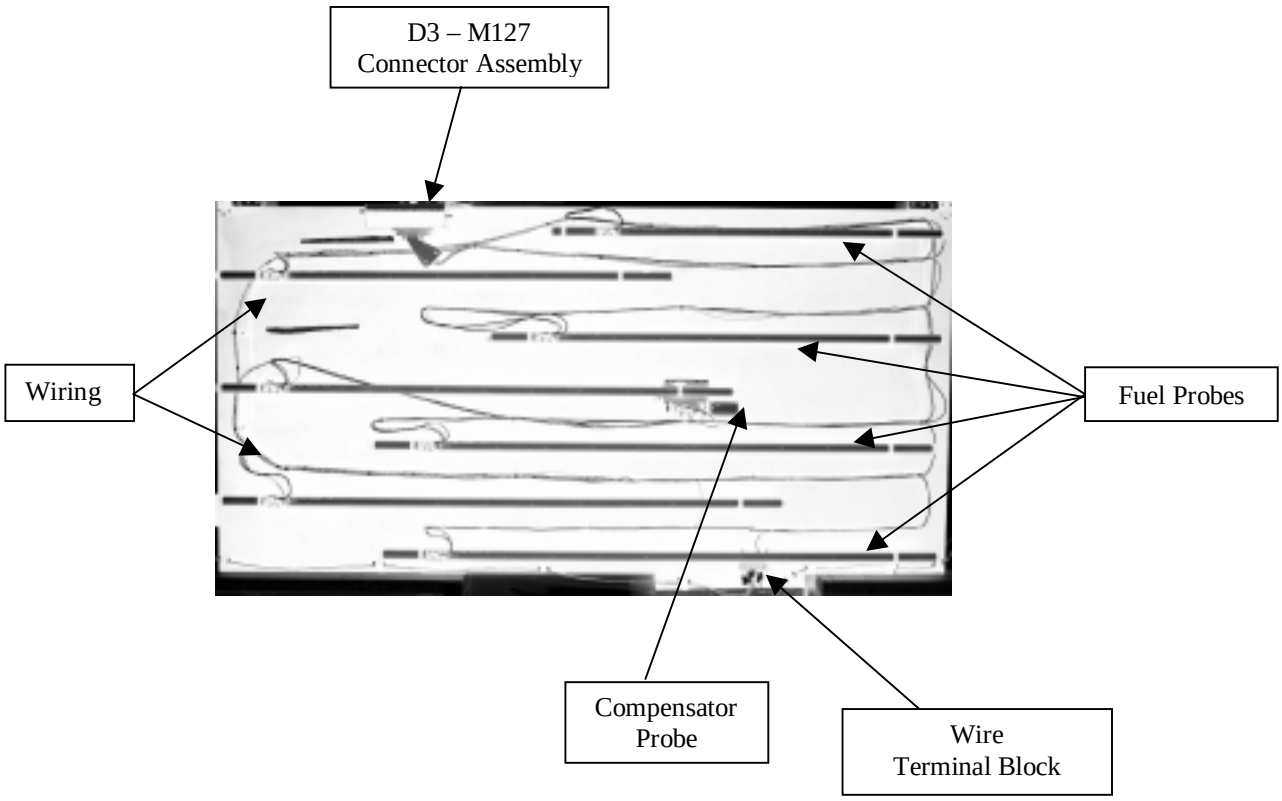

Figure 4.4.1.2-1: FQIS simulator used in NASA LaRC reverberation chamber "B".

4.4.1.2.1 Network Analyzer Measurement Methodology and Technique

The measurement methodology and technique for the input impedance measurements conducted on the laboratory FQIS installation was identical to the measurements taken in Roswell. These measurements were described in Section 4.4.1.1.1 to 4.4.1.1.6.

The vector network analyzer was used to measure reflection coefficient and the reflection coefficient data were transferred to the data acquisition computer. Figure 4.4.1.2.1-1 shows the laboratory test setup. The D3 and M127 connectors were mounted in an aluminum box attached to the ground plane. This configuration simulated the aircraft chassis interactions with the FQIS, and provided a convenient access location for data acquisition purposes.

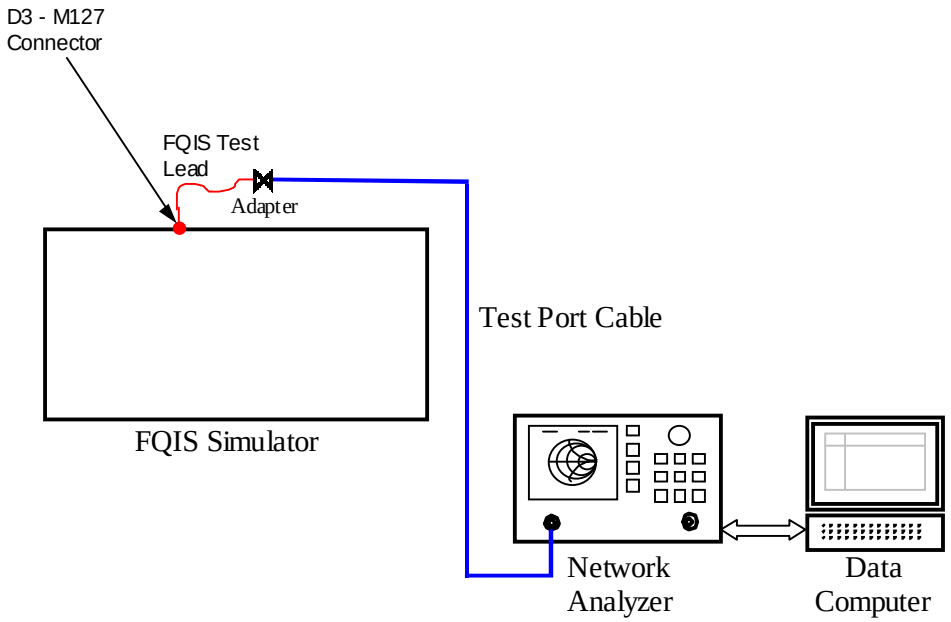

Figure 4.4.1.2.1-1: Laboratory FQIS simulator impedance measurement setup.

4.4.1.2.2 Laboratory FQIS Simulator Impedance Measurement Results.

As described in Section 4.4.1.1.2, the network analyzer data were recorded across the frequency band of interest (300 kHz – 1 GHz). The discrete frequency reflection impedance values were post processed to produce the average impedance for each of the measurement configurations. Table 4.4.1.2.2-1 summarizes the measurement results.

NASA FQIS SIMULATOR						
SIGNAL		**REFERENCE**	**PIN**		**PIN**	**Average Impedance (Ohms)**
HI Z	to	LO Z COMP	1 center	to	3	160.4
HI Z	to	SHIELD	1 center	to	1 shell	56.2
LO Z COMP	to	SHIELD	3	to	1 shell	251.5
LO Z COMP	to	AIRFRAME CHASSIS	3	to	Airframe	394.5
HI Z	to	AIRFRAME CHASSIS	1 center	to	Airframe	305.5
HI Z	to	LO Z	1 center	to	2	186.3
LO Z	to	SHIELD	2	to	1 shell	224.8
LO Z	to	AIRFRAME CHASSIS	2	to	Airframe	329.6
SHIELD	to	AIRFRAME CHASSIS	1 shell	to	Airframe	303.8

Table 4.4.1.2.2-1: Laboratory FQIS simulator average impedance measurement data.

4.4.1.2.3 Resistance and Capacitance Measurement Results for the simulated FQIS

A series of DC resistance and capacitance measurements were performed at NASA LaRC on the simulated FQIS installation. These measurements paralleled the measurements taken in Roswell NM. Table 4.4.1.2.3-1 contains the measurement results for DVM measurements performed at NASA LaRC. All possible combinations of the connectors were measured for comparison purposes to the measurements taken in Roswell.

SIGNAL		**Reference**	**PIN**		**PIN**	**Aircraft DC Resistance (Ohms)**	**Aircraft DC Capacitance (**nF)
HI Z	to	LO Z COMP	1 center	to	3	>20 M	1.81
HI Z	to	SHIELD	1 center	to	1 shell	>20 M	9.30
HI Z	to	LO Z	1 center	to	2	>20 M	2.73
SHIELD	to	LO Z	1 shell	to	2	>20 M	2.87
SHIELD	to	LO Z COMP	1 shell	to	3	>20 M	1.90
LO Z COMP	to	LO Z	3	to	2	>20 M	1.96
LO Z	to	AIRFRAME CHASSIS	2	to	Airframe Chassis	>20 M	1.64
LO Z COMP	to	AIRFRAME CHASSIS	3	to	Airframe Chassis	>20 M	1.56
AIRFRAME CHASSIS	to	LO Z	Airframe Chassis	to	2	>20 M	1.72
HI Z	to	AIRFRAME CHASSIS	1 center	to	Airframe Chassis	>20 M	1.62
SHIELD	to	AIRFRAME CHASSIS	1 shell	to	Airframe Chassis	>20 M	1.63
AIRFRAME CHASSIS	to	AIRFRAME CHASSIS	Airframe Chassis	to	Airframe Chassis	0.1	NA

Table 4.4.1.2.3-1: DC resistance and capacitance measurements conducted on the laboratory FQIS installation.

4.4.1.3 Comparisons of EM Similarity

The data gathered from each FQIS installation represents nine combinations of reflection measurements. These measurements are summarized in Table 4.4.1.1.7-1 and Table 4.4.1.2.2-1. Each reflection measurement had 201 frequencies where the complex reflection coefficient was measured. In the frequency ranges of interest, small changes of the measurement system or the installation will shift the resonant frequencies of the system. The resonant frequency shifting phenomena of the fuel probes is discussed in Section 4.4.4. A comparison of aircraft FQIS input impedance measurements on two separate days showed somewhat different results. These differences were attributed to environmental influence. Statistics of the measurements did not vary appreciably. A comparison of each frequency and the resulting impedance value was not practical. Impedance is generally characterized by the mean value across the frequency band of interest [Ref. 4-4]. The average values of the impedance measurements are compared in Table 4.4.1.3-1. The measurements taken with the DVM were very similar for the two installations. These measurements were taken at low frequencies, and do not characterize the high frequency impedance.

SIMPLE COMPARISON OF AVERAGE IMPEDANCES							
				Aircraft	**Simulator**		
Run No.	**SIGNAL**		**REFERENCE**	**Average Impedance (Ohms)**	**Average Impedance (Ohms)**	**Δ Ohms**	**Δ %**
1	HI Z	to	LO Z COMP	193.9	160.4	33.5	17.3 %
2	HI Z	to	SHIELD	60.9	56.2	4.7	7.7 %
3	LO Z COMP	to	SHIELD	~~54.7~~	251.5	~~246.8~~	~~359.8 %~~
4	LO Z COMP	to	AIRFRAME CHASSIS	395.1	394.5	0.6	0.15 %
5	HI Z	to	AIRFRAME CHASSIS	273.0	305.5	32.5	11.9 %
6	HI Z	to	LO Z	188.8	186.3	2.5	1.3 %
7	LO Z	to	SHIELD	183.3	224.8	41.5	22.6 %
8	LO Z	to	AIRFRAME CHASSIS	323.5	329.6	6.1	1.9 %
9	SHIELD	to	AIRFRAME CHASSIS	265.3	303.8	38.5	14.5 %

Table 4.4.1.3-1: Comparison of aircraft and laboratory FQIS average impedance values .

The data displayed in measurement run number 3 in Table 4.4.1.3-1 displays a large percentage difference in the average impedance. Further examination of the reflection data from run number 3, shows that the data measured for this configuration was invalid. The data remains in this section for completeness and to demonstrate the validity of the comparison method.

Figures 4.4.1.3-1 and 4.4.1.3-2 show the magnitude of the input impedance plotted for the aircraft installation and the reverberation chamber installation. The average impedance is plotted in red for each installation. These average values are very close even though the impedance values vary for many discrete frequencies.

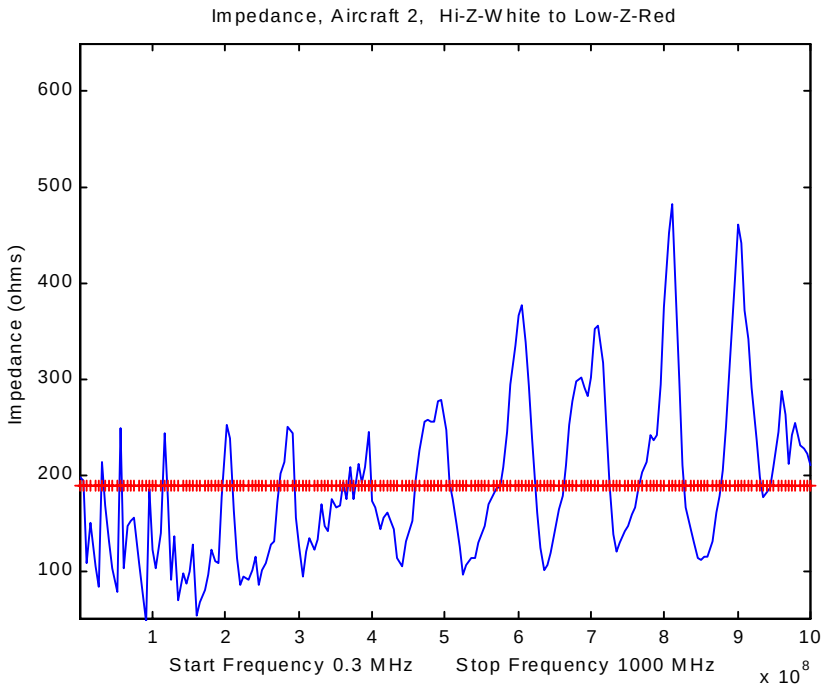

Figure 4.4.1.3-1: Input impedance of the aircraft FQIS wiring with the mean value plotted as the red (+) line.

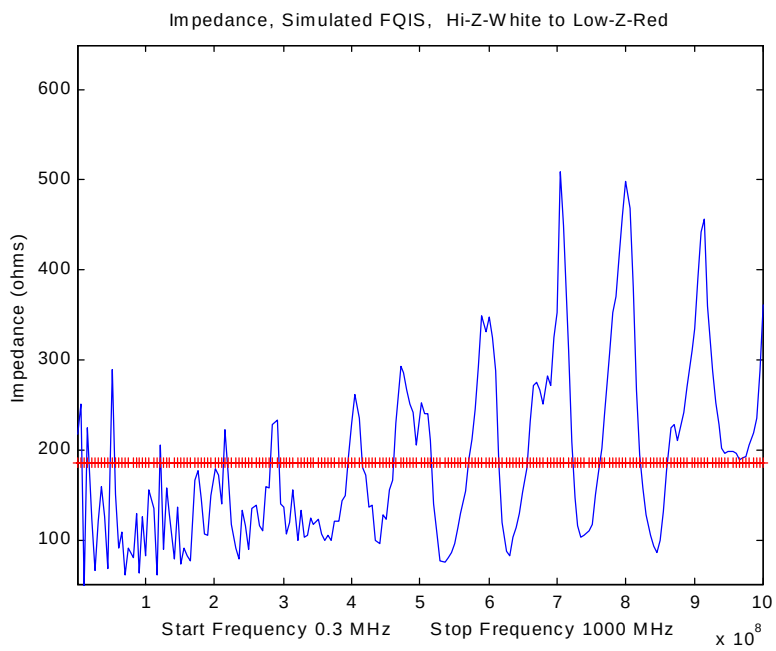

Figure 4.4.1.3-2: Input impedance of the laboratory FQIS wiring with the mean value plotted as the red (+) line.

The plots of Figures 4.4.1.3-1 and 4.4.1.3-2 provide only the magnitude of the impedance. For a complete comparison the complex impedance should be considered. The Smith Chart provides coordinate axis capable of displaying the complex value of the impedance. Figures 4.4.1.3-3 and 4.4.1.3-4 represent plots of the input impedance as measured between the HI Z and LO Z FQIS CWT connections (ie. differential mode) using the Smith Chart coordinate axes. The network analyzer and data-acquisition computer measurement system (as shown in Figures 4.4.1.1.2-1 and 4.4.1.2.1-1) recorded the amount of power that was reflected by the impedance mismatch of the FQIS installation. From this complex reflection coefficient, the impedance was calculated (see Appendix E, Equation E.2-1) [Ref. 4-5]. Both the magnitudes and resonant frequencies of these installations were affected by environmental conditions, resulting in small differences in the impedance measurements of the installations. The impedance measurements show that the two installations were electrically similar for the HI Z to LO Z excitation mode.

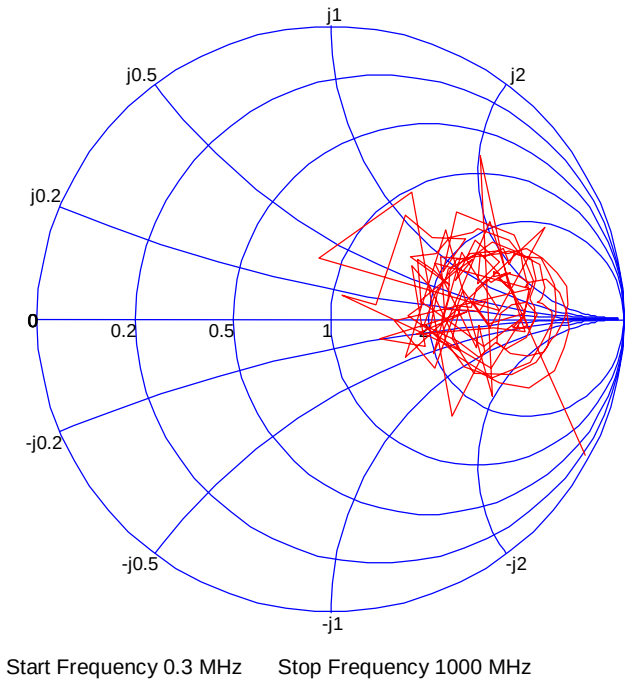

Figure 4.4.1.3-3: Smith Chart plot of the input impedance from aircraft FQIS [HI Z to LO Z]

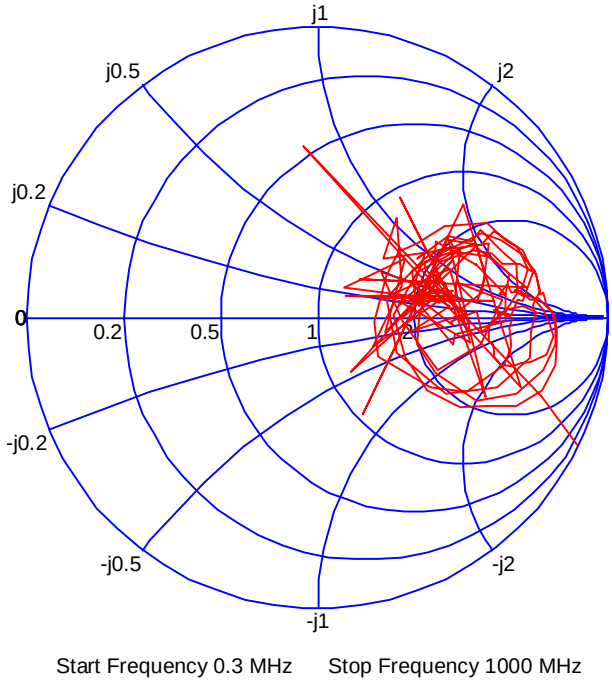

Figure 4.4.1.3-4: Smith Chart plot of the input impedance from the laboratory FQIS [HI Z to LO Z]

A statistical method of comparison was implemented to more easily compare the input impedances between the aircraft installed FQIS and the reverberation chamber installation of the FQIS. A full discussion of the method is provided in Appendix E. The average of the real part and the average of the imaginary part represent the center of the data distribution, when plotted on the Smith Chart. Figure 4.4.1.3-5 shows a statistical data comparison of the impedance of the aircraft-installed FQIS. The black trace represents the aircraft impedance data, and the red star represents the average value of the reflection coefficient plotted as impedance. The green star represents the average value of the reflection coefficient measured in the reverberation chamber installation. The red and green circles represent the standard deviations associated with the impedance of the aircraft and chamber installations, respectively.

The combining of statistical analysis with graphical Smith Chart analysis is unique. However, the basic concepts of each are fundamental [Refs. 4-5 and 4-6]. In fundamental statistical theory, graphical concepts are readily employed to build intuition about problems. Figure 4.4.1.3-5 gives the reader an instant means by which to compare the impedance values from the two installations and gain "geometric intuition" about the similarity of the installations. Figures 4.4.1.3-6 through Figure 4.4.1.3-12 show the entire set of impedance measurements, with aircraft data directly compared with laboratory data for FQIS excitation mode.

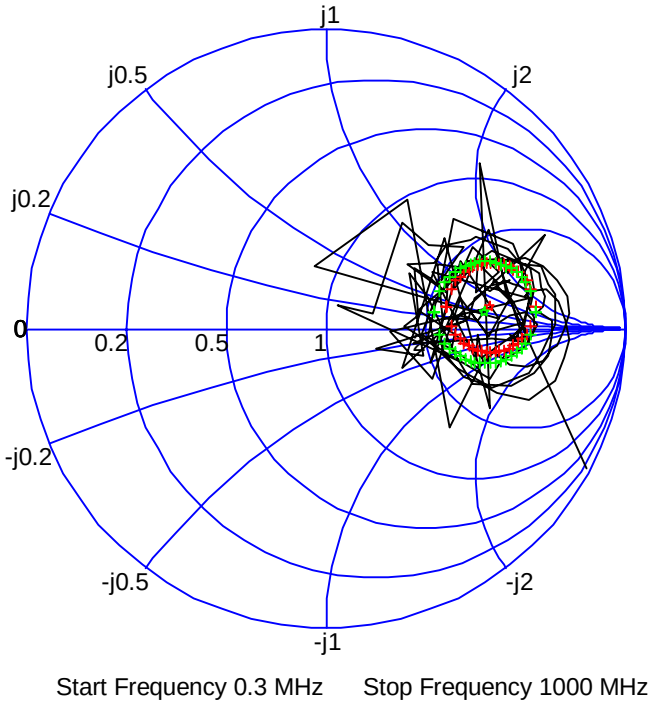

Figure 4.4.1.3-5: Smith Chart plot, aircraft input impedance (black trace), aircraft statistics (red), laboratory FQIS installation statistics (green) [HI Z to LO Z]

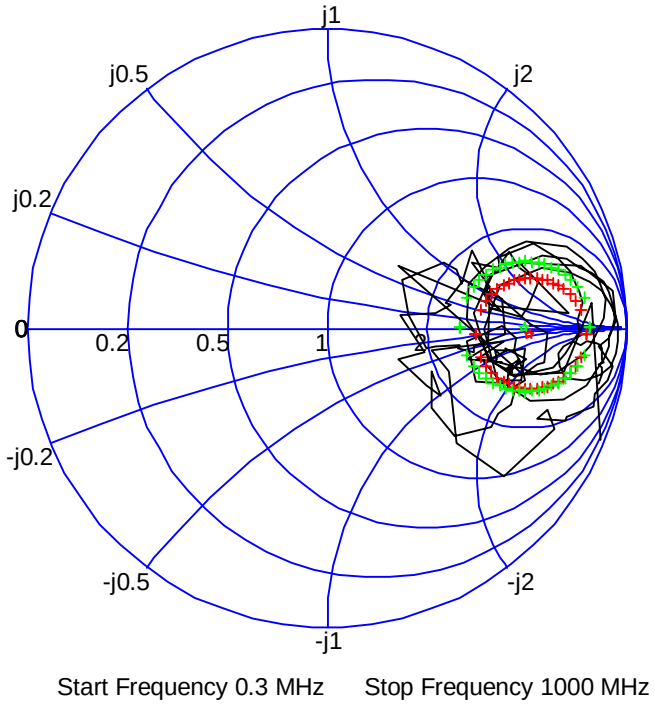

Figure 4.4.1.3-6: Smith Chart plot, aircraft input impedance (black trace), aircraft statistics (red), laboratory FQIS installation statistics (green) [LO Z COMP to Chassis]

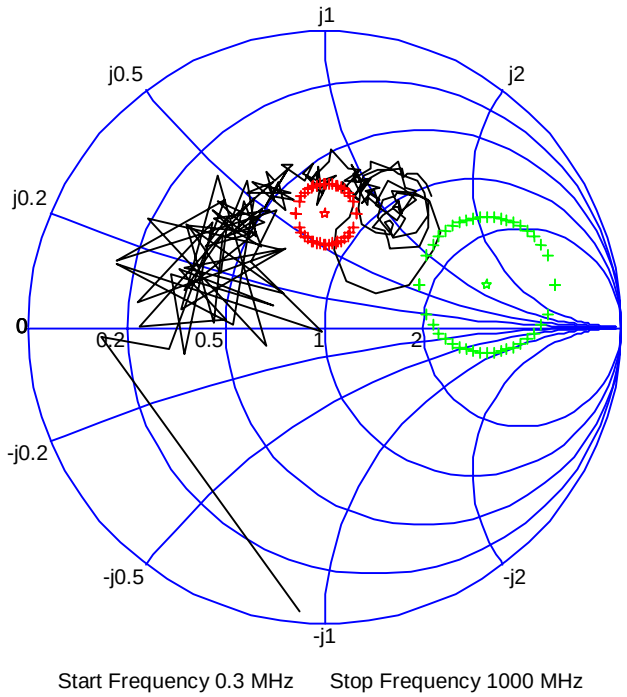

Figure 4.4.1.3-7: Smith Chart plot, aircraft input impedance (black trace), aircraft statistics (red), laboratory FQIS installation statistics (green) [LO Z COMP to Shield]

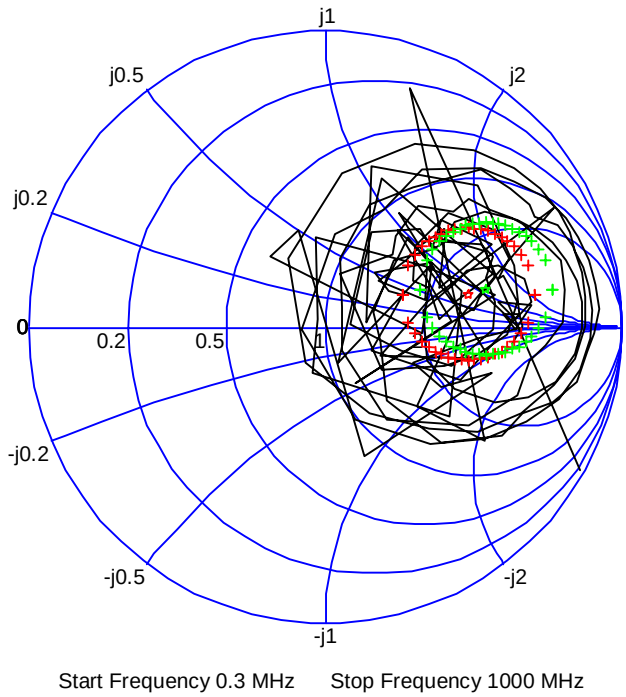

Figure 4.4.1.3-8: Smith Chart plot, aircraft input impedance (black trace), aircraft statistics (red), laboratory FQIS installation statistics (green) [LO Z to Shield]

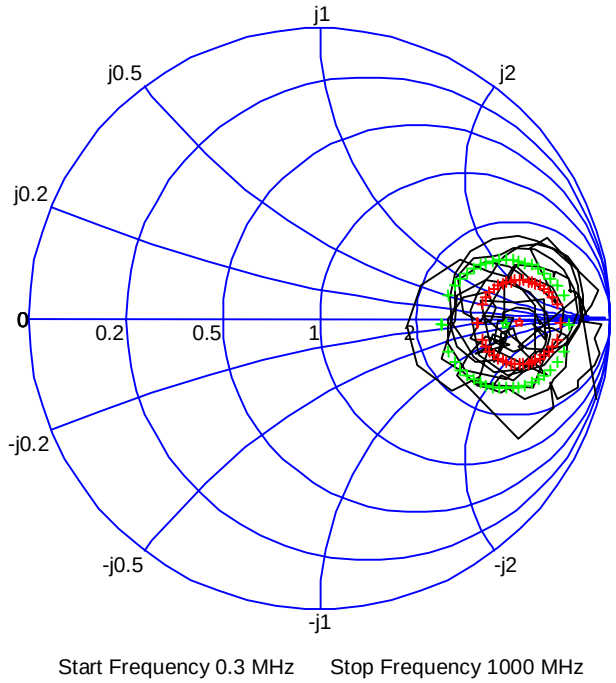

Figure 4.4.1.3-9: Smith Chart plot, aircraft input impedance (black trace), aircraft statistics (red), laboratory FQIS installation statistics (green) [LO Z to Chassis]

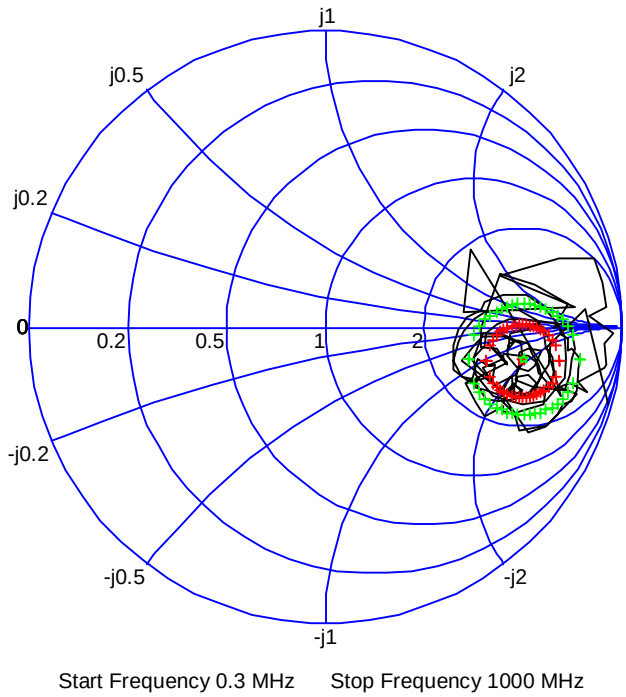

Figure 4.4.1.3-10: Smith Chart plot, aircraft input impedance (black trace), aircraft statistics (red), laboratory FQIS installation statistics (green) [HI Z to Chassis]

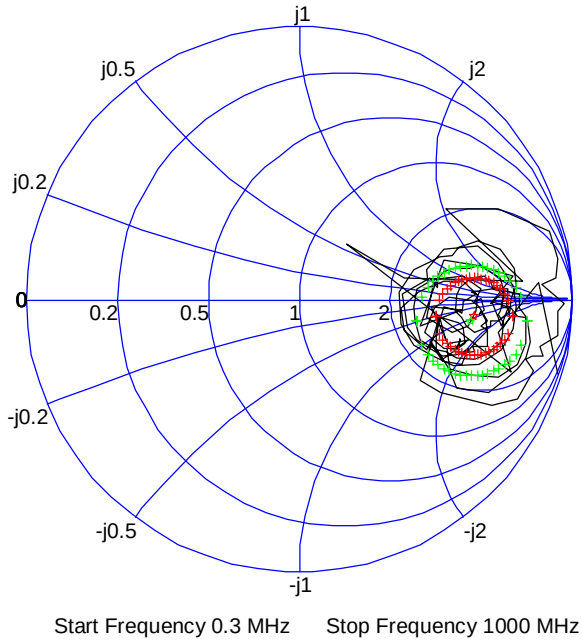

Figure 4.4.1.3-11: Smith Chart plot, aircraft input impedance (black trace), aircraft statistics (red), laboratory FQIS installation statistics (green) [HI Z Shield to Chassis]

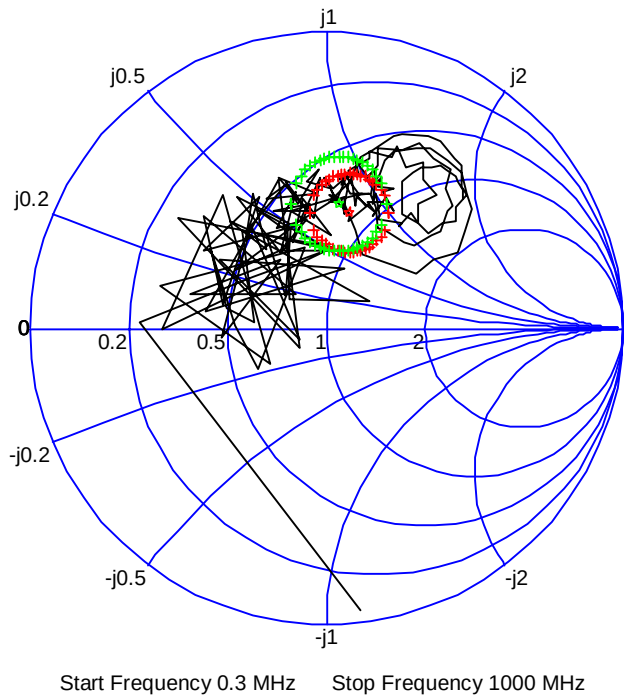

Figure 4.4.1.3-12: Smith Chart plot, aircraft input impedance (black trace), aircraft statistics (red), laboratory FQIS installation statistics (green) [HI Z to Shield]

From Figures 4.4.1.3-6 to 4.4.1.3-12, it can be seen that the impedance averages and standard deviations were very similar for the aircraft and laboratory CWT FQIS installations. One exception is Figure 4.4.1.3-7. The two mean values and the corresponding standard deviation circles were not geometrically close. Comparison to hardcopies of the LO Z COMP-to-Shield aircraft measurements revealed that the data plotted in Figure 4.4.1.3-7 was incorrect. The invalid data is shown here as an example of how the technique of comparing Smith Chart impedance averages and standard deviations will emphasize dissimilarities, when they occur. In the laboratory, repeatability for impedance measurements was found to be excellent.

These plots indicate that the laboratory FQIS installation was very similar to the aircraft FQIS installation in terms of RF impedance between 300 kHz and 1 GHz. The same fuel probes and wiring were installed in the laboratory in a manner comparable to that of the aircraft installation. These input impedance similarities implied that the two installations provided comparable RF power transfer characteristics over the given frequency bandwidth. Furthermore, the reactive characteristics of energy storage, voltage enhancement and current enhancement should be comparable also. This determination was important for validating that subsequent laboratory measurements of voltage/current enhancements were applicable to an aircraft installation.

4.4.2 Cavity Reverberation Measurements

RF power in a CWT can exist in two forms: conducted power on wires and radiated power within the volume of the CWT. To test for susceptibilities of the CWT wiring to RF power, both conditions needed to be simulated.

Conducted power on CWT wiring could be approximated in the laboratory by injecting the same amount directly onto laboratory FQIS wiring installation, and accounting for impedance mismatch conditions. However, to simulate the radiated field environment of the CWT, its reverberation characteristics needed to be determined. Details on the measurement of reverberation characteristics within the CWT of a B-747-100 are described in this section. The same measurements were also made in NASA LaRC reverberation test chamber "B", and a *scale factor* was calculated from the two data sets, to provide an adjustment to the input power for a desired in-cavity EM environment.

4.4.2.1 Retired B-747-100 CWT (Roswell, New Mexico)

4.4.2.1.1 Description of the CWT

The CWT is divided internally into six bays. (The "dry" bay is not part of the CWT.) For this purpose, the bays were labeled according to the Figure 4.4.2.1.1-1. Bays 1 and 2 were toward the rear of the aircraft, while bay 6 was toward the front as shown. (Compare Figure 4.4.2.1.1-1 to Figures 2-2 and 2-3.) The FQIS wiring entry into the CWT was at bay 1. Bays 1 and 2 were similar in dimensions to each other. Bays 3 and 4 were also similar in dimensions. The approximate dimensions of the bays are shown in Table 4.4.2.1.1-1. For simplicity, the approximate rectangular dimension for each bay was calculated by averaging the dimensions in the same direction. The actual shapes were not rectangular, however.

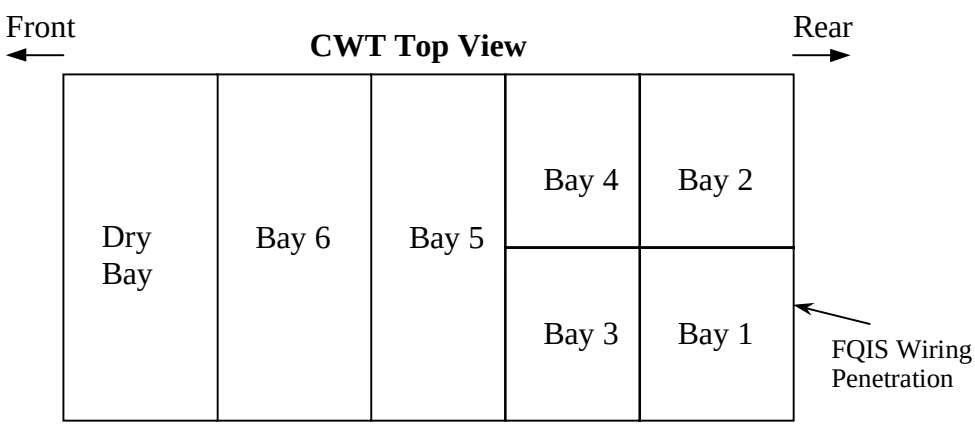

Figure 4.4.2.1.1-1: CWT top view diagram, and the naming notations used for different CWT bays. Data was collected for Bay 1, Bay 3 and Bay 6.

	Average Dimensions			Estimated	
	Length *(m)*	**Height** *(m)*	**Width** *(m)*	**Volume** *(m^3)*	**Surf. Area** *(m^2)*
Bay 1,2 (back)	1.51	1.35	3.24	6.62	22.64
Bay 3,4	1.01	1.59	3.24	5.21	20.06
Bay 5	1.04	1.76	6.48	11.85	39.92
Bay 6 (front)	1.32	1.92	6.48	16.39	46.99

Table 4.4.2.1.1-1: Approximate fuel tank rectangular dimensions.

4.4.2.1.2 Peak Cavity Coupling Factor- Measurement Method

This section describes the method used and the results from characterizing several CWT bays. The same approach was then used to characterize reverberation chamber "B". (Section 4.4.2.2.) The comparison of the two measurements provided the scale factor needed for simulating the radiated field in the CWT using the reverberation chamber for testing purposes.

It was necessary to know the approximate bounds for the peak cavity coupling factors of the CWT bays. The procedure used to measure peak cavity coupling factor is well documented [Refs. 4-7 and 4-8]. Figure 4.4.2.1.2-1 illustrates a typical set-up. In this procedure, a predetermined amount of power at the frequency of interest was transmitted into the bay through an efficient antenna, also called the *transmit antenna*. A second similar antenna, or the *receive antenna*, was attached to a power monitoring device (spectrum analyzer) to probe for power coupling between the two antennas. The maximum ratio of power coupled into the receive antenna to the power radiated from the transmit antenna, for any antenna position combination in the cavity, was called the *peak cavity coupling factor*, at the measurement frequency. The measurement was then repeated at all frequencies of interest.

Power coupling into the receive antenna is very much similar to coupling onto a wire in the cavity. However, the antennas used were very efficient (low resistive loss and low impedance mismatch) in coupling RF field from free space to the measurement system, or vice versa. Thus, the data provided an upper bound on the power that can be coupled onto the wires in the CWT, which were not designed for radiating or coupling purposes.

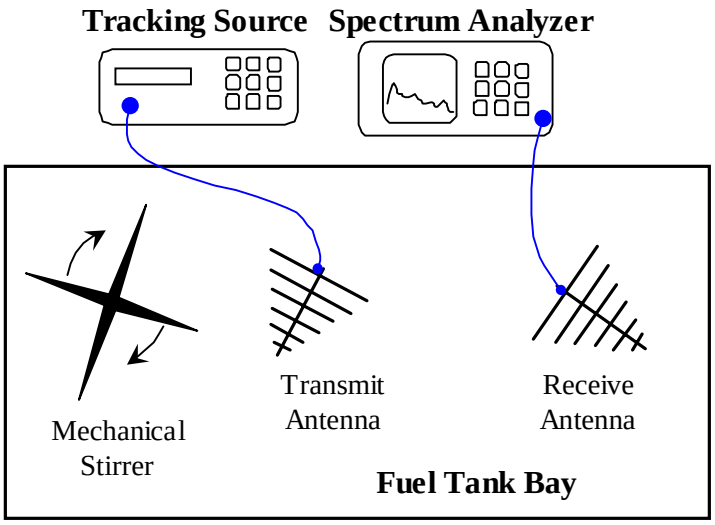

Figure 4.4.2.1.2-1: Mode-stirred measurement method in a CWT bay.

In order to find the peak cavity coupling factor, the receive antenna is typically moved around inside the bay while the measurement is made. However, the *mode-stirred* method makes use of a mechanical stirrer made of large conducting paddles [Refs. 4-7 and 4-8]. The mechanical stirrer effectively changes the boundary conditions, creating different sets of field structure throughout the cavity as it rotates. After one revolution of the stirrer, the receive antenna is exposed to nearly all field magnitudes and polarizations in the cavity. Therefore, this method effectively increases measurement efficiency since there is no need for moving the receive antenna to tens of different locations in the cavity. A spectrum analyzer monitors the power coupled onto the receive antenna and relevant statistics including the peak and average values.

The stirrer used in this measurement consists of a motor driving a set of paddles made of conducting flat plates. The larger the paddle relative to the volume, the more effective it becomes. However, it should not be too large in order to allow room for the transmit and the receive antennas. Figures 4.4.2.1.2-2 and 4.4.2.1.2-3 show the mechanical stirrer and one of the antennas installed in a CWT bay.

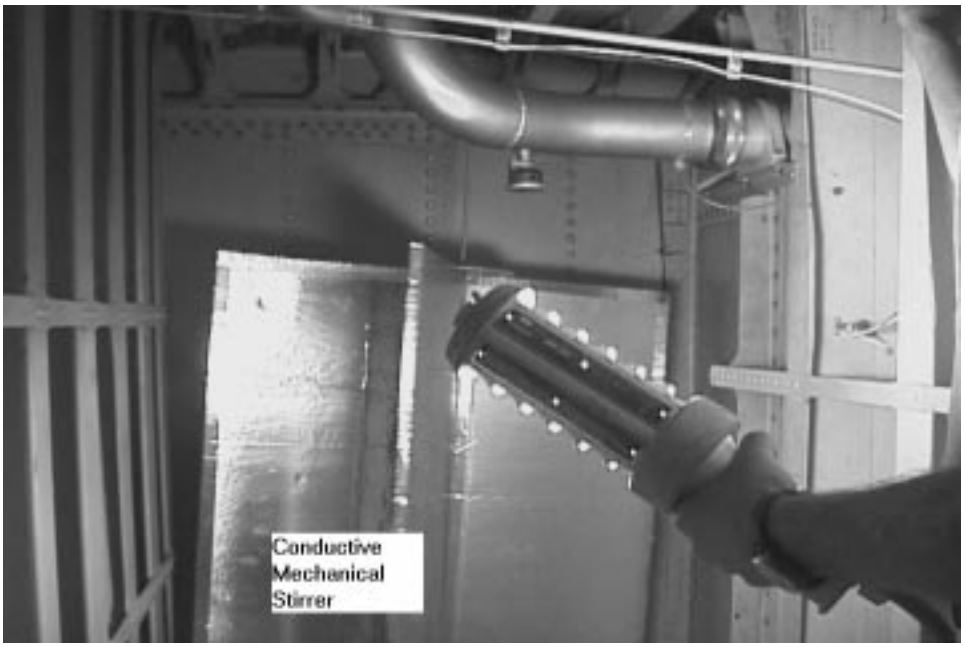

Figure 4.4.2.1.2-2: Mechanical stirrer in one bay of the CWT.

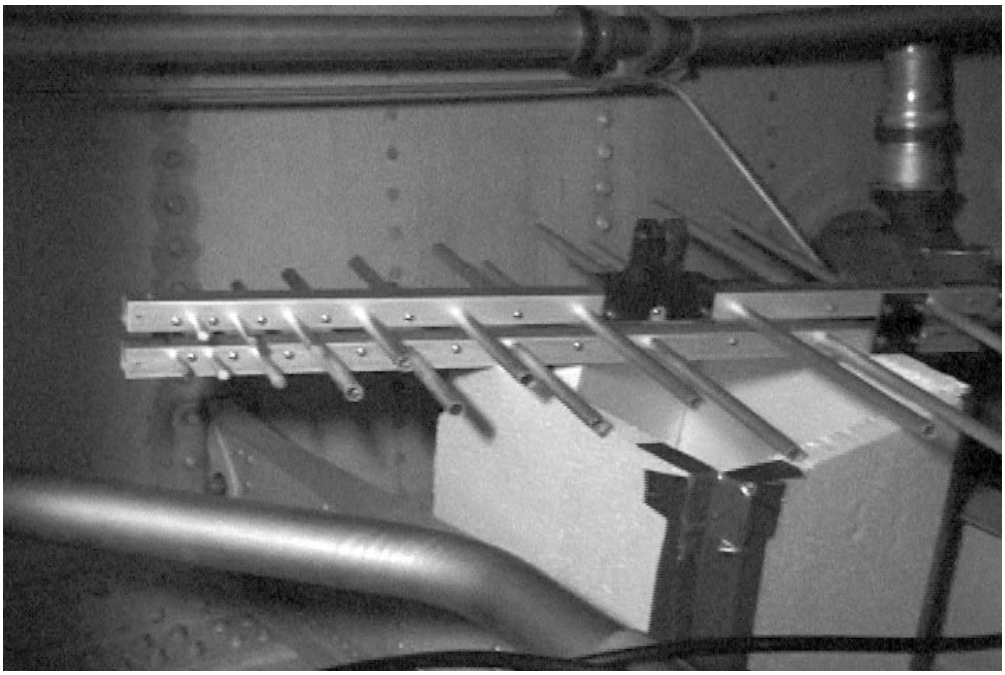

Figure 4.4.2.1.2-3: A log-periodic antenna on the foam support in the CWT.

This technique has been under development for the past 15 years and variations have been, and are being, adopted in the RTCA/DO-160D, MIL-STD 462D, and IEC-1000-4-21 and many other test standards in various industries. A more in-depth discussion on the statistics of the power in the cavity can be found in Reference 4-9.

A small variation to the approach described above using frequency sweeping was used to speed up the test. Instead of staying at a fixed frequency while waiting for the stirrer to complete the revolution, the tracking source and the spectrum analyzer repeatedly swept across the frequency band of interest while the spectrum analyzer was on magnitude peak hold mode. The measurement was stopped after the trace on the display was stabilized, typically after 20-30 paddle rotations or more. The frequency sweep rate across the band was selected to be different from the stirrer rate or from a multiple or fraction thereof. The idea was to get as many different paddle position and frequency combinations as possible.

The advantage of this method was that the measurement speed was very fast, allowing for much more data to be collected within the limited time available at the airplane. A measurement of 600 frequencies can be accomplished in approximately 5 to 10 min, depending on how soon the spectrum analyzer trace stabilizes. For the same number of frequencies, the discrete-frequency approach may take 45 min. The advantage became apparent for measuring coupling between different bays or from passenger cabin to CWT bays. This approach took about 10 to 15 min, or even less once the trace on the spectrum analyzer was stabilized. On the other hand, the discrete-frequency mode-stirred approach took about 60 min for 20 frequencies, as was the case for one set-up at the airplane. Another disadvantage of the discrete-frequency approach was that the measurement could not be stopped early without losing frequency data.

The disadvantage of the frequency-sweeping approach was it could record only the peak value at each frequency, since the spectrum analyzer was on maximum hold. On the other hand, with the discrete-frequency mode-stirred method, each frequency came with complete spectrum analyzer data for a full paddle rotation. Statistical data, including average, standard deviation, and others can then be derived. Modifications to the frequency-sweep procedure using automated data acquisition software could be made to provide similar data as the mode-stirred method, but the set-up complexity goes up along with an increase in the test time. It was determined that the additional statistics on the data, while interesting, were not really necessary to this effort. Much more critical data on many different set-ups were obtained using the frequency-sweep variation to the method. Thus, many of the measurements in this report were made using the frequency-sweep method.

It was important for the frequency sweep not to be too fast. Since each of the CWT bays is a cavity, any signal transmitted inside would have a settling time before reaching steady state. Sweeping the frequency too fast would effectively change the measurement frequency before the steady-state value was reached.

Almost all cavity coupling measurements with two antennas in the same bay were performed using both frequency-sweeping and discrete-frequency mode-stirred methods for validation. The peak coupling values from both methods were compared and the agreement was very good. A representative comparison is shown in Figure 4.4.2.1.2-4. This comparison demonstrates that the sweep time was slow enough and that the results were valid. This proof of data validity is very important since all coupling data between the passenger cabin to the CWT, to be described later, used this frequency-sweeping method for faster speed.

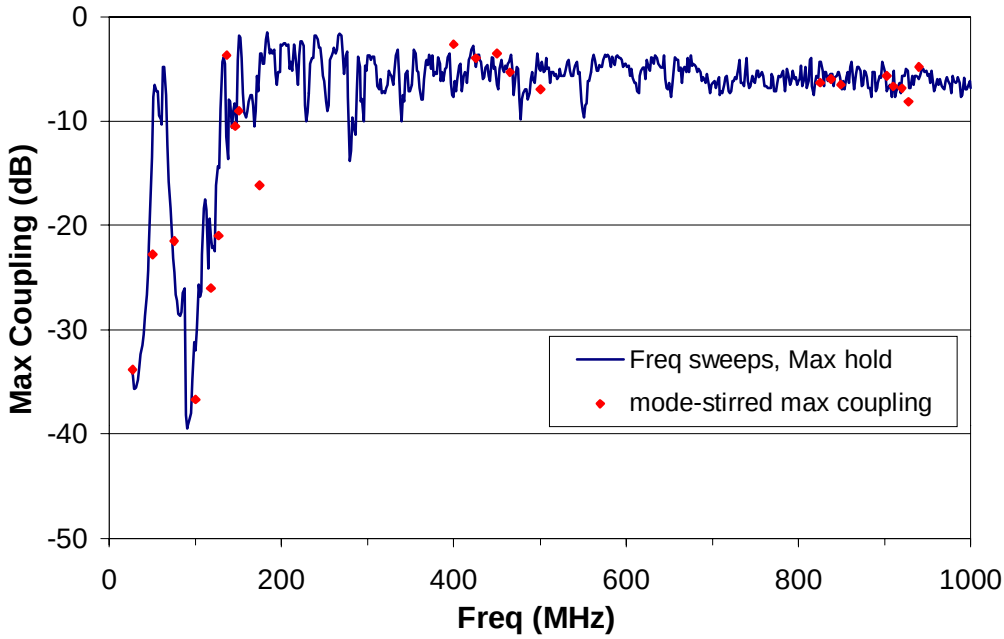

Figure 4.4.2.1.2-4: Comparison of agreement between frequency-sweeping and discrete-frequency approaches. Data are shown for bay 3.

System and cable losses were measured by attaching the ends of the cables at the antenna connectors together, and "through" measurements were made with the same settings at the spectrum analyzer and the tracking source.

In measuring the cavity coupling factors, it was important to ensure that the coupling factors were not affected by the existence of instruments that would not be present during normal operation of the aircraft. The antennas used for transmitting and receiving RF are an example. To estimate cavity loading effects, a cavity *quality factor*, Q, was defined. The value of Q directly relates to the average coupling factor. The presence of an antenna introduces loss, reducing the average coupling power, and, therefore, Q. If the loss figure associated with the antenna, called *antenna Q*, is known, the effects can be subtracted out.

The average coupling factors of the CWT bays with the presence of the antennas were measured at the airplane. In addition, the theoretical antenna Q was computed from an expression given in Reference 4-10. The cavity Q without the antennas was then computed using the expression in Appendix B. More details on Q analysis can be found in Reference 4-10.

The results show that the antennas did not have much of an effect on the Q of the CWT. Thus, the loading effects caused by the antennas can be safely ignored for all radiated field measurements in the CWT. Appendix B shows the comparison of the Q values for a sample CWT bay, with and without the two antennas.

Equipment used for peak cavity coupling measurements are listed below:

Transmit Antennas:

EMCO-3148 Log-Periodic Antenna, 200 MHz to 1 GHz
A&H SAS-200/571 Dual Ridge Horn Antenna, 1 GHz - 18 GHz

Receive Antennas:

EMCO-3146 Log-Periodic Antenna, 200 MHz to 1 GHz
A&H SAS-200/571 Dual Ridge Horn Antenna, 1 GHz - 18 GHz

RF Sources:

HP-85644A Tracking Source, 300 kHz – 6.5 GHz
HP-83752B Synthesized Sweeper, 10 MHz – 20 GHz. This equipment was used in place of the tracking source for discrete-frequency mode-stirred measurements

Spectrum Analyzer

HP-8563E, 9 kHz – 26.5 GHz

4.4.2.1.3 Peak Cavity Coupling Factor- Results

It was decided that the peak cavity coupling factors of only three bays were needed to provide a reasonable estimate of the bound of the data for all six bays. The decision was partially influenced by the limited time available for measurements at the airplane. As a result, bay 1, bay 3 and bay 6 were selected for the following reasons. The FQIS CWT entry was through the bay 1 wall, and it was strongly suspected that radiation in bay 1 would be dominant. It was, therefore, important to include bay 1. In addition, bay 3 was believed to have the largest cavity coupling factor, because its volume was the smallest. Bay 6 was chosen because it had the largest volume. Large cavity volume typically means that resonant modes will start at lower frequencies than in smaller cavities. (Cavity resonance will tend to dramatically increase field strength and power density compared to non-resonance conditions). Data for bays 2 and 4 were not collected since the bays had the same dimensions as bays 1 and 3, respectively, and therefore, the data were expected to be similar.

Peak cavity coupling factors measured in bays 1, 3 and 6 are shown in Figure 4.4.2.1.3-1 from 25 MHz to 1 GHz, and in Figure 4.4.2.1.3-2 from 1 GHz to 6 GHz. In addition, the envelopes that bound all the traces are shown. These envelopes represent worst-case coupling factors between any two highly efficient antennas in the CWT. Any coupling to or from wiring in the CWT should be less. Since the log periodic antennas were used out-of-band between 25-200 MHz, data in this range are shown for completeness only.

In Figure 4.4.2.1.3-2, bay 1 data were collected using the discrete-frequency mode-stirred method only. Due to the slow measurement speed associated with the method, the measurement was made only at a few PED frequencies. This data set was not expected to affect the overall envelope since all data are below the envelope shown. The decision to use the frequency-sweep method was made after this set of data was collected.

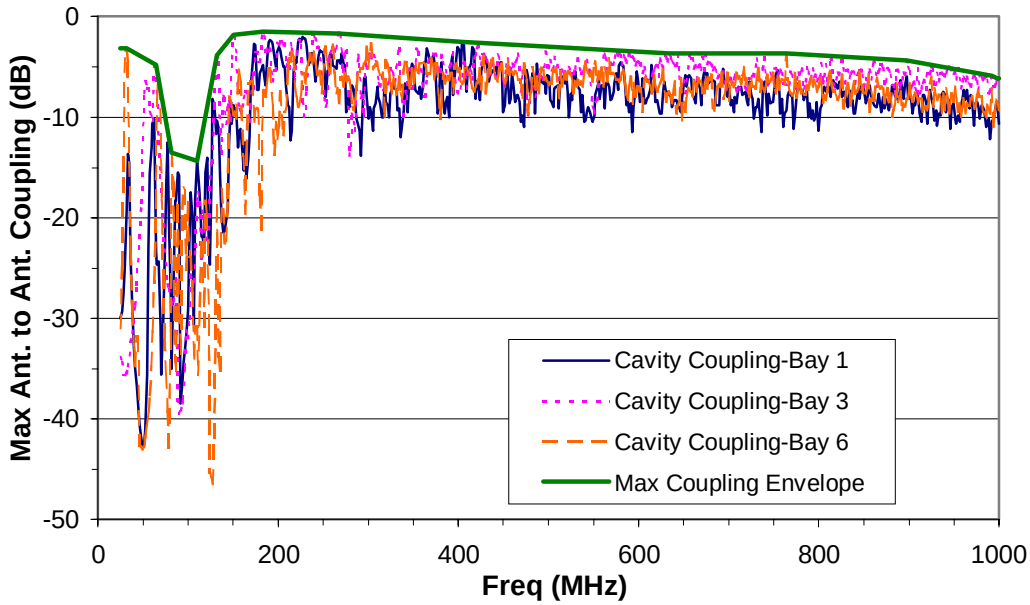

Figure 4.4.2.1.3-1: Peak cavity coupling for bay 1, 3 and 6 (25 MHz - 1 GHz).

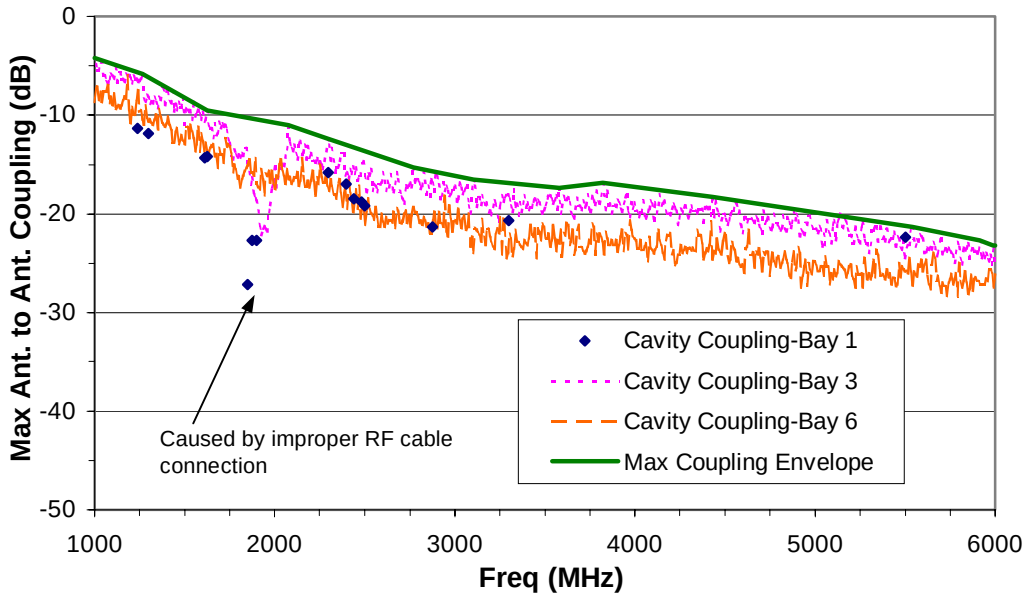

Figure 4.4.2.1.3-2: Peak cavity coupling for bays 1, 3 and 6 (1 – 6 GHz).

In addition, there was an anomaly in the data in Figure 4.4.2.1.3-2 at approximately 1875 MHz for bay 1 and bay 3. This error was detected during the measurement, and later traced to an improper mating at a connector in the antenna path. Tightening the connector fixed the problem; thus no similar anomaly was observed in the data from bay 6. It was determined, that the remaining data were fully usable as long as the anomaly at 1875 MHz was ignored, and that recollecting the data was not worthwhile.

It was observed that the peak cavity coupling factors for bay 3 were generally higher than the rest,

especially at 700 MHz and higher. This result was expected since bay 3 was smaller than the others. Also, the expected early resonance frequency for cavity 6 is not clearly observed in Figure 4.4.2.1.3-1. In fact, the data show resonant frequencies much lower than theoretically possible for each individual bay. An explanation for this behavior is that the whole CWT was contributing to the resonance effects, not just the individual bay. This result indicates that there were strong couplings between the bays. Measurement of the coupling between bay 1 and bay 3 confirmed this tight coupling behavior, as the data in the next section show.

For every setup, special care was taken to ensure the equipment had sufficient dynamic range for accurate measurements. Equipment noise floor data was collected and used to verify the integrity of the data. Dynamic range was not a concern for measurement in the CWT, due to high coupling values, as Figures 4.4.2.1.3-1, 4.4.2.1.3-2 in this section and Figure 4.4.2.1.4-2 in the next section show.

4.4.2.1.4 Bay 1 to Bay 3 Radiated Field Coupling

In addition to measuring cavity coupling factors with both transmit and receive antennas in the same cavity, bay 1 to bay 3 coupling measurement was also made. The purpose was to provide an estimate of the shielding effectiveness between the two bays. This estimate was important as it provided data on how well fields radiated in a bay were coupled to other parts of the CWT. The coupling mechanism can be radiated, such as through apertures and holes, or it can be conducted by coupling onto wires and then re-radiated in other parts of the CWT.

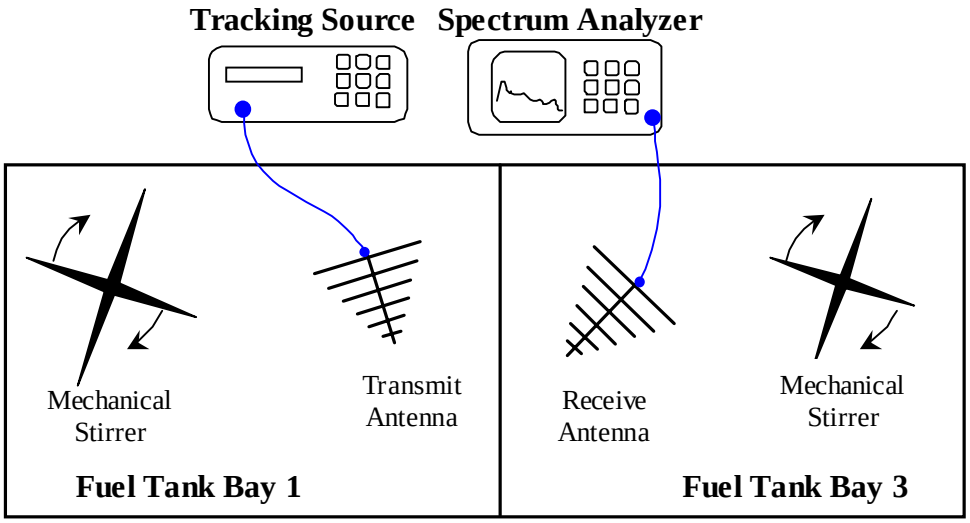

Figure 4.4.2.1.4-1: Bay 1 to bay 3 radiated field coupling.

In this configuration, the transmit antenna was positioned in bay 1 and the receive antenna in bay 3. Mode stirring was accomplished by two sets of stirrers, one in each bay, as shown in Figure 4.4.2.1.4-1. The rates of rotation for the stirrers were not equal, and were chosen to maximize the number of stirrer position combinations. In fact, the rates were approximately 2 and 5 sec per revolution. The spectrum analyzer sweep time was 20 sec, and the trace was on maximum hold for about 2 min for each frequency.

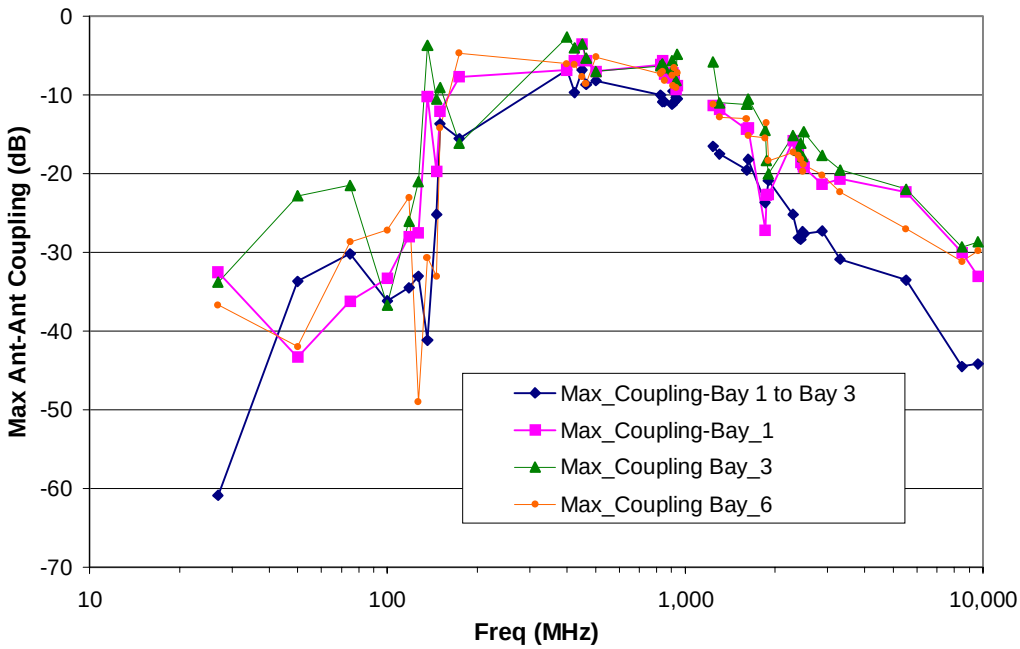

Figure 4.4.2.1.4-2: Bay 1 to bay 3 maximum radiated field coupling.

The data were measured using the previously described discrete-frequency mode-stirred method, where measurement was made one frequency at a time. More details about this technique can be found in Reference 4-11. It was an extremely slow process that took approximately three hours for about 40 frequencies, including setup time. Using the frequency-sweep approach described earlier would have reduced the test time down to tens of minutes for many more frequency points. That was not done in this case, but the technique was used later for other coupling measurements.

The results for bay 1 to bay 3 coupling are shown in Figure 4.4.2.1.4-2 in comparison with the peak cavity coupling factors, where both the transmit and the receive antennas were in the same bay. Again, the data at 1875 MHz should be ignored due to the cable mating problem stated previously. Below 200 MHz, the antennas used were out of band, but were of limited use in comparing with the cavity coupling factors.

It can be seen from the chart that there was little shielding between bay 1 and bay 3 below 1 GHz, when compared to peak cavity coupling factors where both antennas were in the same bay. Above 1 GHz, bay 1 to bay 3 coupling started to separate from the cavity coupling factors for both bay 1 and bay 3. Above 3 GHz, the separation was about 10 dB, which was not very significant.

A conclusion from this data is that there was tight coupling (ie. little shielding) between different bays below 1 GHz. Thus, when the radiating source was located in one bay, EM fields seen by wiring in other bays were nearly as high as those seen by the wires in the bay where the radiating source was located. This result indicated that a one-cavity laboratory reverberation chamber could approximate the multi-bay CWT below 1 GHz. This result also indicated that CWT FQIS currents and voltages could be induced efficiently from one bay to another by radiated fields. This indicated a need to compare radiated versus conducted excitation in the laboratory FQIS installation. (See Section 4.4.5.5.)

4.4.2.2 LaRC Reverberation Chamber "B", with FQIS Components Installed

The same procedure used to measure the peak cavity coupling in the CWT was used to characterize the Reverberation Test Chamber "B". This chamber was a 2.9 m × 3.96 m × 7.01 m rectangular structure, with painted steel walls. A large mechanical stirrer in a corner of the chamber was used for stirring RF energy. The comparison of the measurement results in chamber B to the similar measurement in the CWT provided the scale factor needed for simulating the radiated field in the CWT using the reverberation chamber.

The peak cavity coupling factors for chamber B are shown in Figures 4.4.2.2-1 and 4.4.2.2-2. Unlike the CWT data, where the envelope of the peak coupling was desired, the approximation of the peak coupling was more conservative, since it described the actual capability of the test chamber. The trend line of the approximate peak coupling is also shown in the Figures 4.4.2.2-1 and 4.4.2.2-2.

Below 200 MHz, the data show large variations, making it difficult to estimate the trend line. Large data variations in this range are very typical for any reverberating cavity of similar volume. In this range, the *envelope* of the data is shown instead, as was done for the CWT data. (See Figure 4.4.2.1.3-1.) This should not pose any problem for the comparison, as using the trend line is a more conservative approach for testing purposes. In addition, neither the test chamber nor the CWT bays start to behave like a *good* reverberation chamber until a frequency of about 200 MHz. *Good* reverberation characteristics are defined in Reference 4-7, and allow simulating the CWT using a reverberation chamber. Furthermore, the antennas used in characterizing the CWT and the test chamber were out-of-band below 200 MHz. Thus, the data presented below 200 MHz are shown for comparisons only.

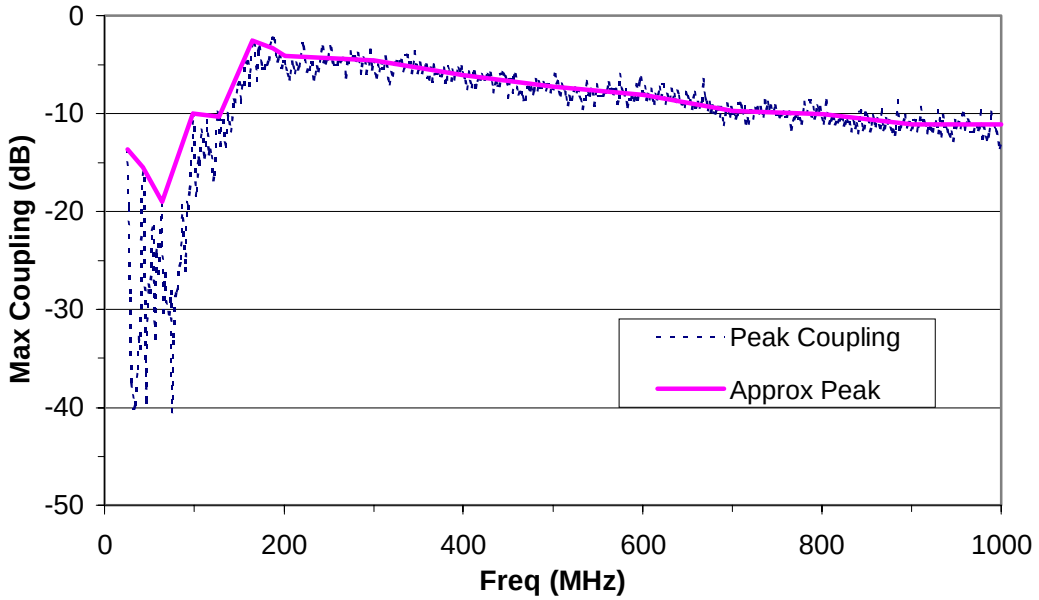

Figure 4.4.2.2-1: Peak cavity coupling in NASA reverberation chamber B (25 MHz - 1 GHz).

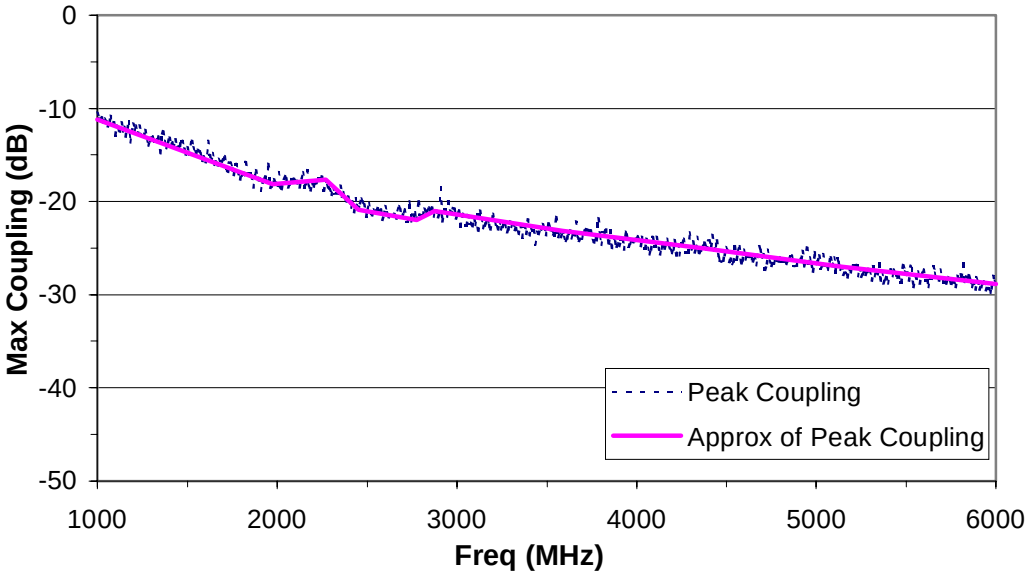

Figure 4.4.2.2-2: Peak cavity coupling in NASA reverberation chamber B (1 GHz - 6 GHz).

4.4.2.3 Comparisons of EM Similarity

Comparing the envelope of the CWT peak coupling factor in Figures 4.4.2.1.3-1 and 4.4.2.1.3-2 to the approximate chamber B's peak coupling factors in Figures 4.4.2.2-1 and 4.4.2.2-2, the scale factor between chamber B and the worst case of the CWT was derived.

For the same radiated power at the transmit antenna, the *scale factor* was defined as the ratio between the power coupled into the receive antenna in chamber "B", as compared to the envelope of the power coupled into the receive antenna in the CWT bays. Therefore, in order to simulate the field environment in the CWT, the input power to the test chamber "B" would have to be compensated according to the scale factor. For example, at a given frequency, if there is 1 W of radiated power in the CWT and the scale factor is 3 dB, 2 W of radiated power in chamber B would be needed for an equivalent radiated field environment. The scale factors, as shown in Figures 4.4.2.3-1 and 4.4.2.3-2, vary between 2.5 dB near 200 MHz to about 7.5 dB above 750 MHz.

It was decided that testing for radiated field susceptibility of wiring, using the scale factor results above, should not be performed below 200 MHz. This was because the radiated field characteristics of small cavities, such as the CWT bays and the test chamber, are not well understood. It is also difficult to radiate from or couple power onto wires efficiently, in cavities of this size across this frequency band. Conducted power coupling is likely to be more efficient in coupling power to all parts of the wires at most frequencies in this range. Thus, it was determined wire-conducted susceptibility tests should provide more useful data below 200 MHz than radiated-field susceptibility tests.

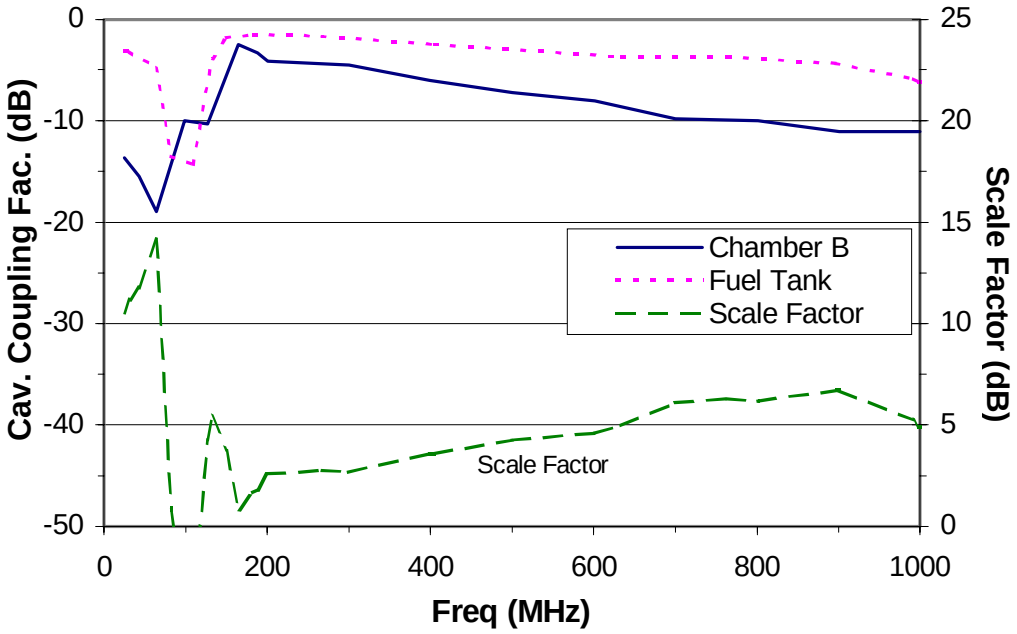

Figure 4.4.2.3-1: Cavity coupling scale factor- NASA test chamber B versus fuel fank (25 MHz – 1 GHz).

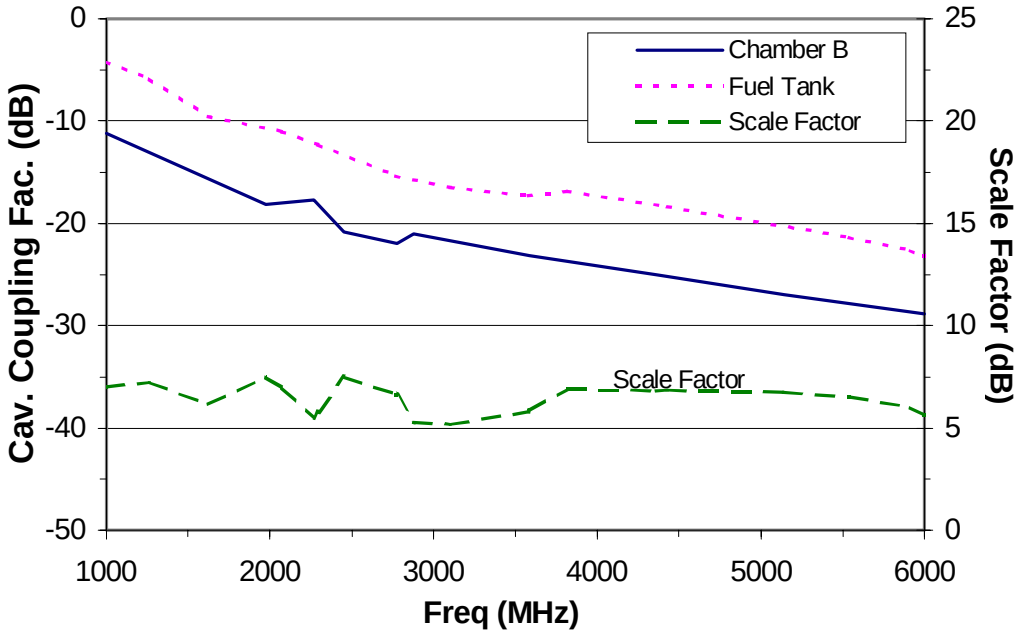

Figure 4.4.2.3-2: Cavity coupling scale factor between NASA test chamber B and CWT.

4.4.3 Aircraft Measurements of Passenger Cabin Coupling to CWT and CWT Wiring

4.4.3.1 Measurement Method, Applicability and Results

There were several possible mechanisms to couple RF energy to a fault location on the FQIS wiring in the CWT from a PED transmitter in the passenger cabin:

- Conducted Coupling:

  Energy coupled onto the FQIS wiring in the passenger cabin, and continued along the FQIS wiring to the fault location to create a sparking/arcing event. This mechanism is typically true at lower frequencies where the wire length is short relative to a wavelength.

- Radiated Coupling:

  i. *Through FQIS Wiring*:

  Energy coupled into the CWT through the FQIS wiring, but re-radiated in the CWT. Energy was then coupled back onto the FQIS near the fault location to create an event. This scenario has validity at higher frequencies where cable length is on the order of a half wavelength or more. At these frequencies, the wires act like an antenna in radiating power. It is difficult to contain the energy on the wires if the distance of travel is long.

  ii. *Not through the FQIS wiring*:

  Energy coupled into the CWT through other means like ducts, pipes, unshielded apertures/holes. The free field was then coupled onto the FQIS wiring near the fault location to create a spark/arc.

It was necessary to measure and bound the amount of power coupled through all the means. To achieve this goal, a known amount of power was delivered inside the passenger cabin to simulate energy radiated from PED transmitter sources. A wide-band log periodic antenna (100 MHz – 1 GHz) and a dual-ridge horn antenna (1 GHz – 18 GHz) were used as radiating sources to cover from 25 MHz to 6 GHz. By measuring the power on the FQIS wiring at the connector, and the radiated power density in the CWT with the FQIS connector both mated and de-mated, the coupling data and the bounds were estimated.

4.4.3.1.1 Power on the FQIS Wiring at CWT Entry

1) Test Method. A diagram of the setup is shown in Figure 4.4.3.1.1-1:

Power coupled on the FQIS at the CWT entry was measured by attaching the FQIS connector to a spectrum analyzer through a custom adapter. Due to limited time, it was impossible to measure power across all possible pin combinations on the connector. It was decided to measure power across the pins in three combinations to represent both differential mode and common mode couplings:

- HI Z to LO Z pins,
- HI Z to LO Z COMP pins, and
- All HI Z, LO Z and LO Z COMP pins tied together relative to airframe chassis.

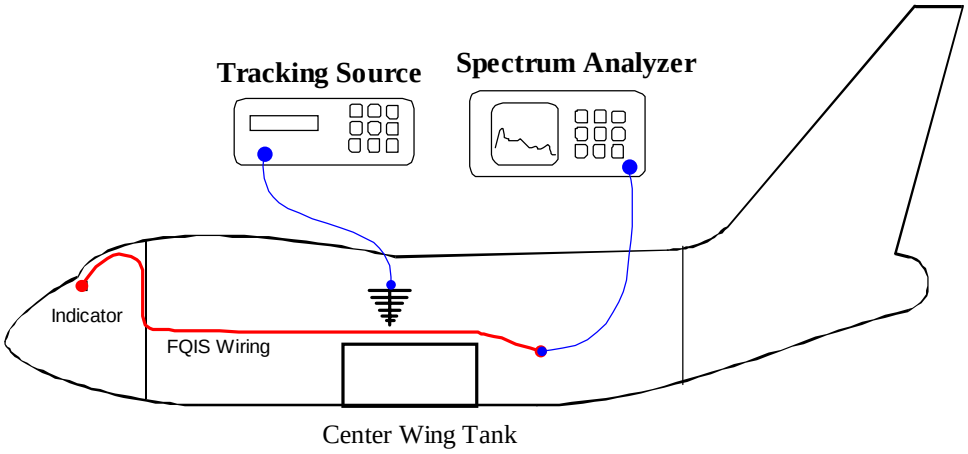

Where:

FQIS wiring external to CWT

RF Cables

Transmit Antenna

Figure 4.4.3.1.1-1: Passenger cabin to FQIS wiring coupling measurement.

More details on the pin configurations of the connector can be found in Section 2.2.

As shown in Figure 4.4.3.1.1-1, an antenna in the passenger cabin transmitted a known amount of RF power. Below 1 GHz, the source output was typically 10 mW, however, a pre-amplifier (HP 83017A) was used above 1 GHz to compensate for higher cable loss. The main area of investigation was within 10 m of the location in the floor where the FQIS wiring penetrates into the left landing gear well. It was determined that this location was the most likely area for maximum coupling above 25 MHz, since much of the power would be lost to radiation otherwise. The locations in the passenger cabin where strong coupling occurred were recorded. Later, it was experimentally determined that the location of highest FQIS coupling, measured at the CWT connector, was in the area closest to where the FQIS wiring penetrates from the passenger cabin to the landing gear wheel well.

The transmit antennas were about 5-10 cm above the floor, and were pointed directly at the wiring while being carried up and down along the length of the wiring. The antennas were polarized tangentially as well as perpendicularly to the wires. In addition, the antennas were also pointed in several random directions to check for other coupling mechanisms. These tests did not show any higher coupling than by directly illuminating the FQIS wiring. Figures 4.4.3.1.1-2 and 4.4.3.1.1-3 show the measurements being performed in the passenger cabin.

Figure 4.4.3.1.1-2: A log-periodic antenna simulating a PED transmitter in passenger cabin below 1 GHz. The antenna was pointing directly at the FQIS wire section under the floor running along the length of the aircraft. Tests were performed with the antenna polarized both parallel and perpendicular to the wires.

Figure 4.4.3.1.1-3: A dual-ridge horn antenna simulating a PED transmitter in passenger cabin above 1 GHz. The antenna was pointing directly at the FQIS wire section under the floor running along the length of the aircraft. Tests were performed with the antenna polarized both parallel and perpendicular to the wires.

Equipment used for the measurements are listed below:

Transmit Antennas:

EMCO-3144HP Log-Periodic Antenna, 100 MHz to 1 GHz
AEL-H1479 Dual Ridge Horn Antenna, 1 GHz to 12 GHz

RF Source:

HP-85644A Tracking Source, 300 kHz – 6.5 GHz
(also used with HP83017A pre-amplifier for frequencies above 1 GHz)

Spectrum Analyzer:

HP-8563E, 9 kHz – 26.5 GHz

All RF cables and the pre-amplifier used in both transmit and receive paths were labeled at the end of the measurements for later calibration back at NASA LaRC. These calibration data were then applied to remove the effects of cable loss and amplifier gain in the measurement data. In addition, transmit path-loss data were collected for several frequencies while performing aircraft measurements. Upon returning to NASA LaRC, the transmit path-loss measurements were repeated, and found to be within 1 dB of what was measured at the aircraft.

2) Test Results. The results from the three measurements are shown in Figures 4.4.3.1.1-4 and 4.4.3.1.1-5 for frequencies below and above 1 GHz. At 1 GHz, there was a change in antennas used. It is important to note that the bound of the data is more important since small differences in wire installation/ positions/ configurations would result in different sets of measurements. The bound, or the envelope is a good representation of the maximum power that bounds all the effects caused by small variations in wiring positions.

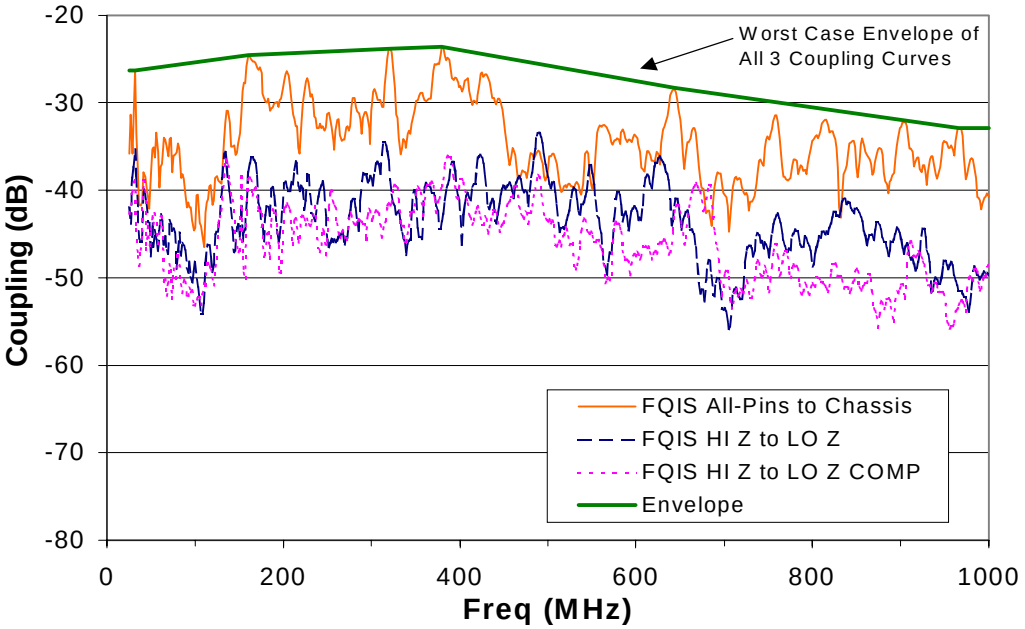

Figure 4.4.3.1.1-4: Coupling from passenger cabin to FQIS wiring (25 MHz - 1 GHz).

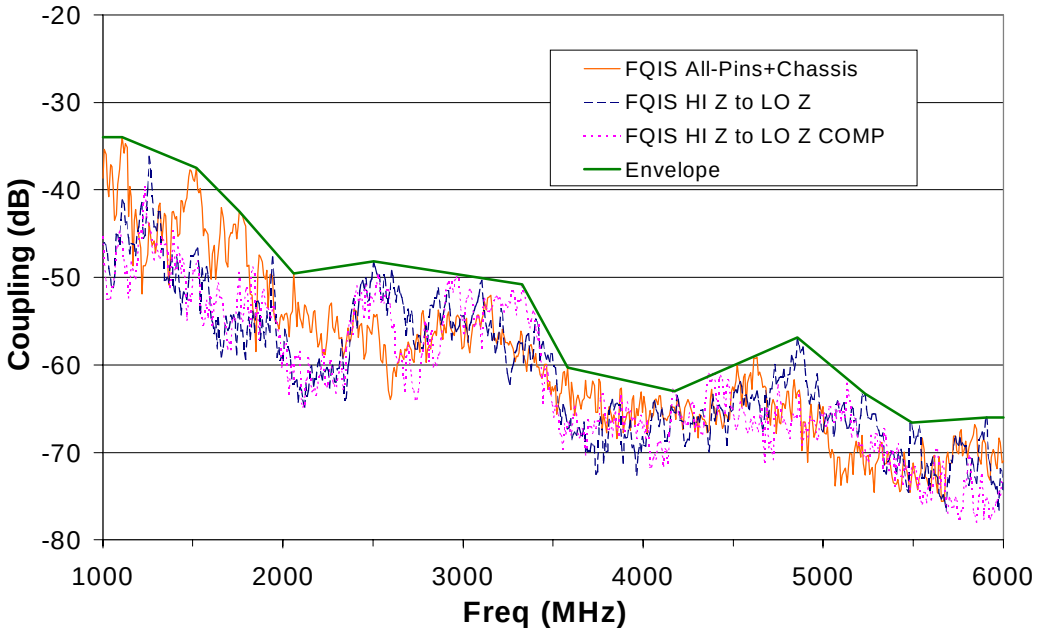

Figure 4.4.3.1.1-5: Coupling from passenger cabin to FQIS wiring (1 GHz - 6 GHz)

As can be observed from Figures 4.4.3.1.1-4 and 4.4.3.1.1-5, the worst case of all three was the power measured with all pins together relative to the plane's chassis, representing the common-mode coupling. Below 1 GHz, the envelope of this data was about 10 dB higher than the data from differential mode coupling, where power was measured across any two pins. This result was not surprising since the wires connected to the pins were so closely placed, any voltage coupled onto one wire was likely to couple to the others as well. Thus, the voltage difference between any two pins should be small, causing only small differential power measured across them as shown in the data. The common mode measurement, on the other hand, measured the power on the wires relative to the chassis, which was not close to the wiring in the passenger cabin. It therefore should be higher, as shown.

Above 1 GHz, there was little difference between the envelope of all three sets of data. Also, the envelope starts to drop off dramatically above 1 GHz. Due to fast drop off in the coupling envelope, together with low PED radiated power above 1 GHz from Figure 4.3.4-1, it was anticipated that PED transmitter sources above 1 GHz would be of little concern in causing a spark.

3) Numerical Corrections to Measured Data. Of the two types of losses associated with a typical antenna, *inefficiency* and *impedance mismatch*, mismatch loss is a concern if the antennas are used out-of-band. Antenna mismatch causes high reflected power, preventing some power from being delivered out of the antenna. Antenna inefficiency, on the other hand, is caused by power absorption by the antenna, which is typically converted to heat.

The antennas used in these measurements were fairly efficient, as little power is absorbed by the antennas and converted to heat. They also had low mismatch loss if used in band. In order to extend the use of the collected data down to 25 MHz, which was out of band for the log periodic antenna used, mismatch losses needed to be addressed.

Typical PEDs were assumed to be 100 percent efficient and to have no mismatch as the worst case. This assumption is typically far-from-true between 25 MHz to 100 MHz, or the antennas would have to be impracticably large. However, since little is known about the upper performance of these antennas, this assumption bounds their performance.

In order to simulate full radiated power, the measured power on the FQIS wiring needed to be scaled up to account for reflected power at the log-periodic and the dual-ridge horn transmit antennas. The scale factor was computed from free space transmit antenna reflection coefficients. This correction procedure had been used in the past and showed good results [Ref. 4-12]. The mathematical expression to correct for antenna mismatch is shown in Appendix C.

No attempt was made to adjust the data for antenna gain difference between the antenna used and typical PED transmitter antennas. It was expected that the log-periodic and the dual-ridge horn antennas provided the worst case since they have higher antenna gains. Most PED transmitter antennas are dipoles of length not larger than half a wavelength at the operating frequencies. The maximum gain for a half-wave dipole is about 2.15 dB. Alternatively, the lowest gain was 7 dB for both the log-periodic and the dual ridge horn antennas according to the manufacturer's data. The test antennas therefore provided an upper bound on the PED transmitter antenna gains and, as a result, the power that could be coupled onto the FQIS wiring.

The data shown were also corrected for the impedance mismatch caused by the introduction of the custom adapter between the FQIS wires and the 50 ohms N connector. This mismatch can cause up to 4 dB error at 25 MHz. A special procedure to measure and correct for this mismatch was developed and applied to the data. More details about this correction can found in Appendix C.

4.4.3.1.2 Coupling from Passenger Cabin to Antenna inside CWT

As stated previously, once the conducted power couples into the CWT, it may conduct straight down the wires to create a spark/arc at a fault location directly. However, if the wires are long with respect to a wavelength, some power may radiate first. The radiated power may re-couple onto some other part of the wire to create a spark/arc. In addition, the radiated power in the passenger cabin can couple into the CWT through other means, like unshielded apertures.

In this section, measurements are presented of radiated field coupling from the passenger cabin to inside the CWT, with the FQIS connector to the CWT mated as well as de-mated. These measurements give an estimate on the upper bounds to the radiated coupling to the inside of the CWT, and how much would be through the FQIS wiring.

1) Test Method. Similar to measurement of coupling onto the FQIS wiring, this measurement also involved a radiating antenna in the passenger cabin. The setup and equipment used in the passenger cabin were identical to the setup and equipment used to measure coupling to the FQIS wiring described previously. Similar to the measuring of coupling onto the wiring, the antennas in the passenger cabin were pointed directly at the FQIS wiring while scanning along the length of the wires. In addition, the antenna was also pointed in multiple random directions to simulate mechanical stirring. However, the results were far below those with the antenna pointed directly at the wiring. The locations in the passenger cabin where maximum coupling to the antenna in the CWT occurred were noted. The set-up is illustrated in Figure 4.4.3.1.2-1.

Inside the CWT, a log periodic antenna (200 MHz - 1 GHz) and a dual ridge horn antenna (1 GHz - 18

GHz) were used to measure the free space power density. These antennas covered two bands 25 MHz to 1 GHz, and 1 GHz to 6 GHz. A spectrum analyzer with trace setting on maximum hold monitored the power coupled onto the receive antenna. The spectrum analyzer setting stayed in this mode until all antenna positions, polarization and directions were covered. The trace was then downloaded to a computer for processing.

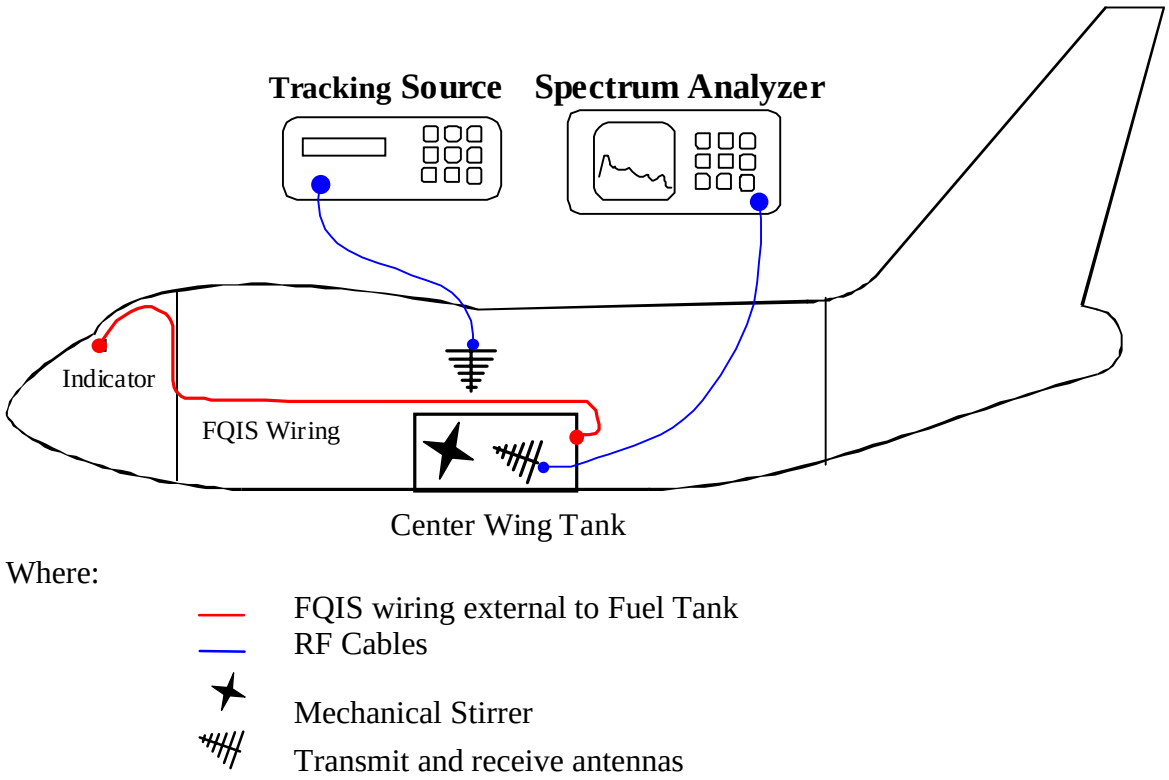

Where:

FQIS wiring external to Fuel Tank
RF Cables
Mechanical Stirrer
Transmit and receive antennas

Figure 4.4.3.1.2-1: Passenger cabin to fuel tank radiated field coupling.

As described previously, the log-periodic antenna in the CWT was used out-of-band from 25 MHz to 200 MHz. Unlike the transmit antenna in the passenger cabin, no attempt was made to correct for antenna mismatch from 25 – 200 MHz. This was because the same antenna transmitting the CWT would create a highly reactive modal structure, effectively altering the antenna transmission characteristics, especially in this frequency range. The effects on the mismatch are not well understood under these circumstances. Thus, it was best to present the results as they were measured without mismatch correction for the receive antenna.

In the CWT bay where the measurements were made, a mechanical stirrer was used to stir the energy. This ensures that the receive antenna “sees” the peak power density in the bay.

Equipment used for the measurements are listed below:

Transmit Antennas in Passenger Cabin:

EMCO-3144HP Log-Periodic Antenna, 100 MHz to 1 GHz
AEL-H1479 Dual Ridge Horn Antenna, 1 GHz to 12 GHz

Receive Antennas in CWT Bay 1:

EMCO-3148 Log-Periodic Antenna, 200 MHz to 1 GHz
A&H SAS-200/571 Dual Ridge Horn Antenna, 1 GHz to 18 GHz

Receive Antennas in CWT Bays 3 & 6:

EMCO-3146 Log-Periodic Antenna, 200 MHz to 1 GHz,
A&H SAS-200/571 Dual Ridge Horn Antenna, 1 GHz to 18 GHz

RF Source:

HP-85644A Tracking Source, 300 kHz – 6.5 GHz
(also used with HP83017A pre-amplifier for frequencies above 1 GHz)

Spectrum Analyzer

HP-8563E, 9 kHz – 26.5 GHz

All RF cables and the pre-amplifier used in both transmit and receive paths were labeled at the end of the measurements for later calibration back at NASA LaRC. These calibration data were then applied to remove the effects of cable loss and amplifier gain in the measurement data. In addition, transmit path-loss data were collected for several frequencies while performing aircraft measurements. Upon returning to NASA LaRC, the transmit path-loss measurements were repeated, and found to be within 1 dB of what was measured at the aircraft.

For all aircraft measurements, the measured data were confirmed to be within the dynamic range of the instruments used. Such effort was especially important in this case, because coupling values from the passenger cabin to the CWT were very low with the FQIS connector de-mated. The envelopes of raw data measured in bays 3 and 6 (not presented here) were only 5-10 dB above the equipment noise floor between 900 MHz to 1 GHz. This margin was considered sufficient, because only the envelopes of the data were of concern. Above 1 GHz, a pre-amplifier was used to ensure that the raw data were high enough in magnitude for instrument sensitivity.

2) Test Results. Due to limited time, coupling to only the three representative bays out of six were measured: Bays 1, 3, and 6. The same measurements were made with the FQIS wiring mated to the CWT as well as de-mated.

a) With FQIS Connector Mated to CWT:

The results are shown in Figure 4.4.3.1.2-2 for frequencies below 1 GHz, and in Figure 4.4.3.1.2-3 for frequencies above 1 GHz. As can be seen on the charts, coupling to bay 1 appeared to dominate between 500 MHz to 2 GHz. Above 3 GHz, coupling to bays 3 and 6 dominated the envelope. This result indicates that the FQIS wiring was no longer a major factor for coupling into the CWT in this range. However, the coupling levels were now so low, as not to be a concern. Above 2 GHz, the envelope of the coupling factors was about -60 dB or less. This result means that for every watt of transmitted power in the passenger cabin, only 1 μW was coupled to an efficient antenna in the CWT. Coupling to the wiring in the CWT should be even less. The worst-case coupling was at about 500 MHz, with a coupling factor

of approximately –43 dB. Even at this frequency, it was about 20 dB (or a factor of 100 in magnitude) lower than the worst-case coupling from the passenger cabin to the FQIS wiring.

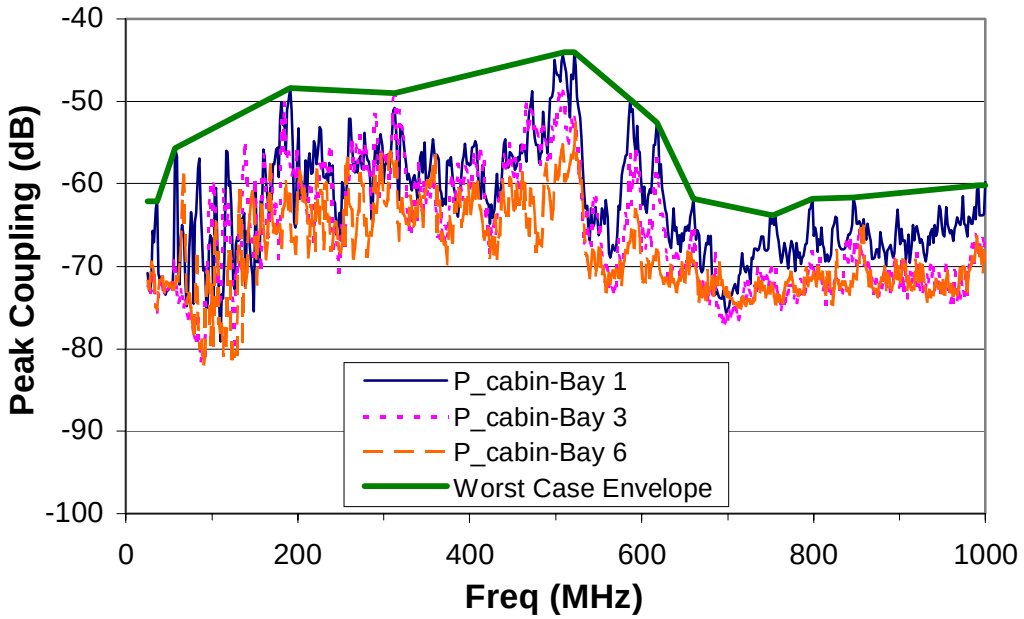

Figure 4.4.3.1.2-2: Peak coupling from passenger cabin to antenna in different bays in the CWT (25 MHz - 1 GHz).

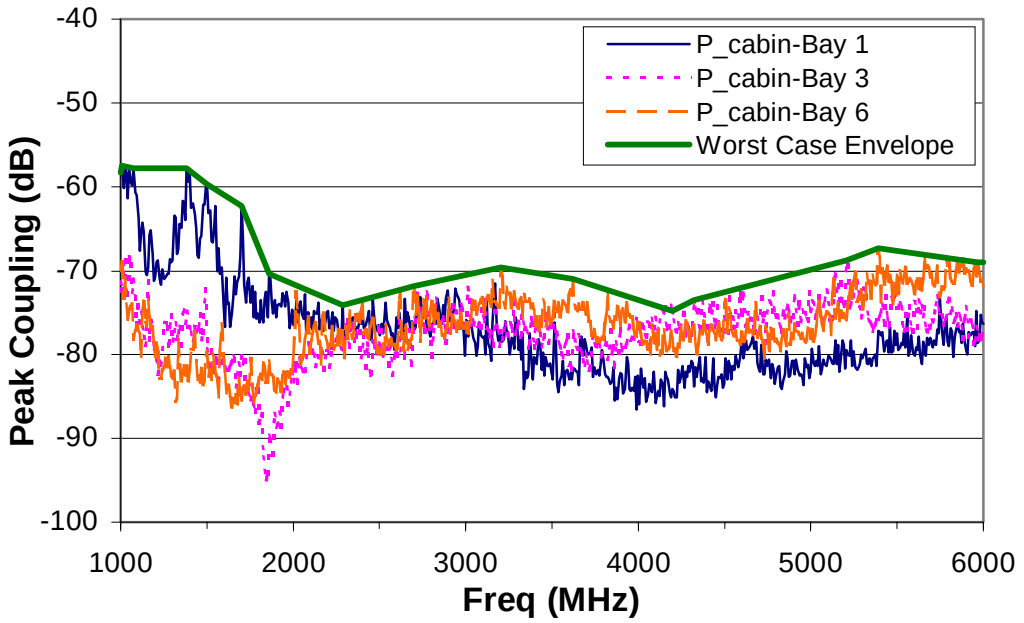

Figure 4.4.3.1.2-3: Peak coupling from passenger cabin to antenna in different bays in the CWT (1 GHz - 6 GHz)

b) FQIS Wires De-mated from CWT:

The same set of measurements was also repeated with the FQIS wiring de-mated from the CWT. The purpose of these measurements was to investigate the contributions to the radiated fields due to coupling mechanisms other than through the FQIS wiring. The results are presented in Figures 4.4.3.1.2-4 and 4.4.3.1.2-5.

These charts show that there were other coupling mechanisms than through the FQIS wiring to contribute to the free field inside the CWT. In addition, the envelope of the data with the FQIS connector mated is also shown for comparison. These comparisons show that at frequencies above approximately 2 GHz, the FQIS wiring did not play a dominant role in contributing to radiated fields within the CWT.

The charts show maximum coupling of approximately –60 dB below 1 GHz, and –70 dB above 1 GHz. These levels were too low to be of concern for this effort. Therefore, no further investigation of these sources on the radiated field environment was made.

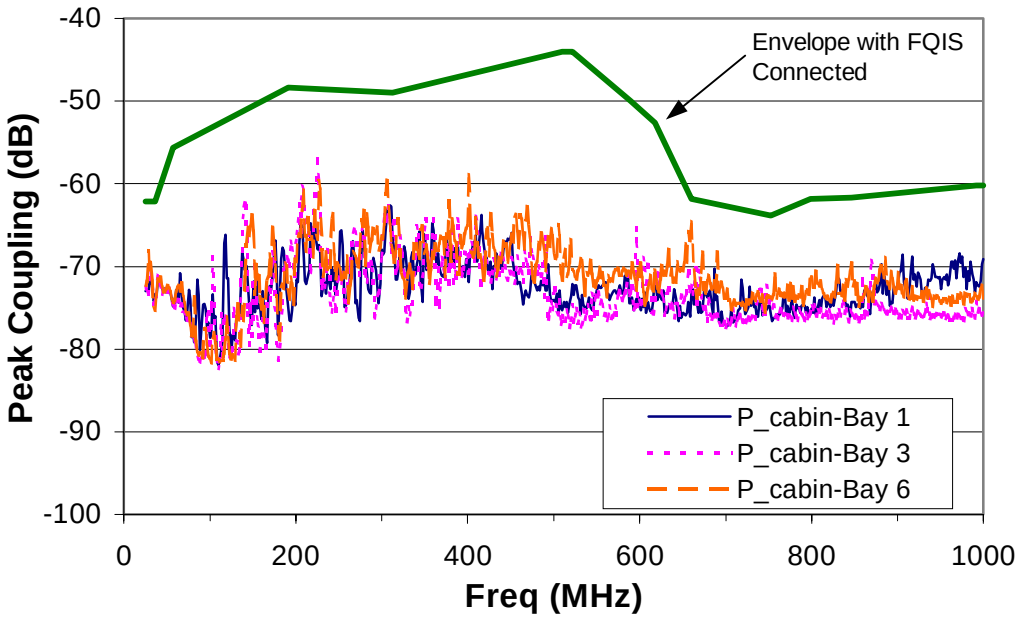

Figure 4.4.3.1.2-4: Peak coupling from passenger cabin to antenna in CWT. FQIS de-mated from CWT. (25 MHz - 1 GHz)

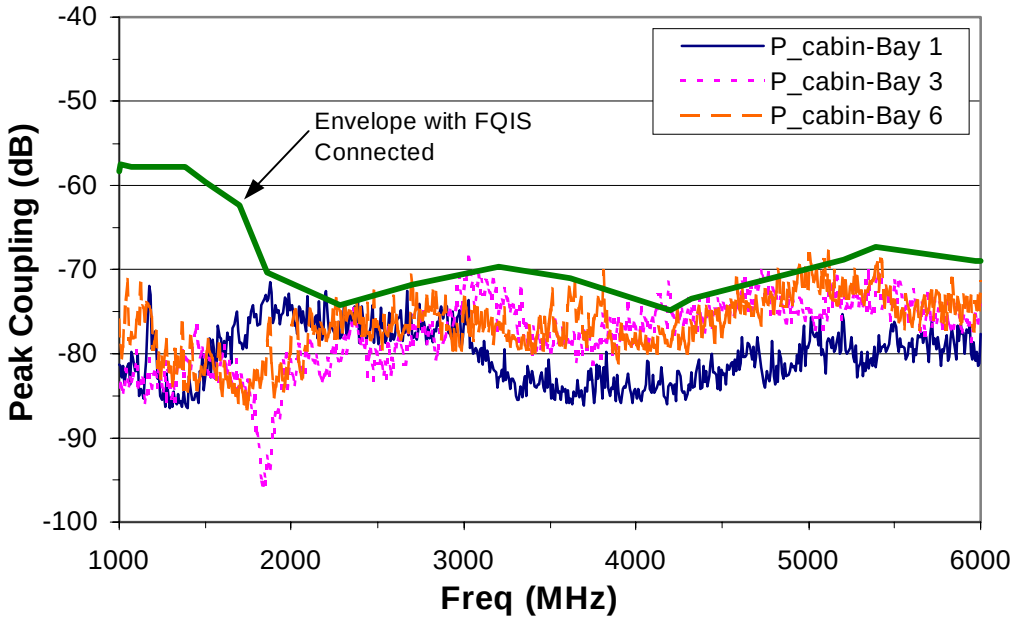

Figure 4.4.3.1.2-5: Peak coupling from passenger cabin to antenna in CWT. FQIS de-mated from CWT. (1 GHz - 6 GHz)

4.4.3.2 Application to PED Threat Levels

Previous data showed that the worst-case coupling from the passenger cabin was from the FQIS wiring. The worst-case coupling to an efficient antenna in the CWT was almost 20 dB lower. Applying these coupling factor envelopes to the PED threats shown in Figure 4.3.4-1 resulted in Figures 4.4.3.2-1 and 4.4.3.2-2.

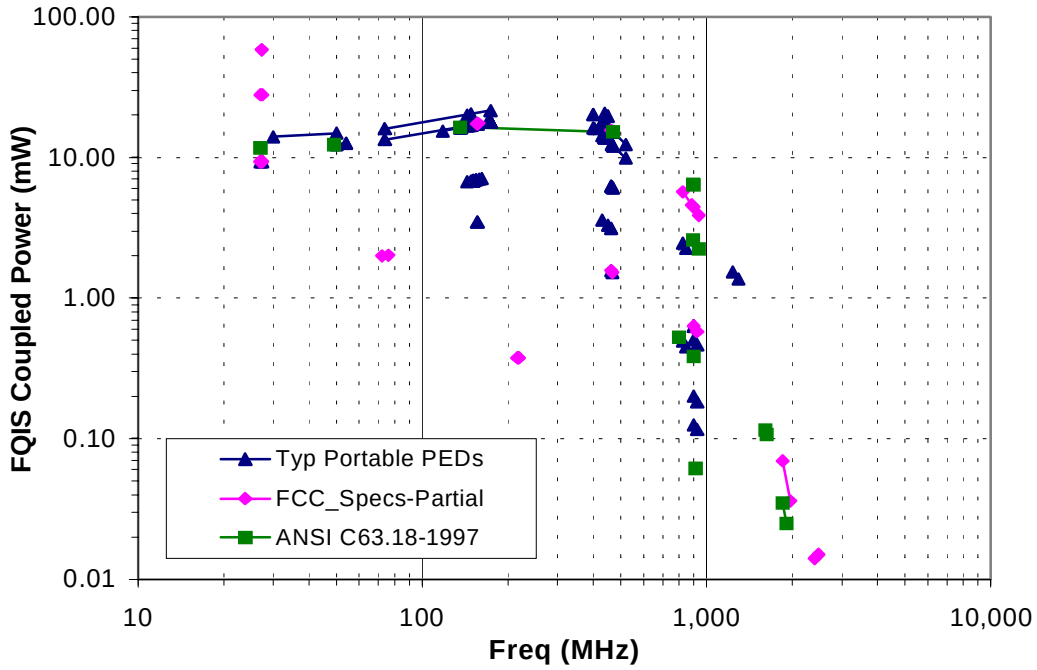

Figure 4.4.3.2-1: PEDs power coupled onto FQIS wiring.

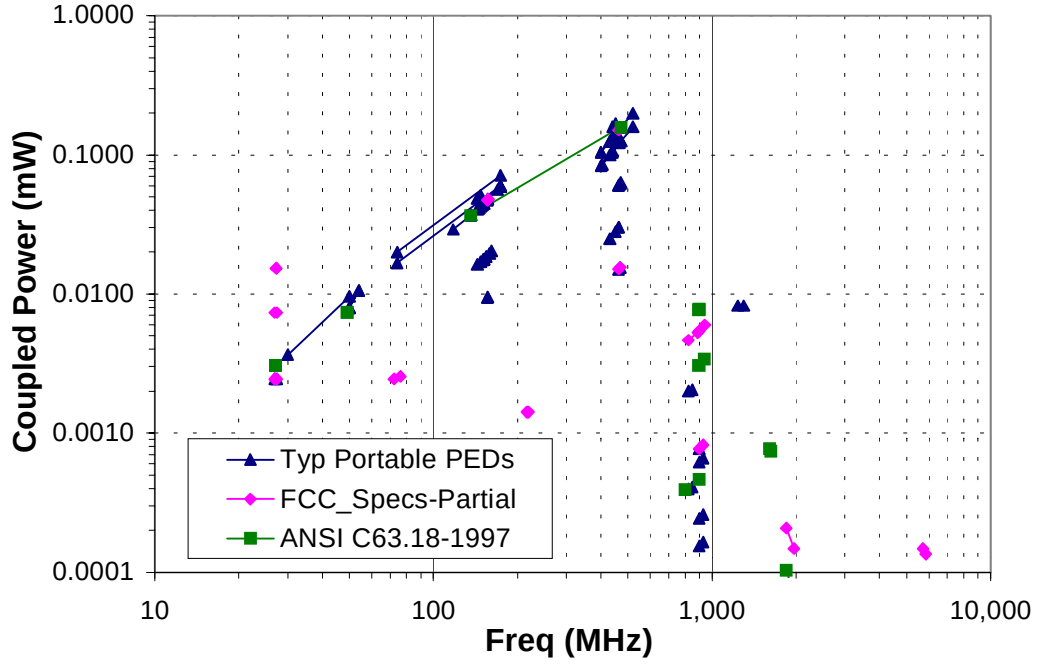

Figure 4.4.3.2-2: PEDs power coupled into antenna in CWT.

For frequencies up to 500 MHz, the worst-case power that could be induced upon on the FQIS was about 30 mW, except for frequencies near 27 MHz. The level drops off sharply after 500 MHz. At 27 MHz, a device radiating at 25 W FCC limit in the passenger cabin, would result in a 59 mW worst-case coupling on the FQIS wiring. However, a more reasonable practical limit for a PED in the passenger cabin was about 10 W or less, since it would have been impractical to carry a 25W device onto the airplane. (The RF power required to create a discharge on the laboratory FQIS installation is reported in Section 4.5.)

Figure 4.4.3.2-2 shows that a maximum PED threat in the passenger cabin could couple a maximum of approximately 0.2 mW of power to an antenna in the CWT. This value bounds the power that could be coupled onto FQIS wires in the CWT by radiated fields.

In both cases it is evident that PED coupling at frequencies above 1 GHz declines significantly. This result was useful for determining frequency limits for subsequent experimental testing.

4.4.4 Isolated Fuel Probe Tests

In section 4.4.1, it was shown that the RF input impedance of the FQIS installation in the laboratory chamber could be compared to an actual CWT. While the exact RF input impedances at a specific frequency were not identical between the two installations, the average values and statistics were very similar. It was also noted that the input impedance could change due to factors that may affect the EM boundary conditions within such a system. These factors could include wire placement within the CWT, temperature, and the presence and location of any object within the CWT. The presence of a varying amount of fuel becomes an obvious factor influencing the CWT EM environment, and therefore, the CWT FQIS input impedance

To explore this issue in detail, a single fuel probe was removed from a retired B-747-100, and instrumented to determine how its specific input impedance characteristics were affected by immersion in varying levels of fuel. A description of the measurement setup is discussed in Section 4.4.4.1, and results and conclusions are provided in Section 4.4.4.2.

4.4.4.1 Measurement setup

This test was performed by NSWC personnel, who had expertise, access to fuel, and the equipment necessary to perform such an analysis safely. The test was designed to measure the impedance of an isolated fuel probe as a function of frequency, and to investigate the effects of different levels of fuel on the input impedance.

Figure 4.4.4.1-1: Equipment necessary for performing the isolated fuel probe tests.

Figure 4.4.4.1-1 shows the complete set of equipment used for the test. The network analyzer served as the primary measurement instrument. The analyzer transmitted a low-level RF signal from the measurement port. The same port was then used to receive the RF reflections from the fuel probe. The output of the network analyzer was less than 1 mW, which was a safe power level for this fuel test. As an extra precaution, a fire extinguisher was included in close vicinity to the test setup. Located directly beside the cart shown in the photograph, was the test fixture designed to provide a non-intrusive method of immersing the probe into fuel.

A diagram of the test setup is shown in Figure 4.4.4.1-2. The figure shows the network analyzer attached to the fuel probe. The test port cable and the measurement adapter were calibrated so that only the reflection of the submersed fuel probe assembly was measured. A plastic container was used to immerse the probe into three different amounts of fuel. The RF reflection, as a function of frequency, was measured with the network analyzer and stored on the computer. This measurement was performed for three configurations: empty; with two inches of fuel; and with two feet of fuel in the container.

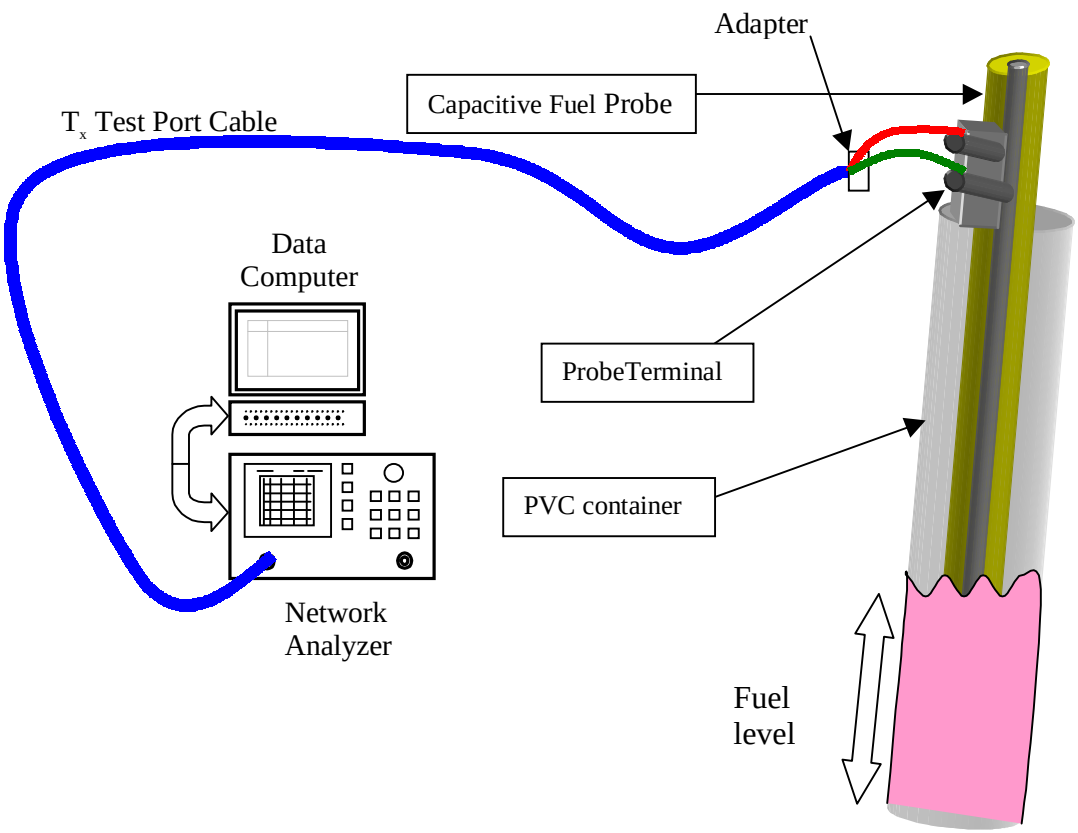

Figure 4.4.4.1-2: Isolated fuel probe test setup.

4.4.4.2 Results and conclusions

Figure 4.4.4.2-1 shows the data gathered in the three measurement, where the complex reflection coefficients for all three configurations are plotted on a Smith Chart. The reflection coefficient was measured for frequencies from 300 kHz to 400 MHz. Highest reflection magnitude is indicated for data points located farthest away from the center of Smith Chart. When the reflection magnitude for a device

is high, less power is absorbed by the system. For more information about the Smith Chart, refer to Appendix E. This plot shows that for the majority of frequencies, there was little chance of dissipating power on the fuel probe. There are several locations where the data are close to the center of the chart. These locations indicate frequencies where the probe best dissipated or radiated applied power.

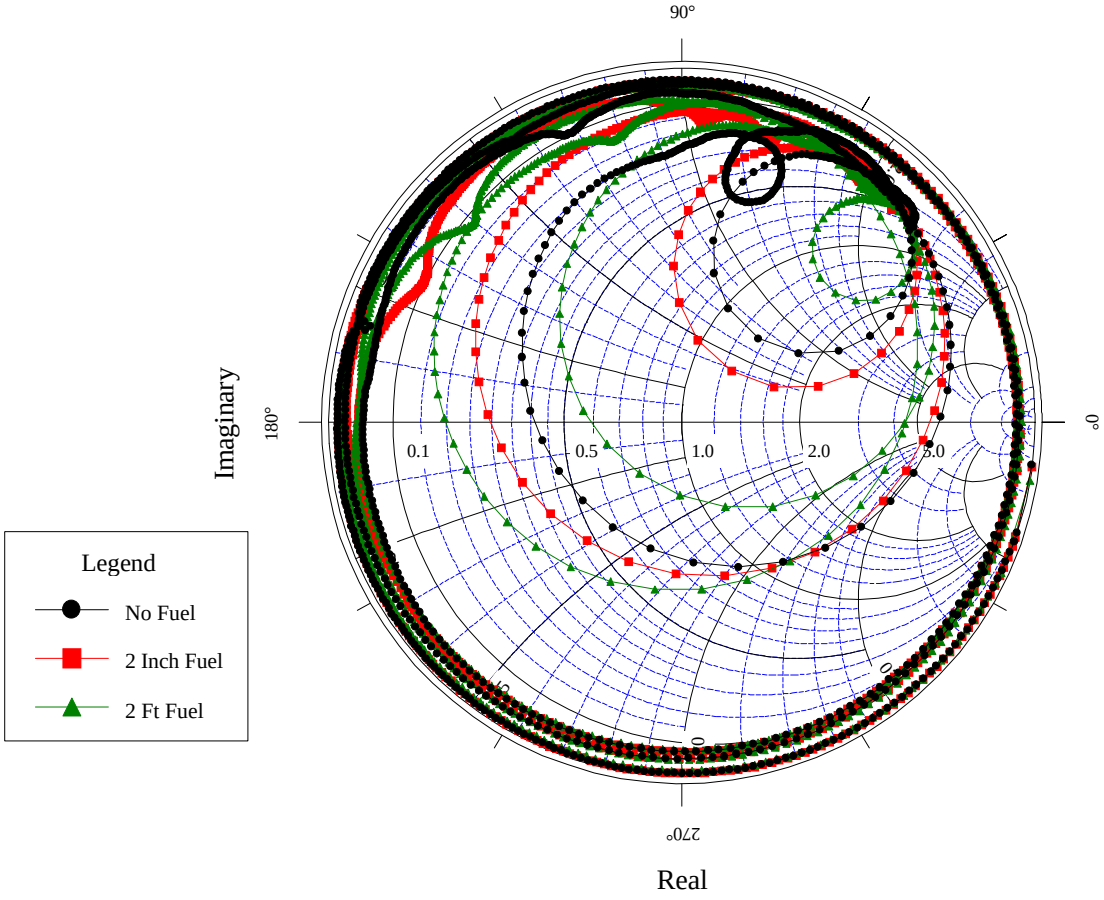

Figure 4.4.4.2-1: Smith Chart view of the complex reflection data for three fuel levels, from 0.3 to 400 MHz.

The magnitude of the reflection coefficient is plotted in Figure 4.4.4.2-2 as a function of frequency. This figure better reveals the resonant frequencies of the fuel probe. The maximum of the plot (1.0) represents total reflection of the RF signal. Total reflection implies that all of the power sent to the probe was reflected back to the source. Conversely, the further down the trace is located on the graph the more power could be coupled onto the fuel probe. These dips in the magnitude graph are referred to as the resonant frequencies of the probe.

In examining the three data runs plotted on Figure 4.4.4.2-2, the resonant frequencies are shifted by the presence of the fuel. The first large dip is generally referred to as the *first resonance*. This first resonance was shifted down only a small amount for the addition of two inches of fuel, but was shifted significantly more with two feet of fuel added. By looking at the dips in Figure 4.4.4.2-2, it can be seen that the fuel probe resonant frequencies were changed by the addition of the fuel, but it is inconclusive as to whether the reflection coefficient magnitude was always lowered or raised.

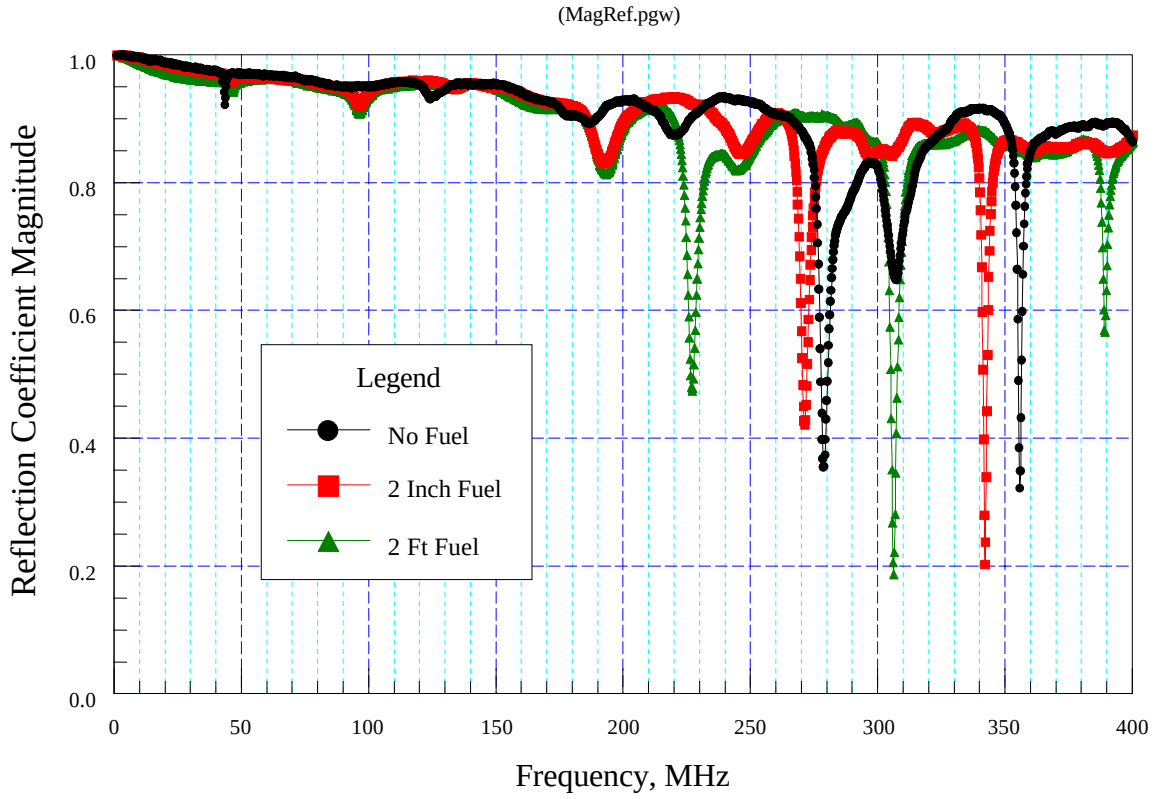

Figure 4.4.4.2-2: Magnitude of the reflection coefficient for three fuel levels.

It can be concluded that the addition of fuel in the CWT shifted the resonant frequencies of the FQIS. Even a small amount of fuel shifted the resonant frequencies of the fuel probe. As expected, the fuel probe was highly reactive, and for most frequencies it reflected most of the applied power. However, there were several resonant frequencies that coupled power to the fuel probe easily. This power was radiated or dissipated in resistive losses. This information, along with the detailed characterization of the FQIS system in the following section, provide a basis for the RF-induced ionization, discharge, and heating test described in Section 4.5.

4.4.5 Detailed Measurement of FQIS Installed in Laboratory

The objective of the conducted-coupling measurements on the FQIS was to measure the induced currents and voltages at the M127 connector assembly and at multiple locations throughout the FQIS simulator. The baseline transfer functions were determined between input power and induced RMS current, as well as input power and induced RMS voltage at the M127 connector. With additional probing beyond the M127 connector into the simulated CWT FQIS components, the frequencies and locations where current or voltage enhancements occurred throughout the CWT FQIS were determined. The data from these detailed characterizations of current and voltage relationships were used to define susceptibility points for the RF-induced ionization, discharge, and heating tests.

4.4.5.1 Laboratory Setup

In Section 4.4.1.3, the NASA LaRC FQIS simulator was demonstrated to be comparable to the aircraft CWT FQIS installation in terms of average impedance and reactive characteristics, from 0.3 to 1000 MHz. Based upon this comparability, the FQIS simulator was qualified for use as a comparison tool in quantifying voltage and current magnitudes induced upon the CWT FQIS, due to RF power applied to the M127 connector. Most instrumentation and laboratory setups used for the current and voltage measurements of this section were the same as described for the impedance measurements of Section 4.4.1, except the network analyzer was configured for transmission, rather than reflection measurements.

Figure 4.4.5.1-1 shows the ten primary test position locations for the detailed electrical characterizations on the FQIS simulator. Test positions were determined prior to the conducted-coupling measurements. The positions identify locations where current and voltage enhancements were likely to occur. Test position TP-1 was established at the input to the FQIS as a reference. The other test positions were primarily at the HI Z or LO Z terminal of the fuel probes. Some of these test positions proved to be locations of current and/or voltage enhancements.

In addition to the test positions shown in Figure 4.4.5.1-1, additional current probing was conducted along individual wire lengths, and additional voltage probing was done on the structure of the fuel probes themselves. No additional locations of significant current and/or voltage enhancements were observed.

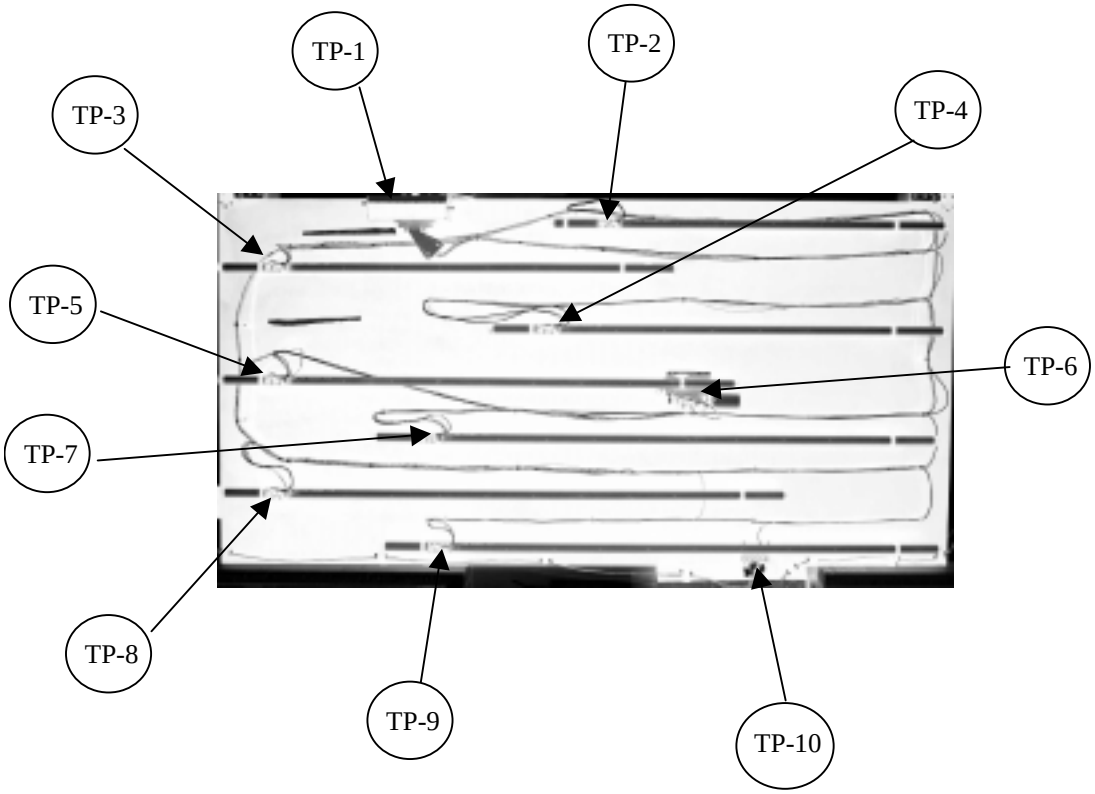

Figure 4.4.5.1-1 Primary current-voltage Test Position (TP) locations.

4.4.5.2 Instrument Setup

The laboratory instruments and system under test (SUT) were configured as depicted in Figures 4.4.5.3-1 and 4.4.5.4-1. The network analyzer was set up to operate and calibrated for transmission measurements. The signal source was set for a logarithmic frequency sweep from 1 MHz to 1 GHz. The resolution was set for 201 points per sweep at a sweep rate of 100 msec. The network analyzer power was established at 0 dBm to assure sufficient dynamic range to conduct transmission measurements through long wire paths.

An adapter device allowed for connection between the test port cable and the FQIS D3-test lead, which connected directly to the M127 connector assembly, making it possible to directly inject signals through this interface, onto the FQIS wiring, and to the fuel probes of the FQIS simulator. The adapter device and a typical common mode pin connection to the D3-M127 input interface of the FQIS can be seen in the foreground of Figure 4.4.5.2-1. Several fuel probes are visible in the background of this figure.

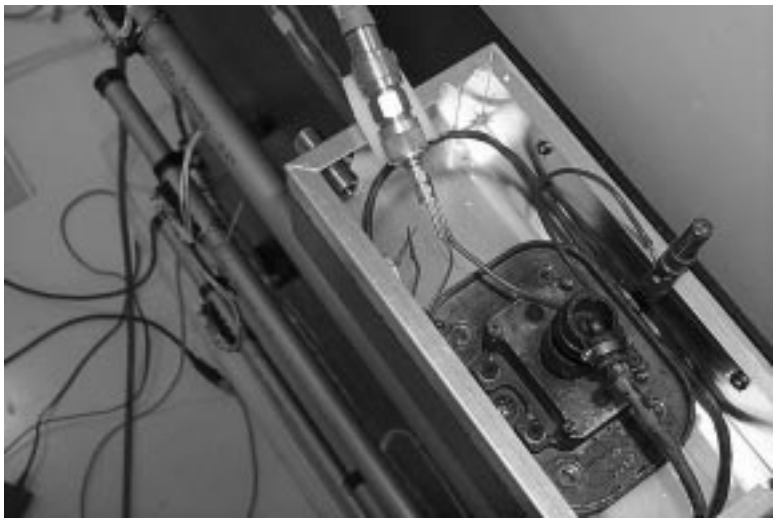

Figure 4.4.5.2-1: RF Type-N Coaxial-to-Pin adapter, D3 test lead, and the FQIS M127 connector .

The adapter device was previously characterized for any mismatch effects using the network analyzer in a time-domain gating mode. Time domain gating is an advanced technique that may be employed to remove connector effects. It provides the capability to remove or greatly reduce the degradation and uncertainty caused by the connector to cable interface and the effects of test leads.

4.4.5.3 Current Enhancement Measurements

During the measurements to determine current enhancements, the measurement system was calibrated and configured in the laboratory as depicted in Figure 4.4.5.3-1. Using the set power level of 0 dBm, the current probe was sequenced through the test position locations according to the defined test matrix of various excitation modes (signal injected on the transmit test port cable) and various sensed paths (signals detected on the receive test port cable). The data were recorded and saved for later analysis. The magnitudes, frequencies, and locations of the most significant current enhancements were documented for additional testing described in Section 4.5 of this report.

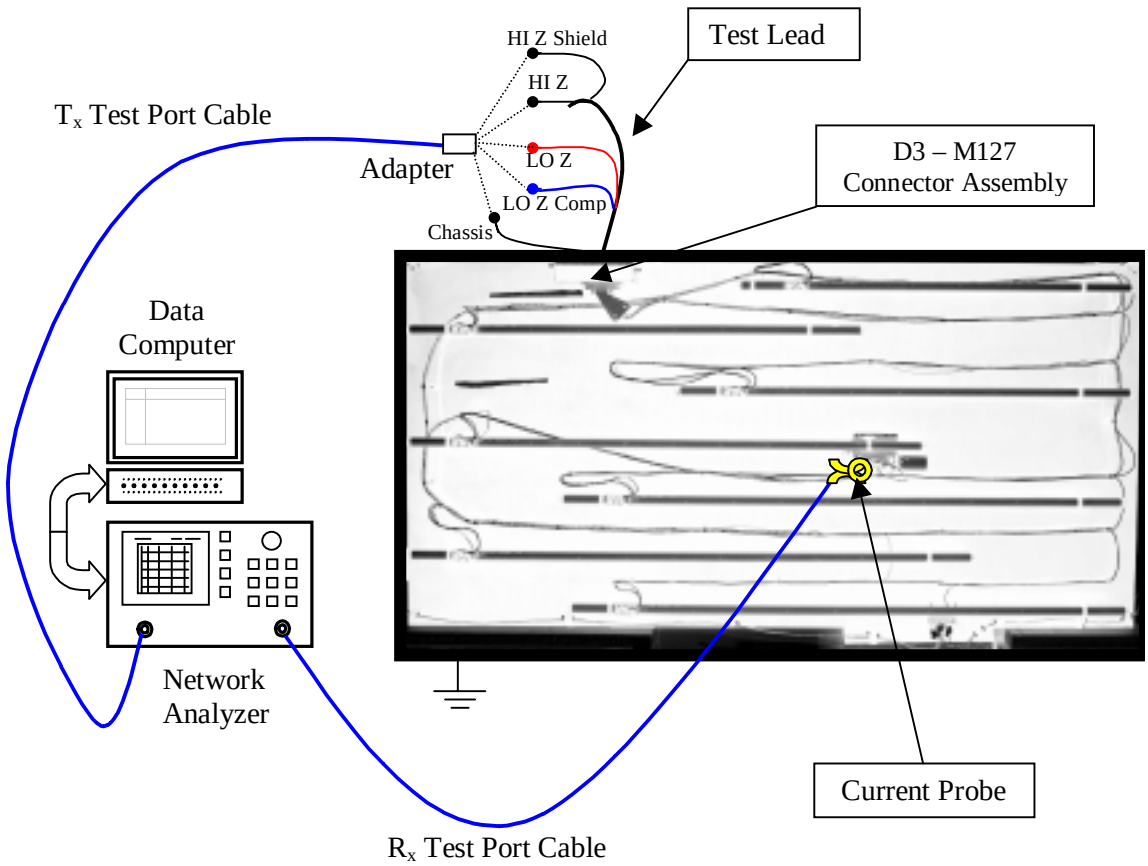

Figure 4.4.5.3-1: Induced current measurement laboratory setup.

4.4.5.4 Voltage Enhancement Measurements

During the measurements to determine voltage enhancements, the measurement system was calibrated and configured in the laboratory as depicted in Figure 4.4.5.4-1. Using a set power level of 0 dBm, the voltage probe was sequenced through the test position locations according to the defined test matrix of various excitation modes (signal injected on the transmit test port cable) and various sensed paths (signals detected on the receive test port cable). The data were recorded and saved for later analysis. The magnitudes, frequencies, and locations of the most significant voltage enhancements were documented for additional testing described in Section 4.5 of this report.

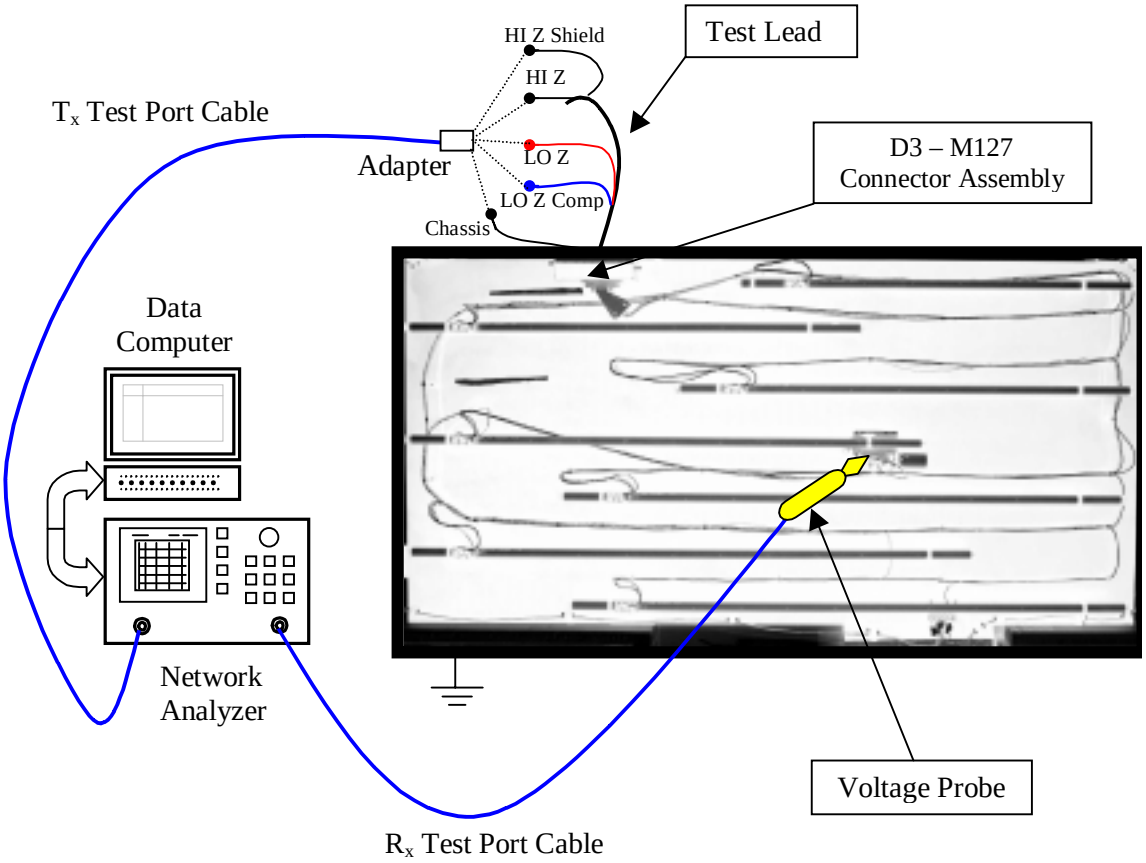

Figure 4.4.5.4-1: Induced voltage measurements laboratory setup.

4.4.5.5 Conducted versus Radiated Excitation Comparison

So far, all measurements described in Section 4.4.5 have related to conductive modes of FQIS excitation. In Section 4.4.3, it was shown that the external FQIS wiring was not the only means for power to enter the CWT, however, it was dominant up to about 2 GHz. (See Figures 4.4.3.1.2-4 and 4.4.3.1.2-5.) Power entering the CWT from paths *other* than the FQIS must couple radiatively to the FQIS wiring. As shown in Section 4.4.3, the CWT was a good reverberating enclosure, and radiated field enhancements did occur. Therefore, it was useful to compare voltages and currents induced upon the CWT wiring from both conducted *and* radiated excitation modes.

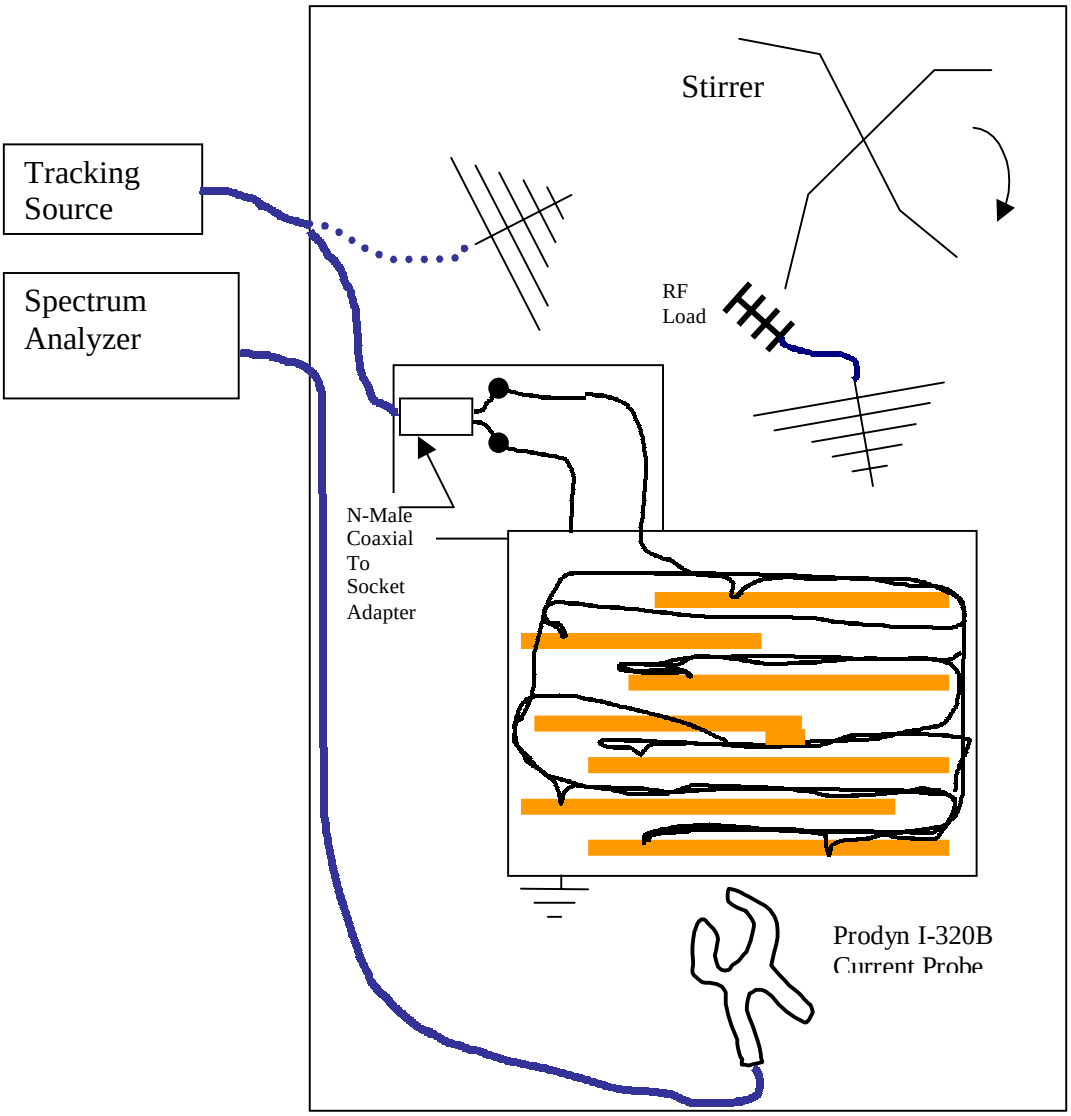

Figure 4.4.5.5-1: Experimental setup for comparing currents induced upon CWT wiring from both conducted and radiated excitations.

4.4.5.5.1 Experiment Setup

A sketch of the experiment setup is shown in Figure 4.4.5.5-1. Because the conducted versus radiated excitation comparison test was of secondary priority, the following simplifying (and time saving) determinations were made:

- Only one conducted mode was selected for comparison with the radiated excitation mode.
- Only current was measured, not voltage. This decision was made because the Prodyn I320B clamp-on current probe was easier and faster to use than the voltage probe. Either method would be sufficient for the relative comparison nature of this data.

Two test data sets were collected: 1) Radiated Mode, using a log periodic antenna (200 MHz – 1 GHz rated bandwidth); 2) Conducted Mode, using the LO Z red to Chassis excitation (because it tended to provide good coupling at all designated test positions). All unused M127 connections were left un-terminated to minimize resistive loading that could result in reduction of induced voltages and currents.

Peak current coupling was measured at eight test position locations (TP-2,3,4,5,6,7,8,9; as shown in Figure 4.4.5.1-1). All measurement data were stored in terms of *power transfer* between the tracking source and spectrum analyzer. Because cable loss and the current-to-power relationship for the Prodyn probe were the same for both radiated and conducted excitations, comparisons of power transfer (in dB) should be equivalent to current comparisons. The cable length connecting the Prodyn current probe was of sufficient length to allow measurements anywhere on the FQIS installation. A second log periodic antenna was present and terminated into a 50 Ohm RF load. This configuration maintained a chamber quality factor similar to that when the calibration was performed. The spectrum analyzer / tracking source measurement system was operated in a similar manner as described in Section 4.4.2 for the peak cavity coupling factor, except that the Prodyn probe was connected to the spectrum analyzer receive path (instead of another antenna). The source output level was +20 dBm (100 mW) to ensure sufficient dynamic range in the measurement system. The mechanical stirrer was operated continuously for all measurements, which permitted measurements of the peak envelope to be made at all frequencies and EM boundary conditions, as the spectrum analyzer was repetitively swept in “Maximum Hold” mode.

4.4.5.5.2 Experiment Data

Both radiated and conducted measurements were performed using the same set of cables, at the same measurement positions, with the same current probe and the same input power level. Only the method of excitation was changed. After many spectrum analyzer frequency sweeps for a particular measurement position, the maximum coupling envelope data were downloaded from the instrument with a standard laptop computer, and stored as a file. Data files were created for each of eight measurement positions for radiated and conducted excitations, resulting in 16 data files. Figure 4.4.5.5.2-1 shows raw data for each measurement position, for both the radiated and conducted excitations. It is important to note that a mismatch loss occurred at the power input for the conducted excitation mode. Such a mismatch loss was negligible when applying power to the antenna because it was designed to minimize this loss. Also, the +20 dBm power level from the source needed to be accounted for in calculating a coupling ratio.

If the maximum coupling location for each frequency is taken, maximum envelopes of these two excitations can be compared directly. This procedure was used along with compensation for mismatch loss and source output power to obtain the Peak Coupling plot shown in Figure 4.4.5.5.2-2.

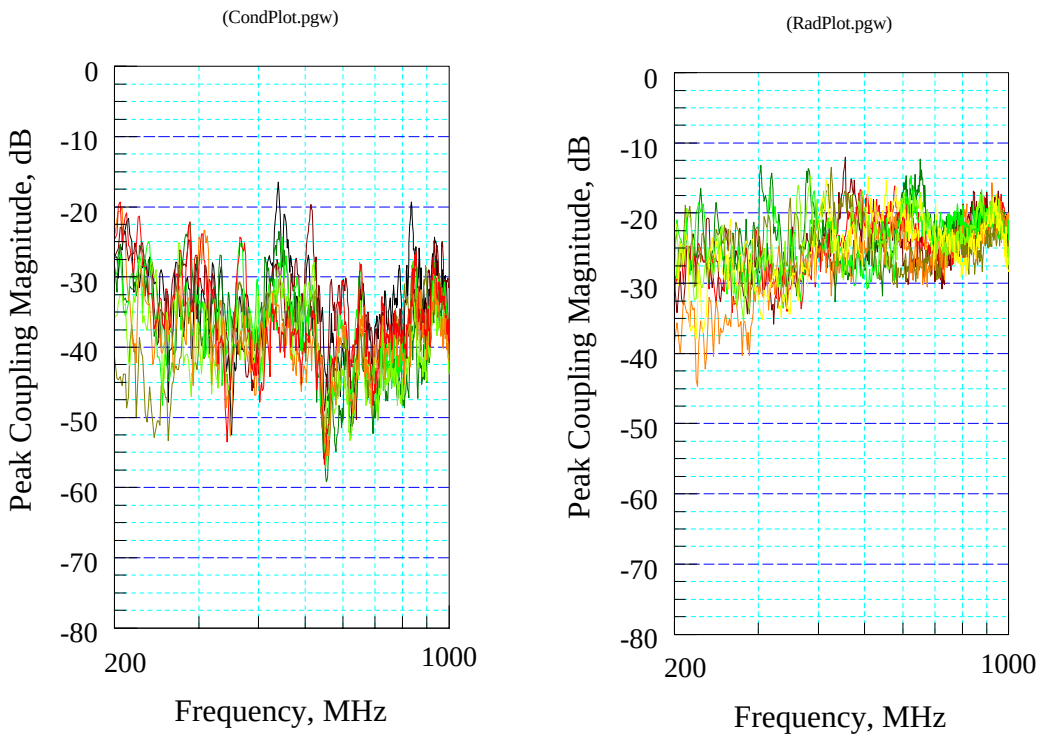

Figure 4.4.5.5.2-1: Data for each of eight measurement positions, for both the conducted (left), and radiated (right) excitations. This data was not corrected for the +20 dBm source output, or for the 50 Ohm mismatch loss that applied to the conducted excitation.

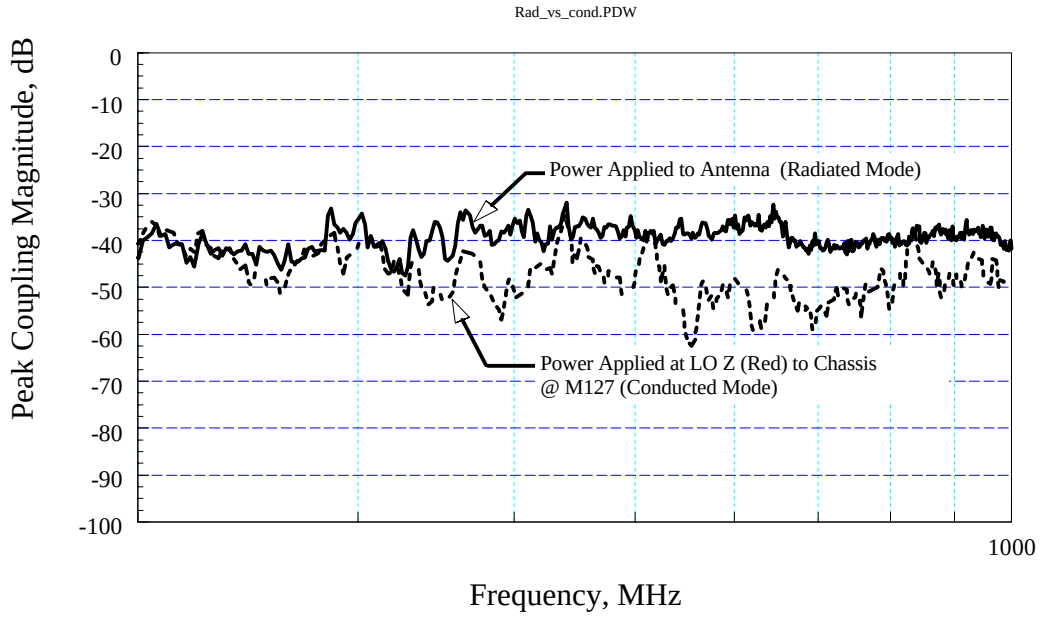

Figure 4.4.5.5.2-2: Maximum (of eight different test position locations) measured coupling from radiated versus conducted excitation modes on the laboratory FQIS installation. This data was corrected for the +20 dBm source output, and mismatch loss at the connector.

4.4.5.5.3 Analysis of Experiment Data

Figures 4.4.5.5.2-1 and 4.4.5.5.2-2 both relate to the laboratory chamber FQIS installation only. Because a given input power will generate a higher maximum radiated coupling in an actual CWT (as compared to the laboratory chamber), the peak radiated coupling (red line) shown in Figure 4.4.5.5.2-2 would probably be higher in the actual CWT. (See Section 4.4.2.3.)

An attempt was made to compare the worst-case coupling values of radiated versus conducted CWT excitations *as generated by a passenger cabin radiated source*. The two calculations below show these comparisons.

FQIS Conducted Path

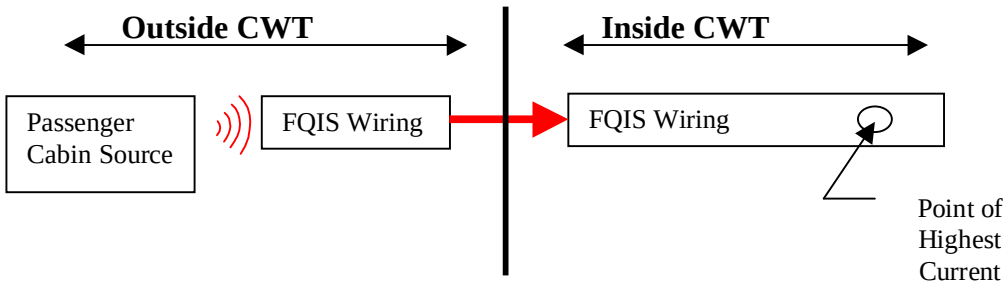

Passenger Cabin to FQIS coupling (worst-case)	-23	dB	(Figure 4.4.3.1.1-4)
FQIS to current probes (worst-case)	-34	dB	(Figure 4.4.5.5.2-2)
Total	= **-57**	**dB**	

Figure 4.4.5.5.3-1: Calculation of worst-case coupling values considering only FQIS wiring as primary coupling path.

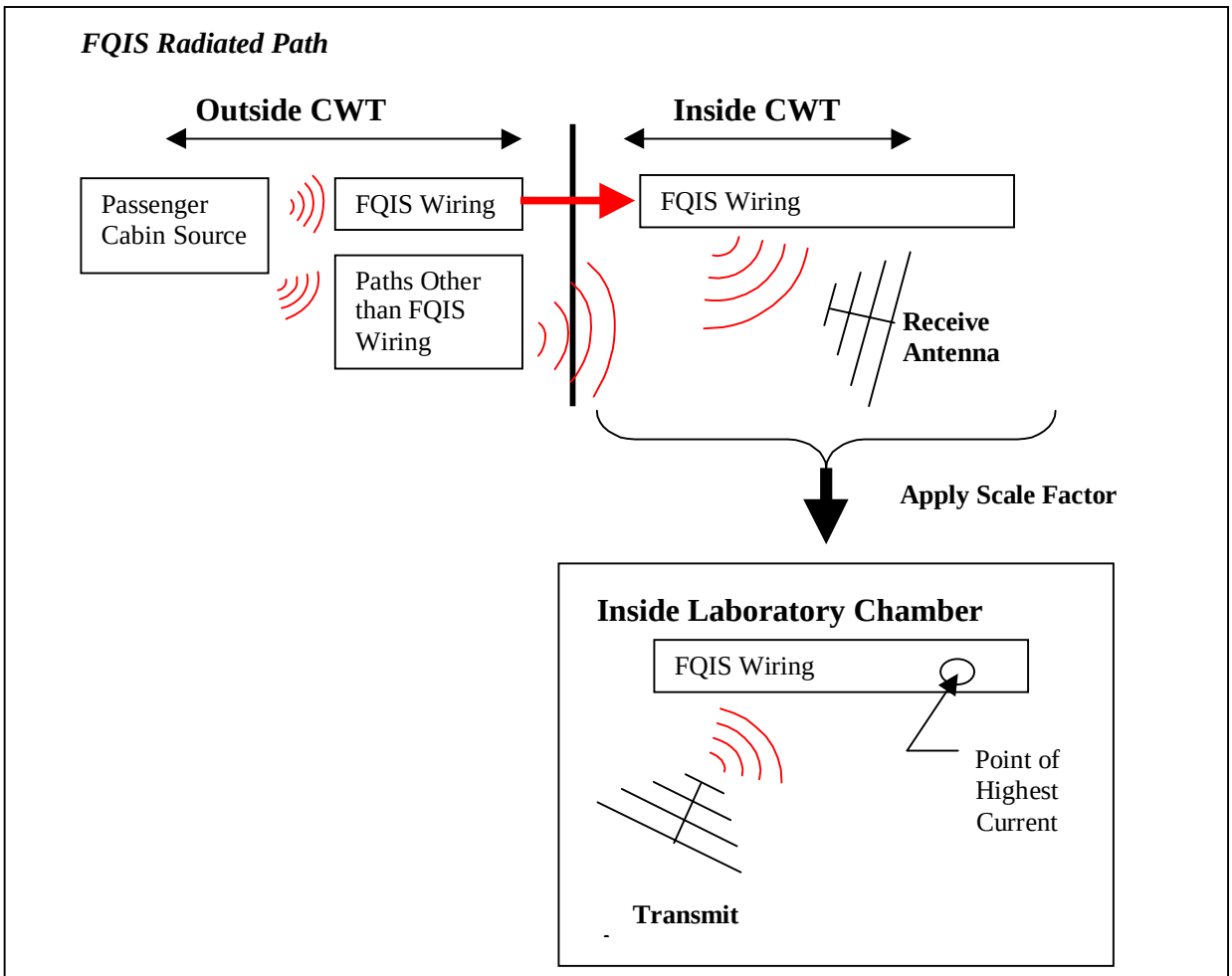

Passenger Cabin to CWT Rcv. Antenna (worst-case)	-44	dB	(Fig.4.4.3.1.2-2,500 MHz)
CWT vs. Lab. Chamber Scale Factor	+4	dB	(Fig. 4.4.2.3-1, 500 MHz)
Transmit Antenna to current probes (in lab chamber)	-32	dB	(Fig 4.4.5.5.2-2)
Total	= **-72**	**dB**	

Figure 4.4.5.5.3-2: Calculation of worst-case coupling values considering multiple coupling paths.

From this data, it is shown that the *FQIS conducted path* coupling from the passenger cabin to the highest current probe output was –57 dB. The *radiated path* coupling from the passenger cabin to the highest current probe output was –72 dB. This comparison shows a difference of about 15 dB for frequencies above 200 MHz. Below 200 MHz, radiated path coupling becomes highly unpredictable (due to limited modes in the limited cavity volume), whereas conducted path coupling becomes more predictable and efficient. Based upon this analysis, it was decided that the primary excitation mode should be conductive for the subsequent RF Induced Ionization, Discharge, and Heating test in the laboratory chamber.

4.4.5.6 Selection of Maximum Voltage and Current Enhancement Positions

Numerous measurements of current and voltage were obtained from the laboratory FQIS installation. Using the laboratory instrumentation setups shown in Figures 4.4.5.3-1 (induced current), and 4.4.5.4-1 (induced voltage), all common-mode excitations and two differential-mode excitations were applied, and data collected at the test positions defined in Figure 4.4.5.1-1. The results from these measurements provided insight about the current and voltage enhancement points of the system. A summary of the data gathered in the coupling measurements for each type of excitation is now discussed. Because of the large amount of data gathered, an independent display of each coupling measurement was impractical. The data was useful in determining the highest current or voltage enhancement from the measurement set, therefore similar data was plotted together on single graphs.

Excitation Mode	Primary Measurement Location	Secondary Measurement Location
HI Z – Chassis	HI Z	HI Z Shield
LO Z COMP (Blue) – Chassis	LO Z COMP (Blue)	HI Z
LO Z (Red) – Chassis	LO Z (Red)	HI Z
HI Z Shield – Chassis	HI Z Shield	HI Z
HI Z – LO Z (Red)	HI Z – LO Z (Red)	HI Z
HI Z – LO Z COMP (Blue)	HI Z – LO Z COMP (Blue)	HI Z

Table 4.4.5.6-1: Summary of excitation modes, and measurement locations for the detailed characterization of the FQIS system installed in the laboratory reverberation chamber.

Table 4.4.5.6-1 shows the different excitation modes investigated in the coupling measurements. For each excitation mode there were two types of measurements taken. The primary set of measurement locations was located on the identical path (the excitation path), and the secondary set of measurements was taken on the Hi Z line for almost all of the excitation modes. The only exception was that when the Hi Z terminal was the excitation, the secondary set of measurements was taken on the Hi Z shield path. For each excitation mode, there were as many as ten test positions on the FQIS where the coupling measurements were taken. A series of composite plots describing the current coupling, and a series describing the voltage coupling, are given.

Figure 4.4.5.6-1 shows a representative composite plot of a data set. This figure represents the coupling of each test location, for the HI Z - Chassis excitation mode. The coupling value is displayed along the amplitude axis. These values represent the net reduction in signal strength as measured by the network analyzer. The coupling values displayed here account for cable losses of the attachment cables, but do not account for a calibration of the probes. Because the maximum coupling was desired, and the calibration was identical for all of the recorded measurements, there was no reason to apply the calibration to the more than 180 coupling measurements.

The complete set of coupling data is displayed in twelve composite data plots. Figure 4.4.5.6-1 through Figure 4.4.5.6-6 represents a summary of all of the FQIS system related current enhancement measurements. From these plots it can be seen that for the upper frequencies the coupling values vary greatly with frequency, and the coupling values are much more stable for low frequencies. The low frequency regions have the highest coupling, and will therefore provide the highest possibility of an

enhancement point. Figures 4.4.5.6-6 through Figure 4.4.5.6-12 represent a summary of all of the FQIS system related voltage enhancement measurements.

A key reason for the acquisition of the coupling data was to establish a worst-case enhancement excitation and the corresponding worst-case test location. The results, from the detailed characterization of the FQIS installed in the NASA LaRC reverberation chamber, provide insight about the current and voltage enhancement points of the system. The measurements were plotted on the same axis in order to show the relative magnitudes of each. The maximum current coupling values are determined by looking for the highest coupling measured with the Prodyn I-320B current probe. By examining each of the six current enhancement plots, it can be seen that the HI Z Shield – Chassis excitation mode produced the highest coupling values (Figure 4.4.5.6-4). From this excitation mode there were four test point locations that had the highest coupling. Each of these only differed slightly, as can be seen in Figure 4.4.5.6-4. Because of restrictions associated with the measurement systems and the time available for the test, only one of these points was selected as a test candidate. From these four positions, TP-2 (see Figure 4.4.5.1-1) was selected for the high-power testing. The worst-case voltage enhancement excitation modes were determined to be LO Z (Red) – Chassis, and LO Z COMP (Blue) – Chassis. From each of these, TP-6 was the worst case enhancement position.

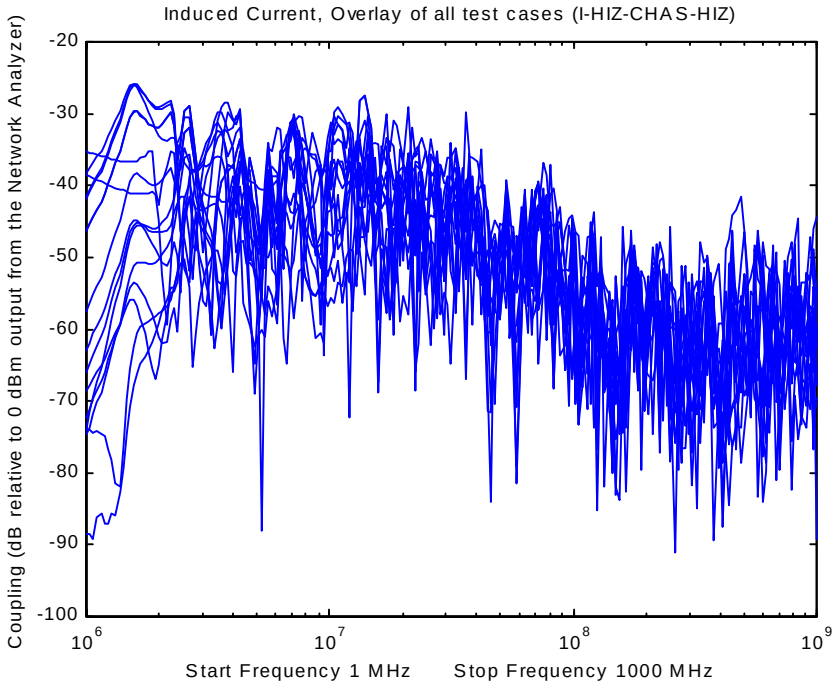

Figure 4.4.5.6-1: Induced current coupling measurements, HI Z – Chassis excitation.

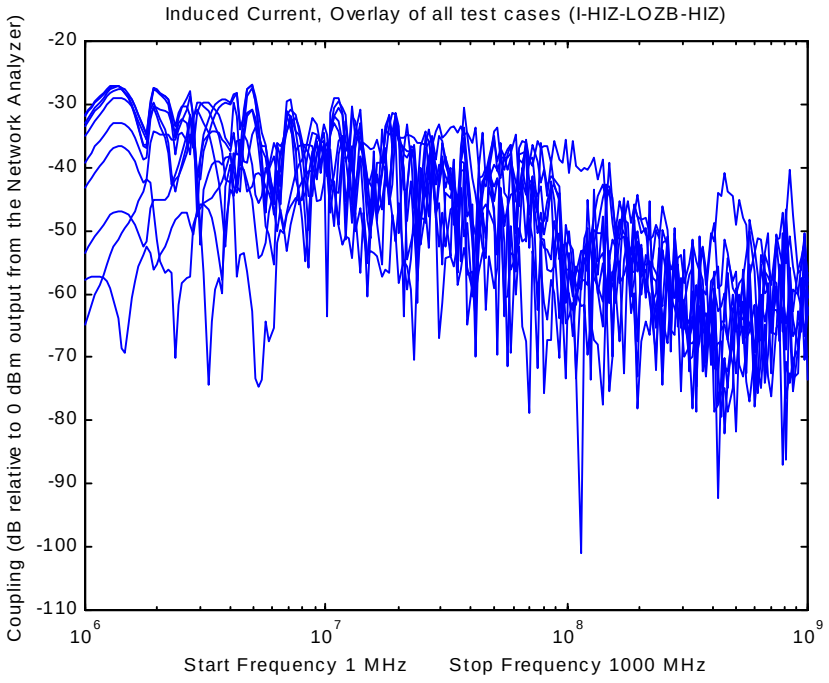

Figure 4.4.5.6-2: Induced current coupling measurements, HI Z – LO Z COMP (blue) excitation.

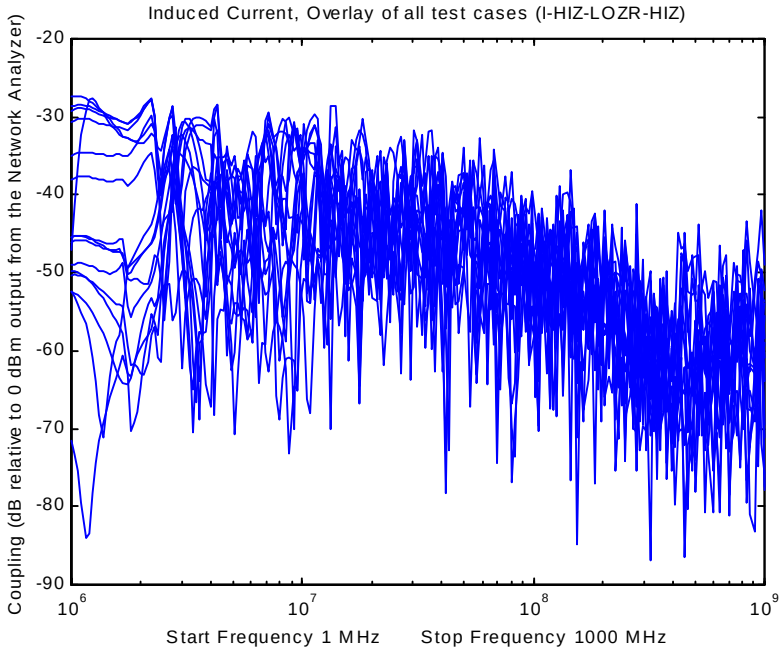

Figure 4.4.5.6-3: Induced current-coupling measurements, HI Z – LO Z (red) excitation.

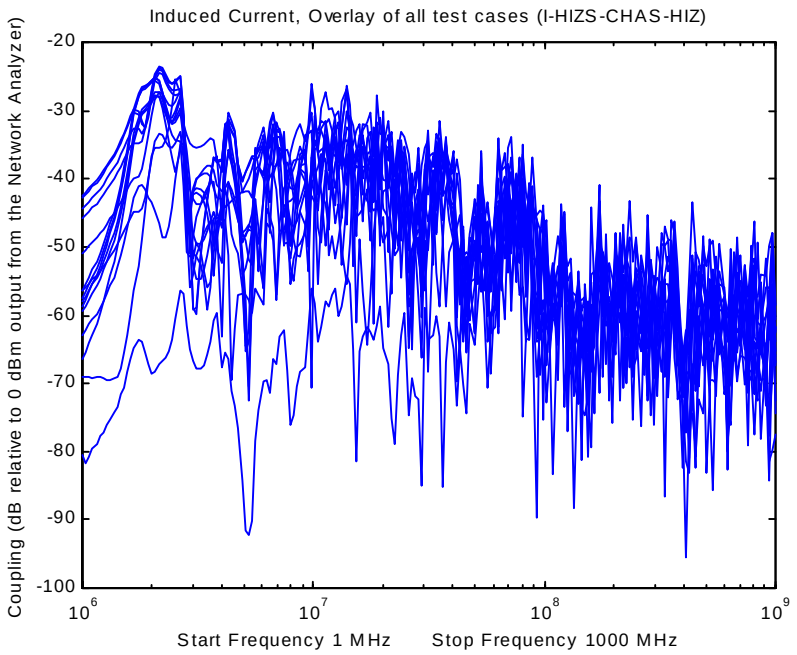

Figure 4.4.5.6-4: Induced current coupling measurements, HI Z Shield – Chassis excitation.

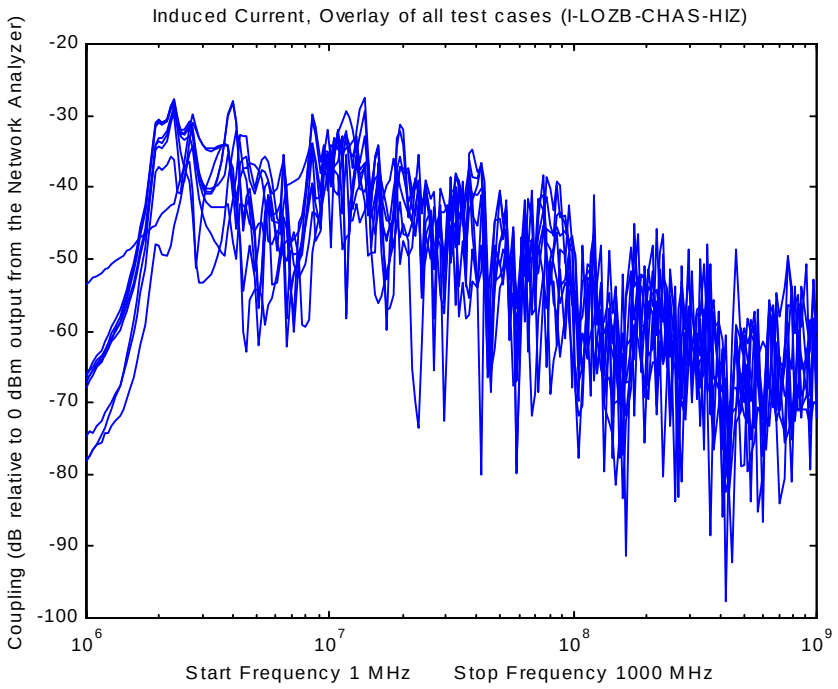

Figure 4.4.5.6-5: Induced current-coupling measurements, LO Z COMP (blue) – Chassis excitation.

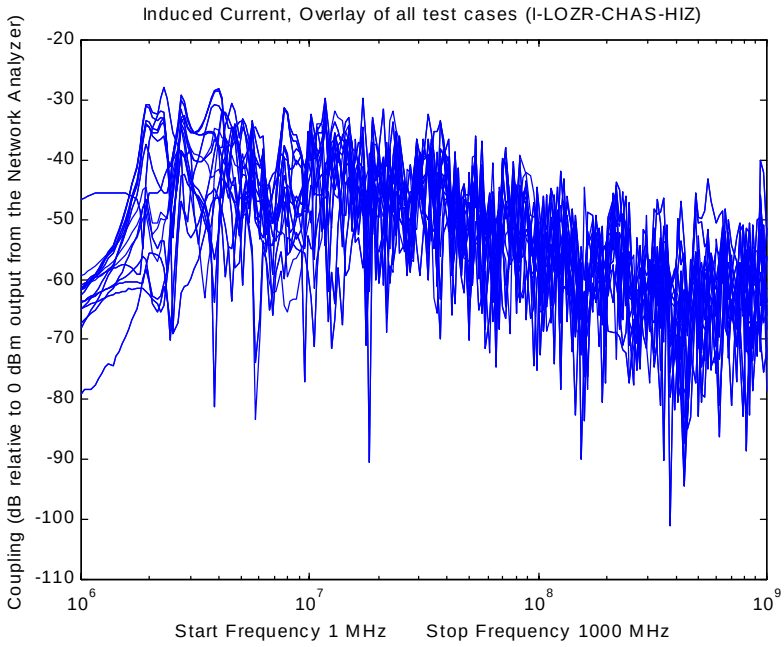

Figure 4.4.5.6-6: Induced current coupling measurements, LO Z (red) – Chassis excitation.

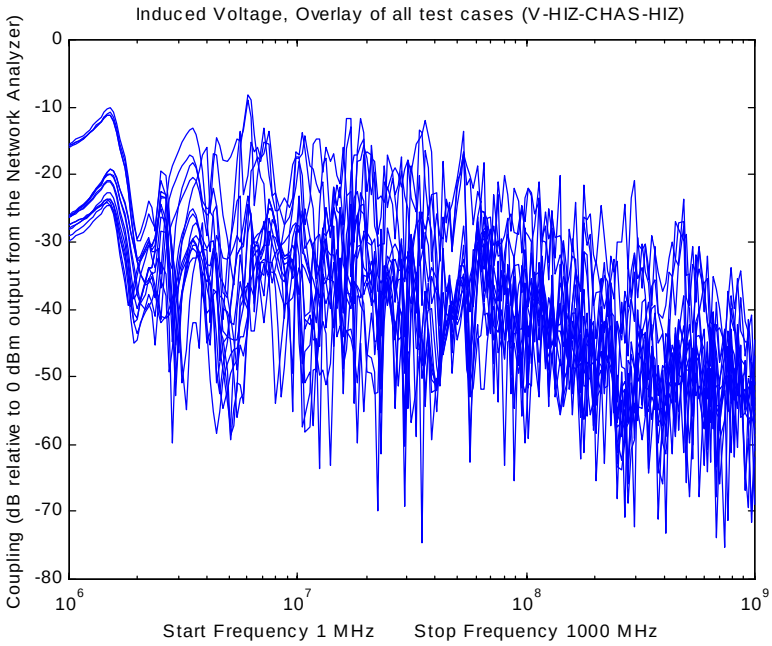

Figure 4.4.5.6-7: Induced voltage coupling measurements, HI Z – Chassis excitation.

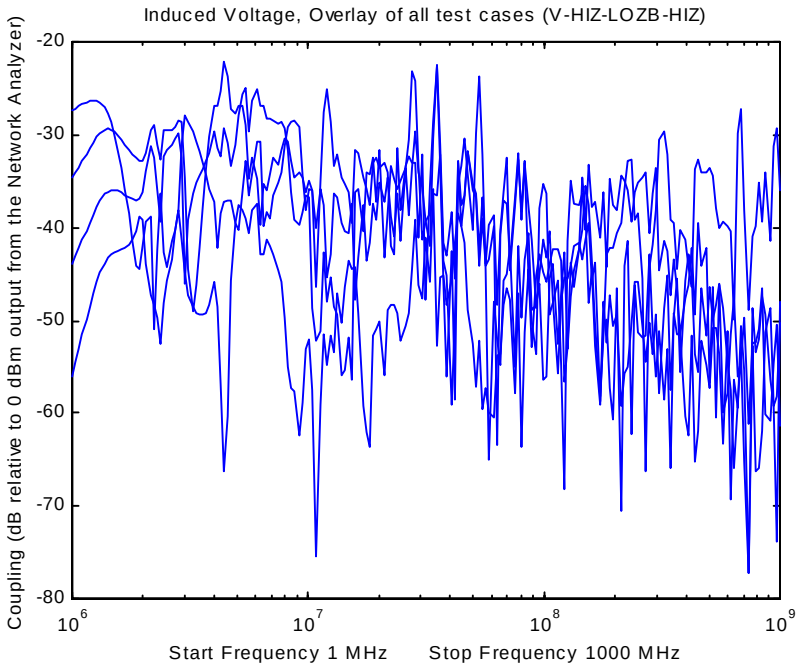

Figure 4.4.5.6-8: Induced voltage-coupling measurements, HI Z – LO Z COMP (blue) excitation.

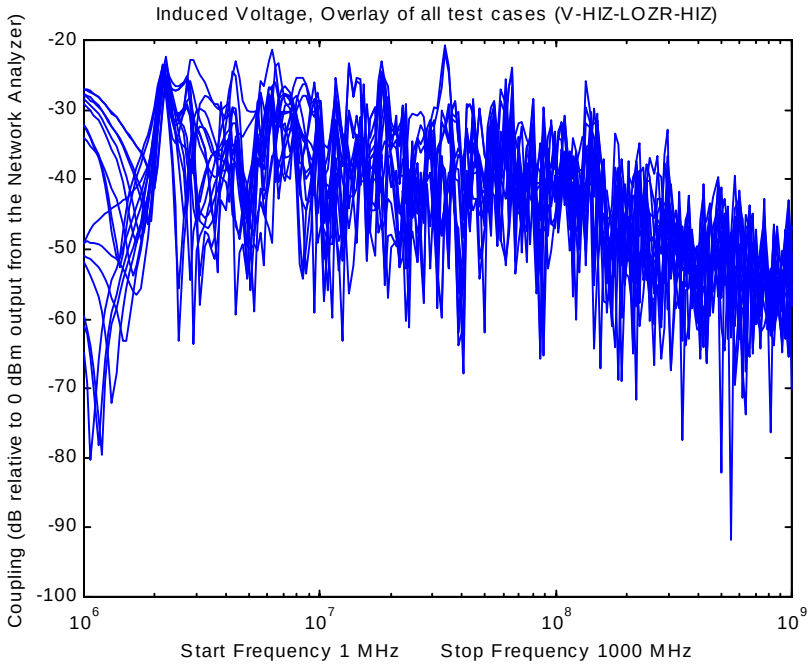

Figure 4.4.5.6-9: Induced voltage-coupling measurements, HI Z – LO Z (red) excitation.

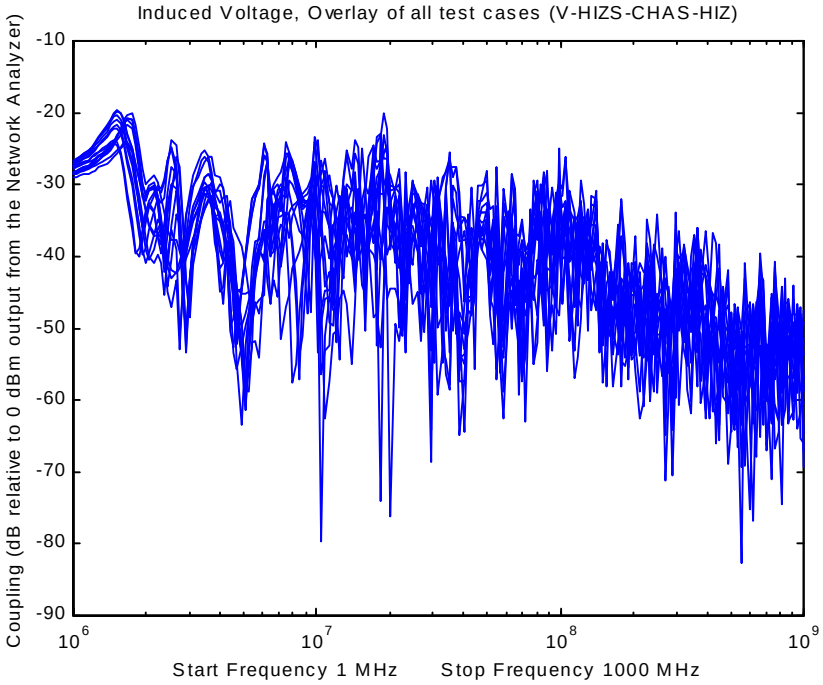

Figure 4.4.5.6-10: Induced voltage coupling measurements, HI Z Shield – Chassis excitation.

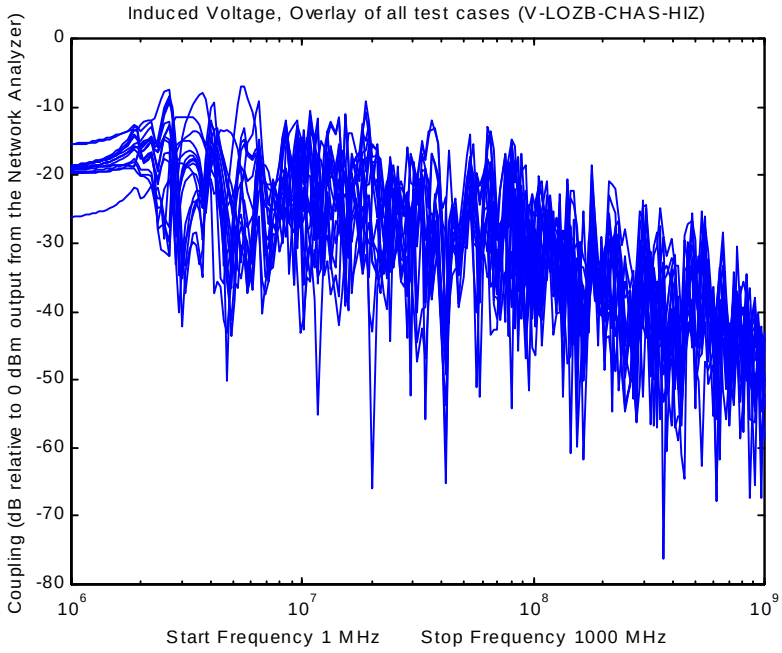

Figure 4.4.5.6-11: Induced voltage-coupling measurements, LO Z COMP (blue) – Chassis excitation.

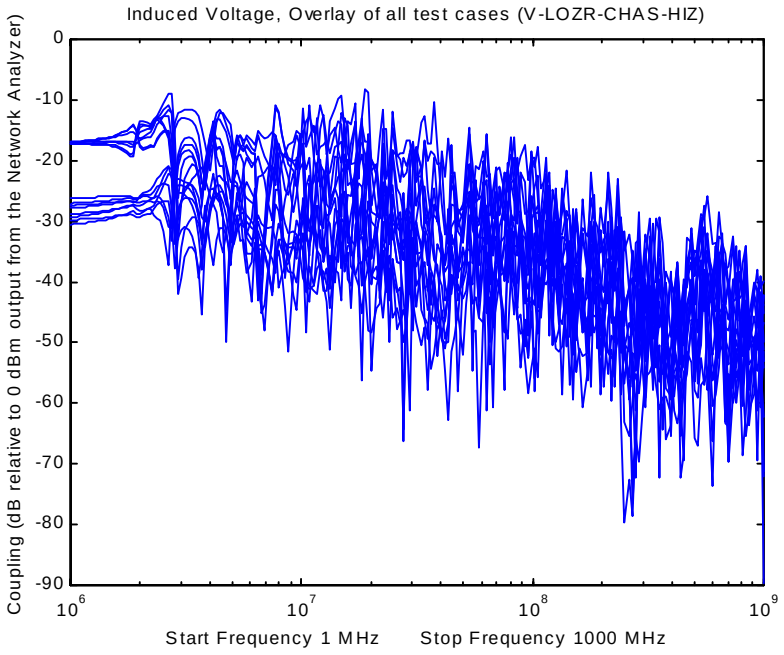

Figure 4.4.5.6-12: Induced voltage coupling measurements, LO Z (red) – Chassis excitation.

4.5 RF Induced Ionization, Discharge, Heating of FQIS Installed in Laboratory Chamber

Since 1967, the U.S. Federal Aviation Administration (FAA) has provided specific guidance for protecting airplane fuel systems against fuel vapor ignition due to lightning, in the form of Advisory Circular 20-53 and subsequent release documents. The preferred means of achieving protection has been to eliminate sources of ignition within aircraft fuel systems. An essential factor is to ensure enough separation of isolated conductors to allow potential differences of thousands of volts, without dielectric breakdown. This practice was evident throughout the CWTs of the retired B-747-100 airplanes observed in New Mexico, and was presumed to be similar to the wiring practice within the TWA-800 CWT.

Because RF signals are harmonically based, they can induce resonant effects upon wiring and fuel quantity probes. More specifically, if a RF signal is applied to the CWT FQIS connector, peak voltages and currents at some locations in the CWT may exceed those present at the input.

The subject of dielectric breakdown in alternating fields becomes rather complex. When the harmonic period of an alternating field becomes shorter than the transit time of gas ions between two conductors, the *Diffusion Theory* of breakdown applies. Diffusion Theory postulates that a field reversal will occur before many of the charged particles are collected at the electrodes, resulting in an increased density of charged particles, which, in turn, causes a field distortion. Depending upon frequency, the minimum breakdown voltage can be reduced by up to 30 to 40 percent [Ref. 4-13]. At even higher frequencies, a resonant situation can develop in which the electron transit time between conductors is comparable to ½ cycle of the applied electric field. When this situation occurs, some electrons collide with conductor surfaces, liberating more electrons just as the electric field passes through zero. The secondary electrons travel back toward the other conductor along with many of the primary electrons that did not collide with the conductor surface. This is known as *multipaction*, and can result in significantly enhanced dielectric breakdown phenomena [Ref. 4-14]. Atmospheric pressures are an effective suppressant against multipaction however, because the electron mean-free-paths are reduced to negligible values (< 0.2μm for nitrogen at 10 km above sea level) [Ref. 4-15]. The TWA-800 accident occurred at about 10,000-ft altitude; therefore, the atmospheric pressure was such that multipaction may essentially be eliminated as a factor for enhancing dielectric breakdown.

Therefore, there are two basic conditions that could contribute to enhanced conditions for electron discharge in the analysis: 1) Resonant enhancements of voltage and current on the CWT FQIS. 2) Alternating field enhancements of ion diffusion lowering the minimum breakdown voltage by 30 or 40 percent.

In this section, data from Section 4.4.5 were used to estimate worst-case voltages and currents that may be induced by a given power level. Experiment setups, instrumentation, and test methodologies that were used to determine whether applied RF power could cause an ionization event or excessive heating are described.

4.5.1 Estimation of CWT Voltage and Current Magnitudes Induced by RF

In Section 4.4.5, methodology and procedures were described to characterize voltages and currents present throughout the FQIS, resulting from various modes of RF excitation over a broad frequency range. When the plots of Section 4.4.5.6 were compared to one another, locations and excitation modes for peak enhancements were found. This comparison, however, said nothing about the magnitude of the enhancements. To determine the magnitude, a reference was required. A suitable reference would appear

to be the point at which power was applied to the FQIS, except it was subject to reflection and reactive effects from the attached circuit. These effects vary as frequency is changed. In fact, voltage and current enhancements due to reflection and reactive effects were exactly what needed to be quantified. The best reference was actually that of a *matched termination*. Such a termination was fabricated with voltage and current measurement points compatible with NASA LaRC voltage and current probes. Calibration reference data were obtained, and are given in Appendix F.

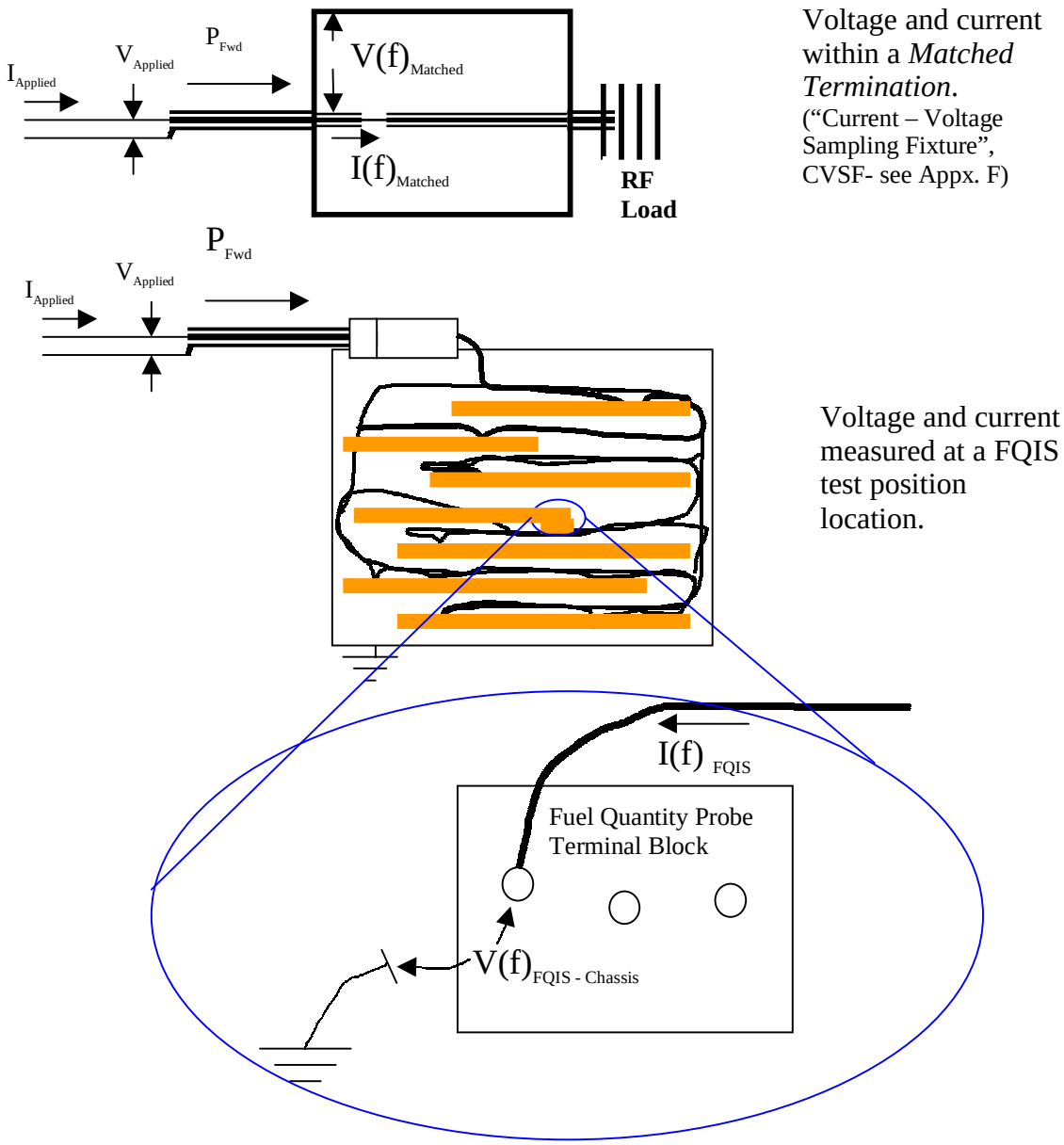

Figure 4.5.1-1: Comparison of voltages and currents for a matched termination versus an FQIS test position location. In this case, a common mode (line to chassis) voltage is depicted for the FQIS test position.

Using Figure 4.5.1-1 as a guide, voltage and current enhancements may be defined as follows:

$$VE(f) = \frac{V(f)_{FQIS-Chassis}}{V(f)_{Matched}} \tag{4.5.1-1}$$

$$CE(f) = \frac{I(f)_{FQIS}}{I(f)_{Matched}} \tag{4.5.1-2}$$

If a given RF signal is applied to the input of either the matched termination or the FQIS input, then:

$$P_{Fwd} = V_{Applied} \times I_{Applied} \tag{4.5.1-3}$$

This equation only addresses the *applied* stimulus. Reflection will affect the total voltage and current magnitudes.

The network analyzer FQIS voltage and current transfer function measurements described in Appendix F can be shown in equation form:

$$FQIS_VTF(f) = VE(f) \times VF_{probe}(f) \tag{4.5.1-4}$$

$$FQIS_CTF(f) = CE(f) \times IF_{probe}(f) \tag{4.5.1-5}$$

FQIS_VTF(f) is equal to the FQIS voltage transfer function, and FQIS_CTF is equal to the FQIS current transfer function, as measured by the network analyzer (S_{21}). VF_{probe} and IF_{probe} are the transfer functions of the respective measurement probes (voltage-voltage, current-current).

A "matched termination" was fabricated, and is described in Appendix F (Current – Voltage Sampling Fixture, CVSF). Its voltage and current transfer measurements can also be represented in equation form:

$$CVSF_VTF(f) = \text{Mismatch Term}(f) \times VF_{probe}(f) \tag{4.5.1-6}$$

$$CVSF_CTF(f) = \text{Mismatch Term}(f) \times IF_{probe}(f) \tag{4.5.1-7}$$

CVSF_VTF(f) is equal to the CVSF voltage transfer function, and CVSF_CTF is equal to the CVSF current transfer function, as measured by the network analyzer (S_{21}). Because the device was not ideal, it presented an impedance mismatch also, however, a network analyzer was used to quantify the Mismatch Terms. Data for the NASA LaRC probes are given in Appendix F.

All measured voltages and currents will be a product of the applied voltages and currents multiplied by the appropriate transfer functions. This relationship can be shown as:

$$VE(f) = \frac{V(f)_{FQIS-Chassis}}{V(f)_{Matched}} = \frac{V(f)_{Applied} \times FQIS_VTF(f)}{V(f)_{Applied} \times CVSF_VTF(f)} \tag{4.5.1-8}$$

$$CE(f) = \frac{I(f)_{FQIS}}{I(f)_{Matched}} = \frac{I(f)_{Applied} \times FQIS_CTF(f)}{I(f)_{Applied} \times CVSF_CTF(f)} \tag{4.5.1-9}$$

All transfer functions and transfer factors were measured in terms of dB, therefore:

$$VE_{dB}(f) = FQIS_VTF_{dB} - CVSF_VTF_{dB} \tag{4.5.1-10}$$

$$CE_{dB}(f) = FQIS_CTF_{dB} - CVSF_CTF_{dB} \tag{4.5.1-11}$$

Data for the worst-case current enhancement point and the two worst-case voltage enhancement points are shown as Figures 4.5.1-2, 4.5.1-3, and 4.5.1-4 below. From these graphs, it can be seen that voltage enhancements of up to 27 dB (~22 times) may occur at some points as compared to those of the 50 Ohm matched input condition.

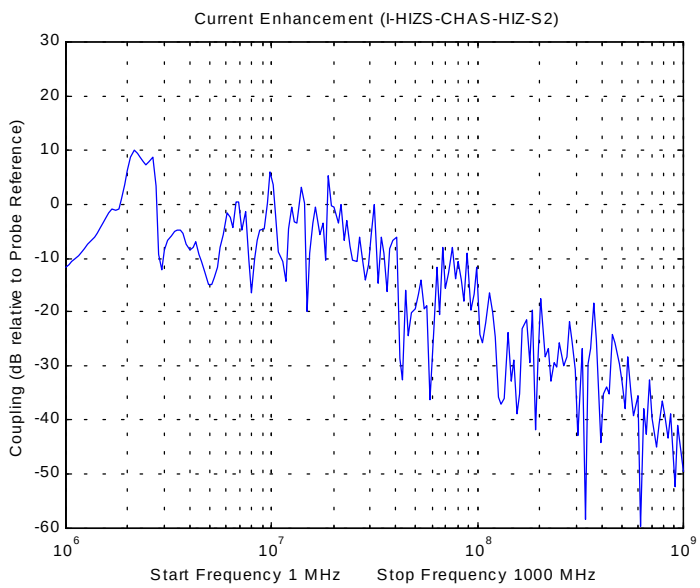

Figure 4.5.1-2: $CE_{dB}(f)$ = {Measured $FQIS_CTF_{dB}$ from HI Z Shield to Chassis at TP-2, when power was applied between HI Z shield and Chassis at the M127 connector} – {$CVSF_CTF_{dB}$}.

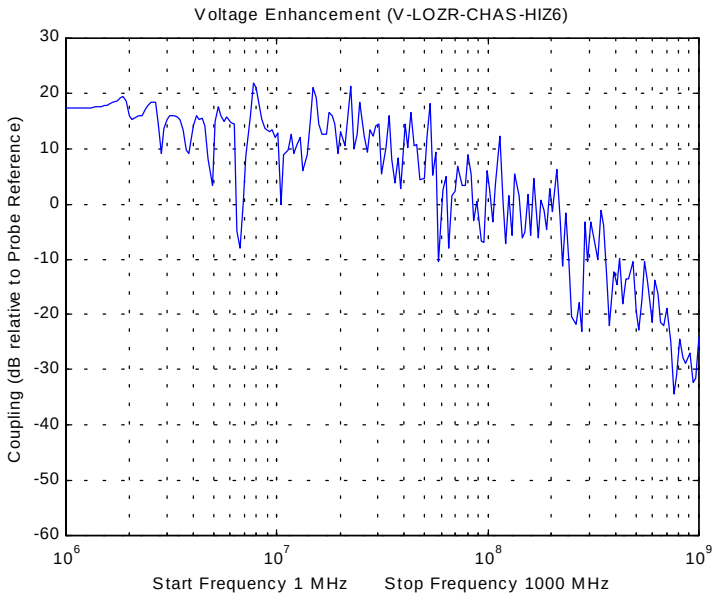

Figure 4.5.1-3: $VE_{dB}(f)$ = {Measured $FQIS_VTF_{dB}$ from HI Z to Chassis at TP-6, when power was applied between the LO Z (red) and Chassis at the M127 connector} – {$CVSF_VTF_{dB}$}.

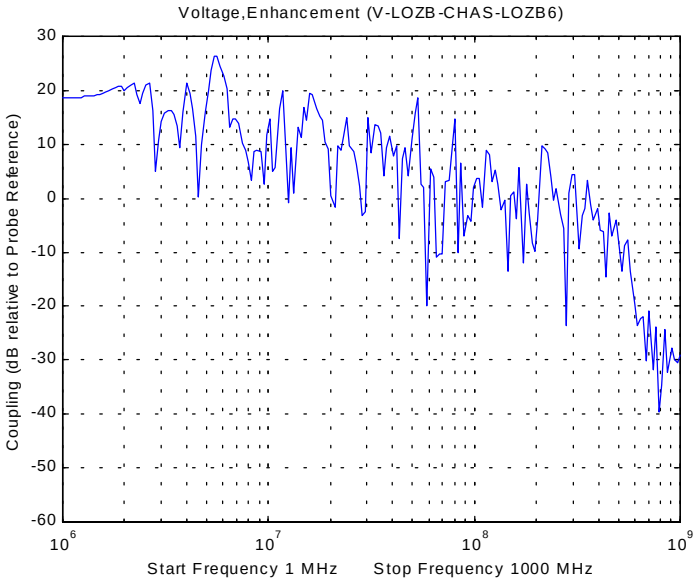

Figure 4.5.1-4: $VE_{dB}(f)$ = {Measured $FQIS_VTF_{dB}$ from LO Z COMP (blue) to Chassis at TP-6, when power was applied between the LO Z COMP (blue) and Chassis at the M127 connector} – {$CVSF_VTF_{dB}$}.

The laboratory RF sources, passive devices and amplifiers used in this testing were designed and calibrated in terms of power delivered to a 50-Ohm resistive impedance. For Z=50 Ohms, the relationship between Power (P) and Voltage (V) is:

$$V = \sqrt{P \times 50} \tag{4.5.1-12}$$

This relationship is plotted in Figure 4.5.1-5. The voltage data multiplied by 22 times are also shown. Because voltage enhancements of 22 times were measured between LO Z COMP (blue) and Chassis at TP-6, voltage as high as 150V (RMS) at TP-6 could be expected with 10 W of applied power at about 550 MHz. (It must be noted that this location and frequency were specific only to the NASA LaRC *laboratory* installation. Frequency and location of maximum voltages will both vary depending upon the specific aircraft installation and fuel level. The *maximum* voltage magnitude should be similar however, because the magnitudes of loss and reactance do not change.)

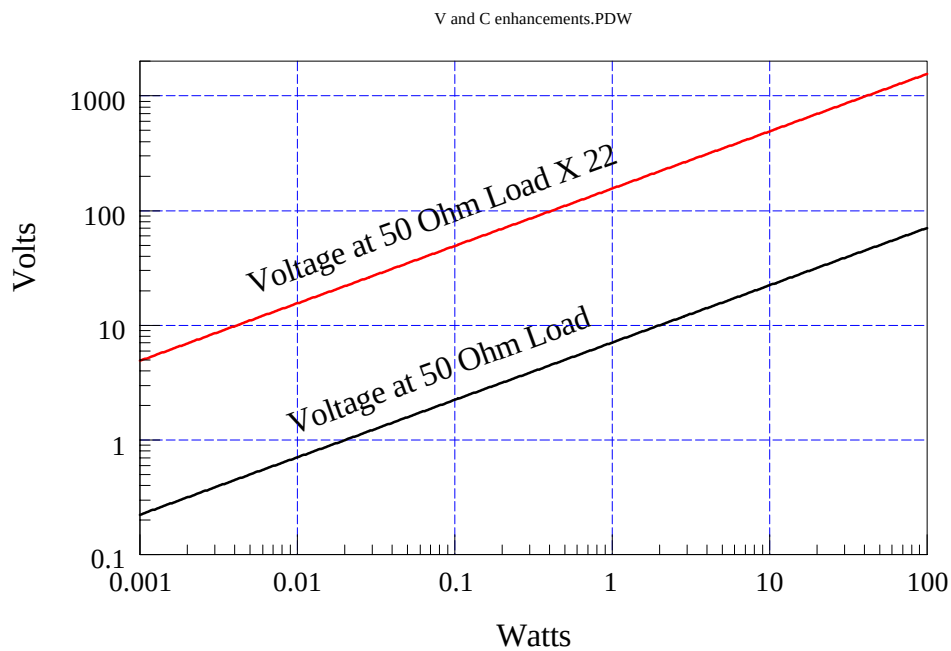

Figure 4.5.1-5: Bottom trace: Voltage versus Power across a 50 Ohm matched load. Top trace: Voltage versus Power across a 50 Ohm matched load X 22. This represents a worst-case bound upon FQIS voltage magnitudes that may be seen with a given input power.

Again, it must be noted that the CWT FQIS connection presented a highly reactive impedance whose magnitude was *not* 50 Ohms, and was usually about 2 or 3 times higher. Higher input impedance magnitudes would result in higher input voltage magnitudes (see Equation 4.5.1-12) at the FQIS connection regardless of whether or not the connection was matched, which would cause the apparent "enhancements" shown in Figures 4.5.1-3 and 4.5.1–4 to be *lower*. It was therefore reasonable to say that the red line ("50 Ohm Voltage X 22") on Figure 4.5.1-5 established a reasonable *worst-case* bound upon the FQIS voltage magnitudes that could be present *somewhere*, with a given input power.

4.5.2 "Weakening" of worst-case test points

From Figure 4.5.1-5, it can be estimated that over 40 W would be required to achieve a worst-case maximum of 1000 V at some point within the CWT. Because the CWT FQIS installation was designed for *thousands of volts* of dielectric-withstand between conductors, it was deemed highly unlikely to expect PED threat level signals to cause dielectric breakdown. (Even with 30 – 40% degradation in dielectric withstand due to alternating fields.) It was decided to extend the testing to include some reasonable fault conditions that could increase the likelihood of dielectric breakdown or localized heating. Two independent fault conditions were introduced, and are described in Figure 4.5.2-1.

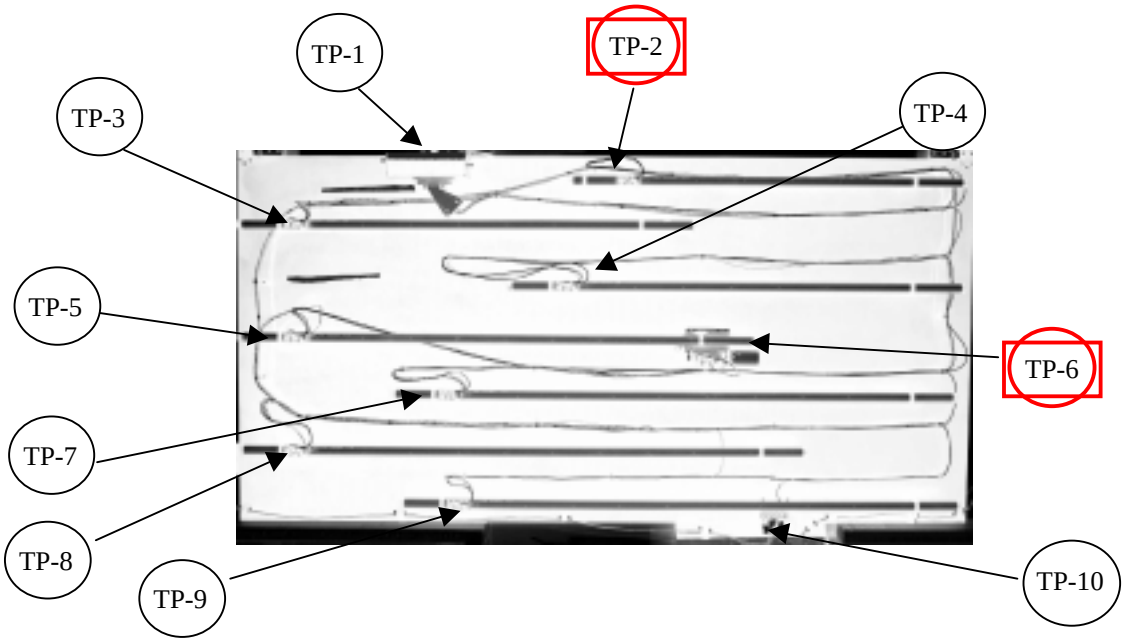

Reduced current carrying capacity at current enhancement location. **TP-2**

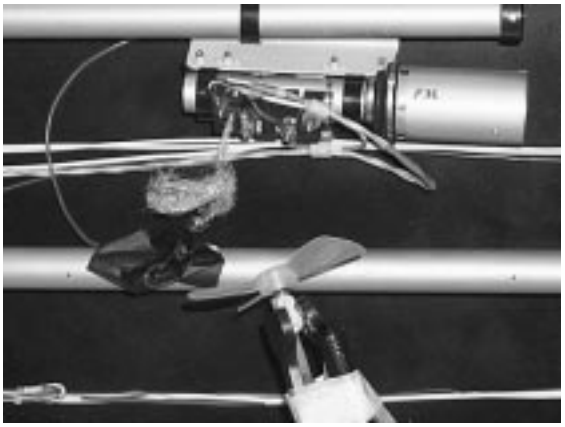

Intermittent short condition at voltage enhancement location. **TP-6**

Figure 4.5.2-1: Introduction of fault conditions to worst-case current and voltage enhancement locations.

4.5.2.1 Reduced Current Carrying Capacity at Current Enhancement Location (TP-2)

The connection of FQIS signal lines to fuel probes was accomplished by crimping "O" lugs onto the bare stranded signal line wires, and securing the "O" lugs to fuel probe terminals. With this termination method, it is sometimes possible that strands of wire can be inadvertently cut when the insulation is removed, or may break due to handling and vibration. When this occurs, the remaining strands will be more resistive than the surrounding conductive path, and can be subject to localized heating as the current is increased. For this test, the HI Z shield pigtail connection to the TP-2 terminal was modified by removing a ½ inch section of all conductive strands except one. When applying RF power between the HI Z shield and Chassis at the M127 connector, this particular location was determined to provide a maximum current enhancement. Any localized heating due to applied RF power could be expected to be most severe at this location.

4.5.2.2 Intermittent Short Condition at Voltage Enhancement Location (TP-6)

To evaluate the potential for a piece of conductive debris to induce an intermittent short condition at some point upon the FQIS, a piece of brass wool was bonded to the supporting structure and made to randomly contact a FQIS probe terminal (by applying forced air through a rotating plastic fan assembly). Two terminals on the compensator probe (TP-6) were determined to provide maximum voltage enhancements. They were the HI Z terminal (when RF power was applied between LO Z (red) and chassis at the M127 connector), and the LO Z COMP (blue) terminal (when RF power was applied between LO Z COMP (blue) and chassis at the M127 connector). An intermittent short at one of these locations could be expected to develop a "break spark" condition with the lowest applied RF power.

4.5.3 Detection Methods

Five different tools were used to monitor for dielectric breakdown and heating events during testing. Each device has unique characteristics in terms of spectral response, sensitivity and directionality. Descriptions and photographs of each are given below. Note that each installation was protected against the effects of the laboratory HIRF environment.

4.5.3.1 Visible Camera

A small "lipstick" size standard video camera is shown in Figure 4.5.3-1. Output from its interface control box was standard NTSC video format. These are commonly used in NASA LaRC's HIRF laboratory for monitoring test articles, and are effective for detecting low-level arc/spark events only if placed a few inches away. The aperture was shielded with a copper screen, and the camera and wiring was protected by a copper tube, with nickel plated copper overbraid shielding the wiring.

4.5.3.2 Infrared Imaging System

An Inframetrics model 600, nitrogen-cooled thermal imaging system was used to detect localized heating events. It was provided and operated by NASA LaRC's Aerodynamic Measurements Branch.

Thermal Imaging System

Visible Light Camera

UVTron

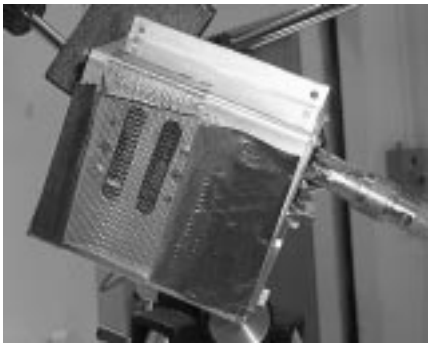

Portable AM Radio

Night Vision System

Figure 4.5.3-1: Detection methods for discharge and localized heating events.

4.5.3.3 UVTron®

A set of ultraviolet detector tubes (manufactured by Hamamatsu) were provided by the Naval Surface Warfare Center, to detect discharge phenomenon. These tubes are extremely sensitive to a narrow range of wavelengths around 200nm, and are essentially unaffected by visible light conditions. Two tubes were housed together and required to detect an ionization event simultaneously before annunciating, to prevent false alarms.

4.5.3.4 AM Radio

Probably the most sensitive device available for detecting discharge phenomena is the household AM radio. For these tests, the ferrite antenna was removed from the radio housing and installed inside the reverberation chamber. Unfortunately, the system was easily upset by relatively low levels of applied EM fields, and was sensitive to electrostatic noise outside the reverberation chamber. It was also unable to localize a source of discharge, but was useful as a supplementary detection device.

4.5.3.5 Night Vision System

Shown in Figure 4.5.3-1 is an AMT MO-32 night vision scope, attached to a standard 8mm camcorder with low-lux capability. This tool was relied upon most in our testing. The scope has a maximum light gain of 65,000 and a field of view of 20 degrees. By using a standard mirror, almost the entire 8ft x 4ft FQIS installation was observable. A small battery powered flashlight provided enough light in the chamber to allow localization of discharge events

4.5.4 Validation of Discharge Detection Devices with Electrostatic Discharge Gun

It was important to confirm that all discharge detection devices could reliably detect spark with less than 0.2 mJ energy released. For this task, a Schaffner NSG 435 Electrostatic Discharge (ESD) simulator gun was used. Such a device is typically used for verifying discharge immunity for consumer products. A schematic diagram of the gun's circuitry is shown in Figure 4.5.4-1. [Ref. 4-17]

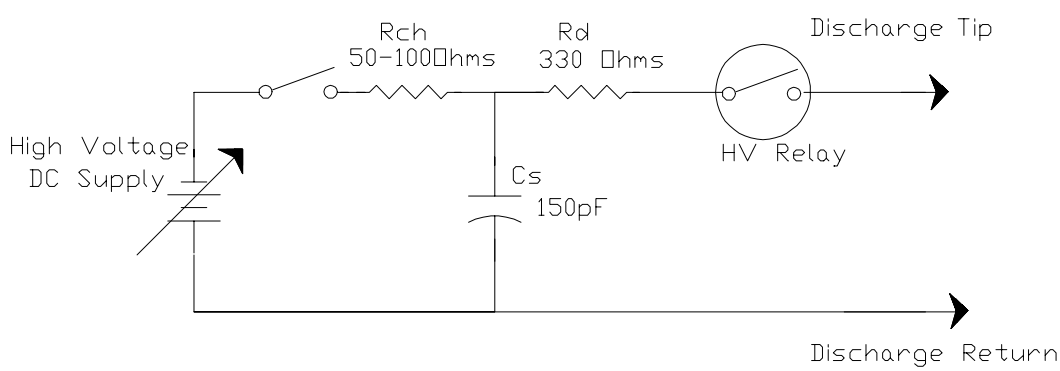

Figure 4.5.4-1: Schematic diagram of electrostatic discharge gun.

When operating, the capacitor (C_s) is charged via an adjustable voltage source (DC), through a charging resistor (R_{ch}). When the voltage across C_s reaches that of the source, the device is ready for discharge.

The total energy stored in the capacitor is given as:

$$\text{StoredEnergy} = \frac{1}{2}CV^2 \tag{4.5.4-1}$$

Upon discharge, all this energy is released via R_d and the spark channel between the Discharge tip and the Discharge return connection. At discharge, maximum power will be transferred to the spark channel if its resistance is equal to R_d=330 Ohms, and the maximum energy released into the spark would be:

$$\text{Maximum Spark Energy} = \frac{1}{4}CV^2 \tag{4.5.4-2}$$

To validate the instrumentation, it was therefore necessary to detect a spark created by a voltage meeting the following equation.

$$V \leq 2.31\,\text{kV} = \sqrt{\frac{4 \times \left(0.2 \cdot 10^{-3}\,\text{Joule}\right)}{\left(150 \cdot 10^{-12}\,\text{Farads}\right)}} \tag{4.5.4-3}$$

The Night Vision System, UVTron and AM radio were all verified and used only in such a way as to reliably detect ESD gun sparks generated with less than 2.31 kV.

4.5.5 "Full" PED Threat Level Test

Originally, three sets of tests were planned, whereby increasing levels of RF power would be applied to the FQIS (using worst-case excitation modes). These tests were termed:

- ***Reduced:*** To simulate the condition of estimated worst-case PED coupling onto FQIS wiring, based upon actual aircraft measurements of maximum induced power from a portable source located anywhere within the passenger cabin.

- ***Full:*** To simulate the condition of the highest power PED, applying power directly from its antenna terminal to the FQIS wiring over the entire frequency band.

- ***Excessive:*** To exceed the condition of a highest power PED, applying power directly from its antenna terminal to the FQIS wiring over the entire frequency band. Power could be increased up to the level of HIRF laboratory capability to establish a margin over any real PED threat.

The *Reduced* threat level test was performed, and did not yield any evidence of discharge or heating, even at the induced fault locations. In addition to conducted excitation, the Reduced threat level test also included a radiated threat element, whereby power was applied to an antenna in the reverberation chamber, at a power level reduced by the passenger cabin coupling factor, but increased by the tank-chamber scale factor.

As noted in Section 1.3.2, the Phase-1 effort required testing to the *Full* test level, without introducing artificial fault conditions. Because of similarity to the Reduced threat level test, and the fact that testing at the Full level was required in Phase-1, setup and results for only the Full threat level test will be provided in this section.

The *Excessive* test level was to be applied only if no arcing/sparking or excessive heating was observed with the Full test level. However, as will be reported in this section, discharge events could be generated with an intermittent short condition when applying the Full test level. Because of the time required to quantify the minimum power required for a discharge event with an intermittent fault (see Section 4.5.6), no Excessive threat level testing was performed.

4.5.5.1 Test Setup

From the PED threat analysis performed in Section 4.3, it was seen that the available power from typical PEDs varies greatly over the frequency range 27 MHz to 6 GHz. Also, as shown in Appendix C.2, the adapter between the FQIS wiring and 50 Ohm RF cable had a mismatch that was non-constant with frequency. In the laboratory, it was possible to adjust the applied power while changing frequency, but instrumentation limitations made this difficult and time-consuming. It was decided that the most effective approach was to determine a worst-case constant for these factors, and select a constant source output level to ensure a *minimum* power level of 10 W was applied to the FQIS wiring across the frequency range 25 MHz to 1 GHz. Instrumentation was configured as shown in Figure 4.5.5.1-1. The sweeping source output power was calculated as follows:

	40.0	dBm	(Highest expected PED threat level. 10 W = 40 dBm)
+	4.0	dB	(Worst-case 50 Ohm source impedance mismatch. See Appendix C.2.)
-	49.3	dB	(Power transfer function from source output, through cabling, amplifier and directional coupler at worst-case PED emission frequency = 27 MHz.)
-	5.3	dBm	(Selected Source Output Level.)

The source was set to sweep from 25 MHz to 1 GHz every 26 seconds. This source setting resulted in FQIS-delivered power ranging from 10 to 30 W, due to amplifier gain variation. Researchers continually monitored the detection devices for evidence of sparking or heating. The intermittent short was applied only between the HI Z terminal and Chassis at TP-6. (The other alternative maximum voltage enhancement location: LO Z COMP to Chassis at TP-6, was not intermittently shorted for the Full level test.) The test was repeated three times, once for each of the following excitation modes:

- HI Z Shield to Chassis
- LO Z COMP (blue) to Chassis
- LO Z (red) to Chassis

(The fourth possible common-mode excitation, HI Z to Chassis, was not tested because it did not result in a maximum voltage or current enhancement, as determined in Section 4.4.5.6.) For each of these excitation modes, the N-Male to Coaxial Socket-Adapter was configured as shown in Figures 4.4.5.3-1 and 4.4.5.4-1.

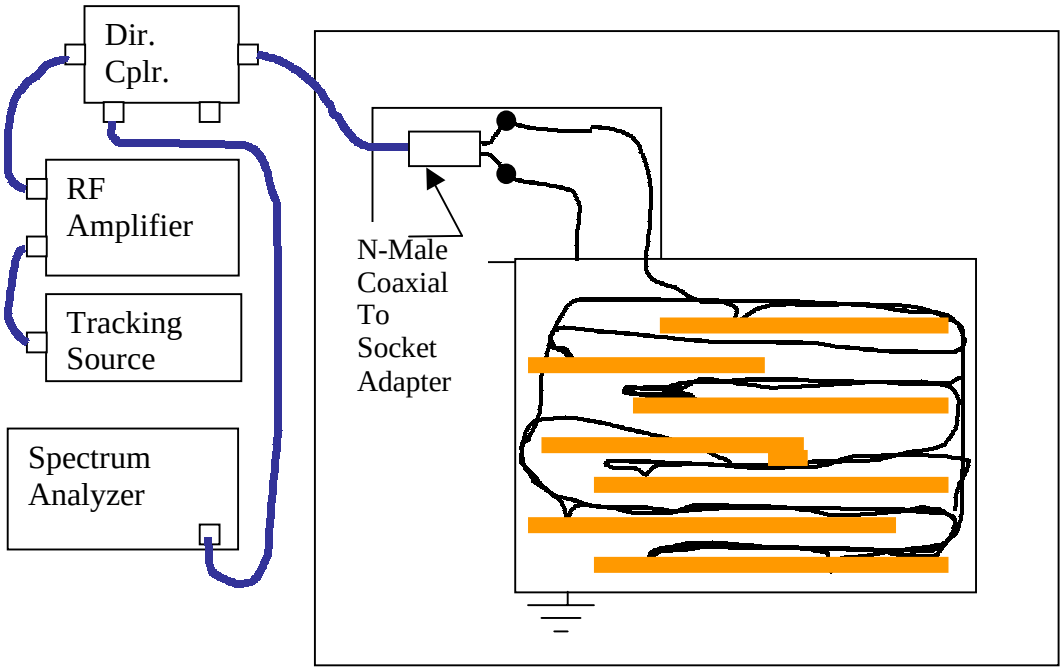

Figure 4.5.5.1-1: Instrumentation setup for "Full" threat level conducted coupling test.

4.5.5.2 Test Results

- HI Z Shield to Chassis Excitation: No discharge events were detected in any location.

- LO Z COMP (blue) to Chassis Excitation: No discharge events were detected in any location.

- LO Z (red) to Chassis Excitation: Sparking *was* detected at the intermittent short condition induced at the TP-6 HI Z terminal. No other locations exhibited detectable discharge events.

The fact that *no other* locations exhibited discharge events was significant because it demonstrated FQIS immunity to applied "Full" PED threat level RF power. This test essentially satisfied the contracted requirement, because the introduction of intermittent fault conditions was not part of the Phase 1 task.

Some localized heating was measured by the thermal imaging system from within the M127 connector shielded box. Temperature increases of about 5 ºF were recorded, and are shown in the imaging system display of Figure 4.5.5.1-2. In this figure, "Area 1" was the location of peak current enhancement (TP-2), and "Area 2" was the location of peak voltage enhancement (TP-6). It can be seen that heating at these locations was negligible.

These results indicated that applying 10 W (or more) RF power directly to the FQIS terminals could not result in discharge or significant localized heating on the CWT FQIS wiring.

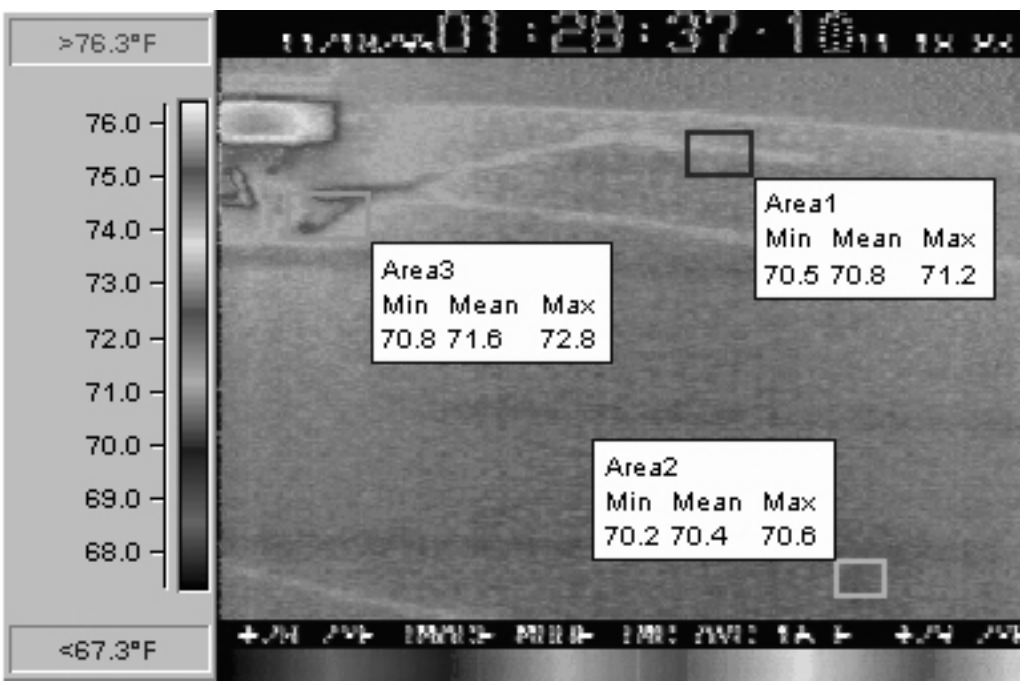

Figure 4.5.5.1-2: Thermal Imager display. For this image, power levels from 24 to 65 W were applied across the LO Z COMP (blue) to Chassis terminals within the M127 connector. Temperature measurement windows were defined at the current enhancement location (TP-2, defined as "Area1"), and at the voltage enhancement location (TP-6, defined as "Area2"). A temperature measurement window was also defined at wires exiting the M127 connector shielded box ("Area3").

4.5.6 Minimum Power for Discharge Test

4.5.6.1 Test Setup

To accurately measure the minimum threshold at which discharge events would occur on the laboratory FQIS installation, a different instrumentation setup was required, and is shown in Figure 4.5.6.1-1.

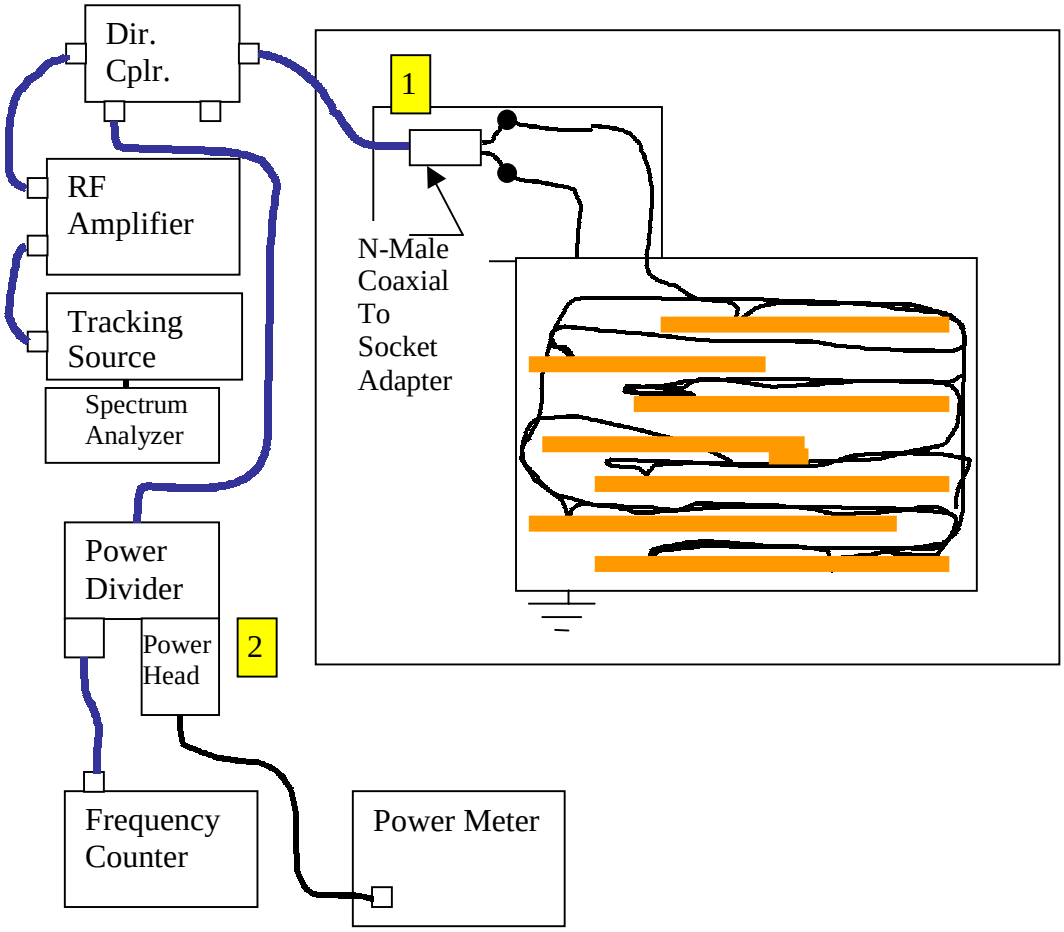

Figure 4.5.6.1-1: Instrumentation Setup for "Minimum Power for Discharge Test".

The night vision detection system was reoriented to focus exclusively upon the intermittent short location (TP-6). The tracking source was repeatedly swept *slowly* across six frequency bands (at increasing power levels) such that readings could be made from the frequency counter and power meter when a discharge occurred. Six frequency bands were defined as follows:

- 1 – 25 MHz
- 25 – 50 MHz
- 50 – 100 MHz
- 100 – 200 MHz
- 200 – 400 MHz
- 400 – 1000 MHz

A calibration was performed to relate power readings at point 1 to point 2, and the 50-Ohm FQIS impedance mismatch loss (from Appendix C.2) was subtracted from the measured power to account for reflections. Two test cases were run, according to the maximum voltage enhancement locations defined by figures 4.5.1-3 and 4.5.1-4.

Excitation at M127 FQIS Connector	Intermittent Short at TP-6 Location
LO Z (red) to Chassis	HI Z to Chassis
LO Z COMP (blue) to Chassis	LO Z COMP (blue) to Chassis

4.5.6.2 Test Results

As would be predicted by figures 4.5.1-3 and 4.5.1-4, somewhat less power was required for generating discharge events at the LO Z COMP (blue) intermittent short location. The testing revealed that an intermittent short circuit could cause FQIS discharge events with as little as 0.17 W of power at frequencies below 10 MHz, when the short was placed at a worst-case location for voltage enhancements. The optimal frequency for generating discharges in the laboratory installation was found to be 6.8 MHz. Figure 4.5.6.2-1 shows each frequency and power level at which a discharge was detected. Figure 4.5.6.2-1 shows a still image of a video-taped discharge event as viewed by the night vision system.

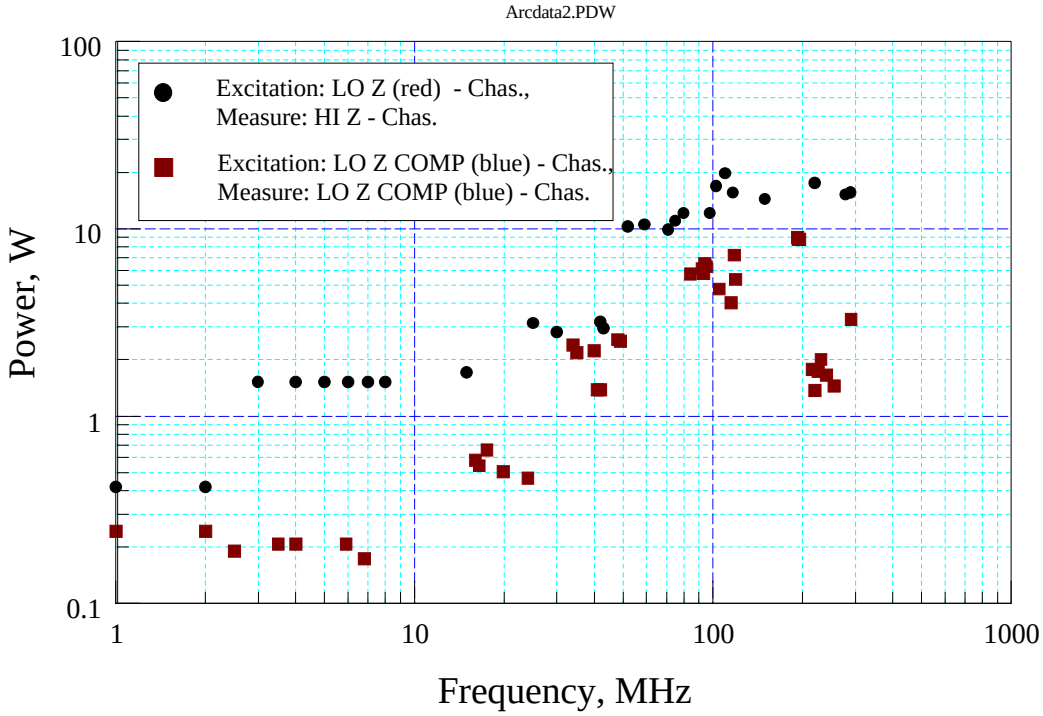

Figure 4.5.6.2-1: Test data showing power required at the FQIS M127 connector for arcing/sparking at location TP-6 in the laboratory installation, with an intermittent short present.

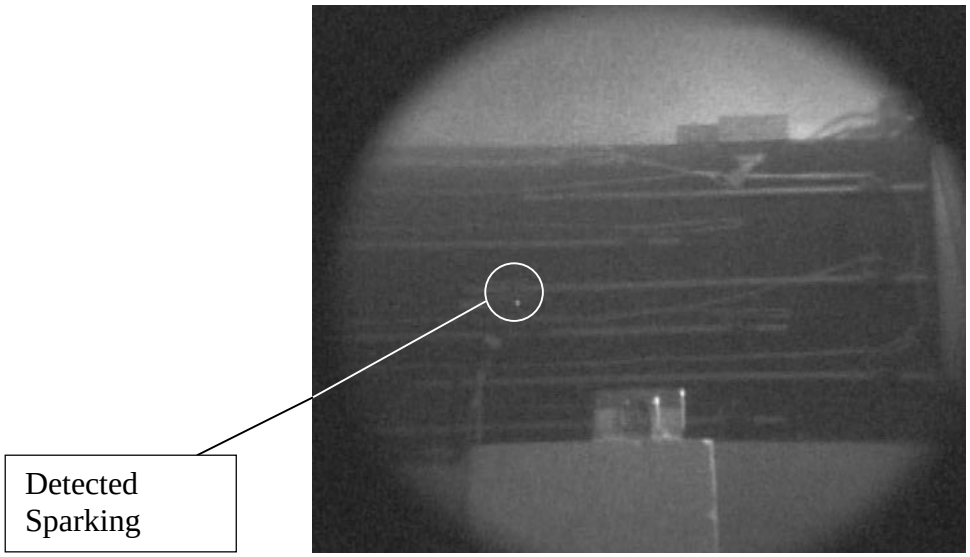

Figure 4.5.6.2-2: Night vision system display showing a discharge event at TP-6. (Note that this image was taken through a mirror, and is therefore reversed.)

Induced fault data was combined with PED threat data (adjusted to account for passenger cabin coupling loss), and the plot of Figure 4.5.6.2-3 was generated. From this figure, it can be seen that a safety margin of about 10 exists between the lowest susceptibility level and the maximum PED threat level. This result indicated that worst-case typical PED RF power could not generate a discharge event on CWT components, even when an intermittent fault condition was present.

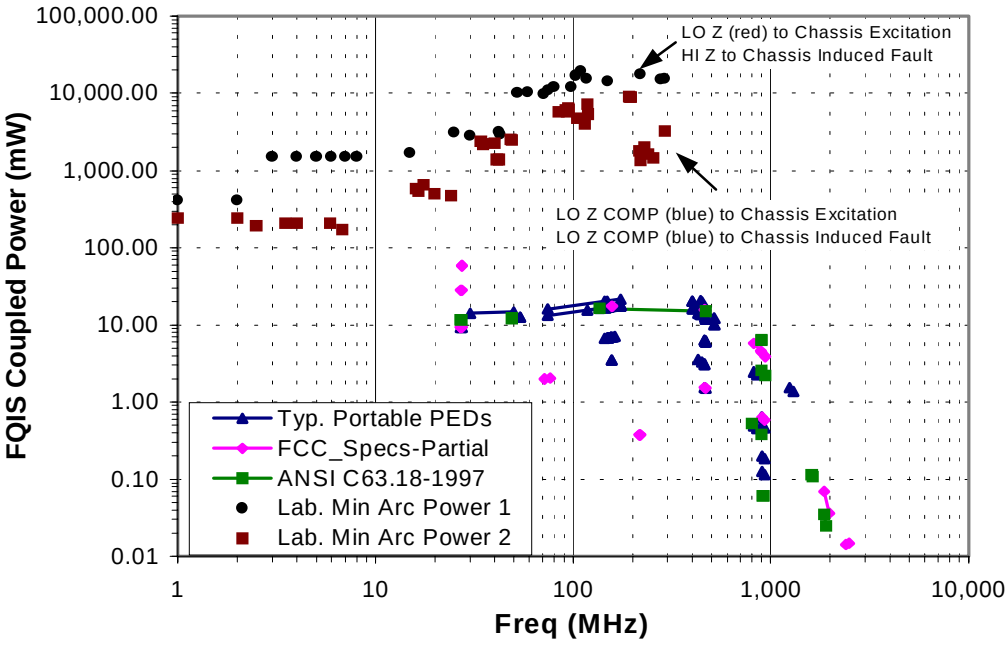

Figure 4.5.6.2-3: FQIS minimum observed arc/spark levels with different excitation and induced faults. Also shown are the adjusted PED threats.

4.5.7 Supplementary Analysis Regarding Threats Below 30 MHz

Early in this investigation, it was determined that all dominant emitters contributing to the TWA-800 EM environment were from pulsed sources operating at over 1 GHz frequency. As a result, the Section 3 analysis applies only to these sources. For the experimental data reported in Section 4.5.6, the laboratory FQIS installation was found to be particularly sensitive to fault-induced arcing below 10MHz, requiring as little as 0.17 W of applied RF power. Most military aircraft, as well as trans-oceanic commercial aircraft are equipped with HF radios that operate between 2 and 30 MHz, and often transmit in excess of several hundred watts. Ground-based, early-warning, over-the-horizon RADAR systems operate between 5 and 28 MHz and can radiate up to 100 MW. It was therefore decided to specifically evaluate whether such transmitters could have been a threat to TWA-800. For this frequency range, the most likely RF source would be the on-board HF radio. However, it is known that the TWA-800 HF radio was not transmitting during its flight. The threat analysis, therefore, needed to consider sources *external* to the aircraft. To assist in this analysis, the JSC provided supplementary data regarding dominant external emitters in this frequency range. In all cases, the transmitters contributing to the (below 30MHz) TWA-800 environment were other airborne HF communication radios. (See Table 4.5.7-1.)

HF Source	Trans. Freq. (MHz)	Trans. Peak Power (kW)	Trans. Ant-enna Gain (dB)	Dist. Xmt / Rcv "Slant Range" (nmi)	Path Loss (dB)	Peak Field Intensity (V/m)	Peak Power Density $\left(\frac{dBm}{m^2}\right)$
USN P-3C BUNO 159319	2.744	1	2.4	2.93	55.92	0.04215	-23.27
USN P-3C BUNO 159319	6.79	1	2.4	2.93	63.78	0.04215	-23.27
USN P-3C BUNO 159319	6.835	1	2.4	2.93	63.84	0.04215	-23.27
USN P-3C BUNO 159319	6.97	1	2.4	2.93	64.01	0.04215	-23.27
USN P-3C BUNO 159319	7.5	1	2.4	2.93	64.65	0.04215	-23.27
USN P-3C BUNO 159319	7.595	1	2.4	2.93	64.76	0.04215	-23.27
USCG WPB-1333 ADAK	7.75	0.2	2.4	5.41	70.26	0.01021	-35.58

Table 4.5.7-1 JSC Data regarding dominant HF emitters. The last 2 columns in this table show the worst-case (highest) EM environment at the TWA-800 explosion location.

Derivation of Maximum Power Intercepted by TWA-800 Aircraft.

For polarization matched antennas aligned for maximum directional radiation and reception, the relationship between received and transmitted power is as follows [Ref. 4-16]:

$$\frac{P_{received}}{P_{transmitted}} = \left(\frac{\lambda}{4\pi R}\right)^2 G_{trans_max} G_{rcv_max} \qquad (4.5.7\text{-}1)$$

Where G_{trans_max} is the maximum gain of the transmitting antenna, G_{rcv_max} is the maximum gain of the receive antenna, R is the distance (*Slant Range*) between antennas, and λ is the wavelength of the transmitted frequency. The JSC data given above assumes orientation of transmitting antennas for maximum gain at the TWA-800 aircraft location. If the aircraft was viewed as an airborne antenna, with optimal alignment and polarization matching the transmitting antenna, Equation 4.5.7-1 describes the maximum power that could have been intercepted. Rearranging the equation:

$$P_{received} = \underbrace{\left[\left(\frac{P_{transmitted}}{4\pi R^2}\right) G_{trans_max}\right]}_{\text{Power Density at Aircraft}} \underbrace{\left[\left(\frac{\lambda^2}{4\pi}\right) G_{rcv_max}\right]}_{\text{Maximum Effective Aperture of Aircraft}} \qquad (4.5.7\text{-}2)$$

Converting the equation to dB,

$$P_{received(dBm)} = \underbrace{\text{Power Density}\,\frac{dBm}{m^2}}_{\text{As reported in JSC Data (Table 6.3-1)}} + \underbrace{10\log\left(\frac{\lambda^2}{4\pi}\right)}_{\text{“Wavelength Factor”}} + \text{Max Airframe Gain}_{dB} \qquad (4.5.7\text{-}3)$$

Where wavelength is related to the transmit frequency (f) by:

$$\lambda = \frac{3 \cdot 10^8}{f} \quad \text{(meters)} \qquad (4.5.7\text{-}4)$$

Again, considering the aircraft as an airborne antenna, its maximum Airframe Gain needed to be estimated. A good bounding estimate was obtained by comparing the aircraft to a dipole wire antenna of the same overall dimension. An actual dipole antenna would have a resistive discontinuity at its midpoint, where all power would be delivered. Because an actual aircraft structure will not deliver all power to a single point, the dipole assumption is very conservative. With a length of about 71 meters and span of about 64 meters, a B-747-100 aircraft could be approximated by dipole lengths ranging from 0.2λ to 7.1λ, when evaluated from 1 MHz to 30 MHz frequency. From Reference 4-16, the maximum gain of a dipole antenna is about 3.3 (5.2dB) at about 1.25λ.

Applying Equation 4.5.7-3 to the data in table 4.5.7-1, and assuming a worst-case maximum Airframe Gain of 5.2 dB, the data shown in table 4.5.7-2 was obtained. Using all the stated worst-case assumptions, it can be seen that the maximum power available in the TWA-800 environment was less than 0.015 W. Even if it was assumed that all RF power available from the 2.744 MHz source was intercepted by the aircraft, and focused at an intermittent short at a worst-case voltage enhancement location in the CWT, there would still be a safety factor of about 11, when compared to the minimum power required for sparking in laboratory testing (0.17 W).

HF Source	Trans. Freq. (MHz)	Peak Power Density $\left(\frac{\text{dBm}}{\text{meter}^2}\right)$ Tbl 4.5.7-1	Wavelength Factor $10\log\left(\frac{\lambda^2}{4\pi}\right)$ (dBmeter^2)	Rcvd. Power $P_{received}$ (dBm)	Rcvd. Power $P_{received}$ (mW)
USN P-3C BUNO 159319	2.744	-23.27	29.782644	11.72	14.843256
USN P-3C BUNO 159319	6.79	-23.27	21.912931	3.85	2.4241409
USN P-3C BUNO 159319	6.835	-23.27	21.855556	3.79	2.392326
USN P-3C BUNO 159319	6.97	-23.27	21.685671	3.62	2.3005509
USN P-3C BUNO 159319	7.5	-23.27	21.049101	2.98	1.9868948
USN P-3C BUNO 159319	7.595	-23.27	20.939771	2.87	1.9375006
USCG WPB-1333 ADAK	7.75	-35.58	20.764292	-9.62	0.1091603

Table 4.5.7-2: Maximum power available to a polarization matched, 1.25λ. dipole antenna at the TWA-800 accident location, aligned for maximum directional radiation and reception from JSC identified HF emitter sources.

4.6 Conclusions for Internal Analysis

In Section 4.3, existing literature resources were used to estimate EM threats from PEDs that may have been present aboard TWA-800. Upon reviewing FCC regulations, manufacturers specifications, and an ANSI standard for evaluating medical devices, it was determined that the most significant PED threats existed between frequencies of 27 MHz and 1 GHz, and were limited to less than approximately 10 W of radiated power.

In Section 4.5, an experimental analysis was used to determine whether RF power emitted from PEDs could cause ionization or excessive localized heating within a B-747-100 CWT. A series of unique and valuable measurements were performed upon two retired B-747-100 aircraft. Detailed CWT data for cavity reverberation, FQIS input impedance, and passenger cabin coupling were collected. A majority of the experimental work involved duplicating the aircraft CWT FQIS installation in a laboratory reverberation chamber, and establishing comparability between the two installations. Once the limitations and scaling factors for this comparability were quantified, detailed laboratory measurements were performed.

The primary laboratory task was to determine whether a discharge event or excessive localized heating could occur if maximum practical PED-threat power levels were applied directly to the CWT FQIS terminals, without introducing artificial fault conditions. A minimum power level of 10 W was applied to the FQIS terminals over a frequency band of 25 MHz to 1 GHz, using all three excitation modes that were experimentally demonstrated to provide maximum voltage and current enhancements. No detectable discharge event was observed on the fault-free FQIS laboratory installation.

A secondary laboratory task was to determine the absolute minimum power required at PED frequencies for a discharge or excessive heating event, when reasonable fault conditions were introduced that could increase the likelihood of dielectric breakdown or localized heating. By inducing an intermittent short circuit at a worst-case location for voltage enhancements, discharge events were induced when applying as little as 1.5 W of RF power at 40 MHz. Considering the passenger cabin to CWT FQIS coupling losses, 1.5 W was at least 10 times greater than the maximum PED threat, even if the PED transmitted from an optimal coupling location in the passenger cabin.

Laboratory testing to determine the absolute minimum power required for a discharge was extended from 25 MHz down to 1 MHz frequency. This testing revealed that an intermittent short circuit could cause FQIS discharge events with as little as 0.17 W of power at frequencies below 10 MHz, when the short was placed at a worst-case location for voltage enhancements. While this finding was unexpected, analysis revealed that the whole TWA-800 aircraft could not have coupled more than 0.015 W of power in this frequency range from the surrounding EM environment at the time of the accident. Commercially available PEDs were determined to be insignificant in terms of radiated power below 25 MHz.

4.7 References for Section 4

[4-1] D. J. Hughes, "Portable Electronic Devices (PEDs) Measured Emission Levels," P1625 E3 Support to the NTSB, 1999.

[4-2] "Solving Difficult Cable Measurements", RF and Microwave Test Seminar, Hewlett Packard Company, 1993.

[4-3] G. Amorese, "RF Impedance Measurement Basics", Back to Basics Seminar, Hewlett Packard Company, 1998.

[4-4] J. Rowell, "Cable Impedance and Structural return Loss Measurement methodologies", Hewlett Packard Company.

[4-5] W. D. Stanley and R. F. Harrington, *Lines and Fields in Electronics Technology*, Prentice-Hall, 1995.

[4-6] Spiegel, M. R., Schaum's Outline Series Theory and Problems of Probability and Statistics, New York: McGraw-Hill, 1975.

[4-7] M. L. Crawford and G.H. Koepke, "Design, Evaluation, and use of a Reverberation Chamber for Performing Electromagnetic Susceptibility/Vulnerability Measurements," NBS Tech. Note 1092, Apr. 1986.

[4-8] "Environmental Conditions and Test Procedures for Airborne Equipment, Radio Frequency Susceptibility (Radiated and Conducted)," RTCA/DO-160D Section 20, July 29, 1997.

[4-9] J. Ladbury, G. Koepke, D. Camell, "Evaluation of the NASA Langley Research Center Mode-Stirred Chamber Facility," NIST Technical Note 1508, Jan. 1998.

[4-10] D. A. Hill, et. al., "Aperture Excitation of Electrically Large, Lossy Cavities," IEEE Trans. On Electromagnetic Compatibility, Vol. 36, No. 3, Aug. 1994.

[4-11] M. O. Hatfield, "Shielding Effectiveness Measurements using Mode-Stirred Chambers: A Comparison of Two Approaches," IEEE Trans. On Electromagnetic Compatibility, Vol. 30, No. 3, Aug. 1988.

[4-12] J. Ladbury, G. Koepke, D. Camell, "Evaluation of the NASA Langley Research Center Mode-Stirred Chamber Facility," NIST Technical Note 1508, Jan. 1998.

[4-13] Antenna Section, NASA Marshall Space Flight Center, "Multipactor Breakdown in Space Electronic Systems", MSFC Internal Note IN-ASTR-71-2, March 12, 1971

[4-14] Hughes Aircraft Company, "The Study of Multipactor Breakdown in Space Electronic Systems", NASA CR-448, July 1966, prepared for NASA Goddard Space Flight Center.

[4-15] CRC Handbook for Chemistry and Physics, CRC Press 63rd Edition, 1982-1983, p. F-163.

[4-16] C. A. Balanis, *Antenna Theory Analysis and Design*, John Wiley & Sons, 1982.

[4-17] User's Manual, Schaffner NSG 435 Electrostatic Discharge Simulator Gun

5 Final Discussion and Overall Conclusions

Aircraft technology is becoming increasingly oriented toward the use of electronic systems. Theories of operation and fundamental components of flight electronic systems are now commonly shared between aircraft and spacecraft, both military and civil. As these electronic systems become more integrated and complex, their designs require more digital circuitry operating at higher frequencies, and at lower power levels. These trends require a continual development of theory, techniques, standards and products to ensure the correct operation of critical electronic systems. These issues are of extreme concern to NASA LaRC researchers.

This investigation provided an investment in tools, techniques, and expertise to be applied to future NASA LaRC activities. Several new analysis and test methods were developed during this effort. A new Modal Analysis/MoM computational EM code was produced for modeling large geometries (such as aircraft) at high frequencies. A methodology for measuring RF impedance of standard aircraft wiring was developed, and a statistical method for comparing impedances was applied. An efficient technique for measuring peak coupling from the aircraft passenger cabin to FQIS wiring was also developed and applied. Several existing technologies were applied to the problem of detecting various spectral signatures of dielectric breakdown and resistive heating in a HIRF environment.

It was determined that the existing open literature reflects a very limited understanding of RF hazards to fuel. Engineers at the NSWC provided insight into military guidelines and documents regarding this issue. The experts at LTI provided valuable information regarding the issues of sparks, combustion processes, and RF threats to fuel. Discussion of these issues was published under separate cover [Ref. 1-6] .

In Section 1, it was stated that the goal of this investigation was to study the potential for RF sources to have excited the TWA-800 FQIS enough to cause arcing, sparking or excessive heating within the CWT. In Section 2, the FQIS and aircraft systems were described from the viewpoint of an EM system. Subsequently, the analysis branched off into two different directions: *computational* for the external source (HIRF) problem, and *experimental* for the internal source (PED) problem. The external and internal source efforts were completely reported in Sections 3 and 4, respectively, and conclusions were given. In order to tie the entire NASA LaRC investigation together, conclusions for the external and internal analyses are restated and discussed in this section.

5.1 Results of External Analysis

Using the maximum field strengths from signal sources identified by the JSC as dominant emitters, the maximum energy available inside the aircraft passenger cabin for each source was estimated using simple formulas. These dominant emitters were all pulsed sources, allowing the threat to be quantified in terms of energy, instead of power. The total available energy inside the aircraft cabin from the maximum dominant emitter (f= 2.875 GHz) was found to be less than 0.1 mJ. Even if this total energy could have been focused into a single discharge event, it was still below the generally accepted estimate of the minimum energy level (0.2 mJ) required to achieve ignition.

To provide a more accurate estimate of how much energy could actually be coupled to the FQIS wiring within the passenger cabin from external sources, numerical modeling was used. The B-747-100 fuselage was assumed to be a large rectangular cavity with rectangular windows on each side. The cavity was assumed to be homogeneous and lossless, with no seats or other structures present. A new, NASA-LaRC developed numerical simulation technique, using a rectangular cavity Green's function and the

integral equation method, estimated EM threats to the CWT due to external EM sources. The Modal/MoM code was validated through agreement with other analytical techniques and measurements. The Modal/MoM approach resulted in a lower number of unknowns compared to other numerical methods, such as the FEM and FDTD methods. Therefore, this new method was able to solve the large-size problems up to frequencies of 1-2 GHz. When applied to the available energy from the 1.294 GHz emitter source, the Modal/MoM approach estimated that CWT FQIS coupled energy levels were several orders of magnitude ($(1 \text{ to } 30) \times 10^{-4}$) less than the maximum available energy.

5.2 Results of Internal Analysis

In Section 4.3, existing literature resources were used to estimate EM threats from PEDs that may have been present aboard TWA-800. Upon reviewing FCC regulations, manufacturers specifications, and an ANSI standard for evaluating medical devices, it was determined that the most significant PED threats existed between frequencies of 27 MHz and 1 GHz, and were limited to less than approximately 10 W of radiated power.

In Section 4.5, an experimental analysis was used to determine whether RF power emitted from PEDs could cause ionization or excessive localized heating within a B-747-100 CWT. A series of unique and valuable measurements were performed upon two retired B-747-100 aircraft. Detailed CWT data for cavity reverberation, FQIS input impedance, and passenger cabin coupling were collected. A majority of the experimental work involved duplicating the aircraft CWT FQIS installation in a laboratory reverberation chamber, and establishing comparability between the two installations. Once the limitations and scaling factors for this comparability were quantified, detailed laboratory measurements were performed.

The primary laboratory task was to determine whether a discharge event or excessive localized heating could occur if maximum practical PED-threat power levels were applied directly to the CWT FQIS terminals, without introducing artificial fault conditions. A minimum power level of 10 W was applied to the FQIS terminals over a frequency band of 25 MHz to 1 GHz, using all three excitation modes that were experimentally demonstrated to provide maximum voltage and current enhancements. No detectable discharge event was observed on the fault-free FQIS laboratory installation.

A secondary laboratory task was to determine the absolute minimum power required at PED frequencies for a discharge or excessive heating event, when reasonable fault conditions were introduced that could increase the likelihood of dielectric breakdown or localized heating. By inducing an intermittent short circuit at a worst-case location for voltage enhancements, discharge events were induced when applying as little as 1.5 W of RF power at 40 MHz. Considering the passenger cabin to CWT FQIS coupling losses, 1.5 W was at least 10 times greater than the maximum PED threat, even if the PED transmitted from an optimal coupling location in the passenger cabin.

Laboratory testing to determine the absolute minimum power required for a discharge was extended from 25 MHz down to 1 MHz frequency. This testing revealed that an intermittent short circuit could cause FQIS discharge events with as little as 0.17 W of power at frequencies below 10 MHz, when the short is placed at a worst-case location for voltage enhancements. While this finding was unexpected, analysis revealed that the whole TWA-800 aircraft could not have coupled more than 0.015 W of power in this frequency range from the surrounding EM environment at the time of the accident. Commercially available PEDs were determined to be insignificant in terms of radiated power below 25 MHz.

5.3 Notes and Applicability

- Subsequent versions of the B-747 included additional shielding on the FQIS system to mitigate interference from other aircraft systems. This practice will tend to increase the safety margin from EMI from non-aircraft systems as well.

- This effort focused exclusively on coupling and the potential for ionization/heating caused by FQIS components within the CWT, as the system was excited by non-aircraft generated EM signals. Existing reports indicate that such signals were far more likely to interfere with, and even damage, sensitive aircraft navigation sensors, displays, processors, and communication equipment.

- A parallel effort conducted by NAWCAD was focused on the susceptibility of the FQIS to induced energy by aircraft-generated (B-747-100) electrical transients to ignite the fuel. The results of their effort are not included in this report.

Appendix A: Definition of Terms

The following definitions are provided to assist the reader in understanding some of the terminology used within this document. It is not intended to be an exhaustive list, nor are the definitions guaranteed to be applicable outside the scope of this report.

admittance -The ratio of effective current to effective voltage in a circuit carrying an alternating current. It is the reciprocal of impedance.

ampere -[A] The ampere is the basic unit of electric current. It is that current which produces a specified force between two parallel wires which are one meter apart in a vacuum.

amplitude -The extreme range of a fluctuating quantity such as an alternating current, generally measured from the average or mean to the extreme.

angle of incidence -The angle that an electromagnetic wave striking a surface makes with a line perpendicular to the surface.

antenna -A device for transmitting and receiving radio waves. In radio transmission a radiating antenna is used to convert a time-varying electric current into an electromagnetic wave or field, which freely propagates through a non-conducting medium such as air or space. Depending on their use and operating frequency, antennas can take the form of a single piece of wire, a dipole, a grid (such as a yagi array), a log periodic, a horn, a helix, a parabolic-shaped dish, or a phase array of active electronic elements upon virtually any flat or convoluted surface.

aperture -An opening or gap through which electromagnetic energy may pass. A cross sectional area of an antenna which is exposed to the electromagnetic signal.

arcing -The band of sparks or incandescent light formed when an electric discharge is conducted from one electrode or conducting surface to another, characterized by relatively high current and low potential difference between electrodes.

attenuation -A reduction in power or signal strength of an electrical source. The loss in power of electromagnetic signals between transmission and reception points.

attenuation factor -The amount by which a signal is reduced in power or strength.

bandwidth -The range of frequencies within a radiation band required to transmit a particular signal. The range of frequencies occupied by a modulated radio-frequency signal. A measure of spectrum (frequency) use or capacity.

calibration -Setting and measuring an instrument against known standards before measuring for accurate results.

calibration standards -A set of devices whose electrical characteristics are well known and traceable to national standards. The devices are used to establish a measuring instrument's operating baseline and enhance measurement accuracy.

capacitance - The charge-storing ability of an electrical capacitor, defined as the magnitude of charge

stored on either plate divided by the applied voltage.

characteristic impedance -(Z_o) The impedance of a circuit that, when connected to the output terminals of a uniform transmission line of arbitrary length, causes the line to appear infinitely long. A uniform line terminated in its characteristic impedance will have no standing waves, no reflections from the end, and a constant ratio of voltage to current at a given frequency at every point on the line.

conductivity - The proportionality constant between current density and applied electric field; a measure of the ease with which a material is capable of conducting an electric current.

coupling (general electromagnetic) -The cause and effect relationship between two electromagnetic entities. Electromagnetic entities include electron flow, electric field and magnetic field.

dielectric - Any material that is electrically insulating.

dielectric constant - A relative measurement of the degree of polarization (shift of positive charge toward the negative electrode and negative charge toward the positive electrode) that occurs when a material is placed in an electric field. The relative measure of the ability of a material to store an electric charge.

dynamic range -A term used to describe signals that are undergoing changes in amplitude across a frequency band. Dynamic range has to do with the range between the extremes of amplitude of an RF signal. Typically bounded by the noise floor at the lower extreme and the peak signal at the upper extreme.

electric arc -Continuous, high-density electric current between two separated conductors in a gas or vapor with a relatively low potential difference, or voltage, across the conductors.

electric field -The region around an electric charge in which an electric force is exerted on another charge. Instead of considering the electric force as a direct interaction of two electric charges at a distance from each other, one charge is considered the source of an electric field that extends outward into the surrounding space.

Electric Field Shielding -(EFS) A logarithmic ratio of the external electric field to the internal electric field of a given structure such as an aircraft fuselage. The value is expressed in decibels and quantifies the shielding effectiveness of the structure.

Electromagnetic Environment -(EME) The sum total of all electromagnetic fields and the associated frequencies, power levels, and polarizations in a given or defined region. The electromagnetic environment is comprised of man-made and natural sources of electromagnetic energy and can be very complex.

Electromagnetic Interference -(EMI) Electromagnetic energy that tends to interfere with the transmission or reception of desired signals.

energy - In physics, energy is the capacity for doing work. It may exist in potential, kinetic, thermal, electrical, chemical, nuclear, or other various forms, and be transformed from one form to another. Electromagnetic energy is expressed in units of work, such as joules or kilowatt-hours.

farad -[F] The farad is the SI unit of the capacitance of an electrical system, that is, its capacity to store electricity. It is a rather large unit as defined and is more often used as a microfarad.

Finite Difference Time Domain -(FDTD) a computational method used in obtaining approximate solutions to partial differential equations in complex electromagnetic models.

fourier transform -A particular integral transform useful in harmonic analysis and the representation of periodic functions such as electromagnetic waves.

frequency -The number of times that an alternating current goes through its complete cycle in one second of time. One cycle per second is also referred to as one hertz; 1000 cycles per second, one kilohertz; 1,000,000 cycles per second, one megahertz: and 1,000,000,000 cycles per second, one gigahertz.

gigahertz -(GHz) One billion cycles per second. Signals operating above 3 GHz are known as microwaves, above 30 GHz they are known as millimeter waves. As one moves above the millimeter waves, signals begin to take on the characteristics of lightwaves.

hertz -[Hz] The hertz is the SI unit of the frequency of a periodic phenomenon. One hertz indicates that 1 cycle of the phenomenon occurs every second. For most work much higher frequencies are needed such as the kilohertz [kHz] and megahertz [MHz].

HIRF Environments - High power electromagnetic fields designated as High Intensity Radiated Fields or High Intensity Radio Frequencies that exists in a defined environment particularly in the vicinity of high power radar sites, broadcast antennas, and other high power RF sources.

impedance -The total opposition offered by an electric circuit to the flow of an alternating current of a single frequency; it is a combination of resistance and reactance and is measured in ohms.

incident wave - Electromagnetic radiation in the form of a plane wave propagating through space and then acting upon a surface or material, at which point energy may be reflected by the surface or material, transmitted through the material, absorbed by the material, or otherwise scattered by the surface or material.

input impedance -The impedance presented at the input of a circuit, connector, or electrical system.

isotropic antenna -A hypothetical omni-directional point-source antenna that serves as an engineering reference for the measurement of antenna gain.

joule -[J] The joule is the SI unit of work or energy. One joule is the amount of work done when an applied force of 1 Newton moves through a distance of 1 m in the direction of the force.

ohm -The ohm is the SI unit of resistance of an electrical conductor. It is equal to the resistance of a circuit in which a potential difference of one volt produces a current of one ampere.

plane wave -An electromagnetic wave whose corresponding crests and troughs that at any instant are in phase and propagates through space as a plane, rather than as a sphere of increasing radius.

polarization - Property of radiated electromagnetic fields, whereby the direction and magnitude of the

harmonically oscillating electric field are related in a specified way.

portable electronic devices -(PEDs) An entire class of personal consumer electronic devices that are small, light-weight, and typically carried with the individual for use wherever the person may travel. Examples include but are not limited to laptop computers, cellular telephones, pagers, electronic games, digital assistants, radios, etc.

power -The time-rate of doing work or delivering energy, expressible as the amount of work done W, or energy transferred, divided by the time interval t--or W/t. The electrical unit of power is the Watt.

reactance -The measure of the opposition that a circuit or a part of a circuit presents to electric current insofar as the current is varying or alternating. Steady electric currents flowing along conductors in one direction undergo opposition called electrical resistance, but no reactance. Reactance is present in addition to resistance in alternating current circuits.

reflected wave -Abrupt change in the direction of propagation of a wave that strikes the boundary between different mediums. At least part of the oncoming wave disturbance remains in the same medium.

resistance -The property of an electric circuit or part of a circuit that transforms electric energy into heat energy by opposing electric current. Resistance involves collisions of the current-carrying charged particles with fixed particles that make up the structure of the conductors.

resolution –The ability to distinguish detail, usually expressed in terms of the size or magnitude of the smallest features that can be distinguished.

resonant frequency -The frequency at which an electrically conducting pathway containing both inductive and capacitive elements will presents a low impedance to an alternating current. The specific frequency of resonance is determined by the values of the circuit inductance and capacitance.

reverberation chamber -An electrically large, highly conductive, RF shielded enclosed environment used to measure electromagnetic compatibility, emissions, and immunity of electrical and electronic devices.

RMS current -In alternating current circuits, the root-mean-square or effective current.

RMS voltage -In alternating current circuits, the root-mean-square or effective voltage.

signal generator or signal source -Electronic test instrument that delivers an accurately calibrated signal at frequencies from the audio to the microwave ranges. It is valuable in the development and testing of electronic hardware. The signal generator provides a signal that can be adjusted according to frequency, output voltage, impedance, waveform, and modulation.

spectrum - The range of electromagnetic radio frequencies used in transmission of voice, data, television, etc., Any particular distribution of wavelengths and frequencies.

transmitter -An electronic device consisting of oscillator, modulator and other circuits which produce a radio or other electromagnetic wave signal for radiation into the atmosphere by an antenna.

volt -[V] The volt is the SI unit of electric potential. One volt is the difference of potential between two points of an electical conductor when a current of 1 ampere flowing between those points dissipates a power of 1 watt.

VSWR -Voltage Standing Wave Ratio: A measurement of mismatch in a cable, waveguide, or antenna system.

watt -[W] The watt is used to measure power or the rate of doing work. One watt is a power of 1 joule per second.

waveguide -Any of a class of devices that confines and directs the propagation of electromagnetic waves, such as radio waves. Waveguides take many shapes and forms. Typical examples include hollow rectangular metallic tubes, coaxial cables, and horns.

Appendix B: Comparison of CWT Cavity Q with and without the Antennas

The relationship between the cavity Q without the antennas, the cavity Q with the antennas, and the Q of the antennas (two antennas in the CWT) is shown in the expression below.

$$\frac{1}{Q_{(without_antennas)}} = \frac{1}{Q_{(with_antennas)}} - \frac{2}{Q_{(antenna)}} \tag{B-1}$$

The Q's of the cavities (with or without the antennas) are based on actual measurements in the CWT. The Q's due to the antennas are theoretical values for a lossless and matched antenna, which provide an upper bound on the cavity loading by any antenna. More details about theoretical Q of an antenna can be found in Reference B-1. Figure B-1 shows the effects of the presence of the antennas in the CWT.

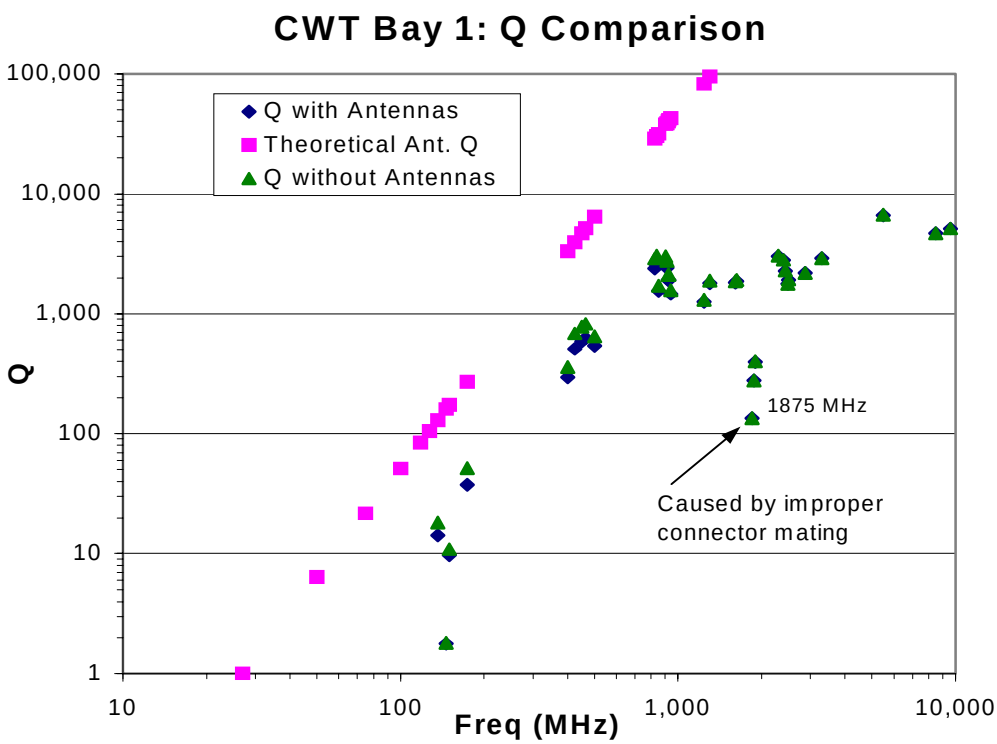

Figure B-1: Cavity Q's, with and without the two antennas, for CWT bay 1. Little effect on the cavity Q caused by the presence of the measuring antennas is observed.

References for Appendix B

[B-1] D. A. Hill, et. al., "Aperture Excitation of Electrically Large, Lossy Cavities," IEEE Trans. On Electromagnetic Compatibility, Vol. 36, No. 3, Aug. 1994.

Appendix C: Mismatch Correction for Out-of-Band Antenna and 50 Ohm Cable Adapter

C.1 Mismatch Correction for Antenna Used Out-of-Band:

If the transmit antenna is used out of band, a numerical scale factor can be applied to the measured data to simulate the in-band transmit antenna condition. This correction factor accounts for antenna mismatch by correcting for the reflected power only. It does not correct for changes in antenna gain or efficiency. The scale factor is computed as

$$\text{ScaleFactor} = \frac{1}{1-\Gamma^2} \quad , \qquad \text{(C-1)}$$

where Γ is the magnitude of the antenna free space reflection coefficient. The scale factor for the transmit antenna is shown in the chart below.

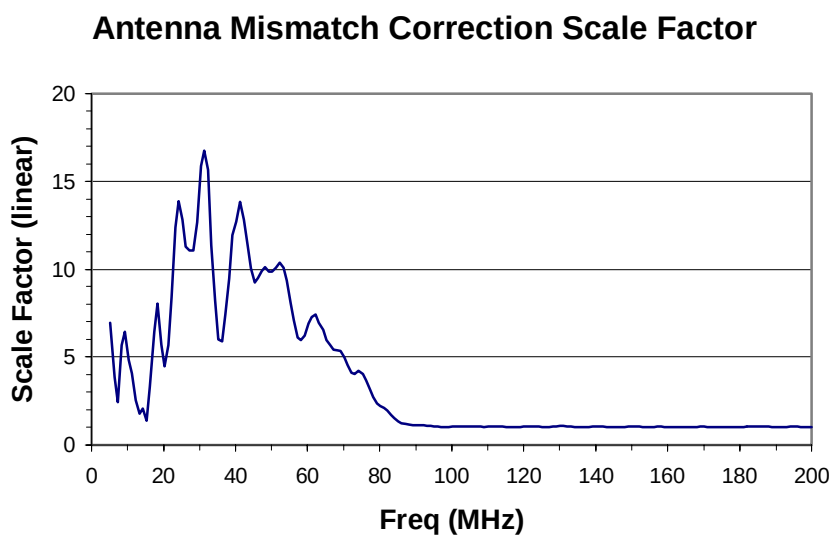

Figure C.1-1: Antenna mismatch correction scale factor

C.2 Mismatch Correction for the Adapter between the FQIS Wiring and 50 Ohm RF Cable

To measure RF power on the FQIS wiring, a custom adapter was fabricated to allow mating between the FQIS wiring to the standard 50 Ohms connector with an N-type adapter. This custom adapter created a mismatch, causing some RF power to be reflected, resulting in inaccurate reading at the power measuring device. The goal was to estimate the power on the FQIS wiring before reaching the adapter.

Assuming the adapter was lossless, the scale factor to apply to the power reading at the spectrum analyzer to correct for the mismatch caused by the adapter was as follows:

$$\text{ScaleFactor} = \frac{1}{1-\Gamma_a^2}, \tag{C-2}$$

$$\text{ScaleFactor(dB)} = 10\log\left(\frac{1}{1-\Gamma_a^2}\right) \quad , \tag{C-3}$$

where Γ_a is the magnitude of the reflection coefficient due to the adapter only. It should be the same whether measured from the FQIS wiring side or from the RF cable side. This fact can be derived using reciprocity for a lossless system.

The trick is how to measure the reflection coefficient due to the adapter only, not of the system. This measurement was accomplished by using a network analyzer to transform the reflection coefficient data from the frequency domain to the time domain. The procedure involves gating out in time domain all other reflections and retaining only those reflections caused by the adapter, then transforming the gated results back to the frequency domain to obtain the desired results. This time-gating technique is very common in network analyzer measurement techniques.

The mismatch correction scale factor in dB for up to 1 GHz is shown in Figure C.2-1 for the Passenger Cabin to the FQIS measurement.

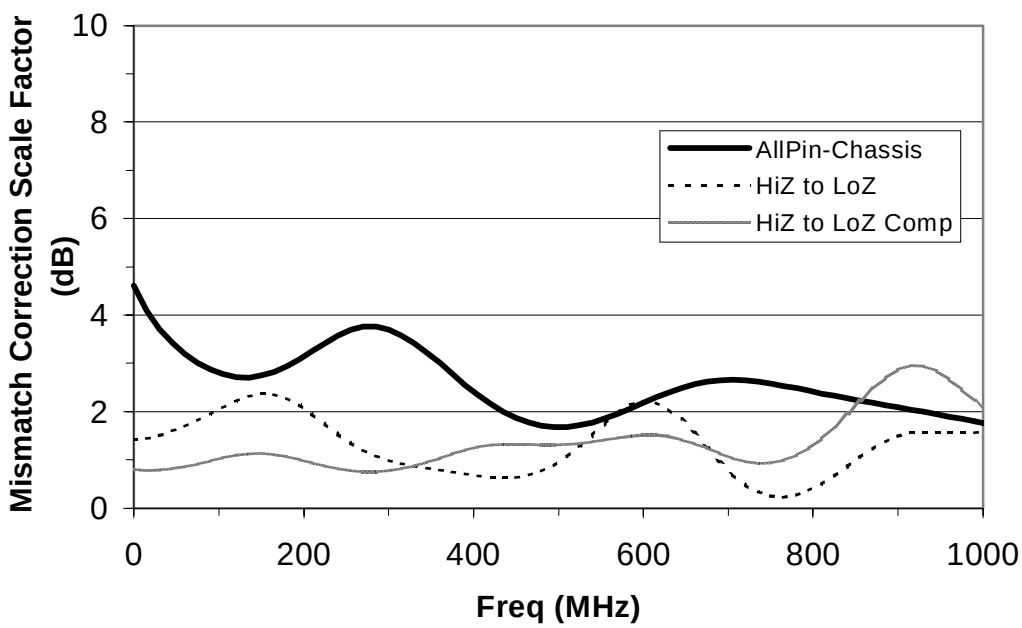

Figure C.2-1: Cable mismatch correction factor.

Appendix D: FQIS Impedance Measurement Theory

D.1 Characteristic Impedance for Aircraft Systems

Impedance is the ratio of the voltage divided by the current in an alternating current circuit. It is the total passive opposition offered to the flow of electric current. Impedance is determined by the particular combination of resistance, inductance, and capacitance in a given circuit. Impedance is a function of frequency, except in the case of purely resistive networks. It is not a property of energy dissipation, but when the circuit, cable, or transmission line is considered lossy, impedance is a real number and dissipation occurs.

$$\overline{Z} = \text{Voltage Wave / Current Wave} \qquad \text{(D-1)}$$

Characteristic impedance ($\overline{Z}_0$) is the impedance of a circuit that, when connected to the output terminals of a uniform transmission line of arbitrary length, causes the line to appear infinitely long. A uniform line terminated in its characteristic impedance, will have no standing waves, no reflections at the end, and a constant ratio of voltage to current at a given frequency at every point on the line. [Ref. D-1]

Characteristic impedance defines the electrical capabilities and operational environment of cable and wiring systems like the aircraft FQIS. Basic electrical properties, such as, resistance, inductance, and capacitance, which are all part of impedance help define the operational properties. It is the electrical "fingerprint" of a cable.

Impedance is a complex mathematical function with real and imaginary components. The equation that defines impedance in complex mathematics is:

$$\overline{Z} = R + jX \quad , \qquad \text{(D-2)}$$

where the letter Z stands for impedance, the real part, R, is the resistance and the imaginary part, X, the reactance. If X is positive, it is called inductive reactance. If X is negative, it is called capacitive reactance. The letter j is the complex descriptor representing the square root of negative one. It defines the phase relationship between resistance and reactance.

The impedance measurement plane can be visualized with the real element, or resistance, on the x-axis and the imaginary element, or reactance, on the y-axis. Capacitors are typically found in the lower half-plane, while inductors are in the upper half-plane. The more ideal an inductor or a capacitor the less resistive it will be.

The values of characteristic impedance typically range from about 50 Ohms to 75 Ohms for coaxial type cable and from about 300 Ohms to 600 Ohms for parallel lines. Special design applications may also range in values from 100 to 200 Ohms for certain shielded pairs. [Ref. D-2]

D.1.1 Measurement Considerations

Impedance cannot be directly measured like voltage. Impedance measurements at radio frequencies (RF) are especially challenging. Engineering trade-offs sometimes have to be made when selecting the best measurement technique for any specific situation. Impedance is the most common measurement performed to determine a cable or wiring network's electrical characteristics. Because RF impedance measurements are challenging, it is important to consider three factors during the measurement design

process before conducting measurements of this kind.

First, one must consider and select an appropriate technique to use to make impedance measurements. Second, if there are any special fixtures or adapters needed to connect to the system one desires to measure, then they need to be acquired or designed and constructed. Third, calibration and compensation techniques should be employed to insure sensible and accurate results.

Perhaps the most important criteria for selecting a measurement technique is the frequency range of interest. Some methods are better suited for low frequency measurements while other methods are more broadband in frequency. One must also consider the expected or anticipated range of impedance values the system may have. Some techniques are limited to the measurement of low values of impedance and others are limited to the measurement of relatively high value impedances. The required measurement accuracy also factors into measurement technique. Increased accuracy is usually directly related to cost and time. However, operator skill and attention to detail can go a long way in improving measurement accuracy. Still, there are physical limitations inherent to all instrumentation that cannot be overcome. These limitations need to be understood and taken into account when considering accuracy and measurement uncertainty. The test conditions are another important consideration when conducting measurements. Measurements in a laboratory environment can be quite different from measurements at a remote field location in the desert. Environmental factors such as temperature, pressure, and humidity can effect instruments and computers. Climate and meteorological factors such as wind and rain can effect measurements as well as the operations and logistics at remote locations. Time itself can also be considered a test condition and must be considered a factor. The measurement parameters of what one needs to measure, such as impedance, and any additional parameters to augment the measurement such as return loss, insertion loss, gains, other scattering or S-parameters and data formats should be considered. Finally, it is very important that the physical characteristics of the system to be measured are well understood and taken into consideration prior to conducting measurements. [Ref. D-3]

D.1.2 Theoretical Impedance of Aircraft Wiring

The electrical wiring typically encountered in the aviation industry can be generalized into three main categories; coaxial, paired, flat, and fiber optic. The physical characteristics of these cable types vary considerably. However, their general purpose is to transmit power or signals from one system to another. The FQIS of the B-747-100 is a combination of coaxial cables, wired pairs, or single wires above a ground plane. Cross sections of these types are depicted in the Figures D.1-1, D.1-2, and D.1-3.

Cable impedance in a coaxial cable at radio frequencies is primarily a function of the physical dimensions and dielectric quality of the cable. As previously defined, cable impedance is the ratio of the voltage to current of a signal traveling in one direction down a cable. For a coaxial cable, the value of the impedance will depend upon the ratio of the inner and outer conductor diameters and the dielectric constant of the material between the inner and outer conductors. The material parameters are defined by the equation,

$$\eta = \sqrt{\frac{\mu}{\varepsilon}} \quad , \qquad \text{(D-3)}$$

where, η is the intrinsic impedance for the material involved,
μ is the permeability of the material, and
ε is the permittivity of the material.

Then, the characteristic impedance for a lossless coaxial cable (see Figure D.1-1) is given by,

$$Z_0 = \sqrt{\frac{\eta}{2\pi}} \ln\left(\frac{b}{a}\right). \tag{D-4}$$

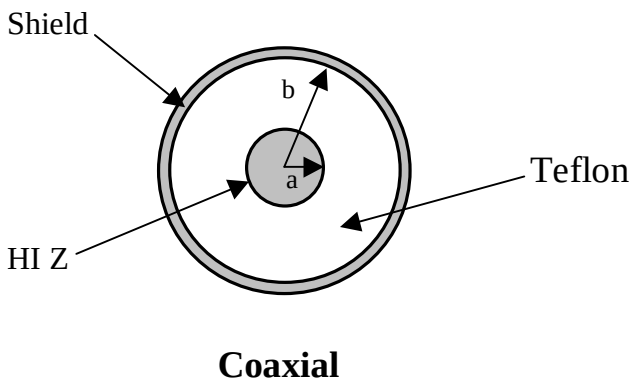

Figure: D.1-1: Cross Section of a Coaxial Cable

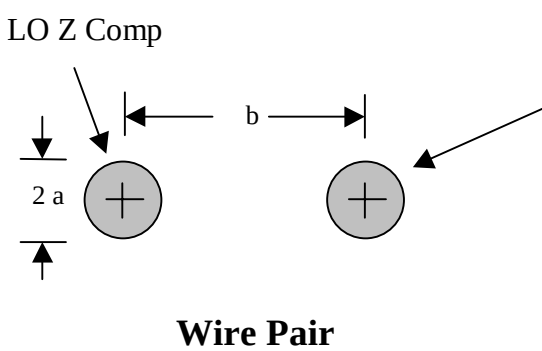

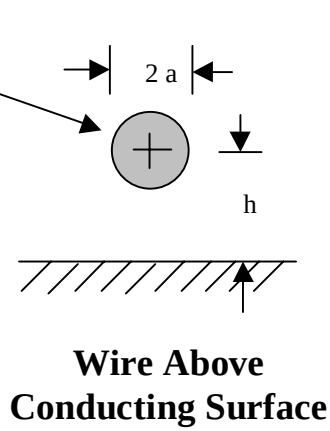

Figure D.1-2: Wire Pair Cross Section

Figure D.1-3: Single Wire above Ground Plane

Impedance of a wire pair or a single wire above a ground plane is primarily a function of the

geometry. The wire or wires diameter, distance separating wires and ground planes, and the dielectric value associated with the separation distance all factor into impedance values. The dielectric value is typically the value for the air that fills the separation space. But, in more complex models and in reality the dielectric material filling a space will not only include air, but also teflon and other plastic wire insulation materials. The wire could also be imbedded or submerged in some other gas, fluid, or solid rather than air. These material changes can have significant effects on wired systems impedance.

Again, once the material parameter is defined, the characteristic impedance for a lossless wire pair (see Figure D.1-2) is given by,

$$Z_0 = \sqrt{\frac{\eta}{\pi}} \cosh^{-1}\left(\frac{b}{2a}\right), \tag{D-5}$$

and the characteristic impedance for a lossless wire above a perfectly conducting surface (see Figure D.1-3) is,

$$Z_0 = \sqrt{\frac{\eta}{2\pi}} \cosh^{-1}\left(\frac{h}{a}\right). \tag{D-6}$$

The value of the conductivity will affect the impedance to the extent that RF signals do not travel on the surface of the conductor, but propagate into the conductor by what is known as skin depth. The finite conductivity also causes losses that increase with RF frequency and can change the effective cable impedance. Also, the construction of the cable can change along the length of the cable with differences in conductor thickness, dielectric material, and outer conductor diameter changing due to limitations in manufacturing. Thus, cable impedance can vary along the length of the cable. [Ref. D-4]

Cable impedance is a specification that is defined only at a discrete point along the cable and at a discrete frequency. However, when commonly referred to, the impedance of the cable is some average of the impedance over the frequency of interest. For the purposes discussed, cable impedance is the average impedance presented at the input of the D3 – M127 connector interface of the CWT over the frequency span from 300 kHz to 1000 MHz.* These are the frequencies, based on surveys, where present PED threats are most likely to occur.

This can be represented as:

$$Z_{avg} = \int_{f_{\min}}^{f_{\max}} \frac{Z_{in}(f)}{(f_{\max} - f_{\min})} df, \tag{D-7}$$

where Z_{in} is the input impedance, and
f is discrete frequency.

******During the measurements additional impedance data was taken from 1 GHz to 3 GHz to augment the computational team's study of high frequency external threats.*

D.2 Measurement Methodology and Technique

Specifications associated with any cable depend upon both the specification definitions and the measurement methodology.

There are several measurement techniques available for conducting impedance measurements. These included the Auto Balancing Bridge method, a current-voltage probe technique, an RF variant of the current-voltage probe, Frequency Domain Network Analysis, and Time Domain Network Analysis. These methods vary a great deal in complexity, frequency response, and accuracy depending on the system to which they are applied. For the purposes of measuring the aircraft system described in this report, it was determined through laboratory research that the Frequency Domain Network Analyzer method would be most suitable for impedance characterization of the FQIS internal to the CWT. This method is also known as the fixed bridge method.

D.2.1 The Bridge Method

The fixed bridge method of impedance measurements is a technique for measuring characteristic impedance using a vector network analyzer and its associated S-parameter test set, a set of calibration standards, and a mathematical technique for emulating a variable bridge. The calculations give the average impedance of the cable and compensation for adapters and connectors to the system under test.

The fixed bridge method with the network analyzer, S-parameter test set, calibration standards, and connector compensation has several advantages. These advantages include minimization of cable mismatch, rapid measurements, very wide frequency range, better directivity provided by the test set, excellent repeatability, calibration enhanced accuracy, and automation that allows the operator to focus on measurement results rather than measurement technique.

The only limitations of the technique involve the conversion of reflection data to impedance values. Many modern network analyzers, such as the HP 8752A that was used, can do the conversions within their own internal processors. An external computer can also be used to perform the mathematical conversion, if required. The other limitation is that the characteristic impedance of a network analyzer test set is typically 50 Ohms. Therefore, any and all measurements are referenced to 50 Ohms. The technique provides very good accuracy if the system under test has an impedance around 50 Ohms, but accuracy is sacrificed away from this central impedance. Nevertheless, the network analyzer method is more than acceptable for impedance values that range between 9 and 600 Ohms. [Ref. D-3]

D.2.2 Basic Theory of Operation

The vector network analyzer fixed bridge method is a reflection measurement technique. An incident wave of RF energy is transmitted or injected into a device or SUT, and the reflection back from the device under test due to the incident wave is measured. The ratio of the reflected wave to the incident wave is called the reflection coefficient (or Γ, gamma). This is shown pictorially in Figure D.2-1. The reflection coefficient is directly related to impedance, and can be manipulated mathematically to give a value for impedance. The network analyzer does this while precisely stepping its signal source through a range of frequencies, thus measuring a unique reflection coefficient and calculating an impedance value for every frequency in the established range. The system under test in this case was the aircraft FQIS internal to the CWT. [Ref. D-5]

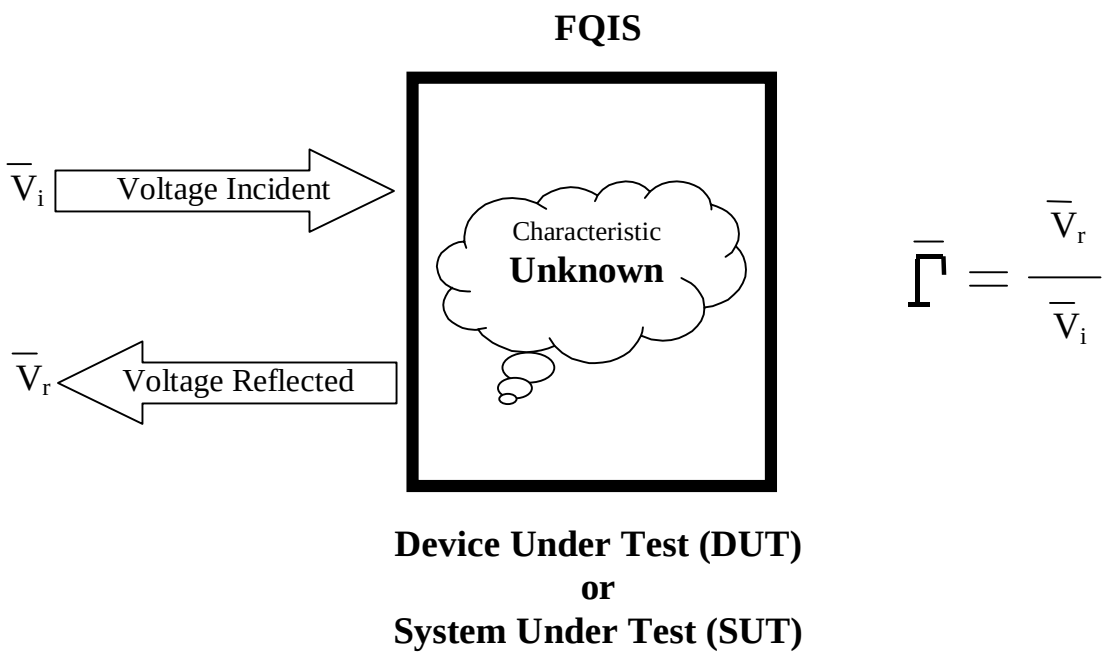

Figure D.2-1: Diagram of the Basic Theory of Reflection Measurements

D.3 References for Appendix D

[D-1] J. Rowell, "Cable Impedance and Structural Return Loss Measurement Methodologies", Hewlett Packard Company.

[D-2] W. D. Stanley, and R. F. Harrington, *Lines and Fields in Electronics Technology*, Prentice-Hall, 1995.

[D-3] "Solving Difficult Cable Measurements", RF and Microwave Test Seminar, Hewlett Packard Company, 1993.

[D-4] D. Roddy, and J. Coolen, *Electronic Communications*, 3rd Edition, Prentice Hall, 1984.

[D-5] G. Amorese, "RF Impedance Measurement Basics", Back to Basics Seminar, Hewlett Packard Company, 1998.

Appendix E: Statistical Analysis of Transmission Line Impedance Using the Smith Chart

This appendix provides an overview of the Smith Chart related to its use in this report. The reflection coefficient will be defined, and the relationship between the reflection coefficient and impedance will be discussed. The Smith Chart will then be introduced as a coordinate transformation of the reflection coefficient. The basic principals of the Smith Chart are described with illustrated examples. Plots showing the reflection coefficient and the corresponding Smith Chart impedance plot will be described. Finally, the use of statistics coupled with Smith Charts will be discussed.

E.1 Reflection coefficient

The reflection coefficient conveys how well the impedances of two transmission media are matched. The efficient transfer of radio frequency (RF) energy from one location to another may require a transmission medium to contain the energy. By examining a system using coaxial transmission lines to transfer RF energy, an intuitive feel for the concept of reflection can be gained. In general, the best coaxial cable is selected to minimize the reflection of energy back to the source. However, if a damaged coax is inadvertently selected, the damage in the coax cable will cause energy that was intended to reach the transmission destination to be reflected back to the source. This reflection will degrade the intended receive signal.

$$\overline{\Gamma} = \frac{incident_voltage_wave}{reflected_voltage_wave} \tag{E.1-1}$$

$$\overline{\Gamma} = \frac{\overline{Z}_L - \overline{Z}_o}{\overline{Z}_L + \overline{Z}_o} = \Gamma_R + j\Gamma_i = \Gamma_{abs}\angle\theta_\Gamma \tag{E.1-2}$$

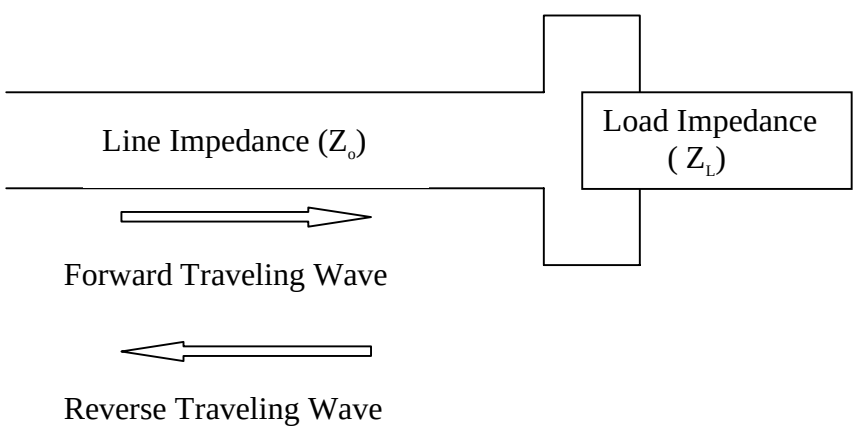

Figure E.1-1: Impedance diagram showing line impedance and load impedance.

Equation E.1-1 and E.1-2 describe the reflection coefficient ($\overline{\Gamma}$) [Ref. E-1]. The reflection coefficient is defined [Ref. E-1] as the ratio of the forward traveling wave to the reflected wave (see Figure E.1-1). The reflection coefficient is also defined in terms of the impedance of the transmission line ($\overline{Z_o}$) and the impedance of the load connected to the line ($\overline{Z_L}$). As shown in Equation E.1-2, the reflection coefficient is in general complex; therefore, it can be written as a real part (Γ_R) and an imaginary part (Γ_I), or in polar form as a magnitude (Γ_{abs}) and phase (Θ_Γ).

These concepts are easily described in an example. By assuming a loss-less transmission line with a characteristic impedance of 50 Ohms hooked to a complex load impedance of 111.8 ∠63.4°, the reflection coefficient can be calculated. Equation E.1-3 shows this calculation. The complex reflection coefficient is calculated to be 0.707∠45°. Figure E.1-2 shows this value plotted on a polar chart.

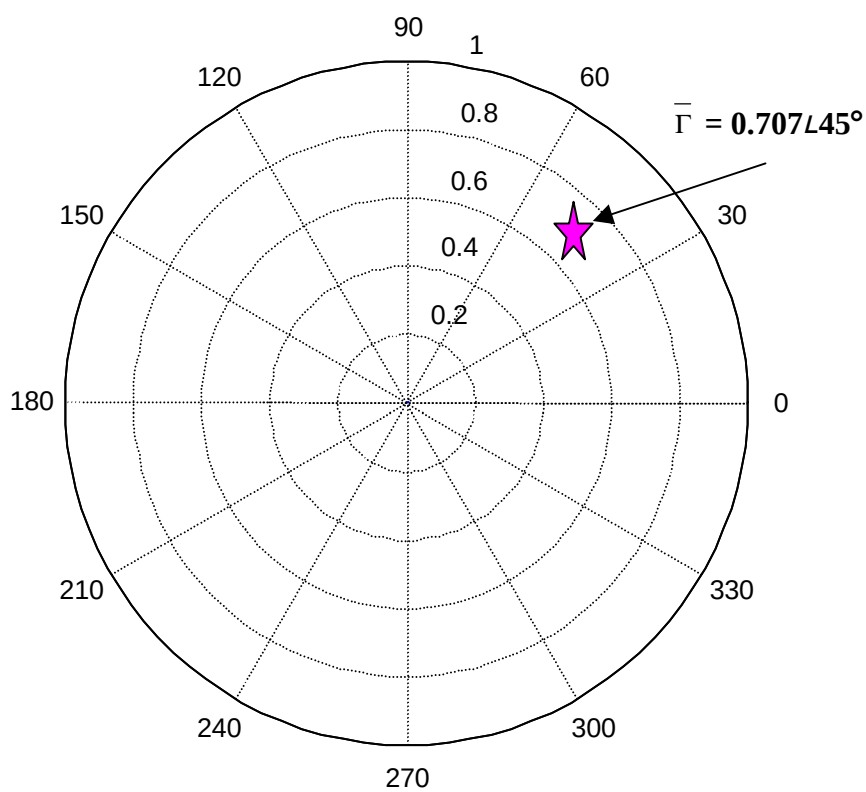

Figure E.1-2: Reflection coefficient plotted on a polar chart.

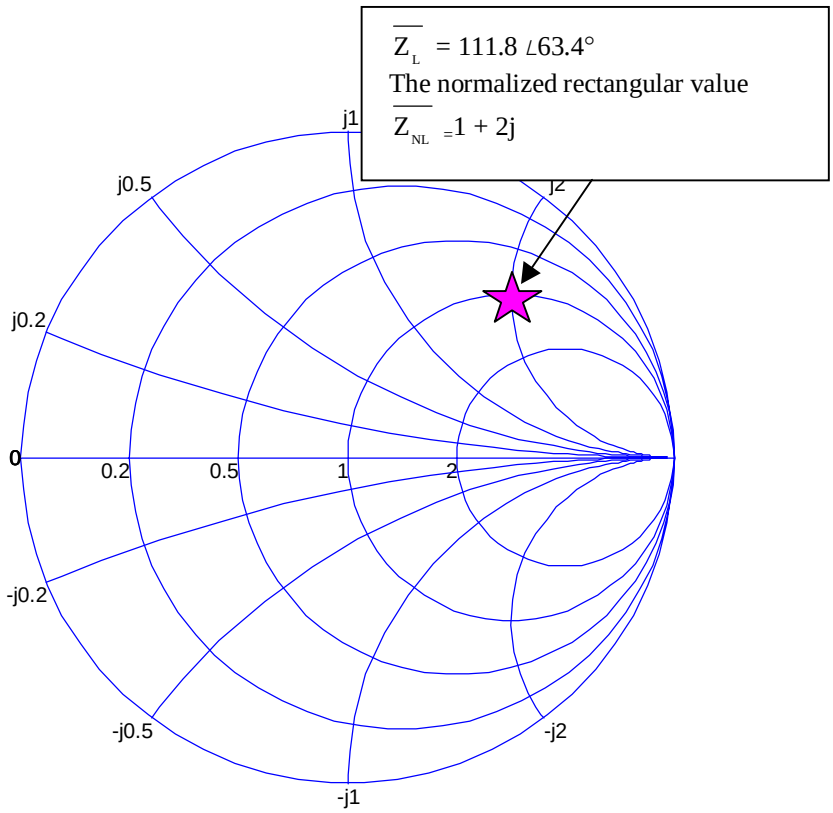

Figure E.2-1: Impedance value plotted on a Smith Chart.

$$\overline{\Gamma} = \frac{\overline{Z}_L - \overline{Z}_o}{\overline{Z}_L + \overline{Z}_o} = \frac{111.8\angle 63.4 - 50}{111.8\angle 63.4 + 50} = \Gamma_R + j\Gamma_i = 0.5 + 0.5j = \Gamma_{abs}\angle\theta_\Gamma = \frac{1}{\sqrt{2}}\angle 45^\circ \qquad \text{(E.1-3)}$$

E.2 Relationship between Impedance and the Reflection coefficient

For a given system impedance (Z_o = 50 Ohms), Equation E.1-3 can be rearranged to solve for the load impedance ($\overline{Z}_L$) [Ref. E-1].

$$\overline{Z_L} = \overline{Z}_o\left(\frac{1+\overline{\Gamma}}{1-\overline{\Gamma}}\right) \qquad \text{(E.2-1)}$$

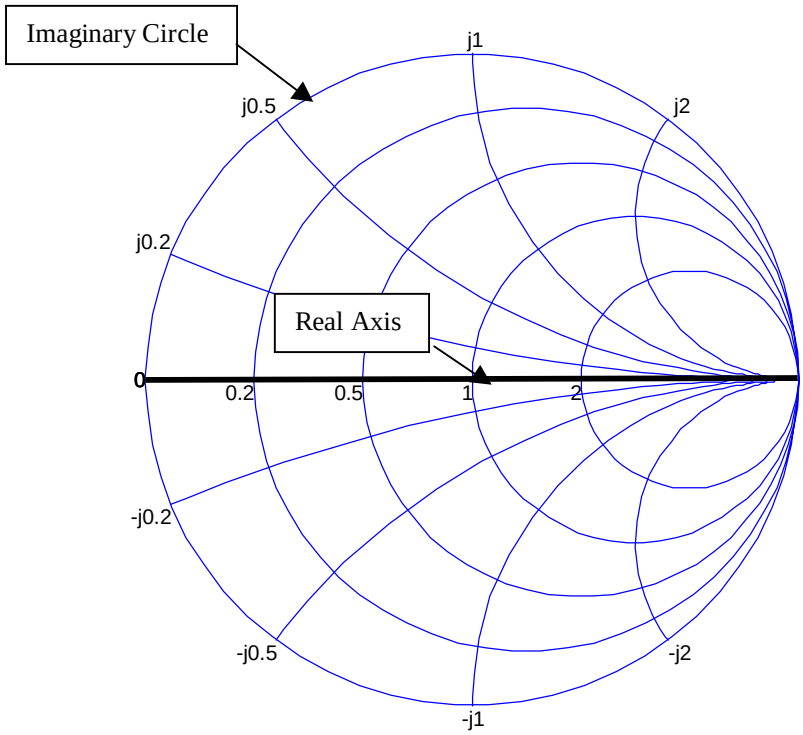

Figure E.2-2: The real and imaginary axes of the Smith Chart.

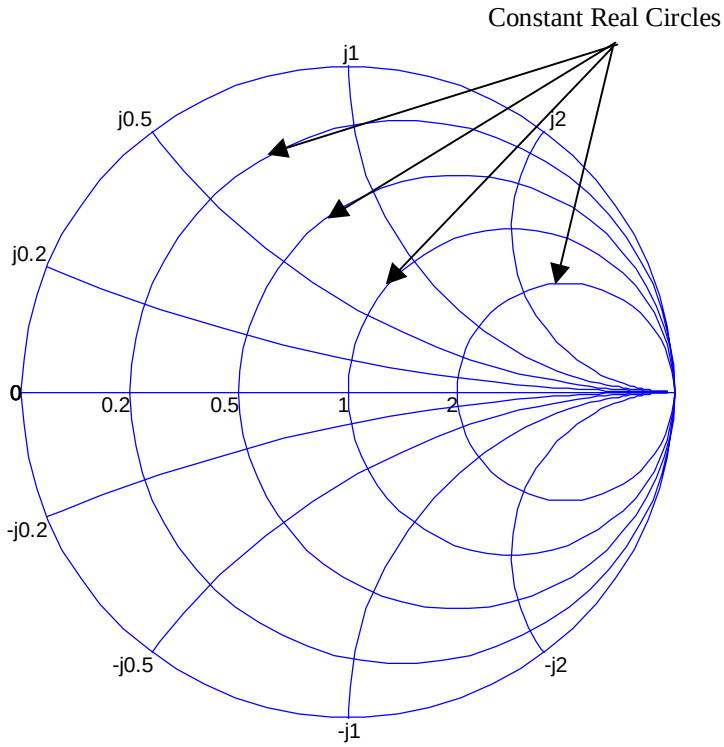

Figure E.2-3: Circles of the Smith Chart represent the real component of the impedance

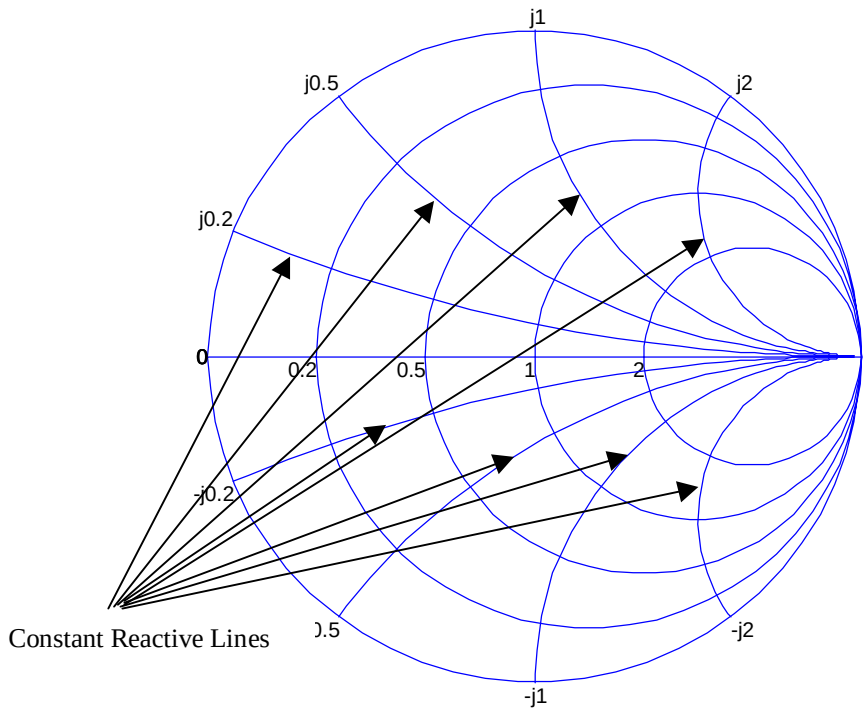

Figure E.2-4: Arcs of the Smith Chart represent the reactive component of the impedance.

If the reflection coefficient of Equation E.1-3 is plugged into Equation E.2-1, the load impedance ($\overline{Z}_L$) is equal to 111.8 ∠63.4°. In order to plot complex impedance points, the Smith Chart is used. The Smith Chart, (developed in 1939 by Phillip H. Smith) [Ref. E-2], has axes capable of displaying the real and imaginary parts of impedance. In order to make use of the Smith Chart axes the impedance values must be normalized to the system impedance ($\overline{Z}_0$). The impedance from the example above (111.8 ∠63.4°) becomes 2.2361 ∠63.4°, or 1 + 2j when displayed in rectangular coordinates. Figure E.2-1 shows this normalized impedance plotted on a Smith Chart axes.

The Smith Chart represents a coordinate transformation of the reflection coefficient. Actually, the transformation is defined by the equation that changes the reflection coefficient to impedance. An interesting and useful characteristic of this transformation is that if the polar axis from the reflection coefficient axis is removed and replaced by an overlay of the Smith Chart, the data would fall on the same locations as if it were plotted as impedance. This makes the Smith Chart very useful in displaying statistics associated with the reflection coefficient.

The Smith Chart has a fundamental set of axes. These are the real line and the imaginary circle (see Figure E.2-2). The coordinate system axes are shown in Figure E.2-3 and Figure E.2-4. These are constant real circles, and constant reactive (imaginary) lines [Ref. E-1]. A purely resistive load represents a point on the real axis corresponding to its normalized value. Also a completely reactive value (like a lossless capacitor) represents a point on the imaginary axis corresponding to its normalized reactance value.

E.3 Statistical Display of Impedance Data

Figure E.2-5 shows a typical test setup used to measure the reflection coefficient of a device under test (DUT). The network analyzer sends out a signal and measures the amount of signal that is reflected from the DUT. This process is repeated for all the frequencies of interest. For example, as described in Section 4.4.1, the network analyzer was used to measure the reflection coefficient of the FQIS of a B-747-100 aircraft. This test was done for frequencies from 300 kHz to 1 GHz. The data from the measurement of the input impedance of the aircraft are shown in Figure E.2-6 plotted on a reflection coefficient axis. Figure E.2-7 shows the same data plotted on the Smith Chart. The data pattern is identical for each, and is independent of the axis chosen. The erratically varying trace represents the impedance values as a function of frequency.

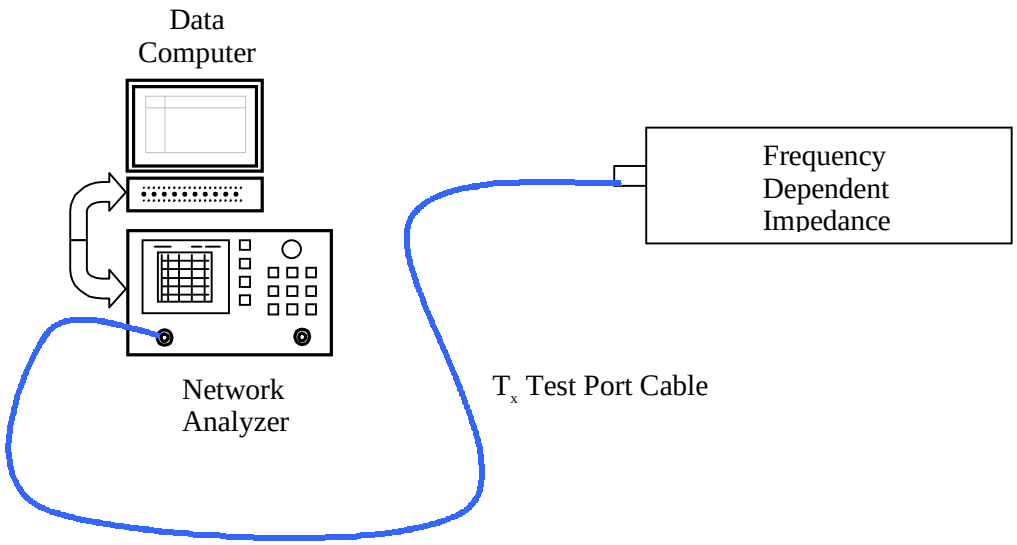

Figure E.2-5: Reflection coefficient measurement setup.

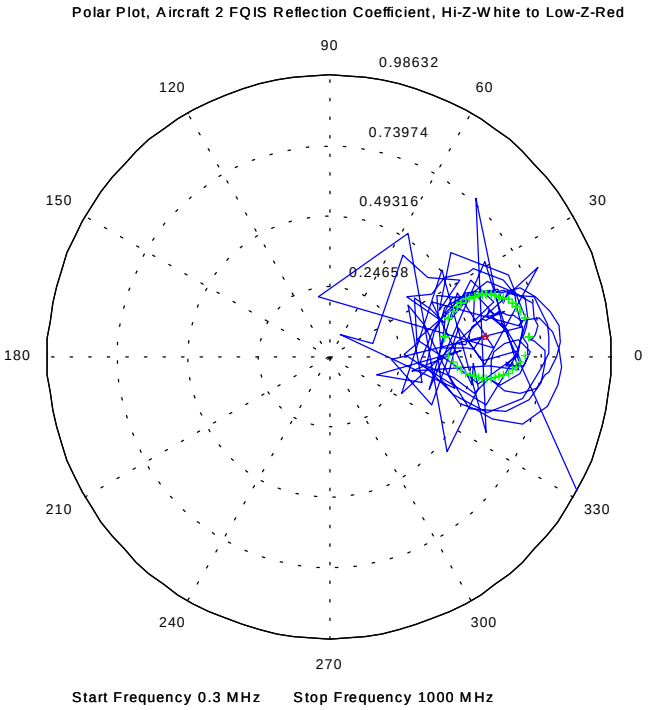

Figure E.2-6: Polar plot of the frequency dependent reflection coefficient, with the mean (red star) and the standard deviation (green circle) displayed.

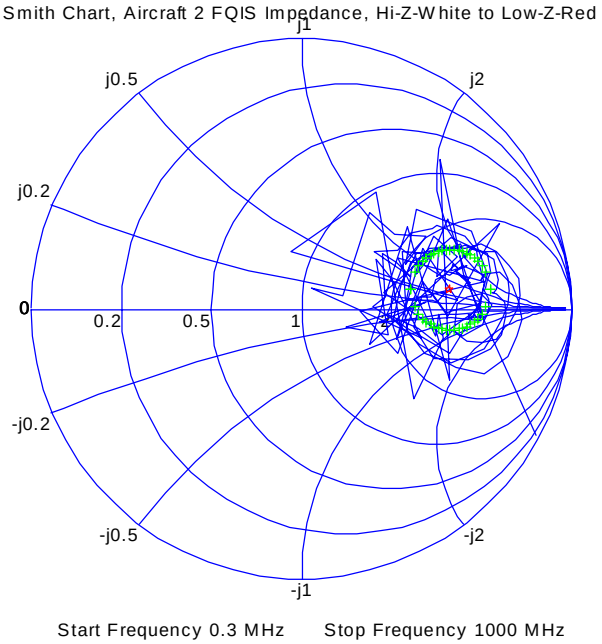

Figure E.2-7: Smith Chart of the frequency dependent reflection coefficient, with the mean (red star) and the standard deviation (green circle) displayed.

A method of comparing these (Figure E.2-6 and Figure E.2-7) seemingly random-looking traces was developed for this effort. Because of the nature of the impedance values, a direct frequency-to-frequency comparison of the impedance values was not practical; therefore, a statistical method was used to compare independent data sets for similarity. The mean of the real part of the reflection coefficient, and the mean of the imaginary part of the reflection coefficient can be computed by Equation E.3-1 [Ref. E-3]

$$\Gamma_{mean} = \frac{1}{N}\sum_{j=1}^{N}\Gamma_j \ , \qquad \text{(E.3-1)}$$

where N is the number of points in the sequence, and Γ_j is the frequency-dependent value of the reflection coefficient. Figure E.2-7 shows the mean value of the real and the mean of the imaginary part of the reflection coefficient plotted as the red star. The green circle on this figure represents a standard deviation circle of the data. The standard deviation can be calculated as in Equation E.3-2 [Ref. E-3]

$$\Gamma_{standard_deviation} = \left(\frac{1}{N-1}\sum_{j=1}^{N}\left(ABS(\overline{\Gamma_j}) - \Gamma_{abs_mean}\right)^2\right)^{\frac{1}{2}}, \qquad \text{(E.3-2)}$$

where N is the number of points in the sequence, and ABS ($\overline{\Gamma_j}$) is the magnitude of the reflection coefficient, and Γ_{abs_mean} is the mean value of the magnitude of the reflection coefficient (Equation E.3-3). The standard deviation circle was realized by scaling a unit circle by the standard deviation of the reflection coefficient, and plotting it around the mean value. These statistical concepts add a means by which to can compare two data sets in a graphical manner.

$$\Gamma_{abs_mean} = \frac{1}{N}\sum_{j=1}^{N}\left(\sqrt{\Gamma_{Real_j}{}^2 + \Gamma_{Imag_j}{}^2}\right) \qquad \text{(E.3-3)}$$

E. 4 References for Appendix E

[E-1] W. D. Stanley, and R. F. Harrington, *Lines and Fields in Electronics Technology*, Prentice-Hall, 1995.

[E-2] J.J. Carr, *Practical Antenna Handbook*, 2nd Edition, Tab Books, 1994.

[E-3] B. Jones, MATLAB Statistics Toolbox User's Guide, Natick, Mass.: The Math Works, Inc.

Appendix F: RF Induced Voltage and Current Measurements in the Laboratory

The task of characterizing the RF voltage and current coupling onto the FQIS required accurate measurements from 300 kHz to 1 GHz. Specialized instruments and calibration fixtures were required. Current and voltage probes that operate in this frequency range were commercially available. These probes were designed to minimize perturbation of the attached RF circuit, and could be used with a RF vector network analyzer. For accurate measurements over the required frequency band, a specialized calibration fixture was designed and constructed.

F.1 Approach

Based upon discussion and experimentation, it was decided that the best technique to satisfy the objective would be to use a network analyzer with high frequency voltage and current probes. A photograph of the laboratory setup is shown in Figure F.1-1. Figure F.1-2 shows a schematic of the measurement system. The network analyzer, with built in S-parameter test set, allowed quick and simple calibration at the point of measurement, and quickly and accurately collected data over a wide range of frequencies.

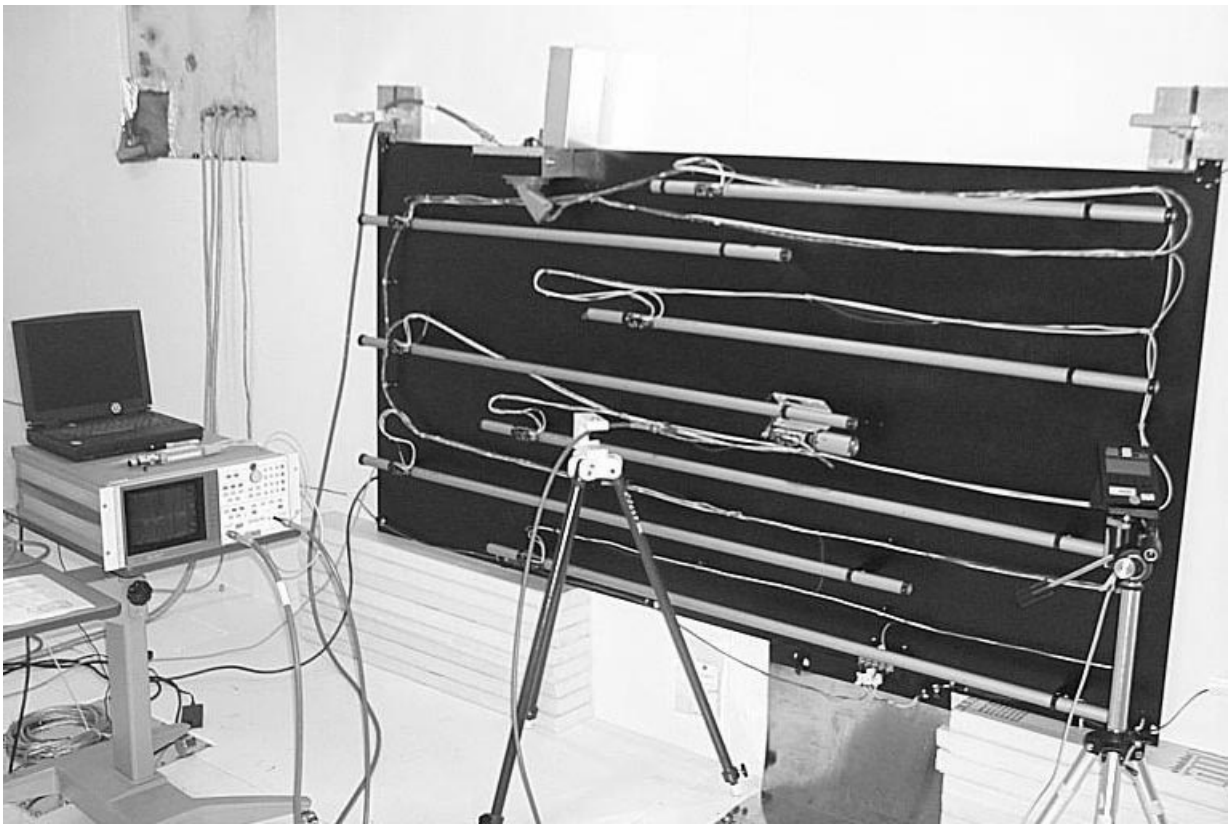

Figure: F.1-1: Photograph: Laboratory network analyzer and high frequency voltage/current probe setup for measurements on the FQIS installation.

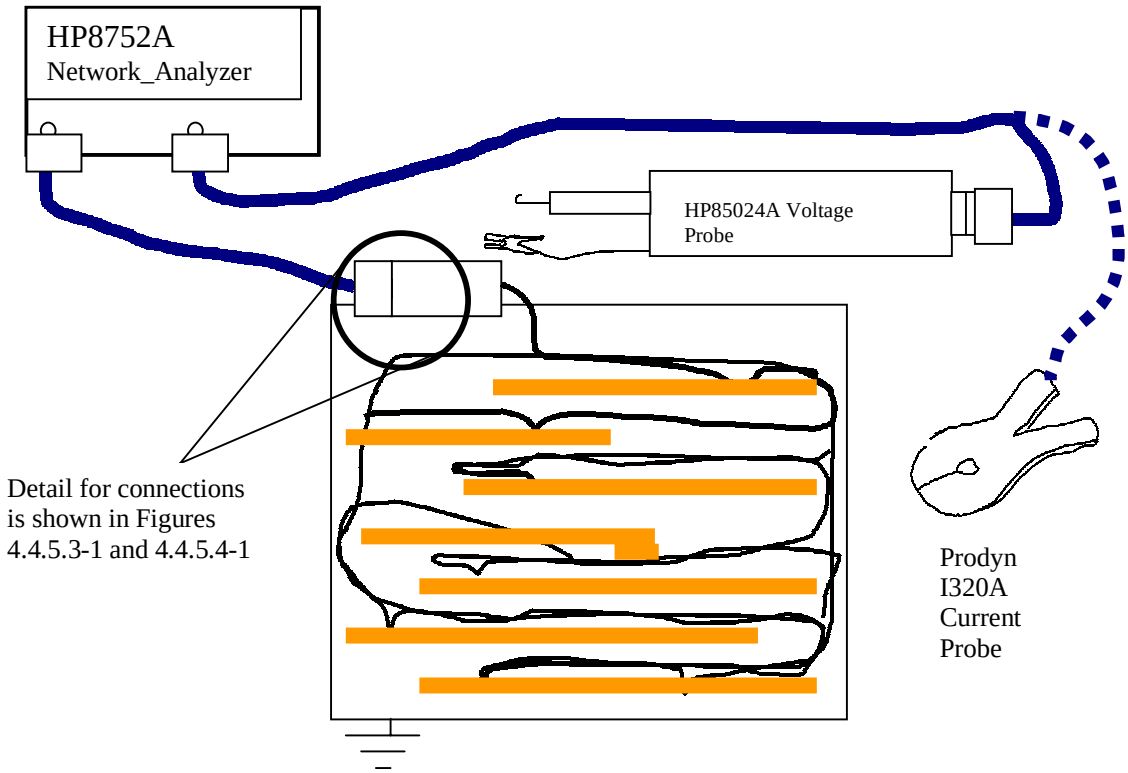

Figure F.1-2: Diagram: Laboratory network analyzer and high frequency voltage/current probe setup for measurements on the FQIS installation.

In addition to the RF vector network analyzer, voltage probe and current probe, several specialized cables and custom made adapters were needed. Calibration data for both probes was acquired with a current-voltage sampling fixture (CVSF), which was designed and constructed at NASA LaRC for this task. The CVSF design is discussed in Section F.5, and derivation of calibration terms is discussed in Section F.6.

F.2 RF Vector Network Analyzer and Data Acquisition Computer

The network analyzer (HP8752A) used to conduct these measurements was the same as used during the aircraft and laboratory impedance measurements. The HP8752A was capable of performing one port reflection measurements or two port transmission measurements in both the frequency and time domains. The analyzer is comprised of a synthesized signal source, a switching S-parameter test set with a nominal 50 Ohm impedance, and a dual channel receiver to measure and display the magnitude and phase of transmitted and reflected power. It contains built in digital signal processing and microprocessors to perform complex mathematical manipulations of measured data and to improve measurement capability and accuracy. Measurement results can be displayed on the network analyzer, plotted, or transferred via GPIB to another data acquisition computer for storage or further analysis.

Figure F.2-1 shows the data acquisition PC and the network analyzer. The data acquisition computer was a standard NEC portable laptop running the Windows 98 operating system. The computer was configured with a GPIB interface for connecting to the network analyzer. Hewlett Packard Visual Engineering Environment (HP VEE) software was installed on the data acquisition computer as the primary control software. Several data acquisition routines were programmed to capture data from the network analyzer in the required engineering formats specific to each type of measurement. The computer was also used as a data storage device and a preliminary data analysis computer. Later, data was transferred from the portable laptop to PC desktop workstations for more in-depth analysis and presentation.

Figure F.2-1: Data acquisition computer and HP 8752A network analyzer.

F.3 Prodyn I-320B Current Probe

The Prodyn I-320B "clamp-on" type current probe was used to sense the magnetic field produced by the alternating current flowing through a wire under test. This probe provides a transfer function between current present on the wire under test to the current induced in its 50 Ohm matched output terminal. Figure F.3-1 shows the current probe attached to the simulated FQIS wiring. The small probe size and shape allowed for convenient and easy installation over conductors as they existed within their normal established arrangement. There was no need to cut or break a conductor current path to insert the sensing device. The probe had an aperture of 0.22 in. diameter, and could be clamped around a wire allowing for the testing of a variety of cables.

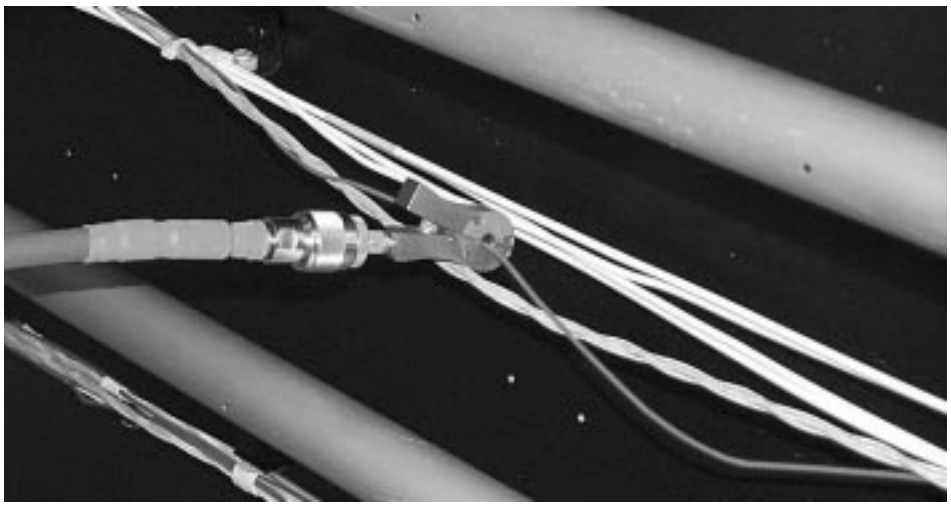

Figure F.3-1: I-320 probe used in induced current measurements on the laboratory FQIS installation.

The relationship between the sensed current and output voltage is

$$V_{out} = Z_T \times I_{sensed}, \qquad \text{(F.3-1)}$$

where I_{sensed} is the Current sensed in the conductor,
Z_T is the Transfer Impedance, and
V_{out} is the Voltage detected at the sensor output

The transfer impedance for the I-320 current probe was specified as $Z_T = 1$. The transfer impedance is a function of how the device was designed and built and relates to the coupling from the conductor to the probe. The $Z_T = 1$ transfer impedance was useful, in that it mathematically simplified the probes current-voltage relationship. The sensor had an output impedance of 50 Ohms, which minimized systematic errors, when mated to the network analyzer measurement system.

The current probe's 3 dB operation points spanned the frequency range from 200 kHz to 500 MHz, with a bandpass characteristic of +/- 0.5 dB. By measuring calibration terms with the CVSF, the reliable range of the device was extended out-of-band to 1000 MHz. The CVSF and its use are described in greater detail in Sections F.5 and F.6.

F.4 Hewlett Packard 85024A High Frequency Voltage Probe

The HP85024A voltage probe (Figure F.4-1) was designed to directly connect to a circuit under test, but provided high isolation due to a 1 MOhm input impedance and low input capacitance at the sensing terminals. The probe was designed specifically for troubleshooting RF signal paths and identifying problem areas, and therefore, was ideally suited for voltage and power testing of the RF-excited FQIS installation. The probe provided a transfer function between voltage present between its sensing terminals to the voltage induced across its 50 Ohm matched output terminal. The 50 Ohm matched output characteristic minimizes systematic mismatch errors with a variety of measurement instruments, such as spectrum analyzers, frequency counters, and oscilloscopes. For the purposes of this test, it was used with the HP8752A vector network analyzer, for which it was particularly designed to operate. The network analyzer supplied operating power for the active probe. The frequency bandwidth was 300 kHz to 3 GHz, which more than covered the potential PED threat regime.

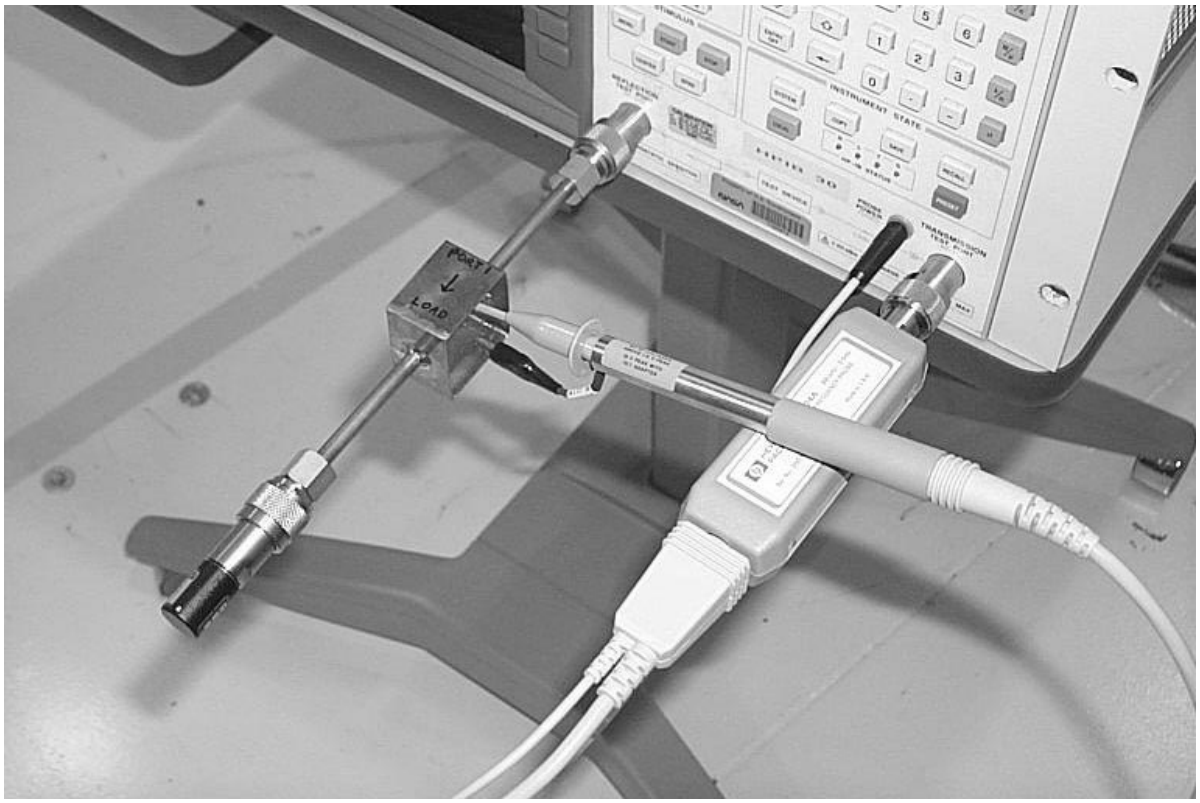

Figure F.4-1: HP 8572A probe used in induced voltage measurements on the laboratory FQIS installation. It is shown here with the CVSF.

F.5 Current – Voltage Sampling Fixture (CVSF): Fabrication and Use

The CVSF was designed by LaRC engineers to provide a calibrated reference for determining the current coupling characteristics of the Prodyn I320B current probe and voltage coupling characteristics of the HP85024A voltage probe. These characteristics would later be expressed as transfer functions for each probe, allowing absolute values of current and voltage enhancements at locations within the FQIS simulator to be measured.

The CVSF consisted of an 8.5-inch length of semi-rigid coaxial transmission line that has had 1 inch of the outer conductor stripped away from the middle so as to expose the Teflon dielectric surrounding the center conductor. A small 1/16th of an inch section in the Teflon was cut away to expose the center conductor. This gap allowed for the tip of the voltage probe to be directly connected to the center conductor. This was the center conductor measurement point. In the same area, the current probe was clamped around the Teflon dielectric while maintaining isolation from the center conductor of the coaxial semi-rigid line. A CVSF schematic is shown in Figure F.5-1, and a photograph is shown in Figure F.5-2.

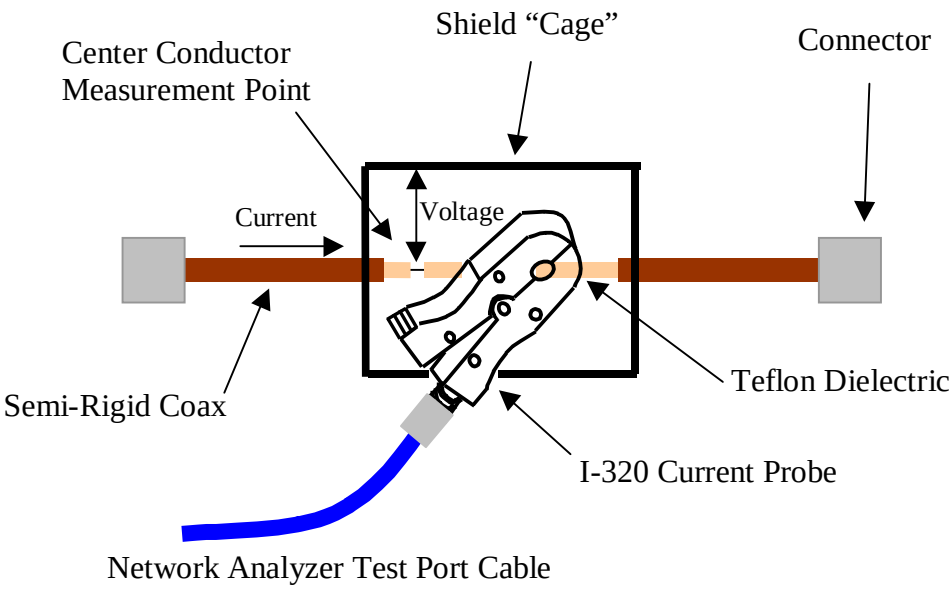

Figure F.5-1: Schematic of the CVSF.

A "cage" enclosed the test area where the probes could be connected to the transmission line. The cage was an extension of the copper shield on the semi-rigid coax. It was a 1 inch wide piece of copper that forms a 1.5 inch x 1.5 inch box around the test area. This shielded box minimized potential stray electric fields that may cause interference or perturbations within the test section. The device had N-type male RF connectors at each end of the semi-rigid coaxial transmission line.

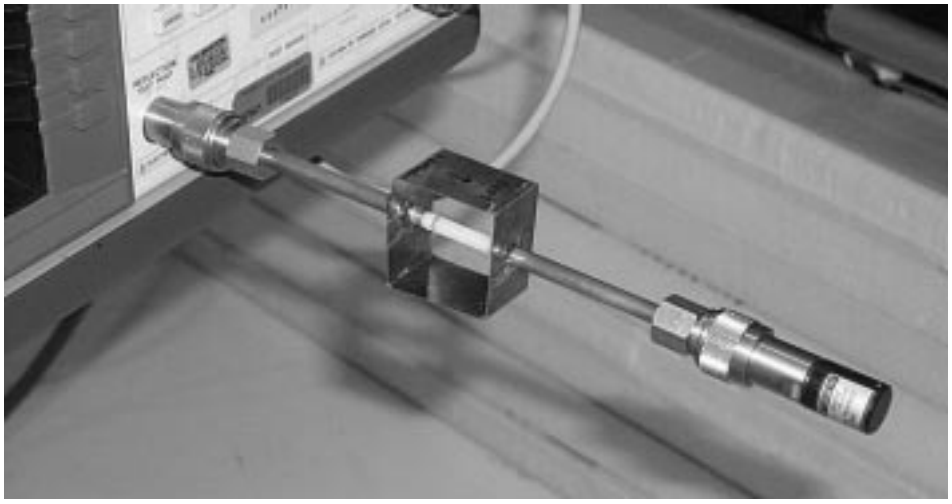

Figure F.5-2: Photograph of the CVSF. It is shown connected to the network analyzer and terminated into a calibrated 50 Ohm load.

F.6 Current – Voltage Sampling Fixture (CVSF): Calibration

For conducted coupling measurements and detailed current-voltage characterization of FQIS installed in the laboratory, it was necessary to characterize the CVSF first. With a given input power, induced currents and voltages at the CVSF measurement point were calculated and compared to measured probe outputs. This defined a calibration curve for both the Prodyn I-320 current probe and the HP 85024A voltage probe. All measurements were performed on the CVSF with the RF vector network analyzer and data acquisition computer, discussed previously.

F.6.1 Network Analyzer Reflection Measurement [S_{11}]

The network analyzer and the data acquisition computer were set up first to measure and store the reflection characteristics of the CVSF. By terminating the CVSF into a 50 Ohm precision load, and calibrating the network analyzer for a reflection (S_{11}) measurement, the mismatch characteristics of the CVSF could be obtained. A general discussion of reflection and transmission measurement theory is provided in Appendix D.

The network analyzer was configured to measure the magnitude and phase of the reflection coefficient from 1 MHz to 1 GHz in a logarithmically spaced frequency format. A 1-port (open, short, load) calibration was performed to remove systematic errors. The CVSF was connected to the reflection port of the network analyzer and the other end of the CVSF was terminated with a 50 Ohm matched calibration load.

Three configurations of the CVSF were measured. First the terminated CVSF alone was measured. Second, the terminated CVSF with its test section perturbed by the current probe was measured. The current probe was loaded into 50 Ohms and clamped around the Teflon dielectric in the test area of the CVSF. Finally, the terminated CVSF with the test area perturbed by the voltage probe was characterized. The voltage probe was connected to the center conductor measurement point in the CVSF test section.

The complex reflection coefficient for each of the fixture states was measured and stored. These files were used later for conducted coupling measurement calibrations.

F.6.2 Network Analyzer Transmission Measurements [S_{21}]

F.6.2.1 CVSF Insertion Loss

The network analyzer and the data acquisition computer were next set up to measure and store the transmission characteristics of the CVSF. The network analyzer was configured to measure the magnitude data associated with signal insertion loss from 1 MHz to 1 GHz in a logarithmic format. A 2-port response (thru) calibration was performed to remove systematic errors. The CVSF was connected to the reflection port of the network analyzer and the other end of the CVSF was connected to the 50-Ohm transmission port of the network analyzer by means of a low-loss test port cable. The transmission insertion loss was measured for the three configuration states of the CVSF as in the case for the reflection measurements described in the earlier paragraph; CVSF alone, CVSF with current probe, and CVSF with voltage probe. The transmission data was stored for these files to also be used later for conducted coupling measurement calibrations.

F.6.2.2 CVSF Probe Transfer Function

The final measurements made using the CVSF were the transfer function measurements. (Figure F.6.2.2-1.) By terminating the CVSF into a 50 Ohm precision load, and calibrating the network analyzer for a response (S_{21}) measurement, a relationship between V_1 and V_2, as well as I_1 and I_2 was measured directly. This configuration setup measures the signal transfer characteristics from the network analyzer into the CVSF through the probe connected within the CVSF test section and back into the network analyzer. This measurement was very important because it, along with the CVSF characterizations, lead directly to the conducted coupling measurements on the simulated FQIS.

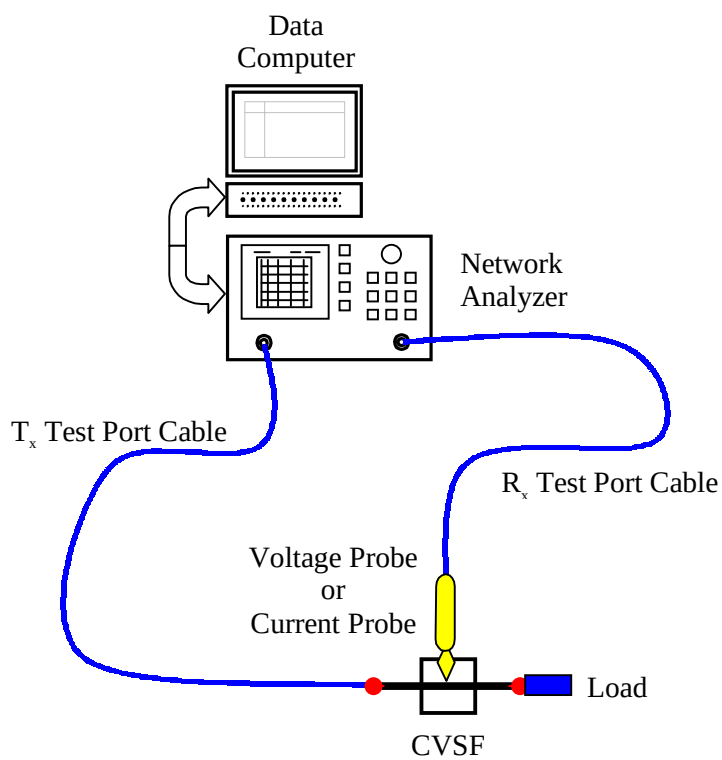

Figure F.6.2.2-1: Transfer function setup showing the use of the CVSF.

F.6.3 Voltage Transfer Function

For the HP85024A voltage probe, a CVSF Voltage Transfer Function (VTF) was defined as (see Figure F.6.3-1)

$$\text{CVSF_VTF} = \text{Voltage Transfer Function} = \frac{V_2}{V_1} \ . \qquad \text{(F.6.3-1)}$$

(RMS voltage is assumed.) Because the CVSF will introduce a small mismatch, the voltage (V_1) is bound by [Ref. F-1]

$$V_1 = \sqrt{P_{fwd} Z_{01}}\left(1 \pm \Gamma\right), \qquad \text{(F.6.3-2)}$$

where Γ is the magnitude of the reflection coefficient, measured by the network analyzer ($\Gamma = |S_{11}|_{Linear_Magnitude}$) as described in Section F.6.1. The factor $1 \pm \Gamma$ bounds measurement errors due to reflection. Reflection coefficient was measured with the voltage probe connected to the fixture. Because the output of the probe connector was designed to be well-matched, V_2 can be written as

$$V_2 = \sqrt{P_{sensed} Z_{02}} \ . \qquad \text{(F.6.3-3)}$$

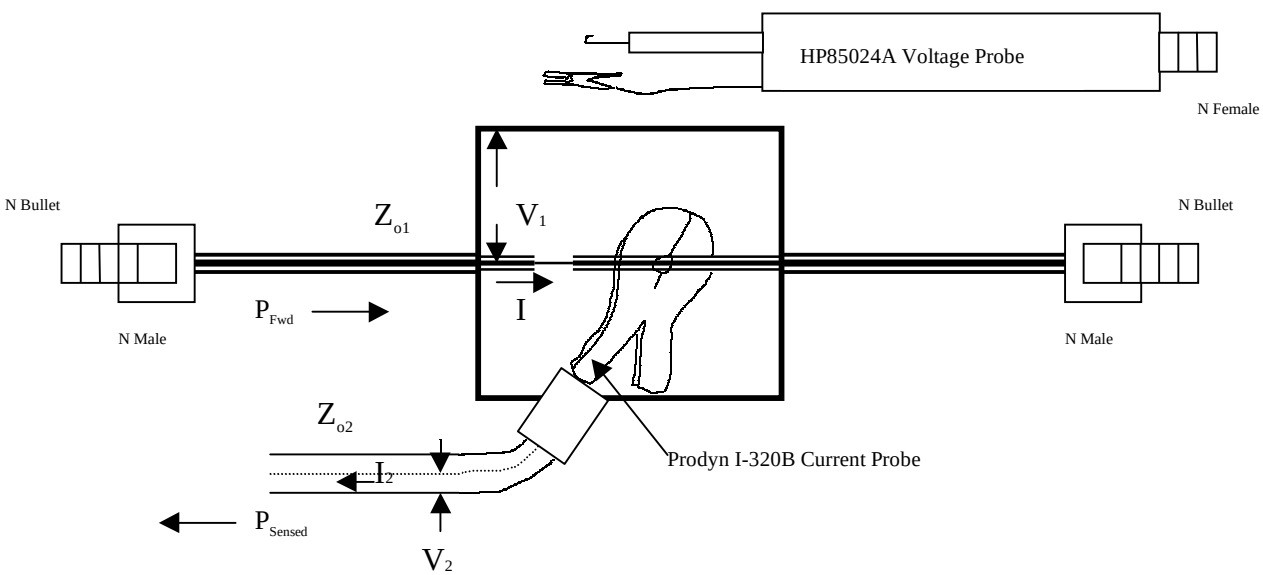

Figure F.6.3-1: Schematic representation of the CVSF, shown with the HP85024A and Prodyn I-320B probes it was intended to calibrate.

The Voltage Transfer Function in dB is therefore

$$\mathrm{CVSF_VTF_{dB}} = 20\mathrm{LOG}\left[\left(\frac{1}{1\pm\Gamma}\right)\sqrt{\frac{P_{sensed}}{P_{fwd}}}\sqrt{\frac{Z_{02}}{Z_{01}}}\right]. \qquad \text{(F.6.3-4)}$$

Considering a network analyzer transmission measurement, as described in Section F.6.2,

$$|S_{21}|(\mathrm{dB}) = 10\mathrm{LOG}\left[\frac{P_{sensed}}{P_{fwd}}\right], \qquad \text{(F.6.3-5)}$$

then:

$$\mathrm{CVSF_VTF_{dB}} = 20\mathrm{LOG}\left[\left(\frac{1}{1\pm\Gamma}\right)\sqrt{\frac{Z_{02}}{Z_{01}}}\sqrt{10^{\frac{|S_{21}|(\mathrm{dB})}{10}}}\right]$$

$$\mathrm{CVSF_VTF_{dB}} = 20\mathrm{LOG}\left(\frac{1}{1\pm\Gamma}\right) + 10\mathrm{LOG}\left[\frac{Z_{02}}{Z_{01}}\right] + 10\mathrm{LOG}\left[10^{\frac{|S_{21}|(\mathrm{dB})}{10}}\right] \qquad \text{(F.6.3-6)}$$

$$\mathrm{CVSF_VTF_{dB}} = 20\mathrm{LOG}\left(\frac{1}{1\pm\Gamma}\right) + 10\mathrm{LOG}\left[\frac{Z_{02}}{Z_{01}}\right] + |S_{21}|(\mathrm{dB})$$

And, since $Z_{01} \cong Z_{02} \cong 50$ Ohms, the CVSF_VTF reduces to

$$\mathrm{CVSF_VTF_{dB}} \cong \underbrace{20\mathrm{LOG}\left[\frac{1}{1\pm\Gamma}\right]}_{\substack{\text{Reflection}\\ \text{Measurement}\\ \text{(Mismatch) Term}}} + \underbrace{|S_{21}|(\mathrm{dB})}_{\substack{\text{Transmission}\\ \text{Measurement}\\ \text{(Probe) Term}}}. \qquad \text{(F.6.3-7)}$$

Data for the HP85024A voltage probe, with error bars is shown in Figure F.6.3-2. The maximum values of this data were subtracted from the FQIS voltage transfer measurements of Section 4.5.1 to provide an estimate of voltage enhancement magnitude versus frequency, at each test point location. A maximum CVSF_VTF magnitude results in a smaller predicted voltage, when subtracted from the FQIS_VTF. This was considered to be the most conservative approach in estimating voltage enhancements.

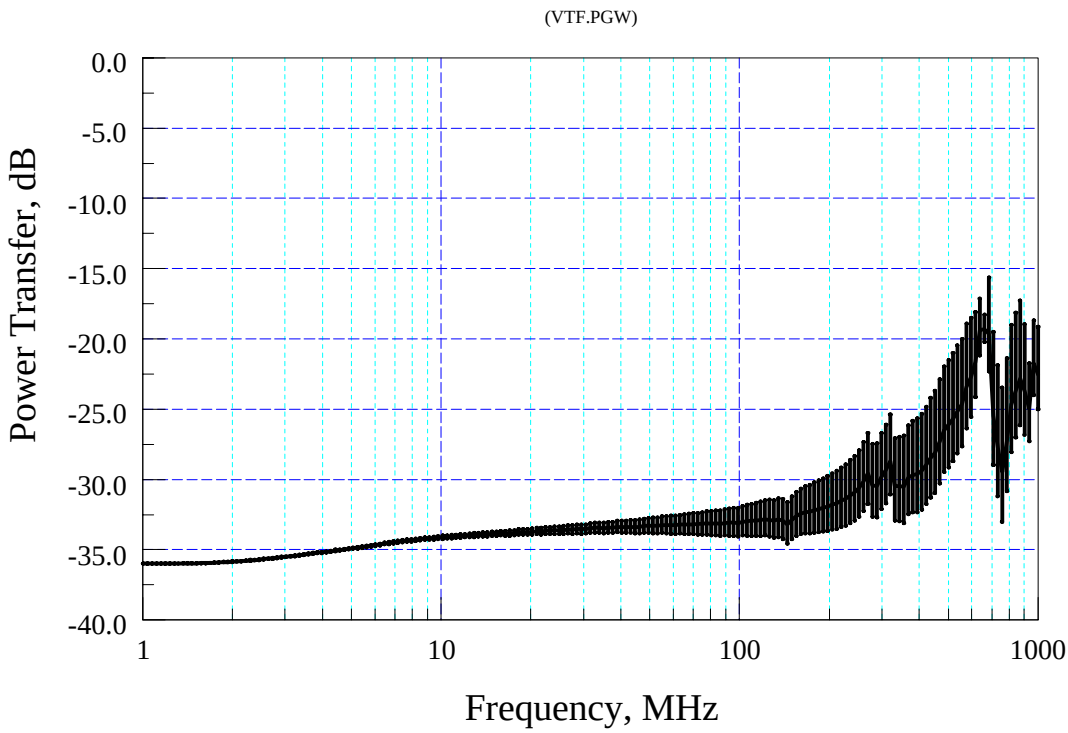

Figure F.6.3-2: HP85024A Voltage Probe *Voltage Transfer Function*, a ratio of output voltage to reference voltage. Error bars show potential bounds of measurement inaccuracy due to calibration fixture reflection.

F.6.4 Current Transfer Function

For the Prodyn I320B current probe, a CVSF Current Transfer Function (CTF) was defined as (see Figure F.6.3-1)

$$\text{CVSF_CTF} = \text{Current Transfer Function} = \frac{I_2}{I_1} \ . \qquad \text{(F.6.4-1)}$$

Because the CVSF will introduce a small mismatch, the RMS current (I_1) is bound by [Ref. F-1]

$$I_1 = \sqrt{\frac{P_{fwd}}{Z_{01}}}\left(1 \mp \Gamma\right), \qquad \text{(F.6.4-2)}$$

where Γ is the magnitude of the reflection coefficient, as measured by the network analyzer ($\Gamma = |S_{11}|_{Linear_Magnitude}$) as described in Section F.6.1. The factor $1 \mp \Gamma$ bounds measurement errors due to reflection. Reflection coefficient was measured *with* the current probe present in the fixture. Because the output of the probe connector was designed to be well matched, I_2 was written as

$$I_2 = \sqrt{\frac{P_{sensed}}{Z_{02}}} . \qquad \text{(F.6.4-3)}$$

The Current Transfer Function in dB is therefore

$$CVSF_CTF_{dB} = 20LOG\left[\left(\frac{1}{1 \mp \Gamma}\right)\sqrt{\frac{P_{sensed}}{P_{fwd}}}\sqrt{\frac{Z_{01}}{Z_{02}}}\right] . \qquad \text{(F.6.4-4)}$$

Considering a network analyzer transmission measurement as described in Section F.6.2

$$|S_{21}|(dB) = 10LOG\left[\frac{P_{sensed}}{P_{fwd}}\right], \qquad \text{(F.6.4-5)}$$

then:

$$CVSF_CTF_{dB} = 20LOG\left[\left(\frac{1}{1 \mp \Gamma}\right)\sqrt{\frac{Z_{01}}{Z_{02}}}\sqrt{10^{\frac{|S_{21}|(dB)}{10}}}\right]$$

$$CVSF_CTF_{dB} = 20LOG\left(\frac{1}{1 \mp \Gamma}\right) + 10LOG\left[\frac{Z_{01}}{Z_{02}}\right] + 10LOG\left[10^{\frac{|S_{21}|(dB)}{10}}\right] \qquad \text{(F.6.4-6)}$$

$$CVSF_CTF_{dB} = 20LOG\left(\frac{1}{1 \mp \Gamma}\right) + 10LOG\left[\frac{Z_{01}}{Z_{02}}\right] + |S_{21}|(dB)$$

And, since $Z_{01} \cong Z_{02} \cong 50$ Ohms, the CTF reduces to

$$CVSF_CTF_{dB} = \underbrace{20LOG\left[\frac{1}{1 \mp \Gamma}\right]}_{\substack{\text{Reflection} \\ \text{Measurement} \\ \text{(Mismatch) Term}}} + \underbrace{|S_{21}|(dB)}_{\substack{\text{Transmission} \\ \text{Measurement} \\ \text{(Probe) Term}}} . \qquad \text{(F.6.4-7)}$$

Data for the Prodyn I320B current probe, with error bars is shown in Figure F.6.4-1. The maximum values of this data were subtracted from the FQIS current transfer measurements of Section 4.5.1 to provide an estimate of current enhancement magnitude versus frequency, at each test point location. A maximum CVSF_CTF magnitude results in a smaller predicted current, when subtracted from the FQIS_CTF. This was considered to be the most conservative approach in estimating current enhancements.

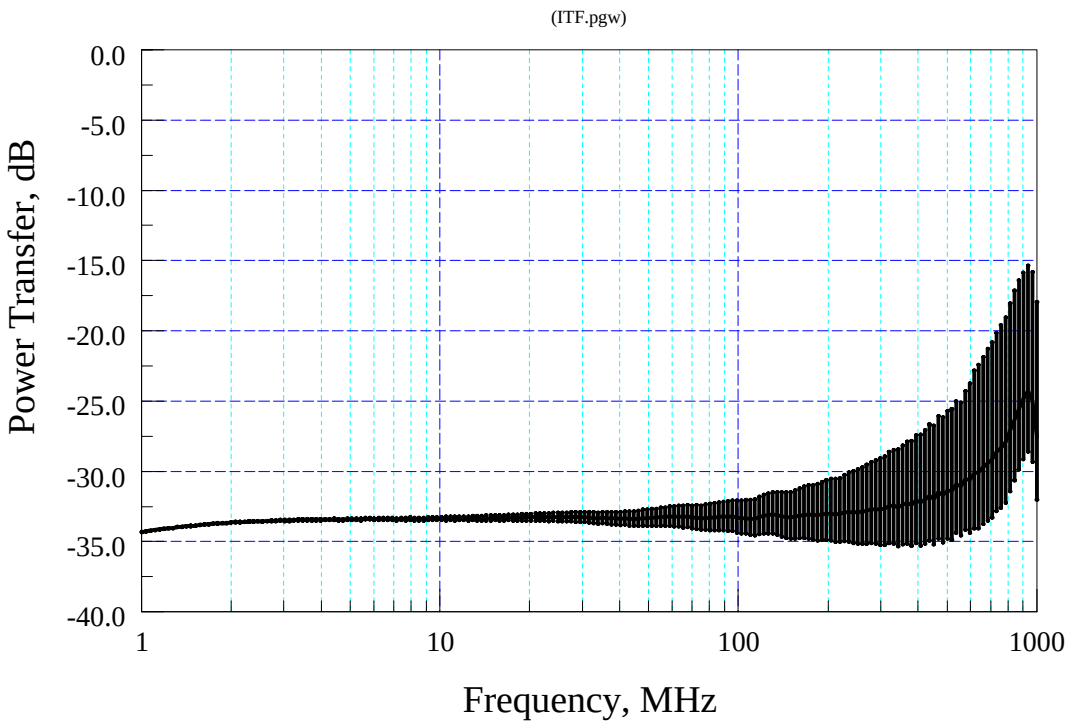

Figure F.6.4-1: Prodyn I320B Probe *Current Transfer Function*, a ratio of output current to reference current. Error bars show potential bounds of measurement inaccuracy due to calibration fixture reflection.

F.7 References for Appendix F

[F-1] P. A. Rizzi, *Microwave Engineering*, 1988, Prentice Hall.

[F-2] Prodyn I-320B Specifications

[F-3] HP85024A Specifications

Appendix G: Manufacturers' Data on Representative Portable Intentional Transmitters

(Also includes data from the JSC report [Ref. G-1])

Devices/ Manufacturers	Model/Product	Standards	Freqs (MHz)	Max Power (W)
Cellular/PCS:				
Qualcomm	QCP-2700	Analog_Cell	824 - 849	0.6
		CDMA PCS	1850 - 1910	0.2
Motorola	13241- 3W	Analog_Cell	824 - 849	3
Satellite Phone:				
Motorola	Satellite Phone	Satellite	1616-1626.5	0.57 ave.
Wireless LAN:				
Lucent Tech	WaveLAN	IEEE 802.11	2400 - 2483.4	0.0316
	WaveLAN/ISA	DSSS	902 - 928	0.1995
		DSSS	2400 - 2483.5	0.0316
	WavePoint	DSSS	902 - 928	0.3162
		DSSS	2400 - 2483.5	0.0316
ICOM	LAN Card	DSSS	2401 - 2483.5	0.1
2-way Pager:				
Motorola	PageWriter2000 (2-way pager)		901 - 902	1
Family Radio Service (FRS):				
ICOM, Motorola. Kenwood	Family Radios	FRS	462.5 - 467.7	0.5
Military:				
Utilicom	LongRanger 2000 & 2020	Spread Spec	902 - 928	0.8
			2400 - 2483.5	0.063
Portable Radio:				
Motorola	Spirit MU22CV		464.5 - 467.925	2
	Spirit SV52		151.6 - 151.95	5
	Spirit SU42		464.5 - 464.55	4
	SP10 VHF		150.8-162	2

	SP21 VHF		151-159	2
	SP21 UHF		462-470	2
	SP50 VHF		150-170	1 to 5
	SP50 UHF		450-470	2 to 5
	P1225 VHF		150-174	5
	P1225 UHF		450-470	5
	GP350 VHF		146-174	5
	GP350 UHF		438-470	4
	P110 VHF		136-174	5
	P110 UHF		438-520	4
	GP300 VHF		146-174	5
	GP300 UHF		403-470	4
	P200 VHF (LowBand)		30-50	6
Maxon				
	SP130,140 VHF		148-174	5
	SP130,140 UHF		440-470	5
	GMRS-21A		462.575-462.625	1
Tekk				
	T-20		151.6-154.6	2
	T-40		462.5-464.5	2
ICOM	IC-T7H		144 - 148	6
			440 - 450	6
	IC-T81A		50-54	5
			74 - 174	5
			400 - 470	5
			1240 - 1300	5
	IC-T2H		74-174	6
	IC-T8A		50 - 54	5
			144- 148	5
			440-450	5
	F30 (VHF)		146-174	5
	F40 (VHF)		430-470	5
RadioShack				
	HTX-200	Ham	144-148	2
	HTX-400	Ham	430-450	1
	BTX-127	Bus.-2way	151.6-154.7	2
	TRC-237	CB	26.965-27.405	4
	HH-940P	Marine Radio	156-157	1

LandMobile:

ICOM	IC-F3	VHF Xceiver	136 - 150	5
			146 - 174	5
	IC-F4	UHF Xceiver	400 - 430	4
			440 - 470	4
	IC-F40LT	UHF Xceiver	400 - 430	5
			440 - 470	5

		470-520	5
IC-A3	AM	118 -136.975	5

NOTE: The intention of this data was to provide an upper bound for possible PED power threat levels in an aircraft. The information was gathered from various internet web sites belonging to equipment manufacturers, online stores, and sale catalogs. However, accuracy was not formally validated with the manufacturers. NASA does not endorse the use of this data for any purpose other than stated herein.

References for Appendix G

[G-1] D. J. Hughes, "Portable Electronic Devices (PEDs) Measured Emission Levels," P1625 E3 Support to the NTSB, 1999.

Appendix H: Partial List of FCC Limits on PEDs

	Frequency (MHz)		Power (W)
	Start	Stop	
Part15: Low-Power, Non-License Transmitter			
Asynchronous (LAN)			
"	1910	1920	0.316
"	2390	2400	0.316
"	1920	1930	0.112
Frequency Hopping			
"	902	928	1
"	2400	2483.5	1
"	5725	5850	1
Part 20: Commercial Mobile Radio Services:			
Data not available at the time of this analysis			
Part 22: Public Mobile Services			
Cellular Blocks A,B	824	890	7
Part 24: Personal Comm Service (PCS)			
Narrow Band	901	902	7
"	930	931	7
"	940	941	7
Wide Band	1850	1890	2
"	1930	1970	2
"	2130	2150	*
"	2180	2200	*
Part 26: General Wireless Comm Service (PCS)			
Blocks A,B,C,D,E	4660	4685	*
Part 27: Wireless Comm Service (WCS)			
Blocks A,B,C,D	2305	2360	0.2
Part 80: Marine Radio Service			
• Marine Radio Service:			
(shipboard)	156	157.5	25
(in harbor)	156	157.5	1
• Mobil Telephone Service:			
(typ. handheld)			5
Part 90: Private Land Mobile Radio Service:			
Data not available at the time of this analysis			
Part 95: Personal Radio Service			
GMRS (FCC95.639)	462.5	467.7	5

Remote Radio Control	27	27	4
"	27.255	27.255	25
"	72	76	0.75
CB (FCC 95.D)	26.965	27.405	4 (CW/AM)
"	26.965	27.405	12 (SSB)
Family Radio Service	462.56	467.72	0.5
Lower Power Radio Service	216	217	0.1
Interactive Video & Data	218	219	0.1

REPORT DOCUMENTATION PAGE

Form Approved
OMB No. 0704-0188

Public reporting burden for this collection of information is estimated to average 1 hour per response, including the time for reviewing instructions, searching existing data sources, gathering and maintaining the data needed, and completing and reviewing the collection of information. Send comments regarding this burden estimate or any other aspect of this collection of information, including suggestions for reducing this burden, to Washington Headquarters Services, Directorate for Information Operations and Reports, 1215 Jefferson Davis Highway, Suite 1204, Arlington, VA 22202-4302, and to the Office of Management and Budget, Paperwork Reduction Project (0704-0188), Washington, DC 20503.

1. AGENCY USE ONLY (*Leave blank*)

2. REPORT DATE
March 2000

3. REPORT TYPE AND DATES COVERED
Technical Publication

4. TITLE AND SUBTITLE
Investigation of Electromagnetic Field Threat to Fuel Tank Wiring of a Transport Aircraft

5. FUNDING NUMBERS
WU 522-14-21-51

6. AUTHOR(S)
Jay J. Ely, Truong X. Nguyen, Kenneth L. Dudley, Stephen A. Scearce, Fred B. Beck, Manohar D. Deshpande, and C. R. Cockrell

7. PERFORMING ORGANIZATION NAME(S) AND ADDRESS(ES)
NASA Langley Research Center
Hampton, VA 23681-2199

8. PERFORMING ORGANIZATION REPORT NUMBER
L-17967

9. SPONSORING/MONITORING AGENCY NAME(S) AND ADDRESS(ES)
National Aeronautics and Space Administration
Washington, DC 20546-0001

10. SPONSORING/MONITORING AGENCY REPORT NUMBER
NASA/TP-2000-209867

11. SUPPLEMENTARY NOTES

12a. DISTRIBUTION/AVAILABILITY STATEMENT
Unclassified-Unlimited
Subject Category 33 Distribution: Standard
Availability: NASA CASI (301) 621-0390

12b. DISTRIBUTION CODE

13. ABSTRACT *(Maximum 200 words)*
National Transportation Safety Board investigators have questioned whether an electrical discharge in the Fuel Quantity Indication System (FQIS) may have initiated the TWA-800 center wing tank explosion. Because the FQIS was designed to be incapable of producing such a discharge on its own, attention has been directed to mechanisms of outside electromagnetic influence. To support the investigation, the NASA Langley Research Center was tasked to study the potential for radiated electromagnetic fields from external radio frequency (RF) transmitters and passenger carried portable electronic devices (PEDs) to excite the FQIS enough to cause arcing, sparking or excessive heating within the fuel tank.

14. SUBJECT TERMS
PED, EMI, NTSB, TWA-800, FQIS, EMI, HIRF, RF, electromagnetic, fuel, radio quantity, spark, arc, ignition, Method of Moments, Modal, impedance, Smith

15. NUMBER OF PAGES
200

16. PRICE CODE
A09

17. SECURITY CLASSIFICATION OF REPORT
Unclassified

18. SECURITY CLASSIFICATION OF THIS PAGE
Unclassified

19. SECURITY CLASSIFICATION OF ABSTRACT
Unclassified

20. LIMITATION OF ABSTRACT
UL